Topological insulators in two dimensions have received much attention recently because they are theoretically expected to show properties that make them very attractive for spintronics applications. For example, they feature spin-momentum-locked edge states that are protected from elastic backscattering. However, current experiments are not able to unambiguously observe all of these predicted characteristics.

One big part of this thesis is dedicated to a better understanding of these experimental shortcomings from a theoretical perspective by studying an important model Hamiltonian which describes the currently most important realization of a two-dimensional topological insulator: quantum wells built from mercury telluride. To this end, the influence of disorder and external magnetic fields is considered. Moreover, the effects of phase-coherence breaking due to inelastic processes are quantitatively investigated and it is shown that they may provide an explanation for the experimentally observed on-edge backscattering.

In addition, the thesis contains a treatise on heterostructures of metallic systems and two-dimensional topological insulators, in which it is shown that such heterostructures generally give rise to perfectly conducting channels, which inherit the protection from backscattering from the topological insulator edge states.

The last part of the thesis deals with transmission-eigenvalue distributions of star-shaped diffusive many-lead devices. Here, it is shown that these distribution functions often feature a cutoff, i.e., a maximal transmission above which the probability of finding a transmission eigenvalue drops to zero. This makes this many-lead scenario very different from the well-known case of two-terminal diffusive transport. The cutoff is seen to be dependent on the geometry and on the total transmission through the device.

Essert Mesoscopic Transport in Topological Insulator Nanostructures

Mesoscopic Transport in Topological Insulator Nanostructures

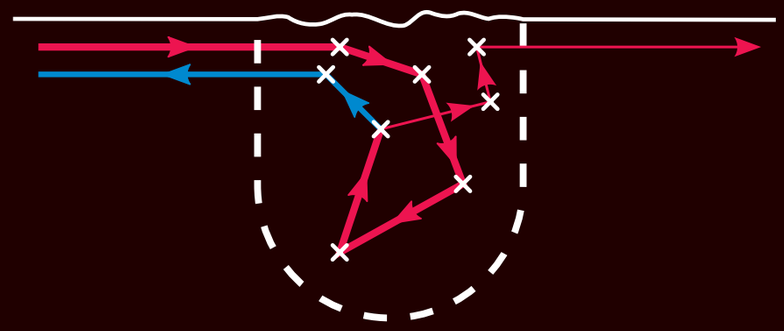

Sven Essert

Mesoscopic Transport in Topological Insulator Nanostructures

Dissertation
zur Erlangung des Doktorgrades
der Naturwissenschaften (Dr. rer. nat.)
der Fakultät für Physik
der Universität Regensburg

vorgelegt von
Sven Essert
aus
Friedberg (Hessen)

im Jahr 2015

Das Promotionsgesuch wurde am 19.10.2015 eingereicht.
Das Kolloquium fand am 18.03.2016 statt.

Die Arbeit wurde von Prof. Dr. Klaus Richter angeleitet.

Prüfungsausschuss:	Vorsitzender:	Prof. Dr. Dieter Weiss
	1. Gutachter:	Prof. Dr. Klaus Richter
	2. Gutachter:	Prof. Dr. Ferdinand Evers
	weiterer Prüfer:	Prof. Dr. Tilo Wettig

Contents

Chapter 1
Introduction

The concept of topological insulators [1, 2] can be considered one of the landmark discoveries in the field of solid-state physics in the last decade. At the time of the discovery, it was quite surprising to many that there was still something new and unknown to be found in the classical band theory of solids: insulators with band structures that differ from band structures of common insulators in terms of topology (and hence the name). After all, band-structure theory has been and still is the work horse of condensed matter physics since its development almost a century ago, and it was thought to be already well understood.

When considering phase transitions between two such insulators that differ in their topology, for example between a topological insulator and a "normal" insulator, one encounters another surprising aspect about this new class of insulators: While in Landau's classical theory [3], a phase transition usually goes hand in hand with the breaking of a symmetry of the system and a local order parameter that quantifies the degree of the symmetry breaking, this is entirely different for transitions between band insulators which differ in their topology. Not only does this phase transition leave the symmetry of the system unchanged (as was already noted for the phase transition between integer quantum Hall plateaus, which can be considered the first experimentally realized "topological insulators"): In many cases, band insulators with a "non-trivial topology" only exist if there is an underlying symmetry that protects them [4, 5]. If the symmetry is broken, many band insulators lose their distinction and it even turns out to be impossible to find topological insulators in one or three dimensions if there are no additional symmetries present. Also, it is not possible to characterize topological insulators by means of a local order parameter.

These newly discovered topologically different band insulators are first of all conceptually very interesting and, by now, they have triggered many theoretical developments even beyond solid-state physics (e. g., in optics and acoustics). More importantly, they also show properties that make them very promising for applications. This mainly has to do with the fact that even though topological insulators are bulk insulators, they feature conducting surface states that arise due to the topologically non-trivial nature of the band structure. In this way, they can be used to easily implement conducting systems of lower dimensionality. Additionally, depending on the symmetry that is behind

the protection of the topological insulator, these "surface states" may show very exotic properties ranging from perfect transmission as in the case of the integer quantum Hall states [6] to non-Abelian statistics as is found for surface states of topological superconductors [7]. The latter, which have some similarities to Majorana fermions and therefore are called Majorana bound states, are envisioned to become important on the road toward topological quantum computation, in which they may allow for relatively robust implementations of (some) quantum logic operations [8, 9].

In this thesis, we will exclusively study topological insulators that are protected by time-reversal symmetry, a symmetry that is usually preserved in solid-state systems that are free of magnetic fields. This particular class of topological insulators exists in two and three dimensions and their surface states also show interesting properties. For example, they may feature surface band structures that can be approximated by single, i. e., non-degenerate, Dirac cones [10], a property that would be forbidden for true bulk systems due to the Fermion doubling theorem [11]. In addition, the surface states typically show a phenomenon that is known as "spin-momentum locking" meaning that the spin is uniquely linked to the propagation direction [12]. This makes them very appealing for spintronics [13], the attempt to implement digital electronics on the basis of the carrier spin polarization. Moreover, hybrid structures with such topological insulators and superconductors are another possible route to realize the abovementioned Majorana bound states [14–16].

However, in practice, there are still many impediments and puzzles, e. g., it is often difficult to produce truly bulk insulating samples, which is a particularly pressing problem for three-dimensional topological insulators. For two-dimensional systems, there are realizations like the HgTe/CdTe quantum wells that do not suffer from this but they are known to have other issues. For example, one experimentally observes edge-state backscattering [17] even though this is theoretically forbidden at very low temperatures [18]. This feature, which is also observed in InAs/GaSb quantum wells [19], another material system that realizes a two-dimensional topological insulator [20], is so far difficult to explain.

In one part of this thesis, we will focus on a better understanding of this "imperfection". We find this particularly important as a better understanding of the observed backscattering may show up ways how to improve the experimental samples. Besides this, we also study other deviations from the clean elastic symmetry-preserving transport regime, in which one expects the edge to be perfectly conducting. For example, we investigate the effect of disorder in combination with an externally applied magnetic field to test the fragility of edge-state transport to mild symmetry breaking.

In addition to these studies that are closely related to current experiments, we also take a more conceptual point of view and generally explore transport in hybrid systems in which topological insulators are combined with non-insulating systems. As will be seen, this leads to the emergence of induced perfectly conducting channels in the metallic region.

At last, this thesis contains a study that deals with a more general aspect of mesoscopic transport in nanostructures which is not restricted to topological insulators: We investigate transport in diffusive systems with more than two leads with particular focus on the emerging transmission-eigenvalue distributions.

In the following, we will provide a short summary of the upcoming chapters and explain how they relate to the topic of this thesis: mesoscopic transport in topological insulators.

In **Chapter 2**, we introduce the concept of topological insulators, motivate why it leads to the emergence of surface states and how one can understand that the topological classification depends on the protecting symmetry. Then we specialize on time-reversal symmetry-protected topological insulators and show why they are expected to feature interesting transport properties. In the end, we will focus on a particular experimental realization of two-dimensional topological insulators that are protected by time-reversal symmetry: quantum-well systems made from HgTe and CdTe, which are not only the first but probably also the best-established realization of a two-dimensional topological insulator. We introduce the model Hamiltonian used to describe this material system, which will be studied throughout the thesis, and show some basic properties of the topological edge states arising from it.

This sets the stage for **Chapter 3**, in which we use this model for a numerical transport study of HgTe/CdTe quantum wells in the topological insulator phase. The main focus will be on the influence of disorder and an additionally applied perpendicular magnetic field [21]. This is interesting as it shows what to expect for the stability of edge transport under the influence of an explicit symmetry breaking. In the course of the chapter, we will see that while one-dimensional edge transport is surprisingly robust under the influence of magnetic fields and short range disorder, this drastically changes when long-range fluctuations of the electrostatic potential (so-called charge puddles) are considered. Such puddles give rise to strong backscattering with applied fields and we will see that their presence may be able to explain the measured results for the magnetoconductance in some samples.

Charge puddles will also be at the heart of **Chapter 4**, in which we study a scenario that might explain the experimentally observed temperature-independent backscattering of the topological edge states [22]. As this is incompatible with a coherent and fully elastic theory, we will study the effect of decoherence due to inelastic interactions. For this, we will use an effective model and also propose an extension to wave-packet transport algorithms, which allows for an explicit treatment of dephasing during the time propagation. In this way, we will be able to quantitatively estimate the influence of dephasing on HgTe/CdTe quantum-well edge transport.

In **Chapter 5**, we return to an elastic and fully coherent transport scenario and we try to go beyond the results obtained from charge puddles in Chapter 3 by turning more generally to the phenomena that arise in heterostructures of metals and topological insulators [23]. For this, we first consider a simple model from which we discover that such heterostructures generally feature perfectly conducting channels that are extended across the metallic regions. Later in the chapter, we show how these may be detected in experimental setups built from HgTe/CdTe quantum wells. In addition, we demonstrate that the emergence of perfectly conducting channels can be understood by means of an effective boundary condition, which mimics the proximity to a two-dimensional topological insulator. This will provide ideas how to induce perfectly conducting channels in other wave-guide structures even without the explicit presence of topological insulators.

During the study of experimental setups that allow for the detection of the induced perfectly conducting channels, we will also consider shot-noise measurements in multi-

terminal devices. Here, we find that the transmission-eigenvalue distributions that arise in such devices are interesting and by far not as well understood as in the simpler case of only two terminals. This motivates the study in **Chapter 6**, in which we study transport in general diffusive multi-terminal devices. The chapter will be a small detour from the main theme of this thesis in the sense that we will not use or study any properties that are particular to topological insulators. Yet, we will be considering mesoscopic transport using similar methods as in the rest of the work. We consider star-shaped diffusive conductors with scattering-matrix models, which we later evaluate using numerical wave-transport calculations. From this, we are able to derive analytical expressions for the transmission-eigenvalue distributions of transmission matrices between pairs of leads in some limiting cases and propose the study of a novel observable that characterizes the splitting of eigenvectors across the leads of a multi-terminal structure.

At last, **Chapter 7** will wrap up and relate the findings of the previous chapters and attempt an outlook toward future research directions.

Chapter 2
Topological insulators

2.1 Topology in solid-state physics

Topology, the discipline of mathematics that studies properties which are robust to "continuous" deformations, has been influential and inspiring to many fields of physics, ranging from the famous study of magnetic monopoles by Dirac [24] to general relativity and quantum field theory [25]. Though, its importance for solid-state physics had not been realized for a long time. It was only with the discovery of the integer quantum Hall effect in the 1980s, which could subsequently be interpreted in terms of a topological invariant by Thouless, Kohmoto, Nightingale, and den Nijs (TKNN) [26, 27], that one found an example in which band structures of solids differed by their topology. However, it took another 20 years to realize the generality of this result. Then, Kane and Mele found a new example for a band insulator with a non-trivial band topology when studying graphene with intrinsic spin-orbit coupling [2, 18]. Here, it was realized that the presence of symmetries, which in the particular case of graphene is the conservation of time-reversal symmetry, allows for a plethora of new topological phases. This opened up the new field of symmetry-protected topological insulators, which tries to classify these topological phases and studies their properties. Up to today, this field has grown and advanced a lot, and now it even covers topological phenomena in metallic phases, like Weyl [28, 29] and Dirac semimetals [30], or extends to exotic symmetries, e. g., so-called statistical symmetries, which are only conserved on the average [31]. Also, the search for topological phenomena in band structures is no longer limited to electrons in solids but now extends to many other fields, like magnonic insulators [32], phonons in mechanically-coupled oscillators [33], acoustic waves in metamaterials [34], cold atoms [35, 36], photonic quasicrystals [37], and periodically driven systems [38, 39], just to mention a few.

In this work, we will not cover most of these more recent developments and we will stick to the class of systems that was originally proposed by Kane and Mele, i. e., topological insulators (TIs) that are protected by time-reversal (TR) symmetry. Even though these systems have been around for a few years by now, many of their properties are still subject to fundamental research, a few of which will be investigated in this thesis. Before we come to that, we try to give a brief introduction on the relation of topology and solid-state physics and add a little background information, which will help to better understand the

context of this work. However, this introduction will be limited to topological phenomena in insulating materials which can be treated by Fermi liquid theory, such that an effective single-electron band-structure description is meaningful. Even though topological order may in general also be very important for strongly correlated systems, they will not be treated in this thesis.

As the treatment in the following sections is meant as a concise introduction to all the concepts and results that we consider necessary for this work, it will be very brief and it will be lacking much of the mathematical rigor that one may wish for. Especially, it will almost be free of any formal mathematical proofs. For a more comprehensive introduction into the subject, we refer to current textbooks on the matter [40–42].

2.2 Topological insulators

2.2.1 Chern insulators and the integer quantum Hall effect

Viewing the band theory of solids from a mathematical perspective, the electronic properties of a material are fully described by a Hermitian operator $H(\mathbf{k})$, which continuously depends on a set of periodic parameters (the Bloch wave vectors which are periodic in the Brillouin zone of the lattice), in combination with an energy E_F (the Fermi energy), which determines the energy below which all bands are occupied at low temperatures. A *band insulator* is characterized by a spectral gap of the operator $H(\mathbf{k})$ around E_F. The goal is to come up with a topological classification of band insulators, i. e., classify them in terms of "continuous" transformations. To be precise what is meant by "continuous" in this particular case, one may define the following topological classification scheme:

Definition 2.1 (**Chern insulator classification**)**.** Two insulators, $\{H_1(\mathbf{k}),\, E_\mathrm{F}^1\}$ and $\{H_2(\mathbf{k}),\, E_\mathrm{F}^2\}$, (with the same number of filled bands) are topologically different if there is no "homotopy", i. e., no continuous function $\{H(\mathbf{k}, a),\, E_\mathrm{F}(a)\}$ from the unit interval, $a \in [0, 1]$, to the space of Hamiltonians and Fermi energies that interpolates between the two insulators, $\{H(\mathbf{k}, a = 0),\, E_\mathrm{F}(a = 0)\} = \{H_1(\mathbf{k}),\, E_\mathrm{F}^1\}$ and $\{H(\mathbf{k}, a = 1),\, E_\mathrm{F}(a = 1)\} = \{H_2(\mathbf{k}),\, E_\mathrm{F}^2\}$, with the property that $\{H(\mathbf{k}, a),\, E_\mathrm{F}(a)\}$ is an insulator [has no state at $E_\mathrm{F}(a)$] for all a.

At first glance, it is not obvious that this definition will allow any differences in insulator topology as it might just as well be that, given this scheme, all insulators turn out to be in the same topological equivalence class. To answer this question about the existence of different equivalence classes, one needs to solve the full mathematical problem which in this particular case boils down to the classification of maps from n-dimensional tori (the Brillouin zone) to the space of N-dimensional subspaces of $\mathbb{C}^{N\times M}$ (the so-called Grassmannian), with N being the number of occupied and M being the number of unoccupied bands [5]. From this, one finds that, given the above classification scheme, all insulators are in the same topological class if the dimension of space, n, is odd. If the spatial dimension is even (the two-dimensional case being physically the most relevant), however, one can show that different topological equivalence classes exist, i. e., that one can find insulators which differ in their topology. The number of such classes is infinite

and can be labeled by an integer number, which is why one calls such insulators to be $\mathbb{Z}$ classifiable. Given a specific insulator $\{H(\mathbf{k}),\, E_\mathrm{F}\}$, one can conveniently work out the corresponding integer number, which specifies the topological class that it belongs to, by calculating the so-called *total first Chern number,* which in this context is also called the TKNN invariant (see above). For two-dimensional (2d) insulators, it takes the form [43]

$$C_1 = \sum_{n:\, E_n(\mathbf{k})<E_\mathrm{F}} \frac{-i}{2\pi} \int_\mathrm{BZ} d^2\mathbf{k}\, \left(\nabla \times \langle u_n(\mathbf{k})|\nabla u_n(\mathbf{k})\rangle\right) \cdot \hat{z}, \tag{2.1}$$

with

$$H(\mathbf{k})\,|u_n(\mathbf{k})\rangle = E_n(\mathbf{k})\,|u_n(\mathbf{k})\rangle \tag{2.2}$$

if the insulator is positioned in the xy-plane. In other words, the Chern number is calculated as a sum over all occupied bands of the insulator (which is why the specification of the Fermi energy is important), in which one is summing up a Brillouin-zone integral for each band. The integrand is known from other contexts as the *Berry curvature* [44]. Mathematically, this makes this definition similar to the classification of closed orientable surfaces in three-dimensional space: There, one finds that the *genus,* an integer number that categorizes topologically different surfaces by counting the number of holes in the surface, can also be obtained by an integral over what is known as the Gauss curvature.

It is important to note that the classification of insulators is not merely an interesting mathematical feature. Instead, it can also be seen to be of relevance for physical observables as one can show from linear response theory that the Hall conductance of a two-dimensional insulator is given by [27, 43, 45]

$$\sigma_{xy} = \frac{e^2}{h} C_1, \tag{2.3}$$

and is thus directly proportional to the topological invariant. As this invariant only attains integer values, one can immediately understand the observed quantization of the Hall plateaus in the integer quantum Hall effect on the grounds of this topological argument. The quantization is also very stable as the invariant can only change if the band gap closes, thus small changes in the material parameters will not modify the Hall conductivity as long as they are weak enough to keep the band gap open. Notice that this argument so far does not include any effects due to strong disorder, which is out of scope of this band picture. Weak disorder which allows for a mean-field treatment or any other inclusion by effective band-structure parameters can be included though.

However, we will see in the next section that there are stronger arguments which guarantee the quantization of the Hall resistance also in the case of strong disorder, at least as long as the bulk material remains insulating.

2.2.2 Bulk-boundary correspondence

One may wonder how an insulating structure can give rise to a finite Hall conductance. The answer to this can also be traced back to topology. If one makes a heterostructure

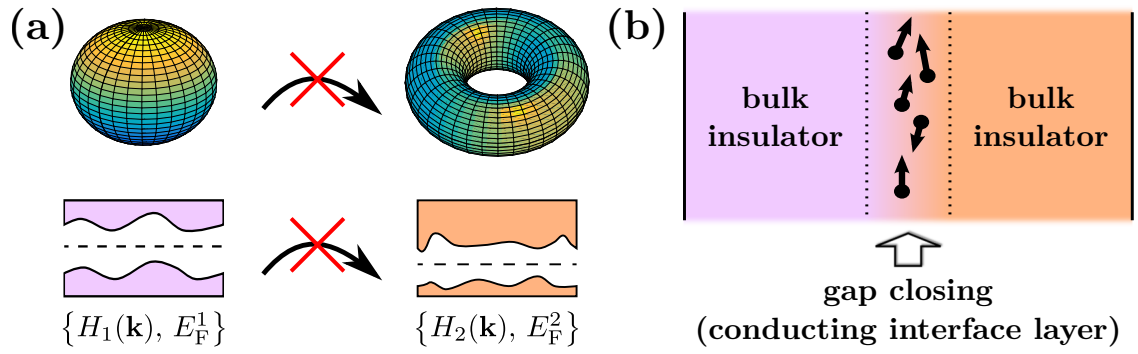

Figure 2.1: This figure illustrates the bulk-boundary correspondance and the physical importance of a topological classification of bulk insulators. If two insulators are topologically distinct as depicted in (a), there is no continuous deformation that connects them that keeps the band gap open. This is similar to the widely known topological classification of closed surfaces, for which one knows that a sphere cannot be smoothly deformed into a torus as one has to close a hole which introduces a discontinuity. In a heterostructure of two such topologically distinct insulators, shown in (b), this becomes physically relevant. Here, the impossibility of a continuous transition between the two bulk materials that keeps the band gap intact enforces a gap closing at the interface, leading to conducting interface states.

between two insulators which differ in their Chern number, we know from Definition 2.1 that there can be no continuous interpolation between the two which leaves the band gap open. They are topologically distinct in a similar fashion as a sphere and a torus, which cannot be smoothly deformed into another, cf. Fig. 2.1(a). However, in a smooth heterostructure of the two insulators, as depicted in Fig. 2.1(b), we expect a continuous change of the Hamiltonian. Therefore, a gap closing is expected somewhere along the heterostructure. This leads to metallic states at the interface. For the specific case of Chern insulators, one can show that the number of edge states that one finds at such an interface is directly related to the difference of the Chern numbers of the adjacent insulators that make up the interface [46, 47]. Moreover, for Chern insulators, these edge states are chiral, meaning that they all propagate in one direction at one interface. Therefore, transport along these edge states is free of backscattering as there are no counterpropagating states at the same edge. This explains why the observed quantum Hall plateaus are remarkably stable and show a very precise conductance quantization. In Fig. 2.1(b), the shown states are not chiral. The reason for this is that this is no property that is enforced by the simple topological argument that the band gap needs to close. In fact, the chiral transport is a peculiarity of Chern insulators, and, as we will see later, there are other TI classifications that enforce conducting interface states in heterostructures that can propagate both ways.

One should add that vacuum can also be viewed as a wide-band semiconductor, which can be fit into the scheme above, yielding $C_1 = 0$. In this way, insulators which have a topological invariant different from vacuum ($C_1 \neq 0$ for Chern insulators) will show edge states already at a simple lattice termination (a boundary to vacuum), which is why they are called "topologically non-trivial". Insulators with the same classification as vacuum, on the other hand, are termed "topologically trivial".

From an application perspective, heterostructures with insulators of non-trivial topology

are very appealing because they allow for an easy creation of conducting low-dimensional systems, which may, as in the case of Chern insulators, even show exotic transport properties. Here, it is important to note that the concept of obtaining a lower-dimensional metallic system from a heterostructure of two insulating systems that differ in their topology is quite general. It would, of course, also apply to heterostructures of insulators in three dimensions, which would yield a 2d metallic system at the interface. However, as we noticed in the last section, the classification according to Definition 2.1 does not allow for non-trivial topology in three (or one) dimensions. Yet, as we will see in the next section, there is a possibility to extend Definition 2.1 which opens up a whole new zoo of topological classifications in all dimensions.

Before this, let us stay with Chern insulators for a second. As we discussed, those are limited to two (or more generally even) dimensions. In addition, what is maybe more problematic from an applications point of view, non-trivial insulators can only be found when TR symmetry is broken. This is so because σ_{xy}, the Hall conductivity, which is directly linked to the topological invariant, cf. Eq. (2.3), is odd under time reversal[1], which implies $\sigma_{xy} = C_1 = 0$ for TR-symmetry-preserving systems. For a long time, one thought that such topologically non-trivial states can only be observed at high external magnetic fields as present in the observation of the integer quantum Hall effect. Very recently however, a *quantum anomalous Hall insulator* could be realized which is a material that shows a non-trivial Chern number (and therefore has chiral edge states) at zero external magnetic field [49]. In this case, TR-symmetry breaking was realized by an internal magnetic ordering. This is conceptually similar to the famous theoretical model by Haldane [50], which describes the observation of a quantized Hall conductance in a graphene-like system that is subject to a staggered magnetic field, which has equal magnitude but opposite sign on the two sublattices such that the overall magnetic field is zero.

2.2.3 Symmetry-protected topological insulators

Starting with the work of Kane and Mele [2, 18], who observed edge states in graphene when including the effect of intrinsic spin-orbit coupling, which could subsequently be interpreted by topological arguments [51], one found that there is a natural extension to the concept of insulator topology, Definition 2.1, in the case where the Hamiltonian has additional symmetries:

Definition 2.2 (**symmetry-protected topological insulator classification**)**.** Two insulators, $\{H_1(\mathbf{k}),\, E_\mathrm{F}^1\}$ and $\{H_2(\mathbf{k}),\, E_\mathrm{F}^2\}$ (with the same number of filled bands), which both have a discrete symmetry, e. g., they commute with the (anti-)unitary operator $\mathcal{O}$, are called "topologically different under the protection of the symmetry" if there is no "homotopy", i. e., no continuous function $\{H(\mathbf{k}, a),\, E_\mathrm{F}(a)\}$ from the unit interval, $a \in [0, 1]$, to the space of Hamiltonians and Fermi energies which interpolates between the two insulators, $\{H(\mathbf{k}, a = 0),\, E_\mathrm{F}(a = 0)\} = \{H_1(\mathbf{k}),\, E_\mathrm{F}^1\}$ and $\{H(\mathbf{k}, a = 1),\, E_\mathrm{F}(a = 1)\} = \{H_2(\mathbf{k}),\, E_\mathrm{F}^2\}$, with the property that $\{H(\mathbf{k}, a),\, E_\mathrm{F}(a)\}$ is an insulator [has no state at $E_\mathrm{F}(a)$] and that $H(\mathbf{k}, a)$ preserves the symmetry for all a.

[1] see, e. g., Ref. [48]

Table 2.1: This table reproduces the results from the topological classification of Refs. [4, 5]. The entries in the columns for the symmetries specify whether the symmetry is present and whether the respective (anti-)unitary operator squares to +1 or -1. The entries in the three rightmost columns show in which dimensions topologically non-trivial states can be found, given that one preserves the listed set of fundamental symmetries. It also shows whether one can expect an infinite number of topologically distinct phases ($\mathbb{Z}$) or whether there is just a finite number of at least 2 topologically different phases classified by a set of $\mathbb{Z}_2$ integers.

Altland-Zirnbauer name	Symmetries			Topological classification		
	TRS	PHS	SLS	1d	2d	3d
A	no	no	no	-	$\mathbb{Z}$	-
AI	+1	no	no	-	-	-
AII	-1	no	no	-	$\mathbb{Z}_2$	$\mathbb{Z}_2$
AIII	no	no	yes	$\mathbb{Z}$	-	$\mathbb{Z}$
BDI	+1	+1	yes	$\mathbb{Z}$	-	-
CII	-1	-1	yes	$\mathbb{Z}$	-	$\mathbb{Z}_2$
D	no	+1	no	$\mathbb{Z}_2$	$\mathbb{Z}$	-
C	no	-1	no	-	$\mathbb{Z}$	-
DIII	-1	+1	yes	$\mathbb{Z}_2$	$\mathbb{Z}_2$	$\mathbb{Z}$
CI	+1	-1	yes	-	-	$\mathbb{Z}$

This additional constraint of preserving the symmetry along the full path between the two systems has a strong influence on the mathematical classification and on the existence of possible topological equivalence classes in various dimensions. For example, we already learned in the last section that if one preserves TR symmetry, one cannot reach the non-trivial Chern insulator classes. From this, one might think that with the additional symmetry constraint in Definition 2.2, one cannot find any non-trivial topological states in two dimensions. However, this is not the case as it turns out that there are TR-symmetric insulators which are in the same equivalence class ($C_1 = 0$) according to Definition 2.1 (they can be connected by a homotopy that breaks TR symmetry) but they remain disconnected when TR symmetry is enforced along the connection path. Therefore, they fall into different classes when using Definition 2.2. Thus, the limitation of the number of possible homotopies can also lead to the emergence of new topological phases, which are then said to be protected by the underlying symmetry as they lose their topological distinction when the symmetry is broken.

The full classification of all possible symmetry-protected TIs in all dimensions is still an ongoing project. However, for the important fundamental (Altland-Zirnbauer [52]) symmetry classes it has already been completed [4,5] and Table 2.1 shows the result of this classification. The listed fundamental symmetries according to which the classification is done are discussed in the following: *Time-reversal symmetry* (TRS), which is the existence of an anti-unitary operator $\mathcal{T} = TK$, which commutes with H, i. e.,

$$\mathcal{T}H = H\mathcal{T}, \tag{2.4}$$

with K meaning complex conjugation and a unitary operator T. This in turn is equivalent to the following relation for the free bulk Hamiltonian $H(\mathbf{k})$:

$$TH^*(-\mathbf{k})T^{-1} = H(\mathbf{k}). \tag{2.5}$$

The next symmetry used in the classification is *particle-hole symmetry* (PHS), which is again an anti-unitary symmetry, which in a similar fashion to before can be expressed as the existence of a unitary operator C such that

$$CH^*(-\mathbf{k})C^{-1} = -H(\mathbf{k}). \tag{2.6}$$

The last symmetry in the table is the so-called *sublattice symmetry* (SLS), which is a (unitary) symmetry under the combined application of T and C, i. e.,

$$TCH(\mathbf{k})C^{-1}T^{-1} = -H(\mathbf{k}). \tag{2.7}$$

Whether the operators C and T square to +1 or -1 makes a difference in the symmetry classification. In this way, one finds the classes listed in Table 2.1, which have been named by Altland and Zirnbauer referring to Cartan's classification of symmetric spaces [53, 54]. The last three columns of the table show the result of the classification. $\mathbb{Z}$ means that for this particular symmetry constraint and this dimensionality, there are countably infinitely many topologically distinct insulators, while $\mathbb{Z}_2$ means that there is only a finite number of topologically different insulators in this symmetry class, which are labeled by a set of $\mathbb{Z}_2$ numbers. There are also many combinations of symmetries and dimensionalities in which no non-trivial topological states can be found.

More recently, the program for the classification of topological states which are protected by a symmetry has been continued to include crystal symmetries like reflection [55, 56] or rotation [57] symmetries. A good overview over the recent progress in the classification of insulators under various symmetries can be found in Ref. [58].

2.2.4 $\mathbb{Z}_2$ topological insulators and time-reversal symmetry

In this thesis, we will study transport in the class of TIs which are only protected by TR symmetry with the time-reversal operator $\mathcal{T}$ squaring to minus one, $\mathcal{T}^2 = -1$, as expected for spin-1/2 particles (Altland-Zirnbauer class AII). As we can read off from Table 2.1, this leads to a $\mathbb{Z}_2$ classification in two and three spatial dimensions. As symmetry-protected TIs of this class were the first discovered, one sometimes just refers to them as *topological insulators* or $\mathbb{Z}_2$ *topological insulators.* The fact that they are protected by a TR symmetry which squares to minus one has important consequences for their transport properties, which is why we will recapitulate some basic consequences of this symmetry in this section.

A Hamiltonian H that preserves TR symmetry, $H\mathcal{T} = \mathcal{T}H$, with $\mathcal{T}^2 = -1$ has a doubly degenerate spectrum and the two degenerate states $|\phi\rangle$ and $|\psi\rangle$ are related to another by the TR operator, $|\phi\rangle = |\mathcal{T}\psi\rangle$ (Kramers theorem) [59]. This is easily seen as the commutation relation obviously guarantees that if $|\psi\rangle$ is an eigenstate of H with energy E, $|\mathcal{T}\psi\rangle$ is also an eigenstate with the same energy. For the overlap of the two

states, one obtains

$$\langle\psi|\mathcal{T}\psi\rangle = \left\langle\mathcal{T}^2\psi|\mathcal{T}\psi\right\rangle = -\langle\psi|\mathcal{T}\psi\rangle = 0, \tag{2.8}$$

in which we used the property that the TR operator $\mathcal{T}$ is anti-unitary. Thus, the two states $|\psi\rangle$ and $|\mathcal{T}\psi\rangle$ are orthogonal, meaning that there are really two degenerate states at this energy.

The degeneracy from Kramers theorem holds for all states of the Hamiltonian including edge states that might arise for topological reasons. Thus, if we consider a heterostructure of two TR-symmetric insulators with a different topological classification, the edge states that we will find—due to the continuity argument brought up in the context of topology for Chern insulators which guarantees a gap closing at the interface—will always come in pairs. This is in contrast to the Chern (integer quantum Hall) insulators discussed above. Also, the two degenerate edge states will be related to another by TR symmetry, which flips the momentum and the spin of the states,

$$\mathcal{T}\,|k,\uparrow\rangle = |-k,\downarrow\rangle\,. \tag{2.9}$$

Therefore, these states will have what is known as a *helical spin texture* meaning that states moving in one direction have the spin pointing opposite to the states which move in the other direction. If there are no more degeneracies of the states, this excludes a uniaxial alignment of the spins, and one will often observe *spin-momentum locking*, i. e., a fixed coupling of the spin and the propagation direction. However, there are certain momenta in the Brillouin zone of the material, the so-called *time-reversal invariant momenta* (TRIM), which are left unaffected by TR symmetry, e. g., $\mathbf{k} = 0$ for which $\mathbf{k} = -\mathbf{k}$. At these single points, the spectrum will always be spin degenerate and we will see that these points will play an important role for the discussion of the surface band structure later.

There is one more consequence of TR symmetry that is closely related to Kramers theorem. This is the forbidden scattering between the Kramers degenerate states (the Kramers pair) $|\psi\rangle$ and $|\mathcal{T}\psi\rangle$. It may be seen as follows: Suppose there is any perturbing Hamiltonian H_1 that causes scattering between states, e. g., a disorder potential, which however preserves TR symmetry, $H_1\mathcal{T} = \mathcal{T}H_1$. Then, this Hamiltonian will never couple states of a Kramers pair,

$$\begin{aligned}\langle\psi|H_1\mathcal{T}\psi\rangle &= \langle\mathcal{T}H_1\mathcal{T}\psi|\mathcal{T}\psi\rangle = \left\langle H_1\mathcal{T}^2\psi|\mathcal{T}\psi\right\rangle \\ &= -\langle H_1\psi|\mathcal{T}\psi\rangle = -\langle\psi|H_1\mathcal{T}\psi\rangle = 0,\end{aligned} \tag{2.10}$$

where we also used the anti-unitary property of $\mathcal{T}$ and the Hermiticity of H_1. This *forbidden backscattering* will be particularly important when considering transport of 2d-TI edge states.

Equipped with this background knowledge, we are now in the position to get a clearer picture of the nature of the topologically non-trivial state in this symmetry class. As said before, we expect a $\mathbb{Z}_2$ classification and it turns out that in two dimensions there are indeed just two types of topologically different phases, one of the two being called the

non-trivial phase. In this phase, one finds that there is always an odd number of Kramers pairs of surface states at every energy [10]. While a perturbation that preserves TR symmetry can easily couple states from different Kramers pairs and open a gap, the two states of a pair cannot be coupled directly, cf. Eq. (2.10). This means that Kramers pairs cannot just disappear but each Kramers pair has to hybridize with another Kramers pair to gap out. This preserves the parity of the number of Kramers pairs of surface states, so an insulator with an odd number of (pairs of) surface states will always keep this odd number and will be topologically different from an insulator with an even number of (pairs of) surface states as the even number of surface states allows the surface bands to gap out completely.

Another way to see this in a band-structure picture is to look at an illustration that was brought up by Fu, Kane, and Mele [10], and which is shown in Fig. 2.2. In the panels (b)–(d), Fig. 2.2 shows possible band structures of a semi-infinite 2d insulator plane, which is sketched in panel (a), and for which the energies are plotted versus the longitudinal momentum k. There is just one free momentum in this case and the Brillouin zone is a one-dimensional line ranging from $k = -\frac{\pi}{a}$ to $k = \frac{\pi}{a}$, with a being the lattice constant along the structure. Shaded in light green color, we see the bulk conduction and the bulk valence band. Also, the position of the Fermi energy is marked. In addition to the shown continuum of bulk states, there may be surface states, which usually come as a discrete set of states that are bound close to the insulator-vacuum interface. Those surface states are not necessarily found in the same energy window as the bulk states and may well form bands inside the insulating bulk gap. In Fig. 2.2(b)–(d), such possible sets of surface states are sketched in black as an illustration. Of course, the surface states, like the whole band structure, must respect TR symmetry and therefore the picture is mirror symmetric around $k = 0$ and there is an enforced degeneracy of states at the TRIM, i. e., at $k = 0$ and $k = \pm\frac{\pi}{a}$. Between these points, the states may well split up and they usually will because of spin-orbit coupling arising from the broken inversion symmetry at the interface (an effect known as *structure-inversion asymmetry*). Now, there are exactly two possible ways in which the surface state bands can connect between the TRIM: one, which is shown in Fig. 2.2(b), where both states originating at $k = 0$ rejoin at $k = \pm\frac{\pi}{a}$; or a situation that is shown in Fig 2.2(c), where the surface states change partners in between the two TRIM. In the former case, in which there will always be an even number of Kramers pairs at E_F, a surface potential could shift the surface bands up or down and could create a true gap. In the latter case however, there will obviously always be a conducting state crossing the Fermi energy for any value of E_F inside the gap, making this the topologically non-trivial phase, in which also the number of Kramers pairs at the Fermi energy will always be odd. Here, the number of pairs is always one for illustration purposes but, as discussed before, one could add an arbitrary number of trivial surface bands, like the ones shown in Fig. 2.2(b), without destroying this protection and changing the topology. The surface bands may hybridize with the bulk bands, which is why they are only shown as dashed lines once their energy and momentum overlaps with the bulk continuum. For a topologically non-trivial situation as shown in Fig. 2.2(c), the fact that the surface bands change partners between the TRIM will usually allow one to approximate the surface band structure around such a crossing point by a linear dispersion, which is why the surface states of TR-protected TIs

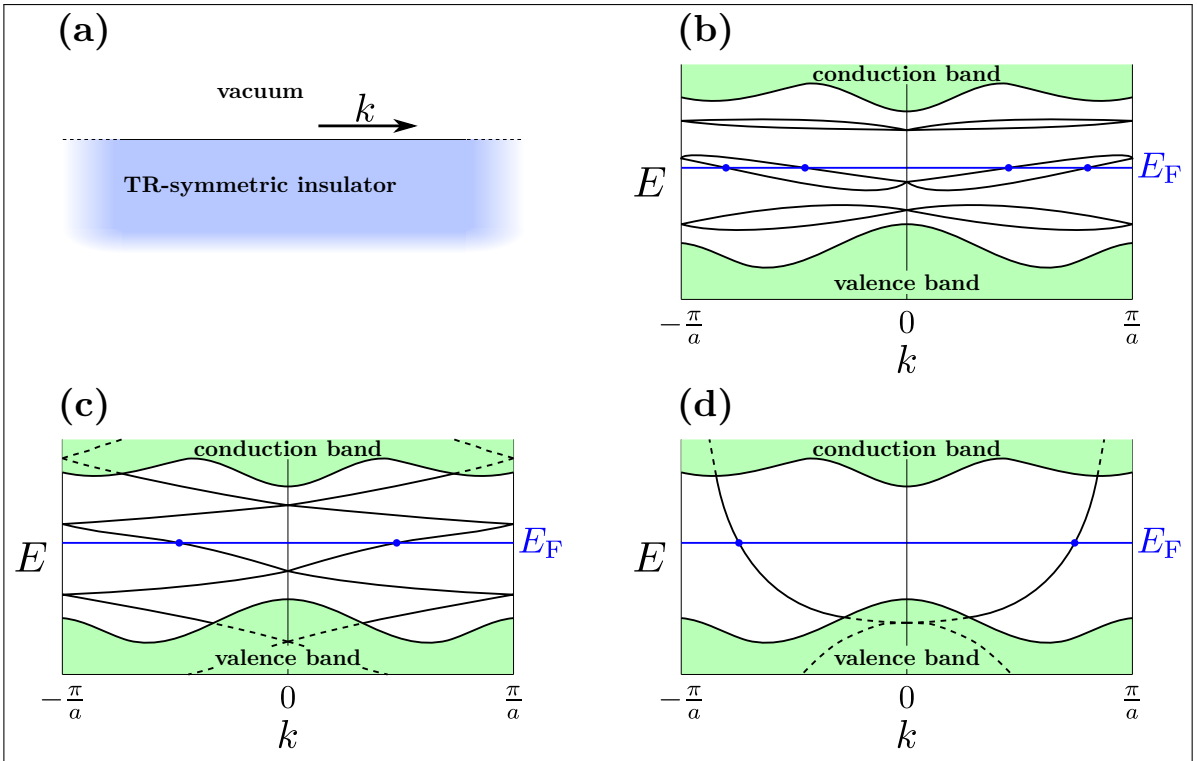

Figure 2.2: This figure illustrates the possible surface band structures of a semi-infinite TR-symmetric insulator as sketched in panel (a) using a similar illustration as Ref. [10]. Due to TR symmetry, the resulting band structure is symmetric in the one-dimensional Brillouin zone. Possible surface band structures are shown in panels (b)–(d). At the TRIM, the surface bands are degenerate and the two states originating from one TRIM may connect to the same degenerate state at the other TRIM, as shown in (b), leading to a topologically trivial situation. Alternatively, they may change partners as in (c) or (d) where a non-trivial situation arises, which leads to an odd number of Kramers pairs at every energy in the gap. (d) illustrates that the surface band structure does not necessarily show a conical/linear dispersion in the topologically non-trivial case.

are usually said to show a relativistic (massless Dirac fermion-like) dispersion. However, even if this is often observed in experiment, one should keep in mind that this linear dispersion is not something that is protected by topological arguments. For example, in a situation shown in Fig. 2.2(d), in which the crossings of the surface bands at the TRIM are deeply buried in the valence and the conduction bands, where they may strongly hybridize with the bulk bands, the notion of a linear surface band dispersion or a Dirac cone may lose its experimental relevance.

All the arguments discussed in the previous paragraphs carry over to three-dimensional TR-protected TIs. Here, the surface Brillouin zone is two dimensional and one finds four TRIM, between which one can draw similar connectivity patterns as shown in Fig. 2.2. The bottom line of this analysis can be summarized as follows: The fact that the two-dimensional bands change partners at a single point can similarly be approximated by a two-dimensional linear dispersion (a Dirac cone) around the respective TRIM. With this, one can again distinguish two main classes of topologically different insulators: (i) Those which show an even number of non-spin degenerate Fermi surfaces (an even number of Dirac cones) at every physical surface of the three-dimensional material, which one

would consider topologically trivial. And (ii) another class which shows an odd number of Dirac cones at every surface, something that is stable against perturbations because the Dirac cones (similar to Kramers pairs) can only annihilate in pairs to open up a gap. Such a system is called a *strong topological insulator*[2].

Similar as with the Chern insulators above, there is also a more mathematical formulation of this topological non-triviality and one can calculate an invariant from the bulk spectrum [similar to Eq. (2.1) for Chern insulators], which immediately allows for a topological classification of the system. However, for the $\mathbb{Z}_2$ invariant this turns out to be a bit more involved than for the Chern number and there are now many different equivalent formulations and prescriptions how it could be calculated [2, 51, 63–66]. One of the more compact forms to write down the invariant, Ξ, for a 2d TI is given as [51]:

$$(-1)^{\Xi} = \prod_{i=1}^{4} \frac{\sqrt{\det\left[w\left(\Gamma_i\right)\right]}}{\mathrm{Pf}\left[w\left(\Gamma_i\right)\right]}, \tag{2.11}$$

with

$$w_{mn}(\mathbf{k}) = \langle u_m(\mathbf{k}) | \mathcal{T} u_n(-\mathbf{k}) \rangle \tag{2.12}$$

being a matrix that describes the overlap of the occupied states $|u_m(\mathbf{k})\rangle$ at $\mathbf{k}$ with the time-reversed partners of the states at $-\mathbf{k}$. TR symmetry implies the relation

$$w(\mathbf{k}) = -w^T(-\mathbf{k}), \tag{2.13}$$

making $w(\mathbf{k})$ antisymmetric at the four TRIM (which are called Γ_i in this notation) of the 2d system. Thus, the Pfaffian[3], which is only defined for an antisymmetric matrix, is well defined and because of the general relation,

$$\left(\mathrm{Pf}\, A\right)^2 = \det A, \tag{2.14}$$

it is clear that the right-hand side of Eq. (2.11) yields either +1 or -1, making Ξ well defined as a $\mathbb{Z}_2$ quantity. The definition of Ξ in Eq. (2.11) also generalizes to the three-dimensional case, for which the product just has to be extended to the 8 (instead of 4) TRIM in the Brillouin zone.

However, it turns out that the straightforward evaluation according to Eq. (2.11) is very cumbersome in practice. This is so because one first has to find expressions for

[2] The reason those systems are called "strong" is that there is also the notion of a "weak topological insulator". In this way, there are actually more than 2 (but still a finite number, which is classified by $\mathbb{Z}_2$ indices) topologically non-trivial phases in three dimensions given the Definition 2.2. Those weak TIs are systems which have an even number of Dirac cones at the surface but which can still be shown to be topologically non-trivial, in the sense that these Dirac cones are guaranteed to exist at the interface (the bulk band gap really has to close in the sense of Definition 2.2). However, this argument is limited to clean systems. Disorder may hybridize the even number of Dirac cones and may make them surface insulators. They may still show interesting transport phenomena and may even be valuable for applications [60–62]. However, we will not study them in this thesis.

[3] The Pfaffian is defined as a polynomial of the matrix entries of an antisymmetric matrix, similar to the determinant. For a detailed definition, see for example Ref. [67].

the eigenstates of the system $|u_m(\mathbf{k})\rangle$ that are continuous in the whole Brillouin zone as the values of $\delta_i = \sqrt{\det\left[w\left(\Gamma_i\right)\right]}/\operatorname{Pf}\left[w\left(\Gamma_i\right)\right]$ may change with a gauge transformation and only the product $(-1)^{\Delta} = \prod_i \delta_i$ is gauge invariant. Thus, an overall continuous representation is necessary. The problem simplifies a lot if the Hamiltonian also preserves parity symmetry, i. e., if there exists a unitary operator P such that $H(-\mathbf{k}) = PH(\mathbf{k})P^{-1}$. Then one can show [68] that there is a gauge in which one can calculate δ_i as a product of the parity eigenvalues $\xi_m(\mathbf{k})$,

$$P\left|u_m(\mathbf{k})\right\rangle = \xi_m(\mathbf{k})\left|u_m(\mathbf{k})\right\rangle, \tag{2.15}$$

of the eigenstates $|u_m(\mathbf{k})\rangle$ at the TRIM,

$$\delta_i = \prod_{m=1}^{N} \xi_{2m}\left(\Gamma_i\right), \tag{2.16}$$

where one only includes every second eigenvalue (one eigenvalue for each Kramers pair).

For non-centrosymmetric insulators, one may resort to other techniques like the tracking of Wannier charge centers to obtain the $\mathbb{Z}_2$ invariant [69].

2.3 HgTe/CdTe quantum wells

After having introduced the concepts of topologically non-trivial phases that are protected by TR symmetry, it is now time to turn to systems in which such states can be observed. The initial proposal of Kane and Mele [18], which considered graphene with intrinisic spin-orbit coupling, turned out to be unrealistic at least for pristine graphene, where the spin-orbit coupling is estimated to be much too small to create an observable gap [70].

This motivated a search for systems in which relativistic effects are larger such that the gap falls into the experimentally accessible range. It turned out that semiconductors with so-called "inverted band structures" are good candidates [71]. In these materials, which contain heavy elements, the relativistic contributions are so strong that their band ordering differs from common semiconductors, like, e. g., GaAs. An example of such an inverted band structure is the one of HgTe, which is shown in Fig. 2.3(a). For comparison, Fig. 2.3(b) shows the band structure of CdTe, which is a material with normal band ordering. We see that in HgTe, the bands which are known as "heavy- and light-hole bands", and which are shown in red color in the plot, are energetically above the so-called electron bands which are colored in blue[4], a phenomenon which is known as "band inversion". The name "hole band" and "electron band" stems from the fact that in normally ordered semiconductors, like CdTe, see Fig. 2.3(b), the hole bands are the valence (the highest fully occupied) bands and the electron band is the conduction (the lowest fully unoccupied) band. In HgTe, this is different. First of all, HgTe is not even a semiconductor as it does not have an energy gap because the Fermi energy is right

[4] In the plot, they are called Γ_8 and Γ_6 like the corresponding irreducible representations of the relevant symmetry group, the double tetrahedral point group T_d^* [72]. They characterize the symmetry transformation behavior of the wave functions of these bands at $k = 0$.

at the touching point of the Γ_8 bands. Therefore, the heavy-hole band is forming the valence while the light-hole band is forming the conduction band. In addition, it has this inverted band structure, which is for a long time known to cause protected interface states [73–75]. However, their properties are usually not so prominently observed as they always coexist with conducting bulk states.

After the discovery of symmetry-protected TIs, ideas emerged to open up a gap in HgTe, which was then expected to be in the topologically non-trivial phase. One of these ideas is to subject the material to strain, by which a band gap opening is expected, which should lead to a 3d TI [68, 76], and indeed, this was also experimentally observed [77–79].

Another fruitful idea, which eventually lead to the first experimental realization of a 2d TI, was to consider quantum-well structures made out of HgTe and a non-inverted material like CdTe[5]. Here, the confinement in such a quantum-well structure leads to subband formation and to a natural opening of a gap, which depends on the quantum-well width. The subbands inherit properties of the bulk bands from which they derive, and the lowest lying subbands are often called E1, H1, H2, and L1 as they mainly stem from the electron band (Γ_6), the heavy-hole, and the light-hole band (both Γ_8). One of these inherited properties is that, at the band edge of the subbands in the quantum well ($k_\parallel = 0$), the projected total angular momentum perpendicular to the well, m_J, is still a good quantum number. This is why states of the heavy-hole band, which are characterized by $m_J = \pm\frac{3}{2}$, do not mix with states of the light-hole and electron band at this point. Therefore, the H1 and the H2 bands at the band edge purely contain heavy-hole states while the E1 and L1 bands generally are a mixture of electron (Γ_6) and light-hole (Γ_8) bands and are named according to the dominating component. Our main focus will be on quantum wells that are engineered such that the Fermi energy is between the two band edges of the subbands E1 and H1 because those two subbands will invert their order upon a change of the quantum-well thickness and give rise to a phase transition to a 2d TI as we will explain below. It turns out that, for the range of thicknesses d_{QW} that we are interested in ($d_{\mathrm{QW}} < 8\,\mathrm{nm}$), the L1 band is found to be energetically well separated ($\Delta E > 80\,\mathrm{meV}$) from those two subbands [81, 82]. Below $d_{\mathrm{QW}} = 7\,\mathrm{nm}$, the H2 band can also be treated as too far away, $\Delta E > 50\,\mathrm{meV}$, from the bands that we are genuinely interested in, the E1 and the H1 bands, which lie closest to the HgTe Fermi level. This is why we neglect the existence of L1 and H2 in the following discussion.

The fact that we are dealing with a quantum well made of materials with opposite band ordering leads to an interesting behavior. Usually, an increase of the thickness of the well mainly decreases the distance between the subbands (as the confinement decreases), so, in our case, we would expect a decrease of the gap, which we know to be absent in the bulk HgTe material. However, for this particular structure, the composition of the bands in terms of the bulk band contributions is also of major importance. For example, for very small quantum-well thicknesses, the transverse wave functions of the

[5] In most experimental realizations of 2d TIs, the alloy $Hg_{0.3}Cd_{0.7}Te$ is used as the quantum-well barrier material. This is also known to display the normal ordered band structure of CdTe [80], which is why we mostly neglect this extra complication in the principal discussion of this section. However, it is of course taken into account in all the quantitative treatments that we refer to, including the ones from which we take the parameters that we use for the calculations shown in this thesis.

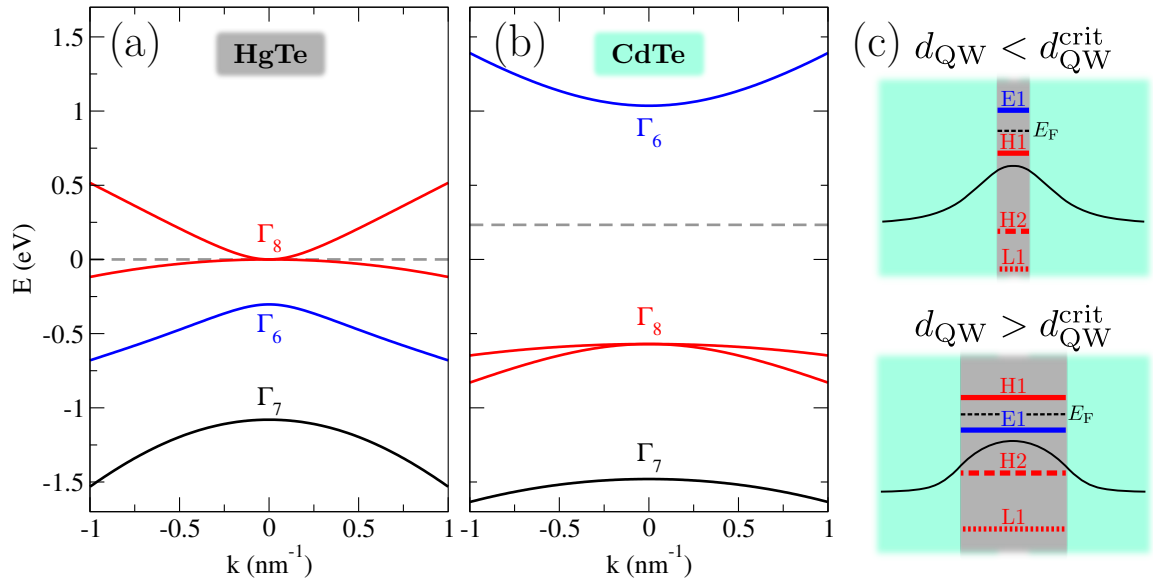

Figure 2.3: (a) and (b) show the bulk band structures of HgTe and CdTe respectively. The Fermi energies are indicated by dashed lines. One notes that HgTe is a semimetal with a band structure that is inverted with respect to CdTe, i. e., with the Γ_8 bands energetically above the Γ_6 bands. (c) shows the expected subband energy structure of a quantum well made from a central layer of HgTe sandwiched between CdTe. Here, the top panel shows the ordering for a thin quantum well below the critical thickness at which E1 and H1 change their order. The bottom panel shows the ordering for a quantum well above the critical thickness. As shown in the sketch, we are focusing on systems for which the Fermi energy is positioned between the E1 and the H1 band edge. In addition, the probability density of a typical quantum-well wave function is shown to emphasize that the states are mainly located in the barrier for thin and in the well for thick quantum wells.

subband states, which are generally oscillating in the HgTe region (bulk conductor) and exponentially decaying in the CdTe region (bulk insulator), have a high probability density in the CdTe region. This is mainly because the HgTe region is so narrow, cf. the sketch in the top panel of Fig. 2.3(c). Therefore, in this limit, the band ordering of the subbands is found to be the same as the one of CdTe (with the electron-band-dominated E1 band lying above the H1 band). This situation reverses in the opposite limit of a thick quantum well, where the subband wave functions are predominantly located in the HgTe layer, cf. the bottom panel in Fig. 2.3(c), and therefore it is expected that the hole-like subbands are above the electron-like subbands. So, one finds that for some critical thickness, which is estimated to lie at $d_{QW}^{crit} \approx 6.2\,\text{nm}$ for a $HgTe/Hg_{0.32}Cd_{0.68}Te$ quantum well [1], the band order of the subbands E1 and H1 inverts, i. e., the band gap between the two closes and reopens for larger thicknesses. Theoretical models predict that this comes along with a topological phase transition to a non-trivial TR-protected TI as we will explain in the next section. For very large thicknesses, the E1 band will also move below the other hole-like bands, but we will only consider thicknesses at which the other subbands, e. g., the H2 band, are still far away. For a full dependence of the band edges in the quantum well as a function of the well thickness, we refer to Refs. [81, 82].

2.3.1 The Bernevig-Hughes-Zhang Hamiltonian

For the purpose of a theoretical description of this band inversion, and the proof that this is indeed a topological phase transition, Bernevig, Hughes, and Zhang derived a Hamiltonian that describes the low-energy behavior of these quantum wells [1],

$$H_{\mathrm{BHZ}} = \begin{pmatrix} h(\mathbf{k}) & \begin{matrix} 0 & 0 \\ 0 & 0 \end{matrix} \\ \begin{matrix} 0 & 0 \\ 0 & 0 \end{matrix} & h^*(-\mathbf{k}) \end{pmatrix}, \tag{2.17}$$

with

$$h(\mathbf{k}) = \begin{pmatrix} C - (B+D)\,\mathbf{k}^2 + M & Ak_+ \\ Ak_- & C + (B-D)\,\mathbf{k}^2 - M \end{pmatrix}, \tag{2.18}$$

and $\mathbf{k}^2 = k_x^2 + k_y^2$, $k_\pm = k_x \pm ik_y$, which is now often just called the *BHZ Hamiltonian*. Its principle form was derived by symmetry considerations and it was later seen to apply also to other quantum-well structures, e. g., the InAs/GaSb material system [20]. For HgTe/CdTe quantum wells, the four basis states of the model are $|\mathrm{E1},\uparrow\rangle$, $|\mathrm{H1},\uparrow\rangle$, $|\mathrm{E1},\downarrow\rangle$, and $|\mathrm{H1},\downarrow\rangle$, meaning that other subbands are neglected in this treatment. Therefore, it should only be used in the range of thicknesses at which this is a good approximation. The parameter C in the Hamiltonian enters just as a constant spectral shift and will be set to zero in this thesis, which fixes the overall offset of our energy scale. However, we will often make use of electrostatic potentials V, which enter the Hamiltonian on the same footing, thus we replace $C = eV$. Often, these potentials will depend on space $V = V(\mathbf{x})$, for example, when including random disorder, or when describing regions which are subject to local gates.

At $\mathbf{k} = 0$, we can directly read off from Eq. (2.18) that the band ordering of the E1 and the H1 band is determined by the parameter M. An inverted band order, i. e., H1 above E1 corresponds to $M < 0$. To show that this comes along with a non-trivial $\mathbb{Z}_2$ classification, we make use of some of the methods that were introduced in Section 2.2.4 and compute the topological invariant. This is instructive as it already shows one major difficulty that we are facing: As we learned from the definition in Section 2.2.3, the topology of the Hamiltonian is a global property for which the full behavior of H throughout the Brillouin zone (BZ) is required. For example, to calculate the topological invariant, one should be able to evaluate integrals of eigenstate wave functions over the whole Brillouin zone, or (in some simpler cases) at least be able to evaluate eigenstate properties at all TRIM. However, the BHZ Hamiltonian is only valid in a small energy and momentum window close to the BZ center, which makes it seem impossible to use it to get a faithful representation of the states at the TRIM at the BZ edge. Worse still, as H_{BHZ} is only a small-$\mathbf{k}$ approximation, the notion of a Brillouin zone does not even exist, i. e., the Hamiltonian is not a mapping that depends on periodic parameters. What saves us in this case is that we know that the Hamiltonian is gapped throughout the Brillouin zone and that the gap closing between the two phases (for $M = 0$) occurs locally at $\mathbf{k} = 0$. Such a *local topological defect* can be shown to be well described by a low-energy

theory that is only well defined in a small region around that defect [1, 83]. To be able to calculate the topological invariant of the system described by such a low-momentum expansion, it is convenient to use a lattice regularization, e. g., to introduce a square grid with lattice constant a, on which we evaluate the derivatives in terms of finite differences. This introduces a Brillouin zone with a periodicity given by the (arbitrarily chosen) lattice constant a and yields the following Hamiltonian:

$$\begin{aligned} h_{\text{lattice}}(\mathbf{k}) = &\begin{pmatrix} C+M & \frac{A}{a}\left(\sin\left(k_x a\right) + i\sin\left(k_y a\right)\right) \\ \frac{A}{a}\left(\sin\left(k_x a\right) - i\sin\left(k_y a\right)\right) & C-M \end{pmatrix} \\ &- \frac{2}{a^2}\left(2 - \cos\left(k_x a\right) - \cos\left(k_y a\right)\right) \begin{pmatrix} B+D & 0 \\ 0 & -B+D \end{pmatrix}, \end{aligned} \tag{2.19}$$

where, for simplicity, only the first of the two 2×2 subblocks is shown. For this Hamiltonian, the calculation of the $\mathbb{Z}_2$ invariant is simple as it respects parity symmetry, $h(-\mathbf{k}) = Ph(\mathbf{k})P^{-1}$, with the parity operator being

$$P = \begin{pmatrix} 1 & 0 \\ 0 & -1 \end{pmatrix}. \tag{2.20}$$

According to Eq. (2.16), all that remains to be done is to multiply the parity eigenvalues of the occupied bands at the four TRIM $(0,0)$, $\left(\frac{\pi}{a},0\right)$, $\left(0,\frac{\pi}{a}\right)$, and $\left(\frac{\pi}{a},\frac{\pi}{a}\right)$. At the first TRIM $\mathbf{k}=0$, this yields

$$\delta_1 = -\operatorname{sgn}\left(M\right)$$

for a Fermi energy chosen at $E_{\text{F}} = C$, at which we find only one occupied band for $h_{\text{lattice}}\left(\mathbf{k}\right)$ with energy $-\left|M\right|$. Of course, this is still Kramers degenerate as the full Hamiltonian, H_{BHZ}, contains another time-reversal invariant block $h^*_{\text{lattice}}\left(-\mathbf{k}\right)$. At the other TRIM, one finds

$$\begin{aligned} \delta_2 = \delta_3 &= -\operatorname{sgn}\left(-\frac{4}{a^2}B + M\right), \\ \delta_4 &= -\operatorname{sgn}\left(-\frac{8}{a^2}B + M\right). \end{aligned}$$

Note, that the parameter D can be neglected here as it shifts both bands equally and does not affect the bands at the zone center. Therefore, for $|D| < |B|$, it does not affect the occupation of the bands. Thus, even at the BZ edge, only the lower of the two bands is occupied, from which one can derive the above formulas. This breaks down for $|D| > |B|$, for which we find a metallic system as there is some momentum at which both bands start being occupied. Then, the behavior around this momentum is important and the low-momentum description obviously loses its meaning. We will exclude such a scenario in the following treatment and assume (in accordance with experiments) that the bulk material is truly insulating. Then the above quantities can be unambiguously obtained. By taking the limit of $a \to 0$, i. e., going into the continuum limit of the lattice description, we find that

$$\delta_2 = \delta_3 = \delta_4 = \operatorname{sgn}\left(B\right).$$

Therefore, the $\mathbb{Z}_2$ topological invariant is given by

$$(-1)^{\Xi} = \delta_1\delta_2\delta_3\delta_4 = -\operatorname{sgn}(B)\operatorname{sgn}(M)\,. \tag{2.21}$$

Thus, we indeed expect a phase transition between topologically trivial, $\Xi = 0$, and topologically non-trivial, $\Xi = 1$, upon a sign change of the parameter M. In principle, this is also expected for a sign change of B. However, such a transition can be shown not to satisfy the requirement of a *local topological transition* [83].

We note that the Hamiltonian as it is stated in Eq. (2.17) does not couple the two spin blocks, which is surprising as we know that we are studying a heavy-element material with broken inversion symmetry (due to the zincblende lattice) for which spin-orbit coupling should be particularly strong. And indeed, one finds additional correction terms to this Hamiltonian that take into account the effect of bulk inversion asymmetry, which to lowest order turn out to be of the form [84]

$$H_{\mathrm{BIA}} = \begin{pmatrix} 0 & 0 & 0 & -\Delta \\ 0 & 0 & \Delta & 0 \\ 0 & \Delta & 0 & 0 \\ -\Delta & 0 & 0 & 0 \end{pmatrix}. \tag{2.22}$$

However, in practice, the obtained numerical values for the parameter Δ are comparatively small. Therefore, it is often well justified to view the two spin blocks as uncoupled. For this thesis, these terms will still be of particular importance as we will be mainly concerned with the on-edge backscattering of edge states, something that is only possible due to such spin-orbit coupling terms.

In addition to bulk inversion asymmetry, the influence of structure inversion asymmetry may also give rise to additional spin-orbit coupling, the strength of which depends on the degree of this asymmetry. This is usually quantified in terms of an electric field $\mathbf{E}_z$ perpendicular to the quantum well, which arises due to charge transfer in an asymmetric structure, or due to the asymmetric application of external gate voltages. These "Rashba" terms can be shown to take the following form [82]:

$$H_{\mathrm{SIA}} = \begin{pmatrix} 0 & 0 & -i\mathcal{R}k_- & 0 \\ 0 & 0 & 0 & 0 \\ i\mathcal{R}k_+ & 0 & 0 & 0 \\ 0 & 0 & 0 & 0 \end{pmatrix}, \tag{2.23}$$

where the strength $\mathcal{R}$ scales linearly with the electric field strength $\mathbf{E}_z$. In this thesis, we will mostly neglect them as it is difficult to quantitatively estimate the strength of the electric field that breaks the symmetry. Still, we will check in Section 3.A.3 that the existence of such a field does not qualitatively change our results.

Under the application of an external perpendicular magnetic field B, one finds addi-

Table 2.2: Parameters for the BHZ Hamiltonian, which are used in this thesis. They have been derived by $k \cdot p$ calculations for $HgTe/Hg_{0.32}Cd_{0.68}Te$ quantum wells with a thickness of $d_{QW} = 7\,\text{nm}$ [82, 84], which is what is most commonly used in experiments.

$A\,(\text{meV} \cdot \text{nm})$	$B\,(\text{meV} \cdot \text{nm}^2)$	$D\,(\text{meV} \cdot \text{nm}^2)$	$M\,(\text{meV})$
364.5	-686	-512	-10

$\Delta\,(\text{meV})$	$\mathcal{R}/\,(e\mathbf{E}_z)\,(\text{nm}^2)$	g_E	g_H
1.6	-15.6	22.7	-1.21

tional terms which stem from the Zeeman coupling [84],

$$H_\text{Z} = \begin{pmatrix} g_\text{E}\mu_\text{B}B & 0 & 0 & 0 \\ 0 & g_\text{H}\mu_\text{B}B & 0 & 0 \\ 0 & 0 & -g_\text{E}\mu_\text{B}B & 0 \\ 0 & 0 & 0 & -g_\text{H}\mu_\text{B}B \end{pmatrix}, \tag{2.24}$$

with μ_B being the Bohr magneton, which are however found to be mostly negligible in weak perpendicular fields as they are usually much weaker than the orbital magnetic field contributions, which is why we also mostly neglect them in this thesis. However, we check the validity of this approximation in Section 3.A.2.

From $k \cdot p$ calculations, realistic parameters for quantum wells with a given thickness can be extracted. In this thesis, we will universally use the parameters that are shown in Table 2.2, which have been derived for a quantum well of 7 nm thickness [82, 84]. This thickness is right "at the sweet spot", meaning that it is already assumed to lead to an inverted band structure with a sizable gap, however, it is also thin enough to be able to neglect the influence of other subbands. The parameters from Table 2.2 indeed give rise to an inverted band structure ($M < 0$) and, as can be seen from Eq. (2.21), they also lead to a non-trivial $\mathbb{Z}_2$ topology as $M \cdot B > 0$.

2.3.2 Topological edge states of the BHZ Hamiltonian

So far, we have been arguing that a non-trivial topology should give rise to conducting edge states if one considers heterostructures with trivial insulators. In this section, we will explicitly calculate and study these states for the case of the BHZ Hamiltonian. To simplify an analytical treatment, we will start with the simple BHZ model, Eq. (2.17), which does not include spin-orbit interaction. In this way, we will be able to obtain analytical expressions for the edge-state wave functions and their dispersion. Later, we will include spin-orbit coupling and evaluate the edge-state properties numerically, which will even allow us to study their energy-dependent spin texture.

In the simple BHZ Hamiltonian, Eq. (2.17), the two spin blocks are completely decoupled and may thereby be treated separately. Each of the blocks, Eq. (2.18), describes a band insulator with a direct band gap at $\mathbf{k} = 0$, which spans the energy range

between $-M$ and M. If the parameters are chosen such that the topological invariant yields a non-trivial insulator, cf. Eq. (2.21), one should obtain protected edge states when studying a heterostructure with a trivial insulator, e. g., vacuum. The simplest model in which one can observe them is to consider a semi-infinite plane of a material that is described by the BHZ Hamiltonian on which one enforces a hard-wall boundary condition on one side, i. e., $\psi(y=0)=\mathbf{0}$. Translational invariance is assumed in the direction along the hard-wall boundary, i. e., k_x is still assumed to be a good quantum number. The geometry is illustrated in Fig. 2.4(a). In addition to the bulk states, which are forbidden in the energy range $E \in [-M, M]$, one can now also find edge-state solutions, which are built from a superposition of exponentially decaying bulk solutions. For a single spin block, one finds two such exponentially decaying bulk solutions in the gap. However, it is only at certain energies and momenta in which the eigenvectors of those solutions (in the subspace E1 and H1) agree such that one can use them to construct a solution of the full problem that satisfies the hard-wall boundary condition. For the spin-up block, i. e., the Hamiltonian from Eq. (2.18), one obtains the following differential equation,

$$\begin{aligned} h(k_x)\psi_{k_x}(y) &= \begin{pmatrix} -(B+D)\left(k_x^2-\partial_y^2\right)+M & A\left(k_x+\partial_y\right) \\ A\left(k_x-\partial_y\right) & (B-D)\left(k_x^2-\partial_y^2\right)-M \end{pmatrix}\psi_{k_x}(y) \\ &= E(k_x)\psi_{k_x}(y), \end{aligned} \tag{2.25}$$

for which, after some algebra, one finds the following normalized edge state solution:

$$\psi_{k_x}(y) = c_1(k_x)\left(e^{-q_+(k_x)y}-e^{-q_-(k_x)y}\right)\begin{pmatrix} c_2(k_x) \\ -1/c_2(k_x) \end{pmatrix}, \tag{2.26}$$

with

$$c_1(k_x) = \frac{1}{2}\sqrt{\frac{A\left(G(k_x)-A^2\right)}{BG(k_x)}}, \tag{2.27}$$

$$c_2(k_x) = \sqrt[4]{\frac{B-D}{B+D}}, \tag{2.28}$$

$$q_\pm(k_x) = \frac{A \pm \sqrt{G(k_x)}}{2\sqrt{B^2-D^2}}, \tag{2.29}$$

and

$$G(k_x) = \frac{A^2B - 4AD\sqrt{B^2-D^2}k_x + 4\left(B^2-D^2\right)\left(Bk_x^2-M\right)}{B}. \tag{2.30}$$

This expression solves Eq. (2.25) for energies in the gap and satisfies the hard-wall boundary condition, $\psi_{k_x}(y=0)=\mathbf{0}$. It yields the following linear dispersion relation:

$$E(k_x) = \frac{A\sqrt{B^2-D^2}k_x - DM}{B}. \tag{2.31}$$

A solution for the spin-down block, with the Hamiltonian $h^*(-\mathbf{k})$, is directly obtained from the above solution by replacing $k_x \to -k_x$, therefore leading to a linear dispersion with opposite slope. The spectrum of such a heterostructure is plotted in Fig. 2.4(c). It matches all our expectations from the previous general discussion: We find two counterpropagating conducting edge states at all energies, which are related by TR symmetry (a flip of spin and momentum). They cross at the TRIM at the zone center. In this case, they show a perfectly linear dispersion, a feature often observed for topological edge states. However, as discussed in Section 2.2.4, this is not strictly required by topological arguments.

A typical plot of a transverse wave function of the edge states is displayed in Fig. 2.4(b). As expected, it is exponentially localized close to the interface in both the E1 and the H1 component. Interestingly, the relative weight of E1 and H1 is constant throughout,

$$w_{\mathrm{E1}} = \int_0^\infty dy \left|\psi_{k_x}^{\mathrm{E1}}(y)\right|^2 = \frac{c_2^2}{c_2^2 + \frac{1}{c_2^2}} = \frac{B-D}{2B}, \tag{2.32}$$

$$w_{\mathrm{H1}} = \int_0^\infty dy \left|\psi_{k_x}^{\mathrm{H1}}(y)\right|^2 = \frac{B+D}{2B}, \tag{2.33}$$

with the H1 component dominating (for our parameters $w_{\mathrm{H1}} \approx 87\,\%$). However, the lateral extent of the edge states strongly changes with the edge-state energy. This may be quantified by calculating the mean distance of the particle from the edge,

$$\langle y \rangle = \langle \psi_{k_x} | y | \psi_{k_x} \rangle = \int_0^\infty dy\, y \left|\psi_{k_x}(y)\right|^2 = \frac{\sqrt{B^2 - D^2}\,(3A^2 - G(k_x))}{A\,(A^2 - G(k_x))}, \tag{2.34}$$

which is plotted as a function of energy in Fig. 2.4(d). We note that even though the edge states are located very close to the edge for energies in the gap ($\langle y \rangle < 50\,\mathrm{nm}$ for $E < 10\,\mathrm{meV}$), the spread of the edge states diverges when they approach the conduction-band touching point (at $E \approx 13\,\mathrm{meV}$) where $G(k_x) \to A^2$. This will not concern us too much in this thesis as we will be studying transport for Fermi energies in the gap. Here, the lateral extent of less than 50 nm only matters for very narrow ribbons [85], in which it would allow a coupling of the edge states of opposite sides. In such narrow ribbons, the semi-infinite plane solutions, i. e., Eq. (2.26), need to be corrected and a gap in the dispersion will open up at the center of the edge-state Dirac cone [86]. However, this gap decreases exponentially with the ribbon width due to the exponential lateral decay of the edge states. For the ribbon widths that we consider in this thesis ($L_y \approx 500\,\mathrm{nm}$), it may be totally neglected.

The additional inclusion of spin-orbit coupling only yields small corrections to the band structure of the edge states. And even though an analytical solution is intractable in this case, one can easily solve for the eigenstates and the dispersion numerically. Results of such a numerical search that includes spin-orbit coupling due to bulk inversion asymmetry, cf. Eq. (2.22), are shown in Fig. 2.5. The main change in the band structure, which is shown in Fig. 2.5(a), is the spin splitting of the bulk bands, which also slightly shifts the point at which the edge states connect to the bulk to lower energies. The edge-state dispersion, however, does not notably change, which is already signaling the

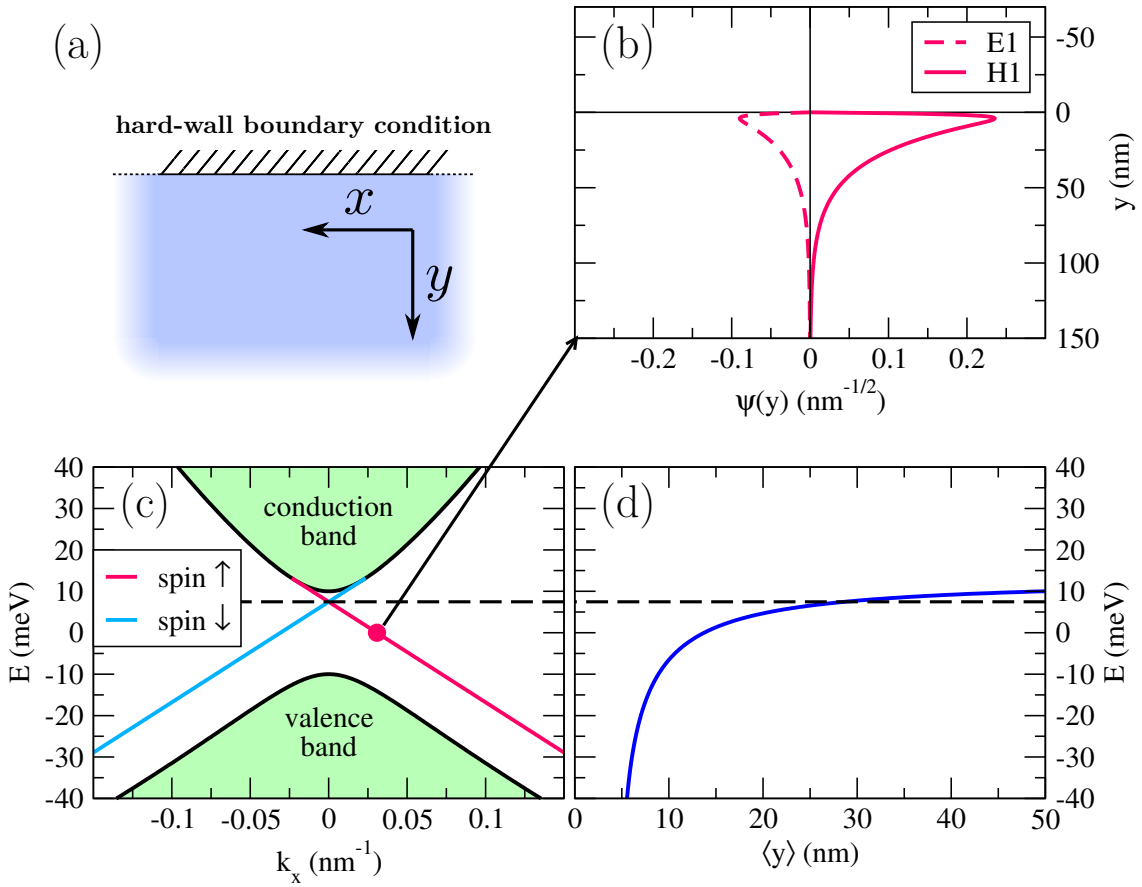

Figure 2.4: The figure illustrates the emergence of topological interface states at edges of non-trivial BHZ insulators. In this figure, only the simplest BHZ model, Eq. (2.17), is considered and the parameters from Table 2.2 are used (modeling a HgTe/CdTe quantum well with 7 nm thickness). When applying hard-wall boundary conditions at one side, as sketched in (a), and calculating the band structure for this wave-guide structure (which is translationally invariant in the x-direction), one obtains a band structure that is shown in (c). It shows the continuum of bulk bands but in addition features spin-polarized pairs of counterpropagating in-gap states with a linear dispersion, Eq. (2.31). An example for a wave function of such a state, Eq. (2.26), is depicted in (b), showing that it is indeed strongly bound to the interface. In (d), the energy dependence of the extent of the wave functions is illustrated by plotting the expectation value for the distance from the edge, Eq. (2.34), as a function of the energy. The energy of the edge-state Dirac point is marked by a dashed line in (c) and (d).

fact that the effective spin-orbit coupling in HgTe/CdTe quantum wells is small. Also, the change of the edge-state spin polarization (the spin expectation value in z-direction, which is depicted as a color change along the curve) is hardly visible in the plot even though the color code was chosen to highlight small deviations from full S_z polarization. For example, if we look at an edge-state wave function like the one obtained for the "mostly spin up" band at $E = 0\,\mathrm{meV}$, which is shown in Fig. 2.5(c), we see that it is almost identical to the one without spin-orbit coupling, Fig. 2.4(b), with the only difference that very small spin-down components are admixed.

Even though this spin admixture is really tiny for most energies in the gap, a close examination of the effects of spin-orbit coupling on the spin structure is still very interesting from a conceptual point of view, also because it is mainly the spin polarization of the edge states that makes them attractive for applications in spintronic devices. Therefore, we decided to look into this in a bit more detail and plot the energy-dependent expectation values for the spin in all directions in Fig. 2.5(b). We only plot the expectation values for one spin band, namely the one that is "mostly spin up", i. e., mainly colored red in Fig. 2.5(a). Due to Kramers symmetry, the spin-expectation values of the other band are simply the negatives of the ones that are shown. As was already expected from the color-coded edge-band plot in Fig. 2.5(a), this band is mostly polarized in the S_z direction. While the S_y expectation value is exactly zero at all energies, this is not true for S_x, which is non-vanishing and in this particular case attains a small component along the momentum vector of the state, i. e., it reverts when the momentum changes sign. This already illustrates the first important effect of spin-orbit coupling, which is also commonly known from other contexts, namely that it acts as a "momentum-dependent effective magnetic field", which tilts the preferred spin direction of the momentum eigenstates. In this case, the spin direction, which points along the z-axis for $\Delta = 0$, is slightly tilted toward the state's momentum direction. In principle, the strength of this tilt (and also the direction) may depend on the momentum (and equally on the energy). In fact, such an energy-dependent spin texture was considered to have important consequences for inelastic backscattering of the edge states [87, 88]. As we can see, in the case of HgTe/CdTe quantum wells, this energy dependence is very weak. Below $E = 5\,\mathrm{meV}$, $\langle S_x \rangle$ and $\langle S_z \rangle$ are practically constant. Only when approaching the conduction band, we observe a stronger change.

There is another effect of spin-orbit coupling terms, like Eq. (2.22) [or equally Eq. (2.23)], for the BHZ model that we consider more interesting: The total spin content of the edge states may actually be reduced! To understand what we mean by this, it helps to remember that for any 2-spinor, as it appears in a non-relativistic description of electrons that takes into account spin (e. g., in the Pauli equation), one will always find a spatial direction into which this spinor is an eigenstate of the (accordingly rotated) spin operator. Physically, this implies that one cannot write down a 2-spinor for which all spin expectation values $\langle S_x \rangle$, $\langle S_y \rangle$, and $\langle S_z \rangle$ vanish as it is a spin eigenstate in a particular direction. Instead, for 2-spinors, we always find

$$\langle S_x \rangle^2 + \langle S_y \rangle^2 + \langle S_z \rangle^2 = 1. \tag{2.35}$$

If we increase the dimension of our spinors beyond two, this relation does not hold any

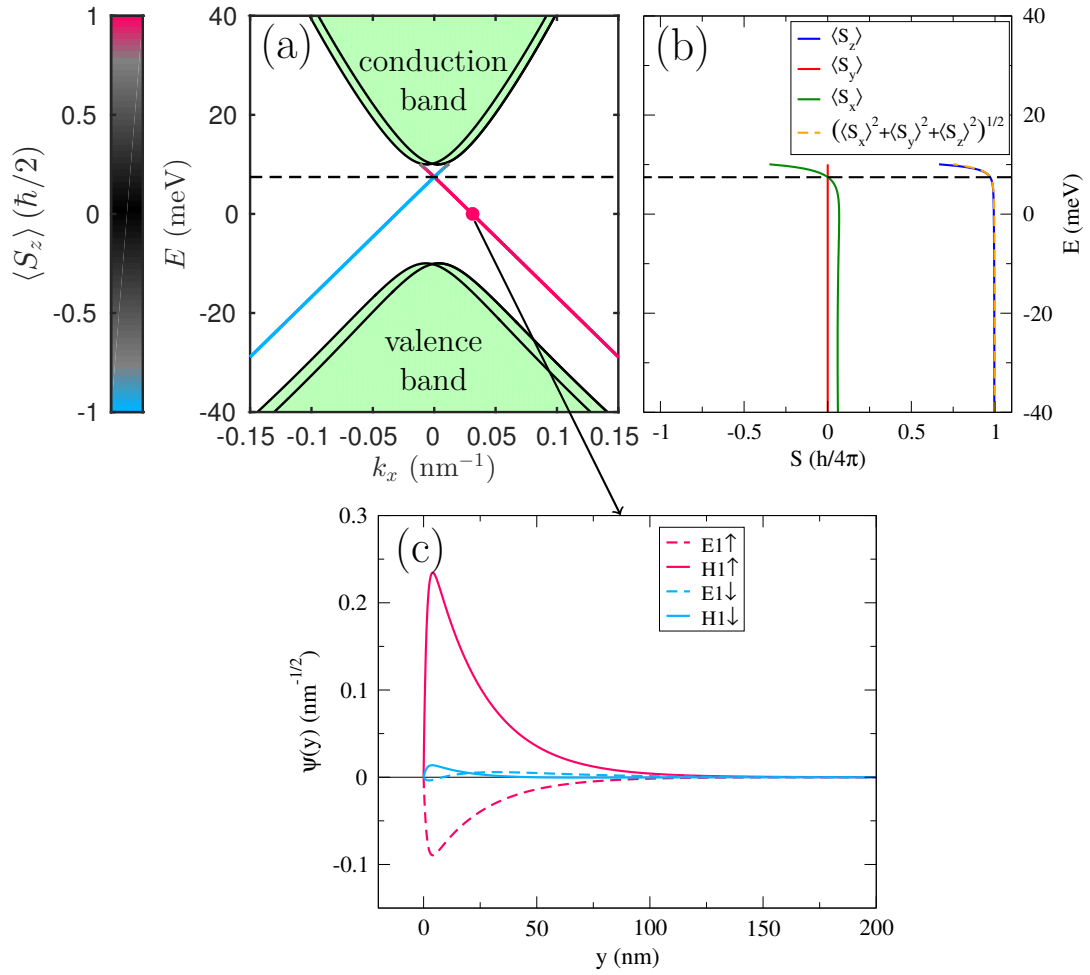

Figure 2.5: This figure illustrates the influence of the effective spin-orbit coupling, here assumed to arise only from bulk inversion asymmetry, i. e., Eq. (2.22), on the properties of the topological edge states. (a) shows a band structure for a semi-infinite plane of a 7 nm thick HgTe/CdTe quantum well with a one-sided hard wall boundary condition, similar to the plot in Fig. 2.4(c) with the only difference being the additional inclusion of spin-orbit coupling. The S_z polarization of the edge states is color coded. (b) shows a more detailed analysis of the energy-dependent spin polarization of the edge states. Here, only the spin polarization of the "mostly spin up" band is shown. As the other edge state is related by Kramers symmetry, all spin expectation values for this band can simply be obtained by a sign flip. In addition to the expectation values of all spin directions, the "total spin content", cf. Eq. (2.36), of the states is shown. The energy of the edge-state Dirac point is marked by a dashed line in (a) and (b). (c) shows the wave function of the edge state that is obtained in the "mostly spin up" band at $E = 0$ meV, which can be directly compared to the result without spin-orbit coupling, cf. Fig. 2.4(b).

longer. This has to do with the fact that we are increasing the degrees of freedom and that we are now allowed to build states which are superpositions of antiparallel 2-spinors (similar to a spin-singlet state for two free particles). For example, in the relativistic Dirac equation, which is naturally defined on a 4-dimensional space of electron/positron and spin degrees of freedom, one could think about a state that consists of an "up electron" and a "down positron" component of equal weight. Such a state will yield $\langle S_i \rangle = 0$ for all spatial directions. In the particular case of the free Dirac equation, such states are not eigenstates of the Hamiltonian, instead we find that the free eigenstates still have a full spin polarization in or against the propagation direction (they are "helicity eigenstates"). In the scenario that we are discussing here, i. e., the BHZ Hamiltonian, which is also naturally defined on the space of 4-dimensional spinors, there is in general no such restriction for the eigenstates/eigenmodes. This is also reflected by the numerical results shown in Fig. 2.5(b), in which we show the total spin content of the states, which we quantify by plotting

$$S_{\mathrm{tot}} = \sqrt{\langle S_x \rangle^2 + \langle S_y \rangle^2 + \langle S_z \rangle^2}, \tag{2.36}$$

and find that there are energies at which this value is indeed below one (the expected value for 2-spinors). Similar to the tilting, this effect is also very weak for HgTe/CdTe quantum wells and may even be difficult to see in the figure. It appears most prominently at the edge-state Dirac point where $\langle S_x \rangle = 0$ which is why one would expect $\langle S_z \rangle = 1$ if the spin only changed its direction. This is not the case as we find that $\langle S_z \rangle$ is below 1 and even tends to decrease for increasing energy. The net spin content is therefore reduced for the edge states, meaning that a single edge-state carrier no longer transports a full unit of $\hbar/2$, which, even though this effect is almost negligible in these particular quantum wells, has important conceptual consequences: The spin Hall conductivity (no matter in which direction) of such an insulator is formally no longer quantized as it is for the BHZ model without spin-orbit coupling. This is a source of great confusion as non-trivial 2d TIs that are protected by TR symmetry are often denoted as "quantum spin Hall insulators", a term which suggests a quantized spin Hall conductivity. As is illustrated by this simple example, this is not necessarily the case. Thinking this a step further, one may even find TR-protected two-dimensional TIs that feature counterpropagating edge states that are fully unpolarized in their spin degree of freedom. They are still ensured to form a Kramers pair, which means that elastic scattering between them is forbidden. Therefore, "quantum spin Hall insulators" feature a quantized edge-state *charge conductance* as long as inelastic backscattering (or similar effects) can be neglected and TR symmetry is fully preserved. In this way, a more suitable name for them would probably be "perfect edge conduction insulators".

To illustrate this effect of edge states with reduced spin polarization, we show in Fig. 2.6(a) a numerically calculated band-structure plot where we artificially increased the intrinsic spin-orbit coupling by a factor of 10 ($\Delta = 16\,\mathrm{meV}$). The corresponding spin polarizations are shown in Fig. 2.6(b). We find that such a system is still topologically non-trivial and features counterpropagating edge states with a strongly bent but still relatively linear dispersion. However, the spin polarization of the edge states is strongly reduced, even when considering states in the middle of the gap. Even though the preferred spin direction is, like in the case for small Δ, mostly given by the z-axis except for energies

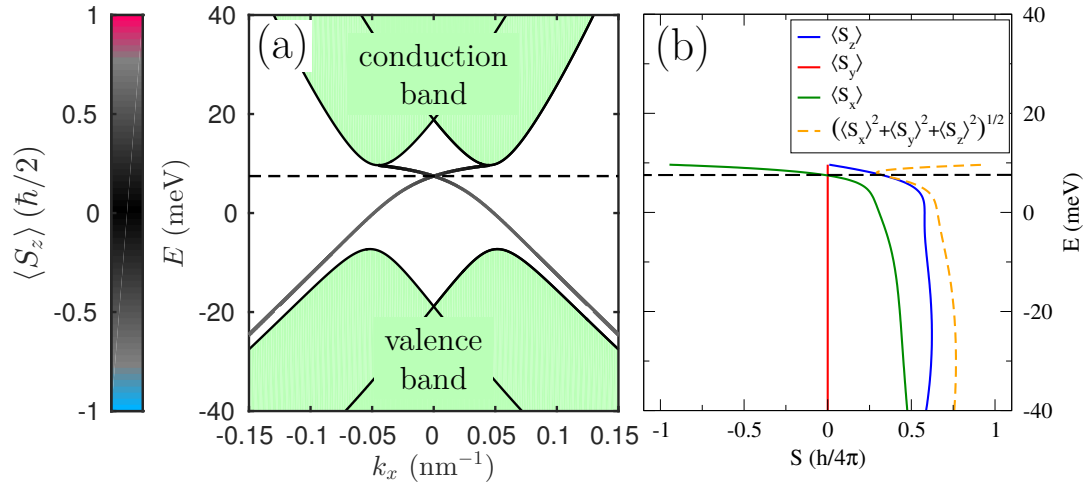

Figure 2.6: This figure shows the band structure (a) and the corresponding edge-state spin polarization (b) in the same fashion as Fig. 2.5, only differing in the choice of the strength of the intrinsic spin-orbit coupling parameter Δ. Here, Δ was artificially increased to the tenfold value, $\Delta = 16\,\mathrm{meV}$. Otherwise, the parameters from Table 2.2 were used.

close to the conduction-band edge, we see that the absolute value of the S_z polarization is only about 60 %. Therefore, one should keep in mind that even though there may be many 2d TIs like the HgTe/CdTe quantum wells that feature an extraordinarily strong spin polarization of their edge states and may be very interesting for spintronic applications, this need not generally be the case.

However, for HgTe/CdTe quantum wells, one can assume that the edge states are to a very good approximation fully S_z polarized for all energies in the gap, even when taking into account intrinsic spin-orbit coupling. We also checked that the additional inclusion of a Rashba term, i. e., of a term as given by Eq. (2.23), does not significantly modify this picture even when one assumes a relatively strong symmetry-breaking electric field of $\mathbf{E}_z = 10^7\,\mathrm{V/m}$. The main influence of such a Rashba term is to increase the bulk-band splitting but it leaves the spin texture almost unchanged.

One thing that should also be mentioned is that we here consider lattice terminations of HgTe/CdTe quantum wells simply in terms of hard-wall boundary conditions. The main motivation for this is that this is the natural boundary condition in a tight-binding representation of the Hamiltonian, where it corresponds to a simple lattice termination. Therefore, it is useful for comparison to many of our later numerical treatments which make use of such a representation. However, it is unclear whether this is really a good model of the experimental situation. Topological edge states are, e. g., also obtained using "infinite mass" or "vanishing surface current" boundary conditions[6] [89–91]. Thinking microscopically, many things can happen at a termination of a quantum-well structure such as a phenomenon known as band bending. This means that, due to charge transfer

[6] We will in fact use such "infinite mass" boundary conditions in the wave-packet transport calculations in Chapter 4 as hard-wall boundary conditions are difficult to implement in this particular numerical method. However, we will add extra terms, which will make the dispersion very similar to the one obtained from hard-wall boundary conditions.

between surface and bulk, there may be electric fields, which are localized at the interface and may significantly shift the bulk bands close to the edge and generally also modify the edge-state band structure. Especially, also the spin structure may be altered as the electrical fields that give rise to band bending are also known to lead to additional (lateral) spin-orbit coupling terms [92, 93], which are not included in our model. In addition to band bending, one might also observe lattice reconstructions close to such an edge. We will not consider these effects (band bending, reconstructions, etc.) in this thesis even though it is possible that they might be necessary for a quantitative comparison to experiments. Their realistic inclusion would, however, require a more microscopical model and certainly a self-consistent treatment of the electrostatic charge transfer at the edges. Research in this direction is very interesting, however, it is out of scope of this thesis.

Luckily, the topological arguments outlined in Section 2.2.2 protect the existence of conducting states at all energies. Those will come in an odd number of Kramers pairs of which at least one pair is immune to elastic backscattering. These features are insensitive to the detailed choice of boundary conditions or to the other effects discussed above, which is why we believe that numerical results with hard-wall (or equivalently infinite-mass) boundary conditions should at least qualitatively capture the transport behavior at HgTe/CdTe quantum-well edges. However, one should keep in mind that the shape of the dispersion and even the spin polarization might be modified in a realistic system as these properties are not topologically protected.

Before closing this section, we would like to add that there is another material system—namely a quantum-well structure made of adjacent layers of InAs and GaSb that are enclosed by a barrier material—which is now also widely believed to allow the realization of a 2d TI [19, 20, 94–96]. As in the case of HgTe/CdTe quantum wells, one can treat this system with an effective description which only takes into account the two quantum-well subbands that are closest to the Fermi energy (and their respective spin degrees of freedom). Thus, this system can also be described by the 4×4 BHZ Hamiltonian with a different set of parameters. The band inversion in this material system is achieved by making use of the "broken gap" band alignment of InAs and GaSb, which means that the valence-band edge of GaSb naturally lies above the conduction-band edge of InAs, meaning that one may, depending on the thicknesses of the different layers, directly end up with an "inverted subband" situation. In this regime, model calculations also predict spin-polarized edge states with a linear dispersion, very similar to what we obtained for HgTe/CdTe quantum wells. Therefore, even though we did not do any explicit calculations using InAs/GaSb parameters in this thesis, we think that many of the results should at least qualitatively also apply to this material system, which is why we will sometimes also consult experimental data on this system for comparison.

2.3.3 Transport calculations for HgTe/CdTe quantum wells

The BHZ model that we presented in this chapter will be the basis of all the TI transport calculations that are shown in this thesis. For a numerical treatment, it is discretized on a lattice and we will mainly use two different algorithms to gain knowledge about the edge-state transport properties. The first of these is the classic recursive Green's function

algorithm [97–99], which we will be using in the form of a software package written by Michael Wimmer [100] who developed a modern implementation that is particularly well suited for dealing with complex geometries (like the ones considered in Chapters 5 and 6). The second algorithm that we will be using is based on an explicit numerical propagation of the time-dependent Schrödinger equation using a polynomial decomposition of the time-evolution operator [101]. Here, a very efficient numerical implementation of this algorithm by Viktor Krückl is used, which is based on a Fourier-space evaluation of momentum operators [102]. With this, one can study the evolution of wave packets and gain information about the transport properties of the edge states and, importantly, one has direct access to time-dependent quantities, which we will make use of in Chapter 4. There, we will also show an extension to the algorithm, which allows the inclusion of the effect of phase-coherence breaking into the time evolution. Well-written and comprehensive descriptions that specifically explain the algorithms used in this thesis can be found in Ref. [103] (recursive Green's functions transport framework) and Ref. [81] (wave-packet time evolution). The employed calculation setups, all relevant parameters, and necessary extensions to the algorithms will be stated in detail where necessary.

For a general reference on quantum transport at low temperatures, for example concerning the Landauer-Büttiker formalism employed in the studies in the following chapters, we refer to Refs. [103–105].

2.4 Summary and outlook

In this section, we would like to summarize the most important results of this overview with regard to the work in the following chapters. We learned that heterostructures of topologically different insulators necessarily lead to the appearance of gapless interface states. For the particular case of a non-trivial TI that is protected by TR symmetry, these interface states always come as a Kramers pair of states and one will always find an odd number of such pairs. HgTe/CdTe quantum wells in a critical window of thicknesses allow the realization of such a non-trivial TR-protected TI, for which the models predict a single pair of edge states at each edge. As long as TR symmetry is globally preserved and as long as the system is fully coherent, scattering between the two states of such a pair is strictly forbidden, cf. Eq. (2.10). Therefore, without magnetic fields, one expects the transmission of the states at one edge not to drop below e^2/h at low temperatures, which was also roughly confirmed by the first experiments [17]. With the application of external magnetic fields, TR symmetry is globally broken which is why the argumentation underlying Eq. (2.10) breaks down and the protection from backscattering is lifted. This will be the main topic of Chapter 3 of this thesis, in which we present a detailed study of the effect of an external magnetic field on the transport properties of HgTe/CdTe quantum wells.

In addition, we saw that the models which are derived from $k \cdot p$ calculations also predict a very strong spin polarization of the edge states. Besides the fact that this is very interesting from the point of view of applications, it also has an influence on the transport properties. As we will discuss in Chapter 4 of this thesis, this is the reason why transport along clean edges is expected to be stable, even when considering the

influence of incoherent (but quasi-elastic) processes. One should, however, keep in mind that the edge-state spin polarization is yet to be experimentally verified. Even though there are first experiments which show that the edge states are polarized in some degree of freedom for which there is an associated Hall effect in the bulk material [106], we do not consider this a conclusive proof of the edge-state spin polarization. Nonetheless, in this thesis, a full edge-state spin polarization will often be assumed.

Chapter 3

Magnetotransport at 2d-TI edges

3.1 2d topological insulators in magnetic fields

As explained in Section 2.2.3, the existence of the $\mathbb{Z}_2$ TIs discussed in this thesis is linked to the overall conservation of time-reversal (TR) symmetry. If TR symmetry is broken, the topological arguments outlined in Section 2.2.2 will no longer guarantee the existence of topological edge states. Thus, if one allows for TR-symmetry breaking, e. g., by a magnetic field, one can in general find a path that continuously connects two Hamiltonians that differ in their $\mathbb{Z}_2$ topological quantum numbers without closing the gap [107]. In practice, however, the fields needed to remove the edge states from a 2d TI turn out to be quite high. It is predicted that, for HgTe/CdTe quantum wells, counterpropagating edge states exist up to perpendicular fields of around 8 teslas (at least in a clean bulk system) [108, 109]. Recent experiments show edge states even up to higher fields, a fact that is yet to be fully understood [110].

At finite fields lower than this critical field, pairs of edge states still exist at the boundary. However, the transport properties of these states may be drastically changed as the magnetic field generally lifts their protection from backscattering, cf. Section 2.4. Because of the inherently one-dimensional nature of edge-state transport, any backscattering will unavoidably lead to Anderson localization [111, 112], which causes an exponential dependence of the channel resistance on the channel length. The question how fast this localization occurs for realistic systems is of course a very important one as it may limit the practical usability of the edge states as 1d transport channels.

Recent experiments aiming at this question yield varying results. The first performed experiments on HgTe/CdTe quantum wells showed a strong almost linear decrease of the transmission with magnetic field, suggesting that the edge states are rather fragile to external perpendicular magnetic fields [17, 84]. Similar findings were reported by other groups [113, 114]. Yet all these results were obtained on long samples, $L \gtrapprox 10\,\mu$m, which did not show the expected quantized conductance of $2\,e^2/h$ at zero field[1]. To our knowledge, there are currently no published results on magnetoconductance measurements on small HgTe/CdTe samples for which the quantized conductance at zero field has

[1] The reason for this length-dependent resistance is not yet understood. A possible model that might explain the underlying mechanism is presented in Chapter 4.

been observed. However, from private communications, we learned that edge transport in these samples is much more robust with respect to external magnetic fields [115]. This picture initially also seemed to apply to the competing InAs/GaSb quantum-well system, in which short samples showed stable edge-state transport up to high fields while long samples—which did not show quantized transport at zero field—were strongly influenced already by weak perpendicular magnetic fields [94]. Newer experiments, however, demonstrated that it is possible to produce long InAs/GaSb quantum-well samples that are robust up to at least 1 T [116].

From the theory perspective, there are already some studies which address the magnetoconductance of 2d-TI edge states from various angles [117–120]. One of them tries to explain the magnetoconductance signature by the accidental formation of edge-state loops, i. e., edge-state quantum dots, at the etched boundary of the nanostructure in which the enclosed magnetic flux may lead to an effective TR-symmetry breaking and a non-zero backscattering which leads to localization [118]. This study predicts the localization length to be B^2-dependent for small fields and to saturate for high fields, at a value which is depending on the density of edge-state loops. Most other theory studies on edge-state magnetoconductance investigate the combined influence of elastic scattering in bulk potential disorder and an external magnetic field. In this group of studies, the results are controversial even though they all use comparable methods. The first and maybe most influential study in this field by Maciejko et al. [119] predicts a very strong breakdown of the edge-state conductance already at small fields with a curve shape that is in good agreement with the experiments on long samples [17, 114]: a cusp-like linear decay. This is, however, in contrast with experiments on short samples [115], which is surprising as the model in Ref. [119] assumes the transport to be elastic and fully coherent, something that should rather be fulfilled in the short than in the long samples. Also, it is different from the numerical findings of other groups, which also find the edge-state transport to be rather uninfluenced by moderate magnetic fields and moderate disorder strengths [117, 120].

In this chapter, we try to resolve this discrepancy and to explain the behavior in both scenarios (long and short samples) in a unified picture. For this, we perform systematic numerical calculations to quantify the influence of perpendicular magnetic fields and bulk disorder on the edge-state transport properties. We focus on the regime of moderate magnetic fields, in which we do not have to consider strong band-structure changes like the transition to the integer quantum Hall regime that is expected at very high fields [108].

We start out by investigating transport in a simple ribbon geometry. From this, we learn that the edge-state transport is very robust with respect to the application of an external magnetic field—as long as the transport is still in the 1d regime. However, we see that very strong disorder or the existence of local electrostatic potentials may create metallic patches, which strongly increase the influence of magnetic fields. Consequently, we will study the transport properties of such charge puddles, i. e., areas subject to a constant electrostatic potential, starting with a single puddle. To allow for a comparison of our results to experiments, we then study consecutive arrangements of such puddles in a model treatment and compare to numerical calculations of the full problem. We conclude by relating our results to the experimental findings.

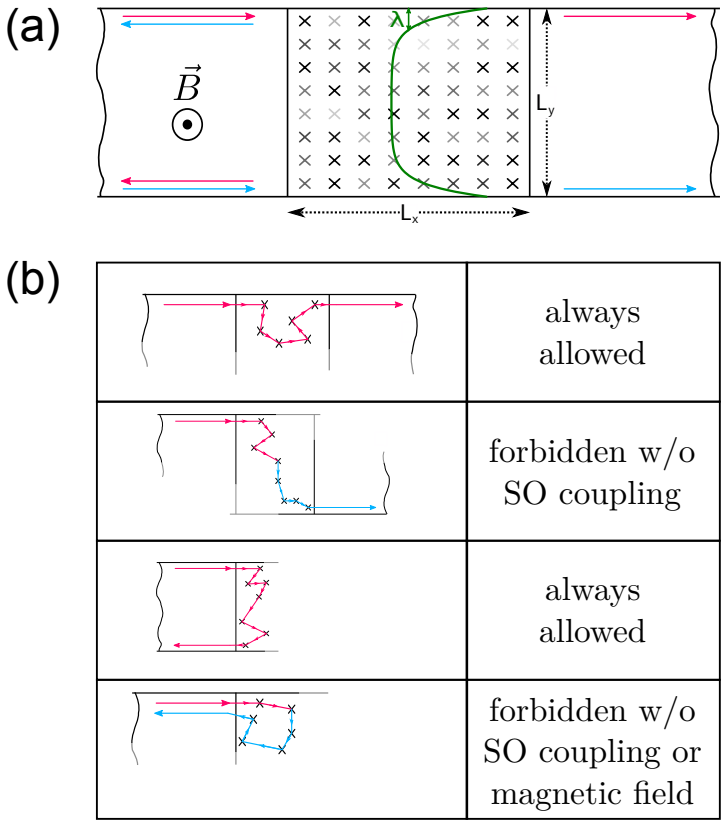

Figure 3.1: (a) shows a sketch of the calculation setup used: a ribbon geometry with a disordered scattering region. Only the spin-polarized topological edge states are present in the leads, where red and blue represent spin up and spin down respectively. As we are considering a scattering problem with incoming current from the left, the incoming modes on the right-hand side of the sample are not shown. To illustrate the meaning of the spread of the LDOS λ, cf. Eq. (3.1), an exemplary transversal LDOS profile together with its corresponding λ value is sketched in green. (b) lists all conceivable scattering paths in this geometry and points out whether they are symmetry forbidden in the absence of spin-orbit (SO) coupling or external magnetic field. Adapted from [21].

3.2 Magnetotransport of disordered ribbons

To study the combined influence of disorder and an applied perpendicular magnetic field, we devise a calculation setup that is sketched in Fig. 3.1(a): a simple ribbon geometry with clean leads and a disordered central scattering region. The BHZ Hamiltonian, Eq. (2.17), is used with HgTe/CdTe material parameters, cf. Table 2.2. It is discretized on a grid with lattice constant $a = 5\,\mathrm{nm}$. Only spin-orbit coupling due to bulk inversion asymmetry, Eq. (2.22), is included describing the case of a completely symmetric quantum well. However, as we show in Section 3.A.3, the inclusion of an additional Rashba term, Eq. (2.23), does not qualitatively change the results presented in this chapter. There, we also show that this even holds for the inclusion of a spatially varying Rashba term that is linked to the local electrostatic potential ("Rashba disorder"), or the inclusion of Zeeman terms, cf. Section 3.A.2, which seem to be of minor importance for the discussed transport at moderate perpendicular magnetic fields. The disorder added to the central region is electrostatic-potential disorder of the Anderson type, i. e., on-site disorder at

each lattice site drawn from a box distribution $V_{\text{dis}} = [-W, W]$ with amplitude[2] W. If not stated differently, the results shown in this chapter are disorder averages over a set of 1000 disorder configurations. The external magnetic field is implemented by a Peierls phase [121] for the hopping matrix elements.

From the discretized Hamiltonian, we obtain the transport properties on the basis of a transport framework by Michael Wimmer, which is using a recursive Green's functions approach [100, 103]. It allows us to extract the transmission and the local density of states (LDOS) in a Landauer-Büttiker picture.

As we are interested in the transport properties of the edge states, we choose the Fermi energy of the system in the gap, $E_{\text{F}} = 0\,\text{meV}$, cf. Fig. 2.5, such that, in a clean system, only edge states contribute to transport. An overview of the possible scattering paths in this setup is shown in Fig. 3.1(b). In addition, the figure shows how the appearance of the individual processes depends on the presence of spin-orbit coupling or on TR-symmetry breaking by an external magnetic field. This is important as the *effective* spin-orbit coupling in HgTe/CdTe is relatively small ($\Delta = 1.6\,\text{meV}$ compared to a bulk energy gap of $\approx 20\,\text{meV}$)[3] so that processes depending on its existence are suppressed. Due to the fact that the bulk of a 2d TI is insulating, there is also a strong suppression for processes that require scattering that connects the two edges of the system, even though they might be generally allowed by the symmetries of the Hamiltonian, e. g., the third process in Fig. 3.1(b). From this, it it clear why elastic transport at the edge of HgTe/CdTe quantum wells is expected to be exceptionally robust: The only non-trivial on-edge scattering requires the existence of TR-symmetry breaking, e. g., by an external magnetic field, and is additionally suppressed by a small effective spin-orbit coupling.

With this background knowledge, we can now look at results for the calculated transmissions at different perpendicular magnetic fields in this geometry, which are shown as blue lines in Fig. 3.2(a). The considered applied magnetic fields correspond to a couple of flux quanta penetrating the ribbon (a field of 0.05 T induces a total flux of $\approx 6\,h/e$). Still, for low disorder strength, $W < 40\,\text{meV}$, we do not observe any effect of the applied magnetic field and the edge states just show undisturbed propagation, leading to the quantized transmission of $2\,e^2/h$ (one conductance quantum from one edge state at each side of the ribbon). At intermediate disorder strengths, $40\,\text{meV} \leq W \leq 150\,\text{meV}$, there is a strong effect of the applied magnetic field, which leads to increased backscattering. However, at these disorder strengths, one also observes a reduction of the transmission at zero field below the quantized value. Without an applied magnetic field, this reduction can only stem from the third backscattering process depicted in Fig. 3.1(b), i. e., from edge-to-edge backscattering, which implies that the insulating behavior of the bulk is already lifted at these disorder strengths. For still

[2] It is important to note that the amplitude of the on-site disorder is not meaningful on its own right in our effective model. As we show in detail in Section 3.A.1 in the appendix to this chapter, it should be always considered together with the chosen lattice discretization and is not independent of it.

[3] This might be surprising because the band inversion that creates the non-trivial topology is due to strong relativistic effects in these heavy-element compounds. Naturally, this goes hand in hand with a large spin-orbit coupling. However, the BHZ model is a low-momentum expansion around a TRIM at which the two states are necessarily degenerate and can be formally decoupled. The effective spin-orbit coupling that describes the splitting when moving away from this TRIM turns out to be small as we already saw in Section 2.3.2.

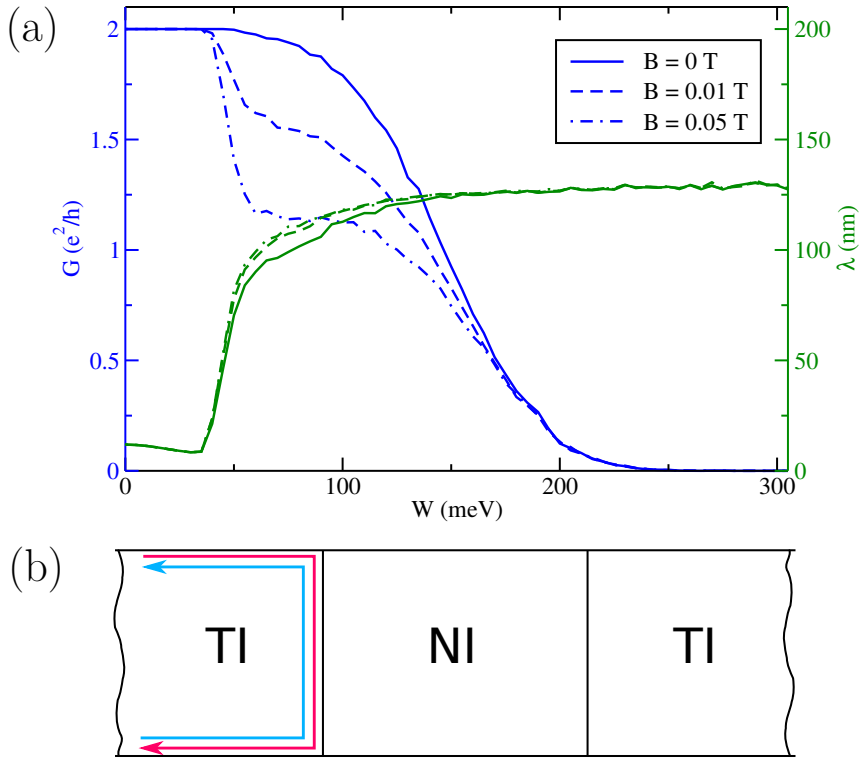

Figure 3.2: (a) Plot of the transmission (blue lines) and of the spread of the LDOS (green lines), cf. Eq. (3.1), for the ribbon geometry sketched in Fig. 3.1(a) calculated at different magnetic fields (full, dashed, dash-dotted) as a function of disorder strength, with $L_x = 1000\,\mathrm{nm}$ and $L_y = 500\,\mathrm{nm}$. (b) Illustration of *topological reflection* in which the different topology (TI: topological insulator, NI: normal insulator) of the scattering region (due to strong disorder) leads to an immediate reflection at the lead boundary. Adapted from [21].

stronger disorder, this trend continues: The transmission at zero field tends to zero but, interestingly, also the effect of the magnetic field diminishes.

To understand these features, it is instructive to analyze the scattering states contributing to transport at the respective disorder strengths and magnetic fields. This can be done by numerically determining the local density of states (LDOS) $d(x, y)$ and using it to calculate a quantity that we call the spread of the local density of states

$$\lambda = \frac{\int dx\, dy \left[y\, \theta\left(\frac{L_y}{2} - y\right) + (L_y - y)\, \theta\left(y - \frac{L_y}{2}\right)\right] d(x,y)}{\int dx\, dy\, d(x,y)}, \tag{3.1}$$

with $\theta(y)$ being the Heaviside step function. The spread of the LDOS λ quantifies the distance of regions with a high LDOS from the sample edge, as schematically indicated in Fig. 3.1(a). It is in a way the ribbon-geometry analogue to the mean distance from the sample edge $\langle y \rangle$ that we discussed in Section 2.3.2, where we studied the extent of the edge states in a semi-infinite plane geometry. Results for λ are shown in Fig. 3.2(a) as green lines. At small disorder strengths, one observes that the transport takes place almost exclusively at the edge of the ribbon ($\lambda < 15\,\mathrm{nm}$). Note that the value in this low-disorder limit is in good agreement with the analytically calculated result of the

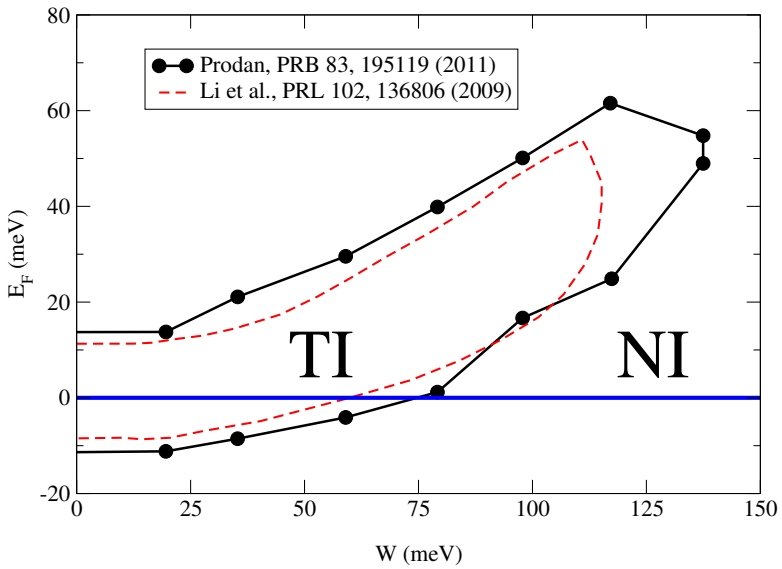

Figure 3.3: Phase diagram for disordered HgTe/CdTe quantum wells. Here, we plotted data from Prodan [122] and Li et al. [123] who extracted the phase boundaries between the topological insulator (TI) and the trivial Anderson insulator (NI) phase for the bulk material using different methods. The disorder scale has been adapted to the convention used in this thesis, where V_{dis} is chosen from the interval $[-W, W]$. The blue line indicates the position of the Fermi energy in our numerical calculations.

mean distance from the edge, Eq. (2.34), which yields $\langle y \rangle = 13.7\,\mathrm{nm}$ at the studied Fermi energy ($E_{\mathrm{F}} = 0\,\mathrm{meV}$). At $W \approx 40\,\mathrm{meV}$, λ increases sharply and saturates at a plateau value of $\lambda \approx L_y/4 = 125\,\mathrm{nm}$ for high disorder strength. This plateau corresponds to a completely flat distribution of the LDOS in the transverse direction. Notably, the position of the sharp transition coincides with the onset of edge-to-edge coupling and the increased magnetic-field effect. The position of the transition itself, however, is largely unaffected by the application of magnetic fields.

These features can be understood by considering the phase diagram for disordered HgTe/CdTe quantum wells, which has already been calculated by other authors [122, 123] and is reproduced in Fig. 3.3. The blue line indicates the Fermi energy for which our numerical calculations were performed. The calculations from these two references use almost the same parameters as the ones used in this thesis, cf. Table 2.2 (Ref. [122] chooses a slightly larger inverted gap $M = -13.5\,\mathrm{meV}$). The main difference is the fact that they neglect any effective spin-orbit coupling, thus they study the model from Eq. (2.17) with decoupled spin blocks. However, as we already learned that the effective spin-orbit coupling in HgTe/CdTe is small, we expect a qualitatively similar phase diagram in our case. Fig. 3.3 shows that a bulk phase transition is expected around $W = 70\,\mathrm{meV}$, where the material turns from a TI to a topologically trivial Anderson insulator. For the model with decoupled spin blocks that they consider, this is a direct insulator-to-insulator transition exactly like the phase transitions between two quantum Hall plateaus[4] [124–126]. When one includes spin-orbit coupling, model studies predict a small metallic phase that separates the two insulators [63, 127–130], which is possible in

[4] In fact, from a symmetry perspective the two spin blocks behave like decoupled Chern insulators (which are in symmetry class A, cf. Table 2.1) with opposite Chern numbers.

the two-dimensional AII symmetry class (*symplectic metal phase*) [131,132]. As discussed before, spin-orbit coupling is very small in our case, which is why we also expect such a true 2d-metal phase to be small. However, even if the metallic phase was completely absent, one should take into account that also the insulator-to-insulator transition leads to quasi-metallic behavior close to the phase transition. This is due to a divergence of the localization length of the bulk states right at the point of the phase transition between the two insulators (of course, such a divergence also occurs at a metal-to-insulator phase transition) [133]. Therefore, for a finite-sized system as the one considered in our numerical calculations, one always expects a window of disorder strengths between the two insulating phases in which the localization length of the bulk states is large compared to the system size. In this window, the bulk of the system will behave like a conductor at the length scales probed—with the wave functions of these extended states showing interesting multifractal properties [124, 134, 135]. Thus, we expect the existence of a metallic phase in our scenario, which is predominantly due to a finite-size effect and only very little due to spin-orbit coupling. Viewed from this perspective, the phase diagram from Fig. 3.3 that does not include spin-orbit coupling suffices for our discussion and we will just keep in mind that the phase transition between the insulators passes through an intermediate metallic regime, the size of which will depend on our system size.

In our data in Fig. 3.2(a), this metallic window is probably responsible for the onset of edge-to-edge scattering and the connected increase of the spread of the LDOS discussed above, which is why we suspect it to start at around $W \approx 40\,\mathrm{meV}$. From there on, it should span the range of "intermediate" disorder strengths, maybe up to $W \lessapprox 100\,\mathrm{meV}$. Interestingly, this is the range of disorder strengths in which we observe the strong effect of the magnetic field. In fact, it is only there that we observe a non-negligible contribution of on-edge backscattering [the fourth process in Fig. 3.1(b)]. In a semiclassical picture of diffusive trajectories, this is understandable as the trajectories need to enclose a sizable magnetic flux in order to lead to an effective breaking of TR symmetry. This is easily possible if the bulk of the system is conducting but it is forbidden in the case of quasi-1d transport enforced by a strongly insulating bulk.

That being said, we can also understand the behavior in the strong disorder limit. Here, the whole scattering region turns into a topologically trivial Anderson insulator and a situation which we dubbed *topological reflection* and which is sketched in Fig. 3.2(b) arises: The edge states forming at the interface are naturally reflected leading to the flat transverse LDOS profile signaled by the value of $\lambda \approx 125\,\mathrm{nm}$ and to the vanishing effect of the magnetic field, which is the hallmark of true one-dimensional transport.

The observation that on-edge backscattering—the process that one would expect to be the key player for the magnetoconductance of the edge states—only contributes in the "intermediate" disorder regime, in which the bulk already starts to conduct and to couple the two edges, may be surprising. And, it makes one wonder about the disorder strength that can be realistically considered to be present in the state-of-the-art experimental samples. To estimate this strength, it may help to make use of the fact that the bulk of the experimental samples is insulating [136], meaning that the disorder should be weak enough such that backscattering processes at zero magnetic field should be suppressed as they require transitions through the bulk, cf. Fig. 3.1(b). From the calculated transmission at zero field (full blue line) in Fig. 3.2(a), we read off that this is

only the case for $W \leq 50\,\mathrm{meV}$. However, to observe backscattering at finite field (another experimental observation), one needs a disorder strength of at least 40 meV, which would set quite strict bounds on the experimentally present disorder strength. To this estimate one might object that the width of our scattering region in the computations is narrow compared to the ribbon widths used in experiments ($L_y^{\mathrm{exp}} \approx 10\,\mu\mathrm{m}$). In wider ribbons, the bulk localization length needs to be larger to couple the two edges and the onset of the decrease of the full blue curve in Fig. 3.2(a) shifts to larger disorder strength, increasing the window of disorder strengths which are compatible with the experimental observations. In principle, this is true, however, the phase transition at $W \approx 70\,\mathrm{meV}$, which has been obtained from finite-size scaling [122], will be a hard upper limit to this window, independent of the size of the ribbon.

As we do not believe the disorder strength in the experiment to incidentally lie in this small disorder window, we investigate an alternative scenario which allows on-edge backscattering without edge-to-edge coupling: disorder which is limited to the edges of the sample. This may well be realistic for the experiments as the patterning process, which is usually done by ion-beam etching, is known to create strong edge disorder. To model this, a configuration as shown in Fig. 3.4(a) is used, in which edge-to-edge coupling is artificially suppressed by limiting the disorder to a region close to the sample edge and leaving a clean strip in between the two edges which is wide enough to guarantee good insulation. Results for such a setup are shown in Fig. 3.4(b). Because of the decoupled edges due to the clean region, the transmission at zero field always perfectly remains at the quantized value. At a finite magnetic field, the results for the conductance at low disorder strengths resemble the above scenario of the fully disordered ribbon: Full transmission and no effect of the magnetic field at very low disorder strength, then, a sudden increase of the LDOS spread in combination with an increased magnetic field effect, again around $W \approx 40\,\mathrm{meV}$ at the insulator-to-metal transition. Increasing the disorder from there on, one observes a decreased backscattering at fixed finite magnetic field. This seems counterintuitive at first sight as one might expect that stronger disorder should lead to more backscattering. However, it makes sense when reconsidering the phase transition to a trivial insulator that occurs at high disorder strengths. This leads to a configuration as depicted in Fig. 3.4(c). In this limit, the transport will be one dimensional as in the case for very low disorder, but it will take a different path, which wraps around the disorder patches. As discussed before, this strictly one-dimensional transport will suppress any effect of the magnetic field which is in good agreement with our observations. The behavior of the spread of the LDOS also corroborates this picture: The curve for λ shows a transition from pure edge transport at the outer edge for low disorder strength over an intermediate metallic region where the transport is fully spread over the disorder region ($\lambda \approx (L_y - L_\mathrm{c})/4 = 75\,\mathrm{nm}$) to edge transport at the inner edge at high disorder strengths ($\lambda \to (L_y - L_\mathrm{c})/2 = 150\,\mathrm{nm}$).

By looking at snapshots of the LDOS $d(x, y)$ of the scattering region for a single disorder configuration which are shown in Fig. 3.5, we can confirm the above explanation that strong disorder leads to a transition from edge transport at the outer edges to edge transport at the inner edges, with very high disorder making the disorder regions act like topologically trivial Anderson insulators. Also, one nicely sees the intermediate metallic regime, in which the transport is completely spread over the whole disorder

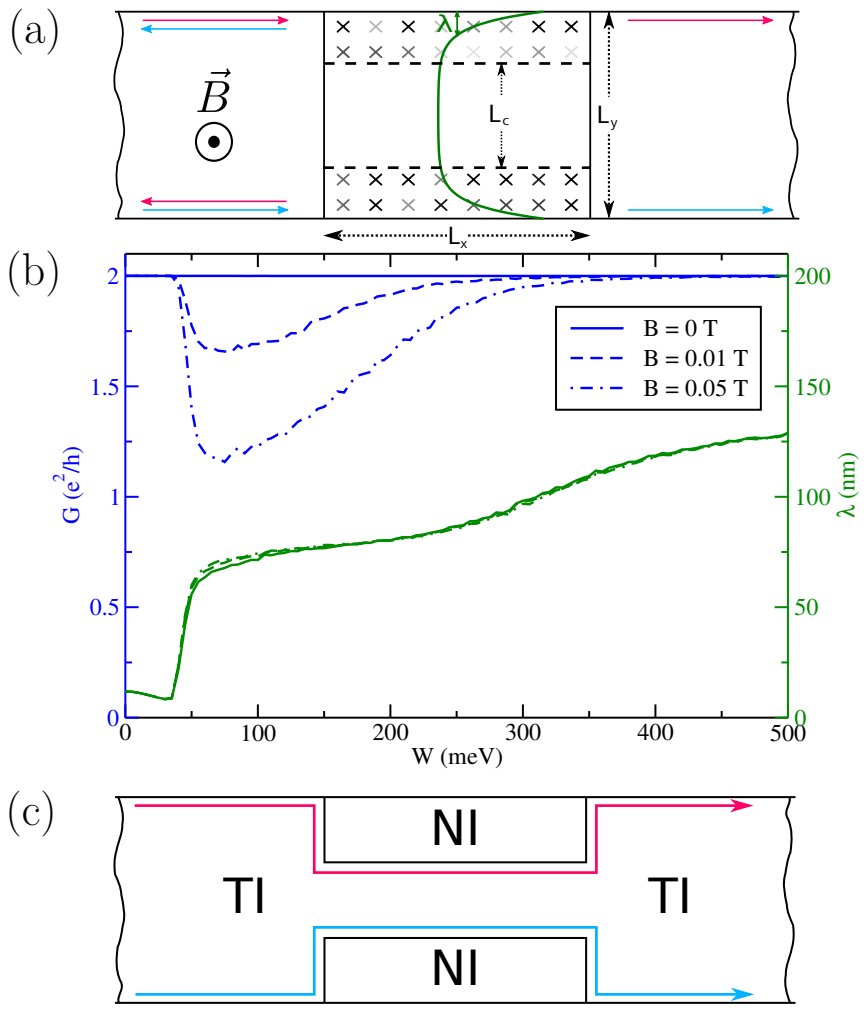

Figure 3.4: (a) shows a sketch of the calculation setup with "disconnected edges", in which the scattering region only includes disorder at the sides and a clean gap is left between the two edges. This suppresses edge-to-edge coupling at any disorder strength. (b) shows results for a calculation of the transmission (blue lines) and λ (green lines), cf. Eq. (3.1), as a function of the disorder strength and at different magnetic fields for the geometry shown in (a), with $L_x = 1000\,\mathrm{nm}$, $L_c = 200\,\mathrm{nm}$, and $L_y = 500\,\mathrm{nm}$. (c) illustrates the situation at strong disorder strengths: the edge states bypass the disorder patches, see also the fourth panel in Fig. 3.5. Adapted from [21].

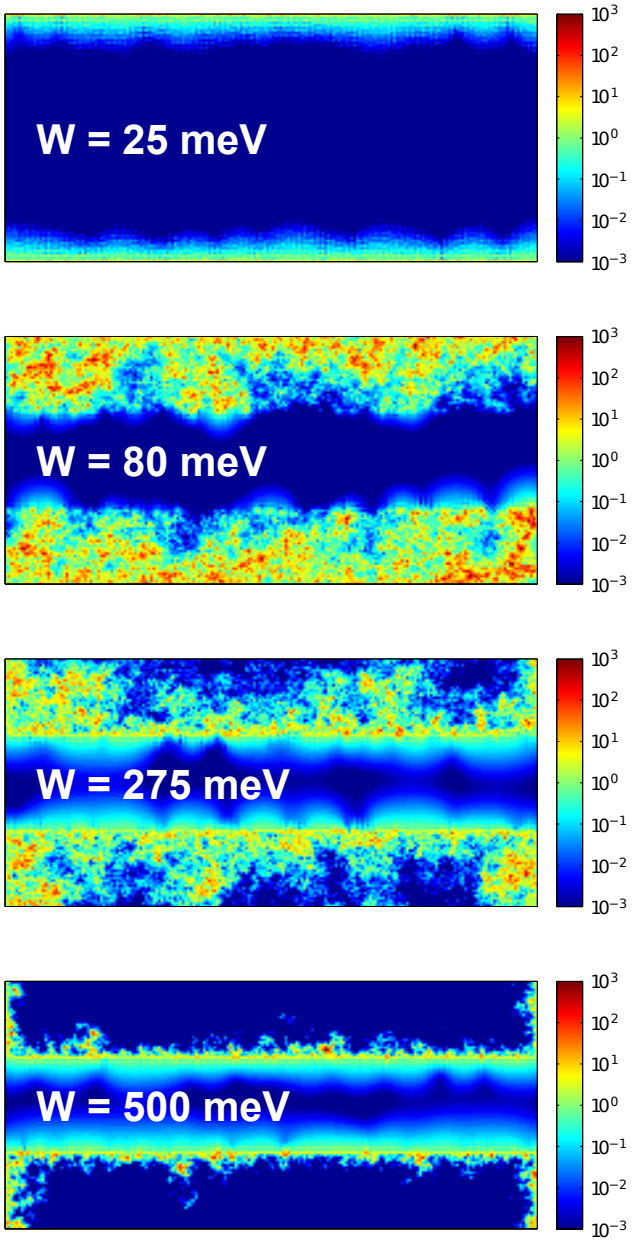

Figure 3.5: Logarithmically scaled plots of the LDOS (arbitrary units) for the central scattering region in the geometry shown in Fig. 3.4(a). The graphs were obtained from a single disorder configuration. They show the transition from the weak disorder regime, in which the transport occurs close to the sample edges, via the intermediate disorder regime, where the quasi-metallic behavior of the disordered regions is observed, to the strong disorder regime, which also features pure edge transport along a relocated phase boundary. Adapted from [21].

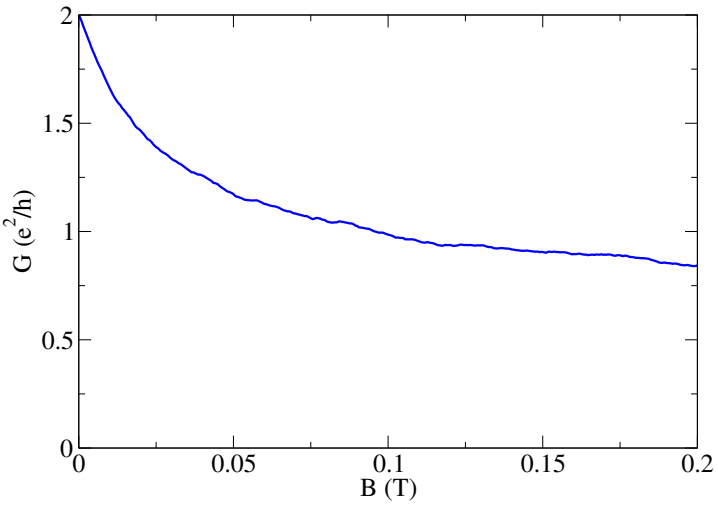

Figure 3.6: Disorder-averaged conductance of a ribbon geometry with a clean non-disordered gap, cf. Fig. 3.4(a), with the same geometry that was used to obtain Fig. 3.4(b), for a fixed disorder strength of $W = 70\,\mathrm{meV}$ and a varying magnetic field. We find that the transmission decreases very rapidly and with an almost linear dependence close to $B = 0$.

region (second panel in Fig. 3.5). The finding that strong disorder may expel topological states has already been observed by other authors in the context of surface states of 3d TIs [137]. However, to our knowledge, the effect of these relocated edge states on transport has not previously been seen and we think that this may show up a new alternative way for patterning 2d TIs: Instead of edging away unwanted material, one could locally introduce strong disorder, e. g., by irradiating the sample with ion beams in order to shape the desired edge-state current paths.

Now is a good point to recapitulate the results obtained so far and to compare to experiments and to previous publications. We found that the transport at the edges of 2d TIs is very stable with respect to disorder and magnetic field as long as it stays essentially one dimensional, which is well fulfilled in a wide range of disorder strengths. This is in good agreement with experiments on small HgTe/CdTe quantum well samples [115] but disagrees with the findings of Ref. [119] where the authors find a strong influence of the magnetic field already at much lower disorder strengths. This disagreement is surprising as they are using a calculation setup that is almost identical to ours. It differs mainly in one point: They artificially put a large additional mass term on the uppermost row of grid points with the intention to decouple the two edges in a similar spirit as we use the clean gap in our calculations. In addition, they are also using a very small clean gap of only 30 nm—too small to provide proper insulation on its own. It seems that this additional mass term leads to the strong magnetoconductance signature that they observe at low disorder strength. We also find this magnetic-field dependence but only in a disorder window that is much closer to the phase transition, and in which the bulk is no longer truly insulating. At these disorder strengths, the disorder is effectively creating local metallic patches. Calculating the magnetic-field dependence of the transmission at such a disorder value, e. g., $W = 70\,\mathrm{meV}$, which is shown in Fig. 3.6, we—like Ref. [119]—find an almost linear dependence of the transmission for low fields. This agrees well with

the experimental results on long samples [17, 114]. Thus, it hints to the existence of local metallic regions close to the edges. However, these regions need not necessarily stem from strong inhomogeneous disorder. Another possible source for them, which we find more likely, is that they are due to locally trapped charges, which create an electrostatic potential similar to a local external gate. Such charges are known to exist in these samples [138] and they create an inhomogeneous potential landscape which—due to the small bulk band gap—often leads to *electron-* or *hole-like puddles*, i. e., regions in which the local electrochemical potential lies in the conduction or valence band. Some theories also hold them responsible for the observed backscattering at zero field [139–142] as they may enhance the effects of electron-electron interactions and phase-coherence breaking, both of which are so far not included in our model. We will quantitatively study the effect of the latter in Chapter 4, where we will see that puddles are indeed an important ingredient for the backscattering due to dephasing. However, for now we stay with the non-interacting fully coherent picture and study how such puddles, i. e., local electrostatic gates, affect the magnetoconductance signature of the edge states.

3.3 Magnetoconductance of charge puddles

To study the influence of a local electrostatic potential—which could be created artificially by a gate or be present intrinsically due to a trapped charge—on topological edge states, we devise a calculation setup that is sketched in Fig. 3.7(a). It consists again of a central disorder region in which a constant electrostatic potential is added at one side. The reason to put the gate only on one side is mainly a numerical one as it helps to keep the transverse extent of the scattering region small[5]. The disorder is mainly included to suppress the mesoscopic fluctuations or interferences due to the specific gate geometry. However, we will choose the disorder weak enough for the bulk material to remain fully insulating ($W < 40\,\mathrm{meV}$). In this way, the bottom edge will always remain in the truly one-dimensional transport regime and will contribute a background signal of one conductance quantum (even at finite magnetic fields), which we can simply ignore in the interpretation of the results.

In Fig. 3.7(b), disorder-averaged results for the transmission through such a setup as a function of the magnetic field for different lengths of the gated region are displayed. We note that all shown curves roughly follow the same pattern: At zero field, one necessarily finds the perfect conductance which starts to decrease as a quadratic function of the field for very small magnetic fields (up to $\approx 0.5\,\mathrm{mT}$) in good agreement with the expected behavior in edge-state Aharonov-Bohm loops [118]. At increasing field, this quickly turns over to an almost linear transmission decay, in strong similarity to the experimental results on long samples [17,114], where a cusp-like signature was observed for small fields, or to the calculations on strong disorder patches, cf. Fig. 3.6.

Interestingly, the edge-state backscattering saturates at higher fields at a value $G(B \gg$

[5]The numerical effort for the employed recursive Green's function method scales unfavorably with respect to the transverse direction ($\propto L_y^3$) when compared to the longitudinal direction ($\propto L_x$). Therefore, it is advantageous for us to choose a narrower scattering region and to compensate for that by taking a large number of impurity averages.

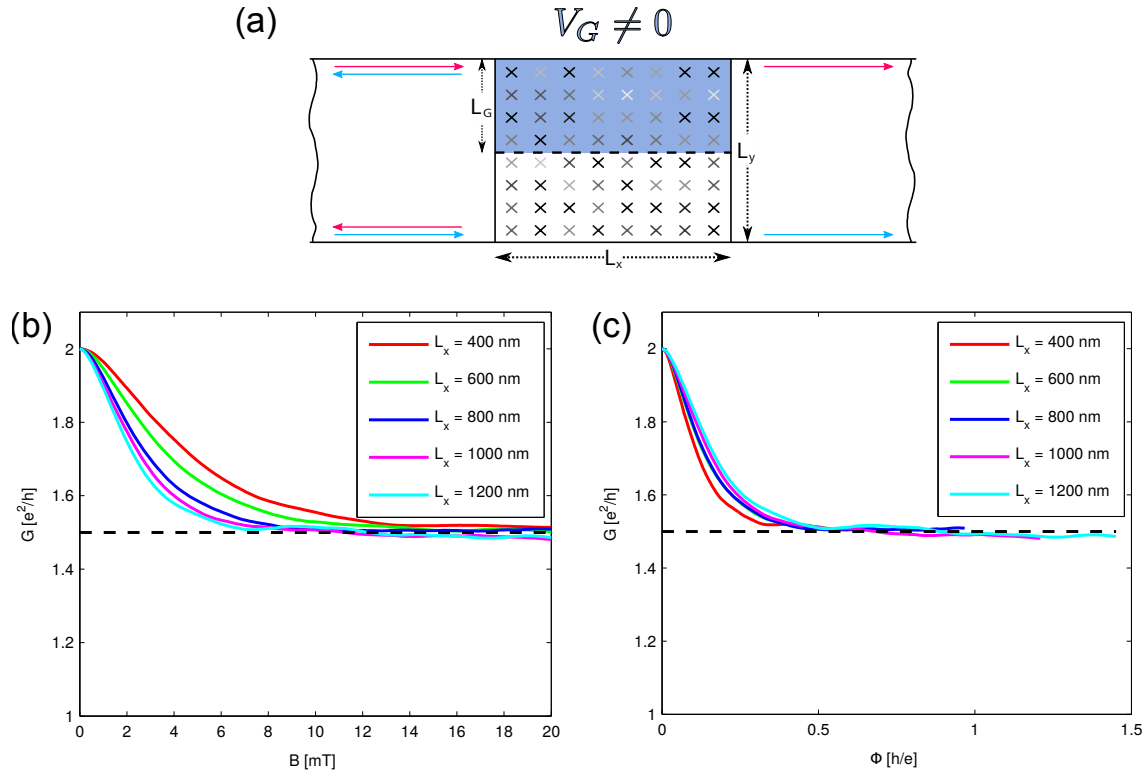

Figure 3.7: (a) shows the calculation setup to study the influence of a locally gated region on the transport of topological edge states. The whole scattering region is (weakly) disordered and one side is covered by a gate that locally shifts the Fermi energy into the valence band. The bottom edge state remains unaffected and always contributes one conductance quantum. (b) Disorder-averaged results for the transmission through the setup sketched in (a) for different lengths of the gated region L_x as a function of the applied magnetic field. The width of the gated region, in which a gate potential of $V_G = 50\,\text{meV}$ is applied, is chosen to be $L_G = 250\,\text{nm}$ at a total scattering region width of $L_y = 500\,\text{nm}$, being subject to a weak disorder potential with amplitude $W = 5\,\text{meV}$. (c) The same data as shown in (b) is replotted as a function of the magnetic flux through the gated area. Here, all curves almost fall on top of each other and show that roughly one flux quantum is enough to cause fully ergodic scattering in the puddle. Adapted from [21].

1) $\approx 1.5\,e^2/h$ that is almost independent of the size of the scattering region. This particular value suggests that the gated region effectively behaves like a chaotic cavity at these magnetic-field strengths, showing completely symmetric random scattering of the electrons. This is confirmed by an analysis of the statistics of the obtained transmission values which can be seen in Fig. 3.8, which shows histograms of the obtained transmission values for varying magnetic field in the case of $L_x = 1000\,\text{nm}$. Starting out with a sharply peaked distribution at small magnetic fields, it turns into a completely flat distribution above a critical field of $B \approx 6\,\text{mT}$. At high fields, the observed transmission for a single realization of such a system will be a random number from the interval $[0, 1]$. This flat distribution of transmission eigenvalues is a hallmark of a single-channel scattering matrix that is drawn from the *circular unitary ensemble* (CUE), which describes the scattering in ergodic cavities [143, 144]. This random-matrix ensemble is defined by a probability distribution that is given by the Haar measure of the unitary group. It can be qualitatively understood as randomly drawn "rotation/reflection matrices" in complex

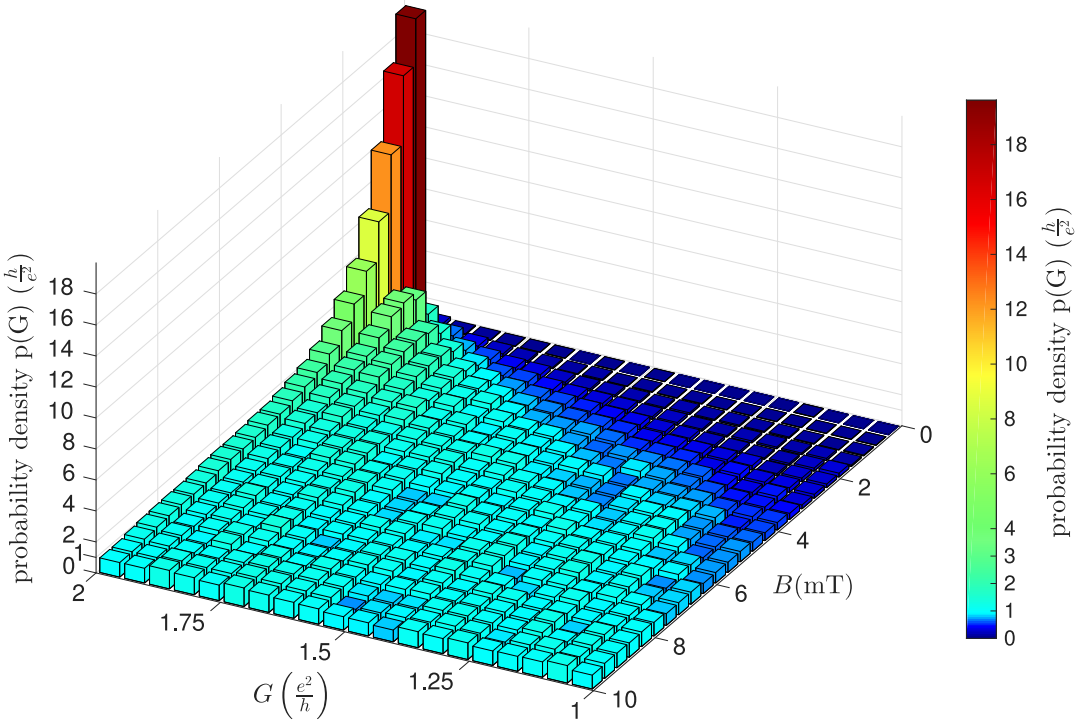

Figure 3.8: The plot shows histograms of the probability density for the transmission at different magnetic fields for the calculation of a one-sided gate of length $L_x = 1000\,\mathrm{nm}$, i. e., the data of which the average transmission is plotted as the pink curve in Fig. 3.7(b). For strong enough magnetic field, the distribution flattens out completely signaling ergodic scattering.

space which are drawn from a "fully isotropic" distribution. This CUE ensemble explains the mean value of $1.5\,e^2/h$ at large fields, which reflects the fully random scattering.

Even though this ergodic behavior is found independently of the length of the scattering region (for the set of lengths considered here), the critical field at which the transition occurs is strongly length dependent. This is understandable from a semiclassical viewpoint: The enclosed flux of the set of scattering trajectories should be large enough in order to fully break TR symmetry to allow for completely ergodic scattering. An increase of the gate length leads to an increase of the average enclosed area, and one would expect the critical field to scale linearly with the gated area. This is indeed what happens as can be seen in Fig. 3.7(c), in which the data from Fig. 3.7(b) is replotted as a function of the magnetic flux through the gated region, $\phi = BA$, in units of the magnetic flux quantum h/e. As a function of the flux, the data shows very similar behavior. Moreover, the data indicates that a flux of only one flux quantum through the gated area suffices to induce the ergodic mean value.

The ergodic regime for sufficiently large fields is not just obtained for a single choice of disorder strength and potential depth but it is found in a larger parameter regime. This is illustrated by Fig. 3.9, which shows the conductance at sufficiently high field $B = 15\,\mathrm{mT}$ under the variation of the disorder strength at fixed gate potential $V_G = 50\,\mathrm{meV}$, Fig. 3.9(a), or the variation of the potential of the gated region at a fixed disorder strength of $W = 5\,\mathrm{meV}$, Fig. 3.9(b). As one can see, there is an extended plateau in either parameter space that is characterized by the CUE behavior described above.

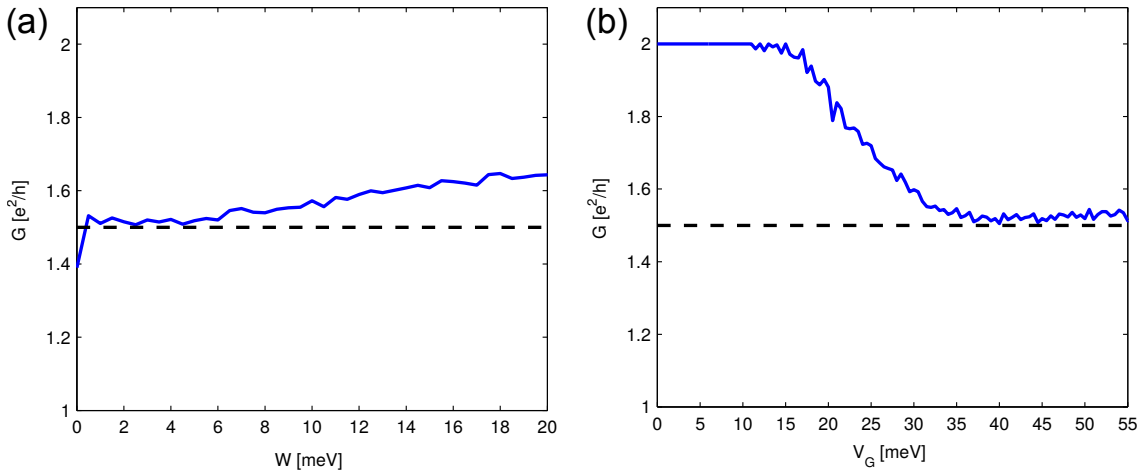

Figure 3.9: Disorder-averaged results for the transmission through a setup with a one-sided gate, cf. Fig. 3.7(a), subject to a magnetic field of $B = 15\,\mathrm{mT}$, and with the following device geometry: $L_\mathrm{G} = 250\,\mathrm{nm}$, $L_y = 500\,\mathrm{nm}$, and $L_x = 1000\,\mathrm{nm}$. In (a) the disorder strength is varied at a constant gate potential $V_\mathrm{G} = 50\,\mathrm{meV}$ and in (b) the gate potential is varied leaving the disorder strength constant at $W = 5\,\mathrm{nm}$. In both panels, a regime is found in which the mean transmission is roughly at $1.5\,e^2/h$ corresponding to completely random scattering. Adapted from [21].

3.4 Transmission properties of consecutive charge puddles

3.4.1 Localization in a chain of CUE scatterers

In the previous section, we discussed the transport properties of a single puddle that is located close to the edge of a HgTe/CdTe quantum-well structure. Such puddles are expected naturally and are supposed to be caused by potential fluctuations due to impurities, which cause such a local metallic behavior due to the small band gap of the material. To understand the transport properties of a larger section of quantum-well edge, it is therefore necessary to consider the conductivity of a series of such puddles. To approach this problem of many scatterers, we will start off with model calculations and also do numerical random-matrix calculations to generally understand what to expect when many puddles are connected in series. Later, we will compare the results of these model calculations with the full numerical treatment of a chain of puddles at the HgTe/CdTe quantum-well edge.

We specialize on the case where the puddles are in the CUE regime discussed at the end of the previous section, which is expected to be found for large puddles and sufficiently strong magnetic fields in a wide parameter range. In this limit, each puddle leads to 50% backscattering on average. The total transmission of two scatterers with transmissions t_1 and t_2 connected in series which are coupled incoherently is given by [104]

$$T = \frac{t_1 t_2}{t_1 + t_2 - t_1 t_2}, \tag{3.2}$$

which can be easily generalized for a chain of N scatterers with transmissions t_n,

$$T = \frac{1}{1 - N + \sum_{n=1}^{N} \frac{1}{t_n}}. \tag{3.3}$$

One might naively expect that if each scatterer on average has a total transmission of $\langle t \rangle = \frac{1}{2}$, the total transmission would be given by

$$\langle T_N \rangle_{\text{incoherent}} \stackrel{?}{=} \frac{1}{1 - N + \sum_{n=1}^{N} \frac{1}{\langle t \rangle}} = \frac{1}{1+N}, \tag{3.4}$$

i. e., that the resistance increases roughly linearly with the amount of puddles and thus with the length of the sample (assuming a roughly constant density of puddles along the edge). In this way, the edge would behave as a metallic resistor with constant specific resistivity. This treatment, however, neglects the width of the probability distribution and the fact that the average over the ensemble should only be taken after calculating the total transmission. In our considered scenario, the completely flat probability distribution then leads to the following integral:

$$\langle T_N \rangle_{\text{incoherent}} = \int_0^1 dt_1 \ldots \int_0^1 dt_N \frac{1}{1 - N + \sum_{n=1}^{N} \frac{1}{t_n}}, \tag{3.5}$$

which can be solved analytically for small N. A numerical solution of the integral is plotted as a red curve in Fig. 3.10(a). It clearly shows that the decay is much faster than the decay described by Eq. (3.4) that is shown as a violet curve for comparison. The log-log plot of the same data in Fig. 3.10(b) reveals that the decay for this scenario where the average is taken over the total transmission is still polynomial unlike in a localized system but the power is no longer linear, instead we have $T \stackrel{\approx}{\propto} N^{-1.3}$. The fact that we find a stronger decay is easily understandable as, in a chain of scatters, a single scatterer with a low transmission causes a low total transmission of the whole chain. If all scatterers transmit completely randomly, the probability of having at least a single scatterer which is badly transmitting strongly increases with the chain length. This makes the higher power plausible. In Eq. (3.4), this was artificially excluded by assuming that each scatterer has a transmission of $\frac{1}{2}$. In this way, we see that the strength of the transmission fluctuations in the ensemble of puddles has a strong effect on the average total transmission of a chain to the degree that it changes the exponent of the power-law decay.

So far, we assumed that the puddles are coupled incoherently meaning that the phase acquired by the reflection on a puddle or by the transmission through a puddle can be neglected. This is a realistic scenario if the dephasing time in the sample is smaller than the propagation time between the two puddles, thus if they are very far apart. For small temperatures and densely spaced puddles, this is not realistic and a fixed phase relation between the puddles will be retained and has to be included into the calculation. Still, to a good approximation, the scattering phases of the puddles can be assumed to be independent.

For two consecutive scatterers with transmissions t_1 and t_2, and a fixed relative

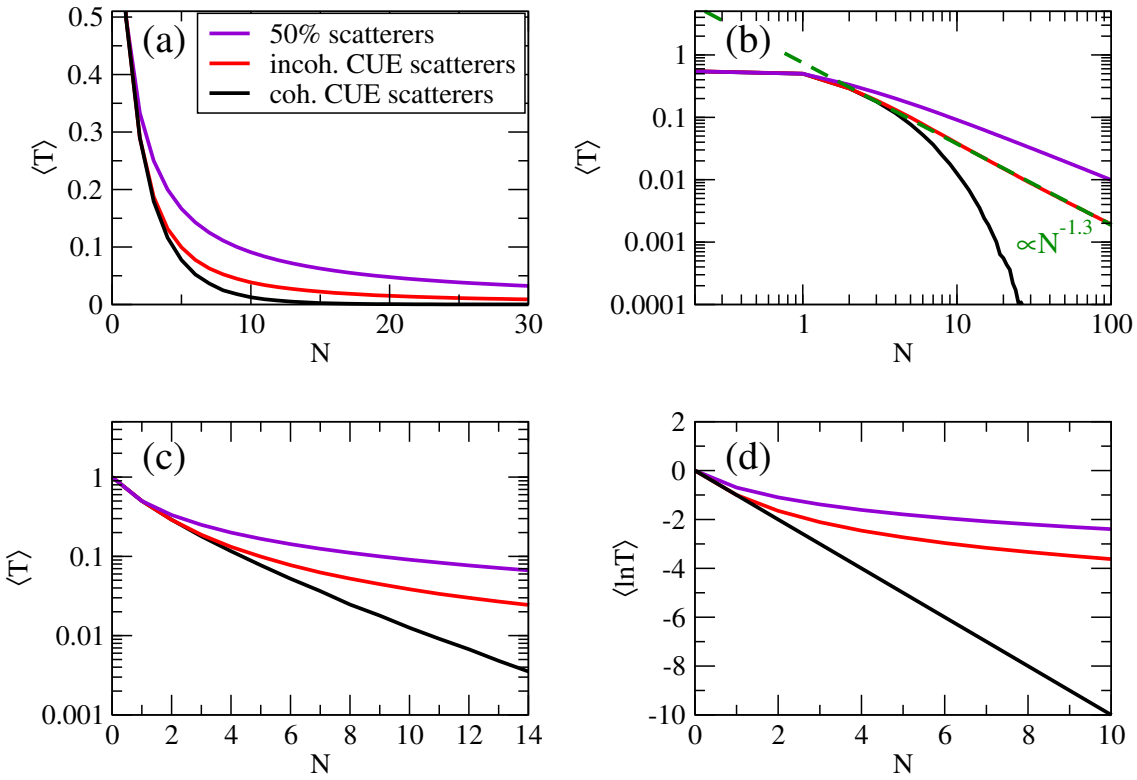

Figure 3.10: The panels (a), (b), and (c) show the averaged transmission through a chain of N scatterers which themselves have a transmission probability of 0.5 on the average. The three panels show the same data but differ in their axis scaling. The violet curve shows the results for scatterers with a fixed transmission of 0.5 which are coupled incoherently. The red and black curves show the results for scatterers which are drawn from the single-channel CUE ensemble discussed in Section 3.3. For this ensemble, the transmissions are uniformly distributed in the unit interval. The red curve shows the result for an incoherent coupling of the scatterers, cf. Eq. (3.5), while the black one shows the result for a coherent coupling. In (b), the green dashed line indicates a fit to $N^{-1.3}$, which describes the average transmission for a chain of incoherently coupled CUE scatterers in the large N limit. (d) shows the averaged logarithmic transmissions for the three scenarios.

scattering phase θ, one finds the following expression for the total transmission [118, 145]:

$$T_{N=2} = \frac{t_1 t_2}{\left|1 + \sqrt{1-t_1}\sqrt{1-t_2}e^{i\theta}\right|^2}. \tag{3.6}$$

Averaging this over the CUE ensemble, we find

$$\langle T_{N=2}\rangle_{\text{coherent}} = \frac{1}{2\pi}\int_0^1 dt_1 \int_0^1 dt_2 \int_0^{2\pi} d\theta \frac{t_1 t_2}{\left|1 + \sqrt{1-t_1}\sqrt{1-t_2}e^{i\theta}\right|^2} \tag{3.7}$$

$$= \frac{\pi^2}{3} - 3 \approx 0.2899, \tag{3.8}$$

which interestingly agrees with the result that is obtained for the incoherent combination of two CUE scatterers. For more than two scatterers, however, this is no longer the case. Also, an analytical solution becomes intractable when considering many puddles.

A numerical treatment is possible though: To find the average of the total transmission in our case, we combine randomly drawn CUE scattering matrices by converting them to transfer matrices and then multiplying them. Results of such a numerical calculation are shown in Figs. 3.10(a), (b), and (c) as black lines. We see that, now, we indeed find the exponential decay that is expected from the scaling theory of localization [146, 147] for a one-dimensional system.

Another important consequence of Eq. (3.6) that was already noted previously [118,145] is that the logarithm of the total transmission,

$$\ln T = \ln t_1 + \ln t_2 - \ln \left| 1 + \sqrt{1-t_1}\sqrt{1-t_2}e^{i\theta} \right|^2 , \tag{3.9}$$

is additive when averaging over all scattering phases because

$$\frac{1}{2\pi}\int_0^{2\pi} d\theta \ln \left| 1 + \sqrt{1-t_1}\sqrt{1-t_2}e^{i\theta} \right|^2 = 0, \tag{3.10}$$

so that

$$\langle \ln T \rangle = \langle \ln t_1 \rangle + \langle \ln t_2 \rangle . \tag{3.11}$$

This is even generally true for all distribution functions of the transmission amplitudes of the separate scatterers. For the special case of CUE scatterers with an equal probability for every possible transmission, we find

$$\langle \ln t \rangle = \int_0^1 dt \ln t = -1, \tag{3.12}$$

and therefore

$$\langle \ln T \rangle_{\text{coherent}} = -N. \tag{3.13}$$

This fact can also be seen in the numerical results shown in Fig. 3.10(d), which compare the averaged logarithm of the total transmission for the case of N coherent and N incoherent scatterers (showing for comparison also the averaged logarithmic transmission for the scenario in which the transmission of each scatterer is fixed to $t = 0.5$). For a chain of only two scatterers, we showed above that the averaged total transmission $\langle T_{N=2} \rangle$ is the same, independent of whether they are coherently or incoherently coupled. Interestingly, the averaged logarithmic transmission $\langle \ln T_{N=2} \rangle$ turns out to be different in the two cases and is therefore sensitive to the coupling. To show this, we calculate $\langle \ln T_{N=2} \rangle$ for the case of incoherent coupling, cf. Eq. (3.5),

$$\langle \ln T_{N=2} \rangle_{\text{incoherent}} = -\int_0^1 dt_1 \int_0^1 dt_2 \log\left(\frac{1}{t_1} + \frac{1}{t_2} - 1\right) \tag{3.14}$$

$$= -\frac{\pi^2}{6} \approx 1.644, \tag{3.15}$$

which differs from the result for two coherent scatterers, $\langle \ln T_{N=2} \rangle_{\text{coherent}} = -2$.

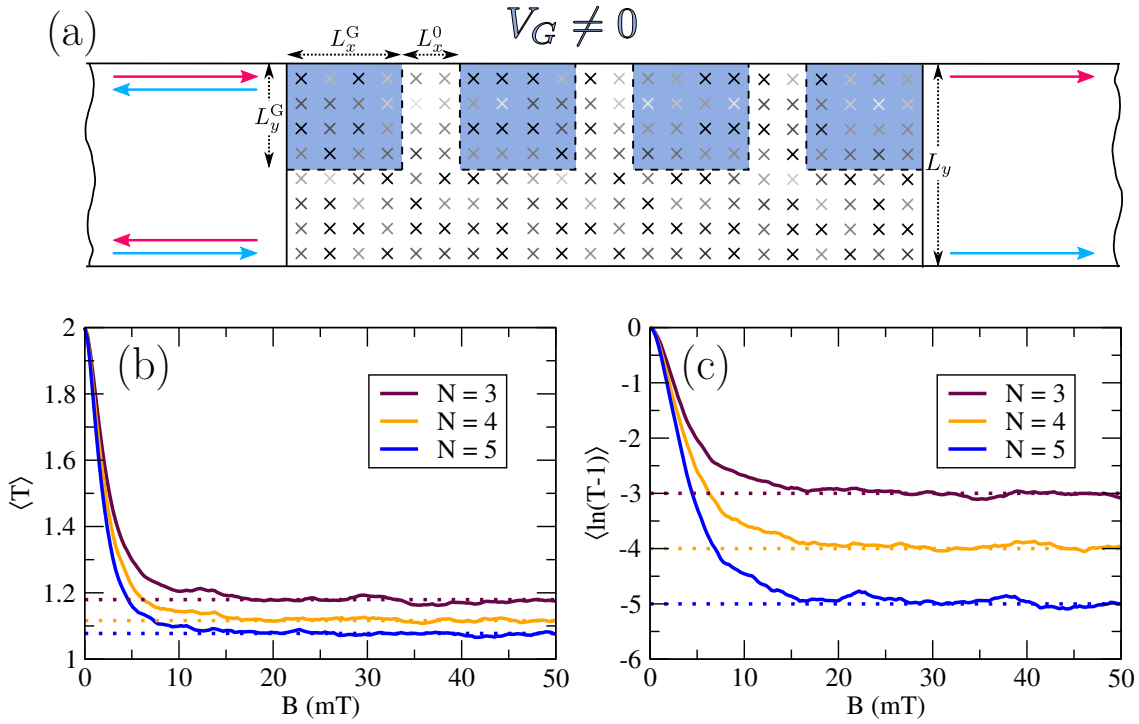

Figure 3.11: (a) shows the setup in which we investigate the transport properties of a chain of charge puddles close to the edge of a 2d TI for the case of 4 puddles, which are defined by local gates. (b) and (c) show the numerical results for a chain of N such puddles as a function of the applied magnetic field, where (b) shows the disorder-averaged transmission and (c) shows the average of the logarithm of the transmission of the top edge. The colored dashed lines indicate the expected values for a chain of coherently coupled CUE scatterers, cf. black lines in Fig. 3.10. The parameters for the puddle geometries are $L_y = 500\,\mathrm{nm}$, $L_y^G = 250\,\mathrm{nm}$, $L_x^G = 600\,\mathrm{nm}$, and $L_x^0 = 300\,\mathrm{nm}$. The gate is chosen at $V_G = 50\,\mathrm{meV}$ and the disorder amplitude is $W = 5\,\mathrm{meV}$.

3.4.2 Numerical treatment of a chain of puddles at the HgTe/CdTe quantum-well edge

To see that these random-matrix results indeed apply for the scattering in a series of puddles, we again perform transport calculations using the recursive Green's function algorithm, considering a series of N puddles of size $250\,\mathrm{nm} \times 600\,\mathrm{nm}$ on the edge of a HgTe/CdTe ribbon. The detailed setup is sketched in Fig. 3.11(a) for the case of 4 puddles. The results for the averaged transmission and the averaged logarithm of the transmission, which are depicted in Figs. 3.11(b) and (c), show that we obtain exactly the behavior which is expected for consecutive CUE scatterers. As the puddles are all of the same size, we also see that we reach the limit in which the CUE scattering is obtained roughly at the same magnetic field independent of the number of scatterers in the chain. As the final value which is reached depends on the number of scatterers, it also affects the initial slope that is measured around $B = 0$. From this calculation, we learn that the detailed potential landscape has a strong influence on the edge transmission. For example, one large gated puddle only leads to a backscattering of 50%, cf. Fig. 3.7, but this will be reached already at small fields. Subdividing the gated region and introducing small gaps, which are not gated, leads to a stronger total reflection in the large-field

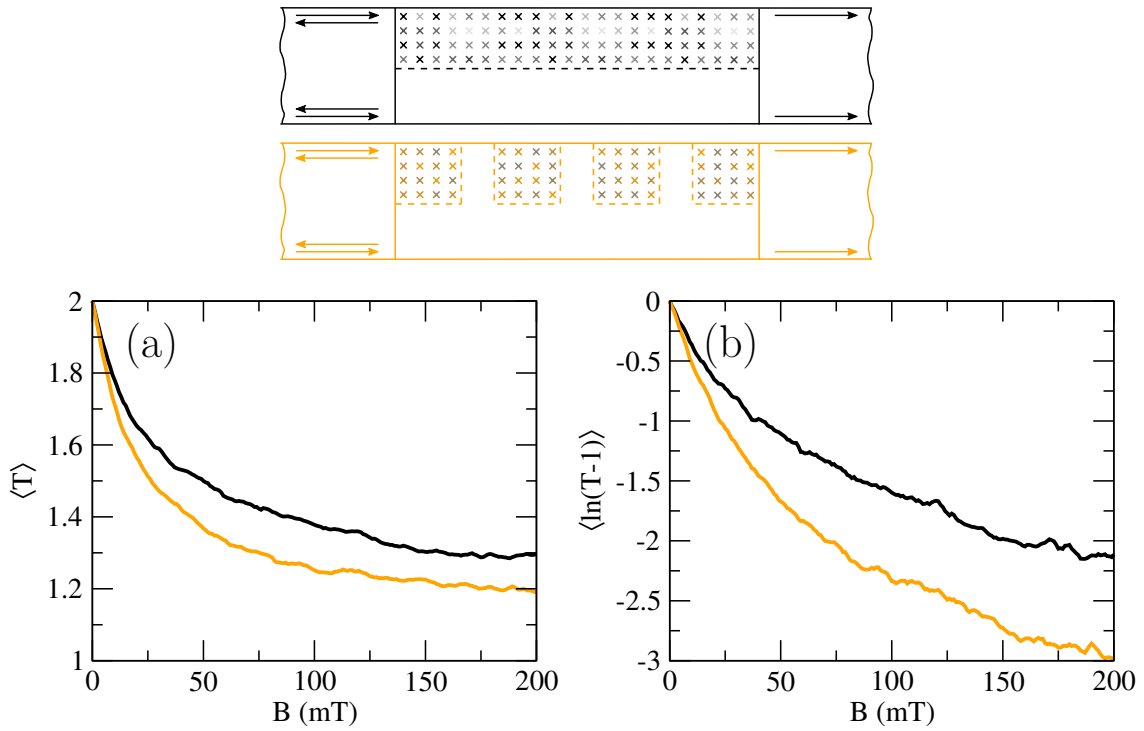

Figure 3.12: The figure shows (a) the transmission and (b) the logarithm of the transmission of an edge section subject to two different disorder patterns shown in the sketch above the figure. The total length of the two arrangements is the same, $L_x = 1500\,\mathrm{nm}$, but the yellow arrangement contains three clean gaps of length $L_x^0 = 100\,\mathrm{nm}$ between the patches of disorder. The width $L_y = 250\,\mathrm{nm}$ and the disorder strength of the two arrangements is the same, $W = 70\,\mathrm{meV}$. Thus, the orange arrangement can be considered less disordered. Still, it leads to stronger reflection, which can be understood by the subsequent coupling of puddles leading to stronger reflection, cf. Fig. 3.10.

limit, cf. Fig. 3.11, but one needs more field to reach this limit.

The puddles, which were patterned by gates in our calculation, could equally also be created by very strong disorder which induces the discussed insulator-metal transition. In this way, the fact that it is really the detailed arrangement of gates (or disorder) that matters can be illustrated even better: Even though these puddles which are created by strong disorder are generally too strongly disordered for being in the CUE regime, meaning they would not have a completely flat distribution of transmission eigenvalues, the principles of combining them are similar to the ones discussed in the last section. In this way, an arrangement that is sketched in orange in Fig. 3.12 with four small such sections of strong disorder yields a transmission that is smaller than the arrangement shown in black in the same figure, which has one big disordered region of the same length. This implies that intermediate non-disordered regions may actually lead to a decrease of the overall transmission, or equally, more disorder may lead to an increased transmission in some configurations. Even though this is a very qualitative discussion, it shows an important point: The detailed microscopic disorder configuration, i. e., the size and distribution of puddles (may they be due to strong disorder or due to local charge fluctuations), has a strong influence on the resistance of the edge, which makes this a quantity that is very difficult to understand on general grounds.

3.4.3 A chain of coherently coupled puddles in weak fields

In the last section, we studied the behavior of a series of puddles in magnetic fields, which are strong enough to induce the CUE behavior supposed that the puddles are generally in the right parameter regime. However, as we learned, the field at which this CUE scattering is reached depends on the puddle size. If the puddles in the sample are all sized differently, this may lead to a complex dependence of the transmission on the magnetic field, which is another reason that makes a direct comparison to experiments difficult. In this section, we would like to investigate the behavior of a chain of scatterers at weak fields, i. e., close to $B = 0\,\mathrm{T}$.

As we discussed in the previous section, it is the average of the logarithmic transmission which is additive in a chain of coherently coupled scatterers, cf. Eq. (3.11),

$$\langle \ln T \rangle = \sum_{n=1}^{\infty} \langle \ln t_n \rangle \,. \tag{3.16}$$

Let us assume for a start that all the puddles in the chain are in the parameter regime where they show CUE scattering for large enough fields. Then, their magnetic-field dependence turns out to be relatively independent of the size if plotted as a function of the magnetic flux through the puddle, ϕ, cf. Fig. 3.7(c). For small fields, it can be well approximated by a linear dependence,

$$\langle t(\phi) \rangle \approx 1 - \frac{\phi}{\phi_\mathrm{c}}, \tag{3.17}$$

with the slope $1/\phi_\mathrm{c}$. For a chain of N puddles of areas A_n, this implies

$$\exp \langle \ln T(B) \rangle = \exp \left(\sum_{n=1}^{N} \langle \ln t(A_n B) \rangle \right) \approx \exp \left(- \sum_{n=1}^{N} \frac{A_n B}{\phi_\mathrm{c}} \right) \tag{3.18}$$

$$= 1 - \frac{B}{\phi_c} \sum_{n=1}^{N} A_n + \mathcal{O}(B^2). \tag{3.19}$$

We find that the slope of the conductance at low fields is related to the total area of the puddles in the sample. Experimentally this slope is an extractable quantity and experiments on long samples yielded values for the slope of the normalized conductance at small fields, $d\left[\sigma(B)/\sigma(0)\right]/dB$, ranging from ≈ 0.5 (1/T) [114] to ≈ 50 (1/T) [17]. As we saw in Fig. 3.7(c), puddles that are in the CUE regime show a slope of the transmission close to zero field that is approximately $\phi_\mathrm{c} \approx 0.5\, h/e$. Using this value, we can estimate that the total puddle area in the experimental samples is between $1000\,\mathrm{nm}^2$ and $100\,000\,\mathrm{nm}^2$, which for a single circular puddle would correspond to a diameter of 35 nm and 350 nm respectively. While the larger area could still be compatible with the assumption that the sample can be understood as a chain of CUE scatterers, the smaller area is contradicting this because a puddle of a linear size of 35 nm is clearly too small to be in the CUE regime. In our calculations, we observed the CUE regime for puddle sizes $\gtrsim 100\,\mathrm{nm}$ at a gate potential of $V_\mathrm{G} = 50\,\mathrm{meV}$. In smaller puddles, there is still a large fraction of the current that ballistically traverses the puddle without scattering

chaotically, thus, resulting in an average transmission that is above 0.5 even with a sizable magnetic field. Puddles with a size below the CUE regime saturate at this higher value and are therefore also expected to have a decreased slope at zero field, i. e., $\phi_c > 0.5\,h/e$. Thus, for these puddles, one would extract a larger area from the above argument, which looks better in line with the experiments. Therefore, from the fact that the total area extracted from the CUE assumption is too small for a chain of CUE puddles (at least in some samples), one might be tempted to conclude that the puddles in the sample are not in the CUE regime, e. g., because they are shallower than $V_G = 35\,\mathrm{meV}$, cf. Fig. 3.9(b), or smaller than 100 nm. This would indeed be an impressive result and a first step toward the understanding of the disorder of these structures.

However, jumping to such a conclusion ignores the important fact that all those measurements also observe backscattering at zero field. This zero-field backscattering is excluded in the fully elastic coherent theory that is used in this chapter, cf. Section 2.4. As we will see in the next chapter though, a puddle does give rise to zero-field backscattering if decoherence is included. Also, Coulomb backscattering, which is enhanced due to the presence of a puddle, allows for backscattering in puddles even without any magnetic field [141, 142]. Both of these processes (decoherence and Coulomb scattering) also cause puddles to scatter randomly if they are strong enough, i. e., they bring the puddles closer to the 50–50 limit already at zero magnetic field. This decreases the influence of the additional magnetic field, and thus, also reduces the slope at zero field, $\phi_c > 0.5\,h/e$, which no longer excludes the existence of larger puddles in these samples.

3.5 Conclusions

In this chapter, we investigated the combined influence of disorder and magnetic field on the edge transport of 2d TIs. The most important result of this is probably that the edge-state transport is very robust with respect to TR-symmetry breaking by the application of a perpendicular external magnetic field as long as the current is carried by quasi one-dimensional edge states. This was not properly recognized in a previous influential theoretical study [119], and it explains the experimental results on small samples, in which the conductance is seen to be robust with respect to external magnetic fields [115].

If, on the other hand, the sample contains extended conducting regions and therefore also has areas in which the current flow is two dimensional, we find that the influence of the magnetic field is strongly increased. In this regime, we observe a magnetic-field dependence of the conductance which is roughly linear in the beginning and saturates for strong fields. Importantly, we find that this general behavior is independent of the "microscopic origin" of the conducting patches, meaning that they could be equally due to charge puddles as studied in the last part of this chapter or due to very strong disorder. Disorder can induce metallic behavior as it triggers an insulator-insulator phase transition to the topologically trivial Anderson insulator phase, for which, at the transition, the localization length of the bulk states diverges and quasi-metallic behavior is observed. As the obtained linear magnetoconductance signature is in good agreement with the experiments on long samples, we take it as a piece of evidence for the existence of metallic

patches in these systems. However, we find it unlikely that these metallic regions in the experiments are due to extremely strong bulk disorder, the reason for this being that this would also lead to bulk conduction which is not observed in current experiments.

Our theory seems to yield good qualitative agreement with the relative change of the conductance due to the magnetic field for long samples if one assumes the existence of charge puddles close to the edge, for which there is also some experimental evidence, or equally if one assumes strong disorder which is limited to the edges of the sample. The fact that small samples are seen to be robust to the application of magnetic fields can then be attributed to the fact that they are short enough not to contain any puddles, while this is practically impossible for large samples, given that the puddles naturally appear in some density in the quantum well.

The quantitative comparison of the experimental results to our theory, which aimed at the extraction of information about, e. g., the size or the distribution of puddles, turned out to be very difficult. Even though our numerical calculations show a certain parameter regime, in which a universal CUE behavior is observed for a single puddle, we could not conclusively determine whether the puddle distribution in the experimental samples can be assumed to lie in this parameter regime. This was mainly because of the unknown strength of the zero-field backscattering of a single puddle. Outside of this CUE regime, the total transmission strongly depends on the detailed disorder configuration. Here, experimental data of the conductance is certainly not sufficient and additional input from complementary measurements would be necessary. Experiments that use scanning gate probes [138] or microwave microscopy imaging [110] are probably a good start in this direction.

Of course, it is also very important to find a convincing explanation for the observed backscattering at zero magnetic field, which cannot be explained by the presented elastic fully coherent transport theory of this chapter. This is still one of the big open problems in this area and we will study one of the proposed zero-field backscattering mechanisms in Chapter 4 of this thesis. However, as we will see, this will not lead to a fully convincing explanation either, at least given the currently available experimental data. So, many of the results from this chapter should be taken with a grain of salt, in the sense that it is not fully clear to which extent the employed models are a good description of the current experimental samples.

Also due to this uncertainty, we would like to emphasize that we find it highly important to conduct experiments on artificial puddles, in which many of the predictions could be checked more thoroughly. For this, it would certainly be desirable to start from a puddle-free quantum well, something that seems to be only possible for small samples (in which then also the quantized conductance is observed).

At last, we should mention that—even though the disorder in the current experimental samples is probably too weak to be close to the phase transition as this would come along with bulk conductance—one may think about artificially increasing it, e. g., by ion-beam irradiation. In this way, the phase transition could be used to pattern devices and control the intended current paths as an alternative to the currently used etching techniques.

3.A Appendix

3.A.1 The influence of the lattice discretization on the effective disorder strength

In this section, we discuss the role of the discretization that is used to map the continuum effective Hamiltonian to a lattice model in the numerical calculations. This discussion will be mainly centered around the influence of the discretization on the effective disorder strength of the employed on-site (Anderson) disorder.

In our case, the numerical discretization is done by applying a finite-differences scheme to the derivatives in the Hamiltonian. As we are interested in the results for the continuum model, we need to make sure that the lattice constant is chosen small enough to obtain converged results for the continuum limit. For this convergence, a choice of $a = 5\,\mathrm{nm}$ is generally considered to be sufficient. When studying a system with Anderson disorder, however, one should keep in mind that a change of the discretization comes with a rescaling of the disorder strength as we will discuss in the following. In Fig. 3.13(a), we show calculations of the simple ribbon geometry, which is shown in Fig. 3.1(a), for different choices of the discretization a and for different magnetic fields. The plotted data for $a = 5\,\mathrm{nm}$ is the same as the one in Fig. 3.2(a). We notice that the general behavior of the system does not change very much with a different discretization, however, the size of the discretization seems to effectively rescale the disorder-strength axis. This has to do with the fact that the discretization length is effectively also the correlation length of the disorder potential when considering on-site disorder. The correlation length, however, has an influence on the mean free path, i. e., on the effective strength of the disorder. For the electron gas, it is known that the mean free path l depends quadratically on the disorder correlation length [148] and on the disorder amplitude, $l \propto W^2 a^2$. To compare whether this relation explains the rescaling in our setup, we replotted the numerical data for the transmission from Fig. 3.13(a) as a function of the quantity Wa in Fig. 3.13(b). In this way, we indeed find an acceptable agreement between the curves, showing that Wa is a consistent measure of the effective disorder strength also for our scenario. The agreement is not perfect especially in the case of an applied magnetic field, which might have to do with the fact that the scenario that we study does not simply depend on the mean free path, which is derived in the weak disorder limit, but is also strongly influenced by the detailed phase diagram of the quantum-well material. The phase transition, which generally occurs at strong disorder, may show different scaling properties and is definitely known to also depend on the correlation length of the disorder [149], which is directly related to the lattice constant in the case of on-site disorder. This in turn changes the disorder strength at which we expect the insulator-to-metal transition and the connected increased effect of the magnetic field. For the qualitative treatment of disorder in this chapter, however, we are satisfied with the agreement of Fig. 3.13(b) and conclude that a change of the discretization of the Hamiltonian can be compensated by an associated rescaling of the disorder strength. With this knowledge, we would like to emphasize that, even though it is sometimes done [114, 119], we believe that it is not meaningful to compare the amplitude of the disorder W at which some critical phenomena occur (e. g.,

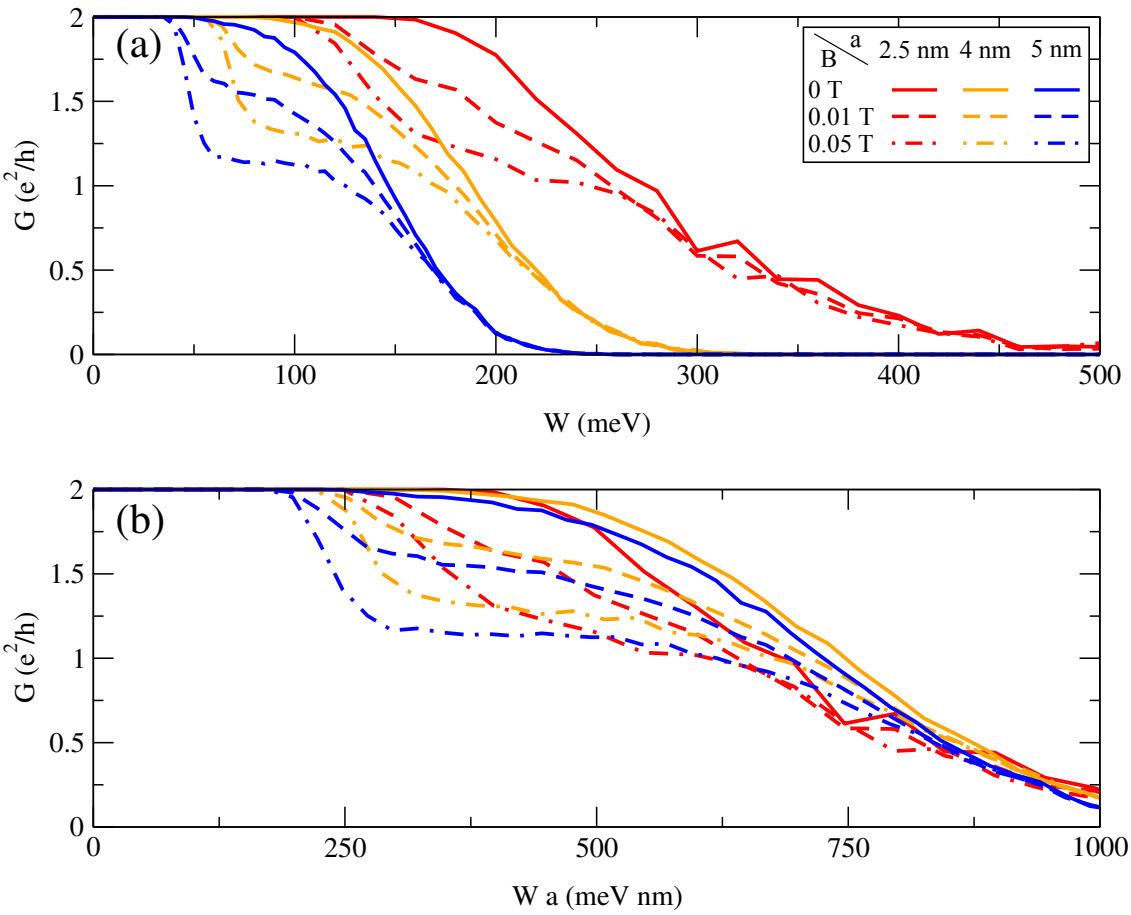

Figure 3.13: (a) shows disorder-averaged transmissions as a function of the disorder strength calculated for the ribbon setup sketched in Fig. 3.1(a) with the same geometry and the same parameters as used in the calculation of Fig. 3.2(b) for different choices of the numerical discretization constant a, which is used to map the continuum effective model to a lattice. As in Fig. 3.2(b), the calculations are performed for different choices of the perpendicular magnetic field (full: $B = 0\,\mathrm{T}$, dashed: $B = 0.01\,\mathrm{T}$, and dash-dotted: $B = 0.05\,\mathrm{T}$), where the color indicates the chosen discretization (blue: $a = 5\,\mathrm{nm}$, orange: $a = 4\,\mathrm{nm}$, and red: $a = 2.5\,\mathrm{nm}$). (b) shows the same data plotted as a function of Wa.

a phase transition) with other energy scales of the problem, like the bulk band gap. This is so because the effective disorder strength is influenced by the discretization a, which is usually arbitrarily chosen. To interpret the disorder amplitude on its own right, one should choose a spatially-correlated disorder potential for which the disorder correlation length is realistically chosen. In our treatment, however, we do not attempt to interpret the amplitude as an energy scale and we use it simply as a knob to tune the disorder strength. Also, we make sure that the phase diagram we compare to, cf. Fig. 3.3, was calculated for the same choice of a, such that we can directly compare the amplitudes. In general, however, one has to be careful when comparing disorder strengths for on-site disorder across publications if a different lattice discretization was used.

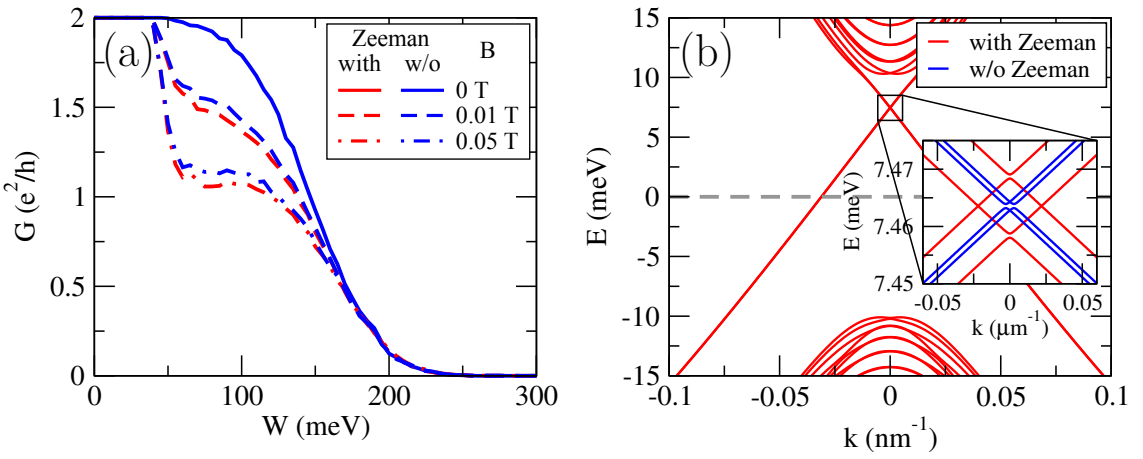

Figure 3.14: The figure shows the influence of the inclusion of Zeeman terms. (a) contains disorder-averaged results for the calculation in a simple ribbon geometry as sketched in Fig. 3.1(a). In addition to the data from Fig. 3.2(a), displayed as blue lines, results of calculations with Zeeman terms are shown. The different line styles indicate different values of the magnetic field. (b) shows the influence of Zeeman terms on the band structure, where the field strength was set to $B = 0.05\,\mathrm{T}$ and orbital terms were neglected. The difference to the calculation without magnetic field is only visible in a very close zoom as shown in the inset. The gray dashed line indicates the Fermi energy at which the calculations of this chapter are performed.

3.A.2 The influence of Zeeman terms

In this section, we study the influence of Zeeman terms on the results for the ribbon geometry, which was studied in Section 3.2 and is shown in Fig. 3.1(a). We show that their inclusion does not lead to a qualitative change of the results. Using Zeeman terms [Eq. (2.24)] of realistic strengths, which have been derived from $k \cdot p$ calculations [84], and for which the parameters are given in Table 2.2, we find very similar results in terms of the transport properties of the ribbon, as shown in Fig. 3.14(a) as red lines. The blue lines show the data from Fig. 3.2(a) for comparison, i. e., the calculations without Zeeman terms. Even though the Zeeman coupling also explicitly breaks TR symmetry and may therefore contribute to backscattering, it seems that this effect is almost negligible compared to the effects of the orbital magnetic field, at least up to the magnetic fields that we consider. Importantly, it does not lead to backscattering as long as the disorder is weak, in line with the main conclusions drawn in Section 3.2.

Also, when considering the influence of Zeeman coupling on the band structure of a ribbon that is subjected to magnetic field, one only finds a tiny effect as demonstrated in Fig. 3.14(b). In this plot, orbital terms are set to zero and only the effect of Zeeman terms at $B = 0.05\,\mathrm{T}$ is shown. There is almost no visible difference. Only in the inset that shows the situation close to the "edge-state Dirac point", we see that the splitting of the edge bands, which is inherently present due to spin-orbit coupling, is slightly increased. We also observe an extremely tiny gap. However, this is not due to the Zeeman terms but due to the finite-width hybridization ($L_y = 500\,\mathrm{nm}$) of neighboring edges in the ribbon geometry [86] and can therefore also be observed in the calculation without magnetic field. At least up to the fields that we consider, we think that it is safe to neglect the Zeeman terms, which we did in all other calculations of this chapter.

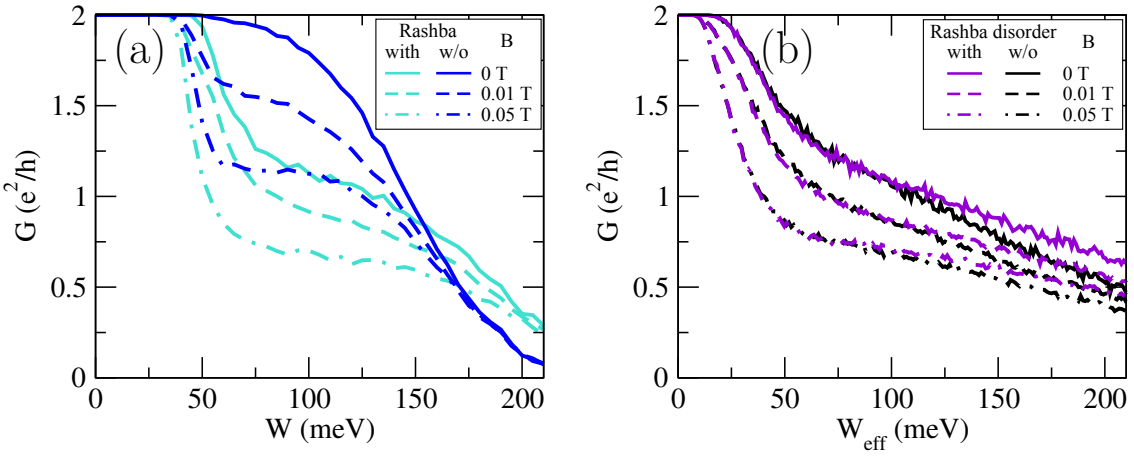

Figure 3.15: (a) shows the influence of a constant Rashba spin-orbit coupling (at $\mathbf{E}_z = 10^7\,\mathrm{V/m}$) on disorder-averaged transport calculations in a simple ribbon geometry as sketched in Fig. 3.1(a). In (b), the same geometry is studied, using a disorder potential which is spatially correlated with a Gaussian profile with a width of $\sigma = 30\,\mathrm{nm}$. In addition, we show results for a calculation in which this disorder potential is used to determine the local electric field for the Rashba spin-orbit interaction, cf. Eq. (3.28), using the proportionality constant $F = 200\,\mathrm{nm}$.

3.A.3 The influence of Rashba spin-orbit coupling and correlated disorder

Rashba spin-orbit coupling, i. e., the effect of structure-inversion asymmetry, may arise in the 2d quantum wells due to electric fields, which may, for example, build up due to the formation of depletion layers at interfaces, due to trapped charges at the gate interface, or due to the voltages applied on external gates. Even though it is known from $k \cdot p$ calculations how to include this effect in the Hamiltonian [82], cf. Eq. (2.23) and the coefficient $\mathcal{R}$ in Table 2.2, one needs at least an estimate of the strength of the electric field $\mathbf{E}_z$, which is not at all easy to find. Therefore, we chose to check the influence of a rather strong constant field of $\mathbf{E}_z = 10^7\,\mathrm{V/m}$, the effect of which is shown in Fig. 3.15(a). We see that the qualitative behavior remains unchanged, e. g., we still do not observe backscattering in the low-disorder regime. However, the backscattering around the phase transition is increased, the difference being particularly pronounced when comparing the calculations without magnetic field. As we know that the presence of spin-orbit coupling terms enlarges the metallic region which separates the two insulating phases, this behavior is understandable.

Current experiments often try to keep the influence of Rashba spin-orbit coupling as small as possible by carefully building a symmetric quantum well, which should at least minimize internal electric fields. This, and the lack of specific information on the magnitude of the electric field in the experimental samples led us to the decision not to include any Rashba spin-orbit coupling in the other calculations shown in this chapter. Of course, one should keep in mind that at least a weak electric field is still likely to be present due to the application of external gate voltages, which are used to tune the Fermi energy into the gap.

In addition to external gate voltages, we usually also assume the existence of disorder

in the quantum well, which in the experiment is believed to be mainly due to trapped charges at the gate-insulator interface. Those charges create an inhomogeneous potential landscape in the quantum well, which is screened in the 2d plane but may give rise to static fields perpendicular to the conducting layer, which are position-dependent and connected to the local disorder potential. We also checked the influence of such a scenario with position-dependent Rashba terms. For this, we changed our disorder model from on-site (Anderson) to spatially-correlated disorder with a Gaussian profile,

$$\langle V(\mathbf{x})V(\mathbf{x}+\mathbf{r})\rangle \propto \exp\left(-\frac{r^2}{2\sigma^2}\right), \tag{3.20}$$

to obtain a more realistic smooth variation of the Rashba field. We practically implement the construction of such a potential landscape by adding up Gaussian functions with standard deviation σ and random amplitudes,

$$V(\mathbf{x}) = \sum_{\mathbf{x}'} v_{\mathbf{x}'} \exp\left(-\frac{|\mathbf{x}-\mathbf{x}'|^2}{2\sigma^2}\right), \tag{3.21}$$

where the sum in $\mathbf{x}'$ runs over every grid point. The $v_{\mathbf{x}'}$ are drawn from a box distribution $[-W, W]$. This leads to a variance of the on-site potential of

$$\left\langle V^2(\mathbf{x})\right\rangle = \frac{W^2}{3}\sum_{\mathbf{x}'} \exp\left(-\frac{|\mathbf{x}'|^2}{\sigma^2}\right), \tag{3.22}$$

where the sum can be evaluated for our square lattice to yield

$$\sum_{\mathbf{x}'} \exp\left(-\frac{|\mathbf{x}'|^2}{\sigma^2}\right) = \sum_{n,m=-\infty}^{\infty} \exp\left(-\frac{a^2}{\sigma^2}\left(n^2+m^2\right)\right) \tag{3.23}$$

$$= \left(\sum_{n=-\infty}^{\infty} \exp\left(-\frac{a^2}{\sigma^2}\right)^{n^2}\right)^2 \tag{3.24}$$

$$= \left[\theta_3\left(0, e^{-\frac{a^2}{\sigma^2}}\right)\right]^2, \tag{3.25}$$

with a being the lattice constant and $\theta_3(z,q)$ being the Jacobi theta function (see §20.2.3 in [150]). For large σ, or equally for small a, one may use the following approximation of the theta function:

$$\theta_3\left(0, e^{-\frac{a^2}{\sigma^2}}\right) \approx \frac{\sqrt{\pi}\sigma}{a}. \tag{3.26}$$

The result for the variance using the correlated disorder, Eq. (3.22), should be compared to the variance of on-site disorder drawn from a box distribution $[-W, W]$, which we otherwise used in this chapter, which yields

$$\left\langle V^2(\mathbf{x})\right\rangle = \frac{W^2}{3}.$$

Thus, at the same choice of W, the two mean variances of the potential differ by a factor that is given by Eq. (3.25). To make the results of the calculations with different disorder models comparable, we present the results for the spatially-correlated disorder as a function of a rescaled disorder strength

$$W_{\text{eff}} = W\theta_3\left(0, e^{-\frac{a^2}{\sigma^2}}\right) \approx W\frac{\sqrt{\pi}\sigma}{a}, \tag{3.27}$$

which would be the corresponding disorder strength for on-site disorder that yields the same potential variance. A similar definition for an effective disorder strength was also used in Ref. [149]. For our choice of the correlation length $\sigma = 30\,\text{nm}$ and the lattice constant $a = 5\,\text{nm}$, this numerical factor amounts to $W_{\text{eff}} \approx 10.6\,W$.

Disorder-averaged results with correlated disorder but without any Rashba spin-orbit coupling are shown in Fig. 3.15(b) as black lines. As we already anticipated from the study of the influence of the lattice discretization on the effect of the disorder, cf. Section 3.A.1, the correlation length increases the effective disorder strength. This explains why we observe backscattering already at lower values of W_{eff} compared to the calculation with on-site disorder, e. g., Fig. 3.15(a). Otherwise, the behavior looks similar: There is no backscattering below a critical disorder threshold, above which we very soon see backscattering already at zero field due to the onset of the phase transition. The main difference is seen in the strong disorder limit, where we observe a much slower decay of the transmission in the case of spatially-correlated disorder. Thus, the phase transition is smeared out a lot more. This is also understandable as finite-size effects due to our comparably narrow ribbon width will be particularly strong for correlated disorder. Here, more detailed calculations with finite-size scaling would be necessary to pinpoint the exact position of the phase boundary.

In the calculation shown as violet lines in Fig. 3.15(b), we also included Rashba spin-orbit coupling, which we chose to be proportional to the local electrostatic potential, thus,

$$\mathcal{R}(\mathbf{x}) = FV(\mathbf{x}). \tag{3.28}$$

Here, $\mathcal{R}$ enters the Hamiltonian as in Eq. (2.23) and the proportionality constant F is set to the numerical value $F = 200\,\text{nm}$. In this way, a local electrostatic potential energy of $V = 75\,\text{meV}$, which is in the range of the investigated effective disorder amplitudes, yields the same Rashba strength as the high field $\mathbf{E}_z = 10^7\,\text{V/m}$ which we considered in the last paragraph. Probably, this is an overestimation of the internal electric fields that arise from disorder. Since we can see that the effect on the transport results is almost negligible, we decided not to include such a Rashba disorder in the other calculations of the chapter.

Chapter 4

2d-TI edge-state backscattering by dephasing in charge puddles

4.1 Temperature-independent backscattering at TI edges

As we outlined in Section 2.2.4, there are simple symmetry arguments which guarantee a protection from elastic backscattering for the edge states of a 2d TI. It is this protection that should prevent their localization, and that together with their full spin-momentum locking, cf. Section 2.3.2, makes them highly attractive for (spin-)electronic applications. However, the so far realized 2d TIs turned out not to behave as sought as they show inherent length-dependent backscattering for device lengths exceeding roughly one micrometer. The mechanism that causes this is yet completely unknown. The intuitive expectation that inelastic processes are behind the backscattering seems ruled out by the experimental observation that the backscattering is very independent of the temperature in an astonishingly large temperature range and one would clearly expect inelastic processes to be strongly temperature dependent. For example, for the InAs/GaSb quantum-well system, combined data from different experiments suggest no change in edge conductance for the temperature range from 20 mK to 30 K [19, 151], covering 3 orders of magnitude! Comparable results were obtained for the HgTe/CdTe material system [17, 136, 139, 152].

For the field of research on 2d TIs, it is very important to explain this behavior. Especially the question whether the backscattering is a peculiarity of the state-of-the-art realizations of 2d TIs is crucial. If this was the case, backscattering could be eliminated by a different design, and an understanding of the backscattering mechanism might show ways to achieve that. Yet, it is in principle also possible that the observed backscattering is an inherent property of all 2d TIs and that the naive elastic single-particle description discussed in Section 2.2.4 will never apply in realistic systems, e. g., due to the fact that the one-dimensional character of the edge states always entails very strong interactions or due to a mechanism that nobody has thought of so far.

An explanation is also important from another perspective: So far, the experimental

evidence from which one concludes that HgTe/CdTe and also InAs/GaSb heterostructures are 2d TIs is the fact that they are edge conductors, which has by now been convincingly shown by many complementary experimental techniques, e. g., by non-local transport measurements [19, 139, 140] or by scanning-squid [136, 151] and microwave-impedance microscopy [110]. However, this alone does not demonstrate the topological origin of these edge states and it is (at least in principle) possible that these edge states are of non-topological origin. Such "trivial" edge states could arise due to surface band bending or could even be introduced by charge redistribution in the patterning process. As we are dealing with a material made from heavy elements, also a spin polarization of such edge states would not be surprising. The main argument why those should be of topological origin is the observation that they appear above a critical thickness of the quantum well at which one also theoretically expects a phase transition to a 2d TI from $k \cdot p$ calculations. This observation is undoubtably a strong piece of evidence for their topological nature. On the other hand, the temperature-independent resistance which increases with the length of the edge would be perfectly understandable for topologically trivial edge states, while it so far remains a complete mystery for the 2d-TI edge states. Also, there are recent measurements which show the existence of edge-state transport in HgTe/CdTe [110] and InAs/GaSb quantum wells [19] at magnetic fields far beyond what would be understandable from $k \cdot p$ calculations. Moreover, other experiments observe edge transport also in parameter regimes in which the system is expected to be topologically trivial [153, 154]. All of these observations could be seen as an argument against the topological interpretation. So, as long as one cannot pinpoint a mechanism that (quantitatively!) is able to explain the backscattering, including the temperature dependence, there should at least be a small bit of doubt about the interpretation that 2d TIs have indeed been observed.

From the theory side, there are already a handful of studies which try to explain the backscattering of the topological edge states. Some of them involve magnetic impurities which break TR symmetry and therefore also allow for an elastic backscattering even at zero temperature [155–157]. However, the concentration of magnetic impurities in the experimental samples is so far believed to be too low to account for the measured backscattering. Other studies consider the effect of backscattering due to the hyperfine interaction with nuclear spins [158] or due to the inelastic backscattering caused by a phonon bath [159], which is—at least at the lowest temperatures—also believed to be irrelevant for the experimental samples. A promising candidate for backscattering is Coulomb backscattering from other carriers on the edge [87,88,160–165], sometimes also in the presence of inhomogeneous Rashba fields. However, these mechanisms typically lead to a power-law temperature dependence of the conductance, which seems incompatible with the experimental results as discussed above. A more promising temperature dependence is obtained from models which consider charged puddles close to the edge that form a quantum dot [141, 142], exactly like the charge puddles that we considered in Chapter 3. Such scenarios predict a logarithmic dependence of the conductance on temperature in some parameter regimes. However, also this relatively weak dependence could so far not be found in experiments. In addition, there is also a discussion that brings up spontaneous time-reversal breaking by means of an exciton condensate, which may cause backscattering [166]. But also in this case, the predicted critical temperature ($T_c \approx 10\,\mathrm{K}$)

seems to be too low to explain the observed temperature independence.

A completely different approach is taken by other studies that also consider inelastic mechanisms but without holding them directly responsible for the backscattering [140,167]. Instead, inelastic processes are just included as a source of decoherence which disturbs the phase evolution of the wave function. This now also lifts the protection from backscattering, which subsequently occurs due to elastic processes. As the elastic processes are then mainly responsible for the backscattering strength, this may explain the temperature independence in a certain regime in which the decoherence is "sufficiently fast". Even though it could be shown in a "proof-of-principle" fashion that this is a conceivable mechanism that would lead to backscattering, the treatment remained rather qualitative as the numerical calculations implemented dephasing ad-hoc by adding virtual leads [167] or by assigning imaginary self energies to some grid points in the calculation [140]. In this way, there was no access to the important question of the relevant time scale corresponding to the "sufficiently fast" limit and whether this limit is quantitatively reached in current experiments.

The purpose of this chapter is to investigate this mechanism, i. e., the influence of dephasing on the backscattering on 2d-TI edge states with a numerical setup that is capable of extracting the relevant time scales and allowing for a quantitative comparison to experiments. We do not attempt to microscopically model the mechanism that is responsible for the dephasing. Instead, we include dephasing as an extrinsic effect which is associated with a time scale, the dephasing time, which enters our model as an external parameter. In this way, our description is not restricted to one specific decoherence process but applies more generally to a wide class of possible mechanisms.

We start by explaining what we mean by dephasing and why it can only lead to backscattering on the edge of a 2d TI if there is a charge puddle close to the edge of the sample. From there, we go on by calculating dwell times of electrons in such charge puddles and use these to estimate the influence of dephasing on the basis of a model. Later, we develop a new scheme to explicitly include the dephasing process in wave-packet evolution algorithms and verify that this leads to results that are consistent with the model calculation. In the end, we try to relate these results to current experimental data and discuss whether this mechanism can explain the experimentally observed temperature-independent backscattering.

4.2 Backscattering by dephasing

In this work, we will use the terms *dephasing* and *decoherence* synonymously and we let them subsume all processes which break the unitary time evolution of the conduction electrons. It is natural to assume the existence of such processes in a solid because the conduction electrons usually have to be regarded as an open quantum system, which is coupled to an environment of other quantum systems, e. g., other carriers, phonons, or trapped charges. In this way, the system may exchange energy and "information" with the environment. Therefore, it is reasonable to change the fully coherent single-particle wave function picture to a density-matrix description in which such incoherent processes can be accounted for. How the dephasing affects the density matrix can be studied by the

theory of *einselection (environment-induced superselection)* [168, 169]. It was found that the dephasing effect of the environment can be understood as continuous measurements performed on the system with a time-constant τ_ϕ, which we call the *dephasing time*. Those measurements will lead to an asymptotic decay of the off-diagonal components of the reduced density matrix of the system ρ_s on the time scale of τ_ϕ, i. e.,

$$\rho_\mathrm{s}(t_0) = \begin{pmatrix} a_{11} & a_{12} & a_{13} & \cdots \\ a_{21} & a_{22} & a_{23} & \cdots \\ a_{31} & a_{32} & a_{33} & \cdots \\ \vdots & \vdots & \vdots & \ddots \end{pmatrix} \rightarrow \rho_\mathrm{s}(t_0 + \tau_\phi) = \begin{pmatrix} a_{11} & 0 & 0 & \cdots \\ 0 & a_{22} & 0 & \cdots \\ 0 & 0 & a_{33} & \\ \vdots & \vdots & & \ddots \end{pmatrix}. \tag{4.1}$$

The basis in which this decay occurs, i. e., the basis representation implicitly used in Eq. (4.1), is called the *pointer basis* [170]. It describes the observable that is continuously monitored by the environment and, in general, it strongly depends on the system under consideration, the environment, and the coupling between the two. The determination of the pointer basis for a general environment is still a largely unsolved problem. However, there are a few special cases in which one can say more and we will discuss them in Section 4.4.1, where the pointer basis will play an important role for the explicit inclusion of dephasing in the dynamical calculations. Until then, we just record the fact that the measurements by the environment project the density matrix on eigenstates of observables that are effectively measured by the environment and lead to vanishing interferences between pointer states.

For the special scenario of edge transport along edges of a 2d TI, this mechanism already has an important consequence. As all systems which could be candidates for the dephasing mechanism (e. g., carrier electrons or phonons) are not expected to be magnetically ordered, it seems safe to assume that the measurements performed by the environment will not project the spin degree of freedom, i. e., the dephasing does not flip the spin. In regions of the sample where the complete spin-momentum locking is intact, e. g., along clean or moderately disordered edges, this implies that dephasing cannot lead to backscattering as this would require a full spin flip. This no longer holds for a charge puddle close to the edge in which the local Fermi energy lies in the bulk band allowing for the existence of many densely spaced levels which are strongly spin mixed due to spin-orbit coupling. This makes an incoming electron wave packet lose its spin polarization very quickly as depicted in Fig. 4.1, which shows actual snapshots from the calculations performed in Section 4.3.1. In fact, the time required for the spin relaxation in the puddle τ_s is so small ($\approx 100\,\mathrm{ns}$) that it can be safely assumed to occur instantaneously for the model treatment presented in Section 4.3.2. Once the spin is mixed, even dephasing that preserves the spin will lead to backscattering. In this way, it is understandable that the total backscattering strength due to the combined effect of dephasing and elastic backscattering is governed by an interplay of the dephasing time τ_ϕ and the dwell time of the electrons in the puddle τ_d. If τ_d is small compared to τ_ϕ, the resulting backscattering from a single puddle will be small because most of the density will leave the puddle before being affected by the dephasing. In the opposite limit, all electrons entering the puddle will completely lose their phase memory meaning that they will eventually exit the puddle in a completely random direction.

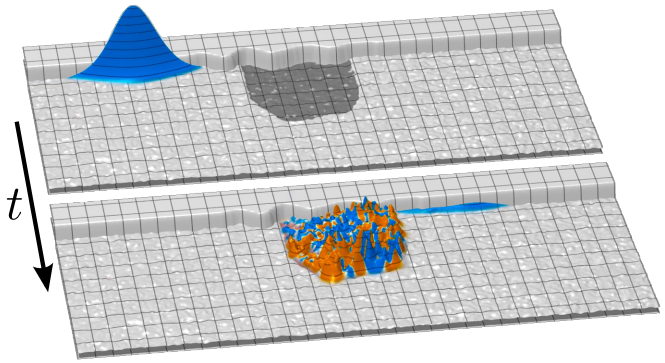

Figure 4.1: Snapshot of a time evolution of a wave packet which approaches a charge puddle situated along the edge of a 2d TI, i. e., the calculations from Section 4.3.1. In the beginning of the calculation, the wave packet starts out fully spin polarized in the up direction (the spin of the wave packet is color coded, blue: up, orange: down). As long as the wave packet is fully spin polarized, dephasing does not cause backscattering. However, because of spin-momentum locking, the spin-polarized wave packet moves to the right and enters the puddle, shown in the second frame. In the puddle, the spin gets mixed very fast due to spin-orbit scattering. Now, dephasing may lead to backscattering. Adapted from [22].

4.3 Dephasing in a model treatment

4.3.1 Dwell-time calculations

According to the considerations above, the relation between the dwell time in the puddle and the dephasing time is decisive for the amount of backscattering along the edge. Hence, to estimate whether dephasing can explain the observed temperature-independent backscattering, we proceed as follows:

1. We calculate the dwell time in a charge puddle as a function of the puddle size.

2. For given puddles (and, thus, corresponding dwell times), we then use a model to calculate the backscattering (and thereby the transmission) as a function of the dephasing time (in Section 4.3.2).

The obtained dependence of the transmission on τ_d (i. e., the puddle size) and on τ_ϕ allows to extract a range of parameters for τ_d and τ_ϕ, in which dephasing would explain the observed temperature-independent backscattering. In how far such an explanation would be realistic can then be determined by comparison of these parameters with measured data for the puddle size and the dephasing time.

For the calculation of the dwell time, we use a different numerical method than the one applied in Chapter 3. Instead of calculating static transport properties, we directly study the time evolution of wave packets and thereby obtain the full time dependence of quantum transport. This was achieved in a joint research project with Viktor Krückl who performed the numerical calculations of the time-dependent probability densities presented in this chapter using a program which he himself developed. The employed algorithm is explicitly integrating the time-dependent Schrödinger equation in a very efficient way by evaluating momentum operators in Fourier space and expanding the

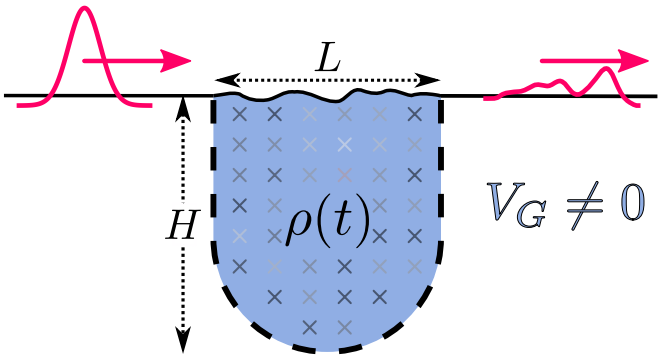

Figure 4.2: The figure shows a sketch of the calculation setup used to calculate the dwell time of an electron in a charge puddle close to the edge of a 2d TI. A fully spin-polarized edge-state electron wave packet starts at $t = 0$ close to the puddle. The puddle is defined by an electrostatic potential $V_G = 40\,\text{meV}$, which creates a local hole-conducting region. It is semi-stadium shaped with a height such that the area is given by L^2, i. e., $H = \left(\frac{3}{2} - \frac{\pi}{8}\right) L$. The upper edge is subject to mild shape disorder. The target quantity which is calculated is the time-dependent density in the puddle $\rho(t)$. Because of TR symmetry, all electron density eventually exits the puddle to the right.

time-evolution operator in Chebyshev polynomials [81, 101, 102]. It was already shown to be very suitable for calculating the edge-transport properties of 2d TIs [85].

Using a setup as sketched in Fig. 4.2, we calculate the time evolution of a wave packet that is starting at $t = 0$ on the edge of a 2d TI and, in the course of time, approaches a puddle which is situated at the edge. As in the previous chapter, the BHZ Hamiltonian, Eq. (2.17), with material parameters for HgTe/CdTe quantum wells is used, cf. Table 2.2, including only the spin-orbit coupling due to bulk inversion asymmetry, Δ, cf. Eq. (2.22). This Hamiltonian is discretized with a lattice constant of $a = 7\,\text{nm}$. The initial wave packet has a width of 90 nm, containing energies which roughly span the gap of the 2d TI. The puddle is chosen to be semi-stadion shaped and is defined by a local electrostatic potential of $V_G = 40\,\text{meV}$, which creates a hole-conducting region. The upper edge of the puddle is subjected to a smooth boundary disorder with an amplitude of 20 nm and electrostatic disorder with an amplitude of 5 meV is added in the puddle to add some degree of self averaging to the dynamics. In this way, a small number of impurity configurations is already enough to reach convergence.

The central observable which is extracted from the calculations is the time-dependent probability density $\rho(t)$ for finding an electron in the puddle. Impurity-averaged results over 100 disorder configurations for such calculations of $\rho(t)$ with different puddle sizes are shown in Fig. 4.3, with $\rho(t)$ being normalized to the total probability density of the incoming wave packet. The behavior for short times, displayed in Fig. 4.3(a), shows that the wave packet enters the puddle in a time window of approximately 1 ps, which is signaled by a steep rise in density. After about another picosecond, there is a small fraction of the density, 2 – 12 % (depending on the puddle size), that exits the puddle after traversing it ballistically, i. e., after 0.2 – 0.8 ps. However, the major part of the density remains in the puddle and decays to a good approximation linearly (see fits by black dashed lines) for a longer period of time as can be also seen in the plot of $\rho(t)$ in Fig. 4.3(b), which shows a larger time window. The slopes determined from the linear fits are displayed in Fig. 4.3(c) as a function of the puddle size, where one notes that the

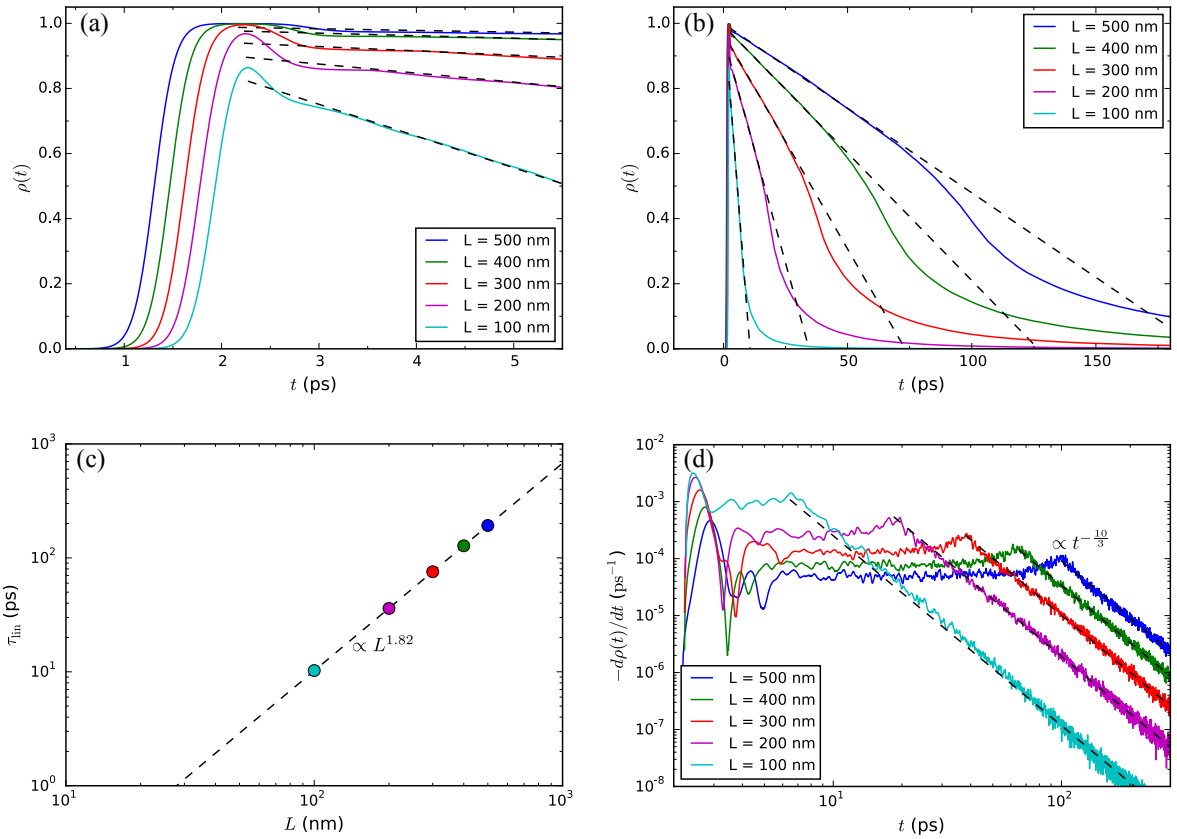

Figure 4.3: Time-dependent probability density $\rho(t)$ to find the electron in a puddle of length L which is approached by a wave packet starting close to the puddle at $t = 0$, see Fig. 4.2 for the detailed setup. (a) shows $\rho(t)$ for short times in which the steep rise signals the entry of the wave packet into the puddle. (b) shows $\rho(t)$ for longer times illustrating the linear decay (fitted by dashed lines) for intermediate times. (c) shows the time constants for the linear decay τ_{lin} extracted from the fits. (d) shows the current exiting the puddle [negative derivative of $\rho(t)$]. The initial plateau corresponding to the linear decay turns over to a power law which is approximately given by $t^{-\frac{10}{3}}$ for long times. Adapted from [22].

linear decay time τ_{lin}, i. e., the time after which the puddle empties completely assuming a steady linear decay, roughly scales like $\propto L^{1.82}$.

Due to the forbidden backscattering on the edge, the maximal density in the puddle ranges close to one for the larger puddles, meaning that almost all the incoming electron flux is coupled into the puddle. When the density in the puddle drops below ≈ 0.5, the time dependence of $\rho(t)$ turns over into a power law. To make this more visible, Fig. 4.3(d) shows a plot of the negative time derivative of the density, i. e., the outflow from the puddle, in a log-log plot. The linear density decay is clearly seen as an initial plateau of the outflow with additional oscillations which can possibly be related to ballistic orbits in the puddle. This is then followed by a power-law decay, which is well described by a $t^{-\frac{10}{3}}$ dependence for puddles larger than 200 nm, which implies a $t^{-\frac{7}{3}}$ dependence for the density decay. Fits using this exponent are shown as black dashed lines. For a puddle size of 100 nm, the best-fitting power seems to be a bit smaller, closer to $t^{-3.5}$, i. e., $\rho(t) \propto t^{-2.5}$. Power-law decays of the density are expected for quantum-dot systems [171] and comparable curve shapes (with an initial linear decay and a subsequent power-law decay) have already been observed in wave-packet transport calculations on other mesoscopic billiard systems [172].

4.3.2 Backscattering in the limit of strong dephasing events

Using the data obtained in the previous section, we are now in a position to estimate the effect of dephasing on the transport properties of charge puddles by means of a simple model, which is based on a few assumptions:

1. The dephasing process is assumed to be a discrete process which happens instantaneously at event times t_n. The dephasing events are assumed to be fully uncorrelated and the probability distribution of the mean time between two events is described by an exponential distribution (Poisson process),

$$p(t_n - t_{n-1}) = \frac{1}{\tau_\phi} e^{-(t_n - t_{n-1})/\tau_\phi}, \tag{4.2}$$

   with time constant τ_ϕ.

2. The dephasing is assumed to be spin conserving. As already discussed in Section 4.2, this has the important consequence that only the dephasing events which occur while the electron is in the puddle can eventually lead to backscattering. The spin mixing due to spin-orbit scattering in the puddle is assumed to be instantaneous, which is quite well fulfilled for the puddles that we consider ($\tau_s \approx 100$ ns).

3. Each dephasing event is assumed to lead to full phase-coherence loss. For the puddle sizes that we consider, the scattering in the puddle is ergodic to a good approximation. Therefore, a full dephasing, i. e., a full memory loss of the electron, implies that the density which is in the puddle at the time of the event will exit the puddle in a random direction in the course of the subsequent dynamics.

On the basis of these assumptions and the numerically calculated time-dependent density in the puddle, $\rho(t)$, we can calculate the expected average reflection due to dephasing. For this, we also make use of the fact that the obtained $\rho(t)$ curves are piecewise monotonous and naturally consist of two time domains: a (short) monotonous rise of the density followed by a (long) monotonous decay. The total probability of reflection for a given time constant of the dephasing events τ_ϕ can then be calculated from the numerically obtained $\rho(t)$ by the following formula:

$$\begin{aligned} R(\tau_\phi) =& \frac{1}{2\tau_\phi}\left[\int_{-\infty}^{t_{\max}} dt_1 \rho(t_1) e^{-\frac{t_{\max}-t_1}{\tau_\phi}} + \int_{t_{\max}}^{\infty} dt_2 \rho(t_2) e^{-\frac{t_2-t_{\max}}{\tau_\phi}}\right] \\ & - \frac{1}{\tau_\phi^2 \rho_{\max}} \int_{-\infty}^{t_{\max}} dt_1 \int_{t_{\max}}^{\infty} dt_2 \rho(t_1)\rho(t_2) e^{-\frac{t_2-t_1}{\tau_\phi}}, \end{aligned} \tag{4.3}$$

with $t_{\max}$ being the time at which $\rho(t)$ reaches its maximum $\rho_{\max}$. The equation consists of three terms on the right-hand side, the first two of which describe the backscattering in the time domain of the rise and the decay respectively, as well as a third term which accounts for the double counting. The formula is best understood by first just considering the second term which accounts for the backscattering due to events during the monotonous decay of $\rho(t)$, at times $t_2 > t_{\max}$. Because each event leads to full dephasing, the first event in this time window will fully determine the backscattered fraction (which is given by half the density in the puddle at the time of the event). All subsequent events will not lead to more backscattering as the dynamics in the puddle has already been fully randomized by the first event. The backscattered fraction can therefore simply be calculated as half the expectation value of the density in the puddle with the probability density given by the exponential distribution, which describes the probability for the occurance of the first event after the maximum of the density is reached. This is exactly the second term on the right-hand side of Eq. (4.3). The first term in this equation can be understood in a similar fashion by considering the time domain of the monotonous rise of $\rho(t)$. Here, one can reverse the previous argument and only consider the last event in this time domain, which will determine the amount of backscattered density in this domain. The last term in Eq. (4.3) accounts for the double counting if one allows events both in the time window of the rise and of the decay.

For the special curve shape obtained for $\rho(t)$, which consists of a very steep rise and a decay which can be well approximated to be linear in the initial time window of the decay,

$$\rho(t) \approx \theta(t - t_{\max})\rho_{\max}\left(1 - \frac{t - t_{\max}}{\tau_{\text{lin}}}\right), \tag{4.4}$$

one can even analytically integrate Eq. (4.3) to yield

$$R \approx \frac{1}{2\tau_\phi}\int_{t_{\max}}^{t_{\max}+\tau_{\text{lin}}} dt_2 \rho_{\max}\left(1 - \frac{t_2 - t_{\max}}{\tau_{\text{lin}}}\right) e^{-\frac{t_2-t_{\max}}{\tau_\phi}} \tag{4.5}$$

$$= \frac{\rho_{\max}}{2}\left[1 - \frac{\tau_\phi}{\tau_{\text{lin}}}\left(1 - e^{-\frac{\tau_{\text{lin}}}{\tau_\phi}}\right)\right], \tag{4.6}$$

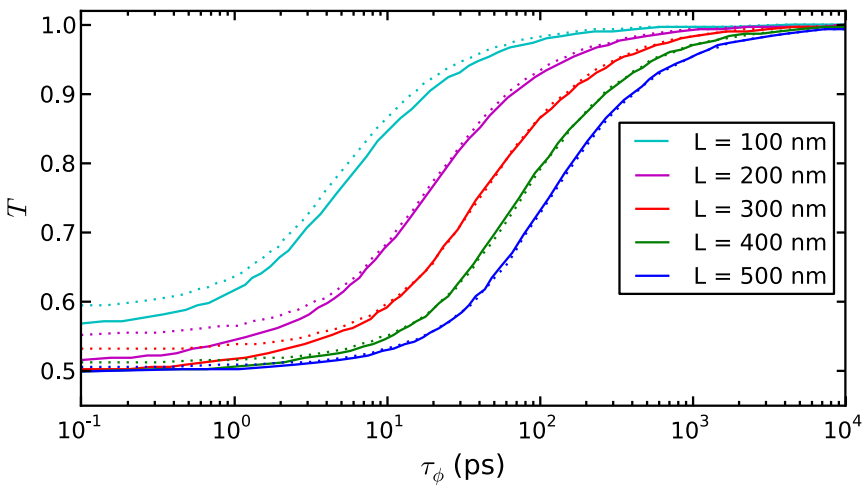

Figure 4.4: Average transmission for quantum dots of different sizes at the edge of a 2d TI as a function of the dephasing time τ_ϕ as extracted from the model calculation. The full lines show the evaluation of the formula which includes the full calculated shape of $\rho(t)$, Eq. (4.3), and the dotted lines use Eq. (4.6), which assumes a linear decay only. Adapted from [22].

$$T = 1 - R = 1 - \frac{\rho_{\max}}{2} + \frac{\rho_{\max}\tau_\phi}{2\tau_{\text{lin}}}\left(1 - e^{-\frac{\tau_{\text{lin}}}{\tau_\phi}}\right). \tag{4.7}$$

Here τ_{lin} is the constant of the linear decay, which together with $\rho_{\max}$ can be extracted from linear fits to the time-dependent densities in the puddle, cf. Fig. 4.3(c).

With these formulas, we can now calculate the expected average transmission through a puddle, which is shown in Fig. 4.4. The results from the simplified formula, Eq. (4.7), which assumes a linear decay throughout (dashed lines) agrees well with the calculations using the full $\rho(t)$ curve, Eq. (4.3) (full lines). This shows that the power-law decay can be neglected in this calculation as it is exponentially suppressed in the integral. All curves show a characteristic sigmoidal shape with two asymptotic limits. For long dephasing times, we obtain full transmission which is expected from the protection from backscattering for fully coherent transport. In the limit of short dephasing times, we find a saturation of the transmission at a value close to $T = 0.5$ for the larger puddles and a value slightly above that for small puddles. This saturation stems from the fact that each electron entering the puddle will get completely randomized as long as the dephasing time is short compared to the dwell time, which makes the transmission saturate at $T = 1 - \rho_{\max}/2$. For small puddles, there is always a significant fraction of electron density that ballistically bypasses the puddle which leads to $\rho_{\max}$ being significantly smaller than one, i. e., to a saturation of T at a value above 0.5. The value for $\rho_{\max}$ which is extracted from the linear fits to the numerically computed density is slightly below the true value of $\rho_{\max}$ of $\rho(t)$ [as can be seen from the plots of the fit functions in Fig. 4.3(a)], which explains why the dashed curves in Fig. 4.4, which are computed using $\rho_{\max}$ from the linear fits, overestimate the saturation value of the transmission in the strong dephasing limit.

The plateau at short dephasing times in Fig. 4.4 is interesting as it might be the key to the experimentally observed temperature-independent backscattering: Even though the

dephasing time itself is expected to strongly vary with temperature (as it is likely caused by inelastic processes), the conductance will be almost independent of the dephasing time (thus temperature) if the puddle is in this strong-dephasing regime (Note the logarithmic scale used for τ_ϕ in Fig. 4.4). To make a numerical example: If one considers a puddle of 500 nm size (dark blue line in Fig. 4.4), the transmission of a single puddle will be almost independent of the dephasing time as long as the dephasing time is shorter than ≈ 10 ps. Thus, if the actual dephasing time in current experiments is below 10 ps at all experimentally accessible temperatures and the puddles occurring are all larger than 500 nm, a temperature-independent conductance would be perfectly in line with our calculations.

Before discussing in detail if this scenario is realistic for the state-of-the-art experiments on HgTe/CdTe quantum wells, which we will do in Section 4.5, we would first like to introduce an alternative numerical technique which allows us to study the electron dynamics in the presence of dephasing.

4.4 Explicit numerical treatment of dephasing

4.4.1 Description of the algorithm

Until now, we have treated the dephasing only on an ad-hoc model level, but we had no means to include it into the dynamical calculation. In this section, we will introduce an algorithm which allows to implement dephasing into the time evolution. It was jointly developed with Viktor Krückl who also performed the shown numerical calculations. As we discussed in Section 4.2, a full treatment of dephasing requires a time evolution of the density matrix of the system. This turns out to be prohibitively costly for the systems that we want to consider. The scheme presented in this section is therefore a workaround that allows to approximately include dephasing also in a description based on the single-particle wave-function evolution. We achieve this in a similar way as the model treatment discussed in the last section by limiting the dephasing events to discrete times, which we again take to be drawn from an exponential distribution (Poisson process) with time constant τ_e. Between these events, the propagation is taken to be fully coherent. The required suppression of the interference between pointer states, which is the characteristic sign of dephasing, is implemented by representing the wave function in the "pointer basis" $\left\{|\psi_n^\mathrm{P}\rangle\right\}$ at the time of the event t_1,

$$|\psi(t_1)\rangle = \sum_n a_n |\psi_n^\mathrm{P}\rangle, \tag{4.8}$$

and then randomizing the phases of the coefficients to obtain the wave function for the continuing coherent evolution after the event,

$$|\psi(t_1+\epsilon)\rangle = \sum_n a'_n |\psi_n^\mathrm{P}\rangle, \tag{4.9}$$

with

$$a'_n = a_n e^{iq_n\pi}, \tag{4.10}$$

and the $q_n \in [-Q, Q]$ randomly drawn from a box distribution. The degree of phase randomization, i. e., the strength of the dephasing is controlled by the parameter Q, which can take a value from the interval $[0, 1]$, where $Q = 1$ corresponds to the case of instantaneous full phase randomization that was discussed in the model study discussed in the last section. In this way, this algorithm, in contrast to before, also allows us to study the scenario of "weak dephasing events" in which many events are required to achieve full phase-coherence loss. In this case, the time constant of the event τ_e is no longer equal to the time constant of the full phase-coherence loss τ_ϕ. However, as we are dealing with a simple Poisson process, one can work out the relation between the two in the following way: Imagine the effect of dephasing on a system energy eigenstate $|\psi_E(t)\rangle$ in the hypothetical scenario that the pointer basis is also chosen as the basis of system energy eigenstates. Then the dephasing can really be viewed as pure phase randomization without any additional projection. After n dephasing events, the average autocorrelation of the state $|\psi_E(t)\rangle$ at time t and the initial state is given by

$$\langle\psi_E(0)|\psi_E(t)\rangle = \frac{1}{(2Q)^n}\int\!\!\cdots\!\!\int_{-Q}^{Q} dq_1 \cdots dq_n \exp\left(i\pi\sum_{j=1}^{n} q_j\right) e^{-iEt/\hbar}, \tag{4.11}$$

or simply

$$\frac{\langle\psi_E(0)|\psi_E(t)\rangle}{\langle\psi_E(0)|\psi_E(t)\rangle_\mathrm{coherent}} = \frac{1}{(2Q)^n}\int\!\!\cdots\!\!\int_{-Q}^{Q} dq_1 \cdots dq_n \exp\left(i\pi\sum_{j=1}^{n} q_j\right) \tag{4.12}$$

when normalizing it to the autocorrelation without any decoherence. The integrals on the right-hand side can be worked out,

$$\begin{aligned}\int\!\!\cdots\!\!\int_{-Q}^{Q} dq_1 \ldots dq_n \exp\left(i\pi\sum_{j=1}^{n} q_j\right) &= \frac{1}{(2Q)^n}\int\!\!\cdots\!\!\int_{-Q}^{Q} dq_1 \cdots dq_n \cos\left(\pi\sum_{j=1}^{n} q_j\right) \\ &= \left(\frac{1}{2Q}\int_{-Q}^{Q} dq \cos(\pi q)\right)^n = \left(\frac{\sin(\pi Q)}{\pi Q}\right)^n. \end{aligned} \tag{4.13}$$

Now we still need to include the probability for n events occurring in a time interval of length t. This is given by the Poisson distribution,

$$P(n) = \frac{t^n}{\tau_\mathrm{e}^n}\frac{1}{n!}e^{-\frac{t}{\tau_\mathrm{e}}}. \tag{4.14}$$

With this, we can now calculate the average normalized autocorrelation after time t as a weighted sum over the number of occurred events:

$$\begin{aligned}\left\langle\frac{\langle\psi_E(0)|\psi_E(t)\rangle}{\langle\psi_E(0)|\psi_E(t)\rangle_\mathrm{coherent}}\right\rangle &= \sum_{n=0}^{\infty} P(n)\left(\frac{\sin(\pi Q)}{\pi Q}\right)^n \\ &= \sum_{n=0}^{\infty}\frac{1}{n!}\left(\frac{t}{\tau_\mathrm{e}}\frac{\sin(\pi Q)}{\pi Q}\right)^n e^{-\frac{t}{\tau_\mathrm{e}}} = \exp\left[\frac{t}{\tau_\mathrm{e}}\frac{\sin(\pi Q)}{\pi Q} - \frac{t}{\tau_\mathrm{e}}\right]\end{aligned}$$

$$= \exp\left[-\frac{t}{\tau_\mathrm{e}}\left(1 - \frac{\sin(\pi Q)}{\pi Q}\right)\right] = \exp\left[-\frac{t}{\tau_\phi}\right], \tag{4.15}$$

with

$$\tau_\phi = \frac{\pi Q}{\pi Q - \sin(\pi Q)} \cdot \tau_\mathrm{e}, \tag{4.16}$$

which is the desired relation between the time constant for the events τ_e and the resulting dephasing time τ_ϕ.

So far, we have not specified the pointer basis which is used to decompose the states as shown in Eq. (4.8). As hinted to in Section 4.2, not much is known about the form of the pointer basis in a general environment. There are, however, a few cases in which one can say more about the nature of the pointer states. In the limit where the coupling to the environment is weak, the pointer states were found to be the energy eigenstates of the system [173]. On the other hand, for a very strong coupling to the environment, as is often the case for an externally connected measurement device, the pointer states turn out to be eigenstates of the coupling Hamiltonian [170, 174]. For any measurement sensitive to position, these would be the position eigenstates. Between those two extreme cases, the pointer states are generally local both in momentum as well as in position—at least when considering a local interaction with the environment, like electron-electron or electron-phonon interaction. This was also found for the example of quantum Brownian motion [175], where the pointer states were seen to be coherent states, i. e., wave packets localized in phase space. We want to describe an open system in this intermediate coupling regime, which is why we propose the following set of states, which we call *local energy eigenstates*,

$$|\psi_n^P\rangle \propto \int_{t_1-\Delta t}^{t_1+\Delta t} dt\, \psi(t) e^{iE_n t/\hbar}. \tag{4.17}$$

They can be understood as short-term Fourier transforms of the system wave function $\psi(t)$ at a fixed set of energies. This may seem a strange choice at first glance, but it fulfills the above requirements: In the limit of a long time window of the Fourier transform $\Delta t \gg 1$, $|\psi_n^P\rangle$ becomes an exact eigenstate of the system at energy E_n, i. e., the pointer basis is the one required for a system with weak coupling to the environment as discussed above. For a shorter Δt, the state is still localized in energy to some degree, in addition, it is also localized in space because it stems from a finite propagation of the wave function, which does not allow the wave packet to extent infinitely far. Thus, we find a convenient way to generate a pointer basis, which is relatively unbiased with respect to energy or spin. It comes at the computational cost of an auxiliary wave function propagation of length $2\Delta t$ at each dephasing event, in order to generate the pointer basis—a limitation that we can live with as the propagation algorithm is relatively efficient. However, it makes the limit of very frequent dephasing computationally demanding.

In practice, we choose a fixed set of 11 energies in the gap of the TI $E_n = \{0\,\mathrm{meV}, \pm 1.5\,\mathrm{meV}, \ldots, \pm 7.5\,\mathrm{meV}\}$ for which we perform the integral shown in Eq. (4.17) to obtain the pointer states from the auxiliary propagation, the length of which we choose to be $\Delta t = 1\,\mathrm{ps}$. These states are then orthonormalized in order to make them form a proper basis. As this basis is in general not complete, we allow for a small residual in

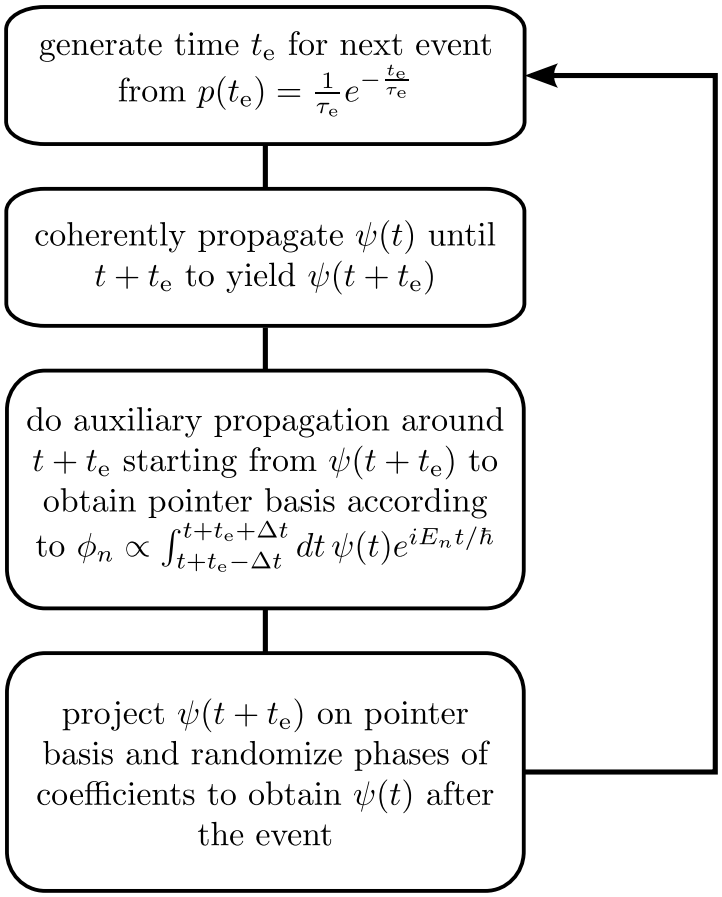

Figure 4.5: Flowchart which illustrates the steps of the dephasing algorithm used in this section. A video that illustrates the workings of the algorithm can be found in the Supplemental Material of Ref. [22].

the decomposition of the wave function,

$$|\psi(t_1)\rangle = \sum_{n=1}^{11} a_n |\psi_n^\mathrm{P}\rangle + |\Delta\psi\rangle, \tag{4.18}$$

with the subsequent phase randomization described above, cf. Eq. (4.10). An overview of the algorithm summarizing all the important steps is shown in Fig. 4.5. The dephasing implemented in this way roughly conserves the energy, the spatial extent of the probability density, and the total spin of the wave packet. In this way, it satisfies the expectations of an interaction with a non-magnetic environment. Moreover, the way it is designed, it is very general and may be applied to an arbitrary mesoscopic system.

4.4.2 Results for intermediate dephasing strength

We use the algorithm presented in the previous section to calculate the dynamics and the transmission for 400 nm sized puddles of different shapes as shown in the inset of Fig. 4.6(d). Different from the scenario in the model study in Section 4.3.2, we choose to study the limit of "weak dephasing events", i. e., we set the parameter Q which

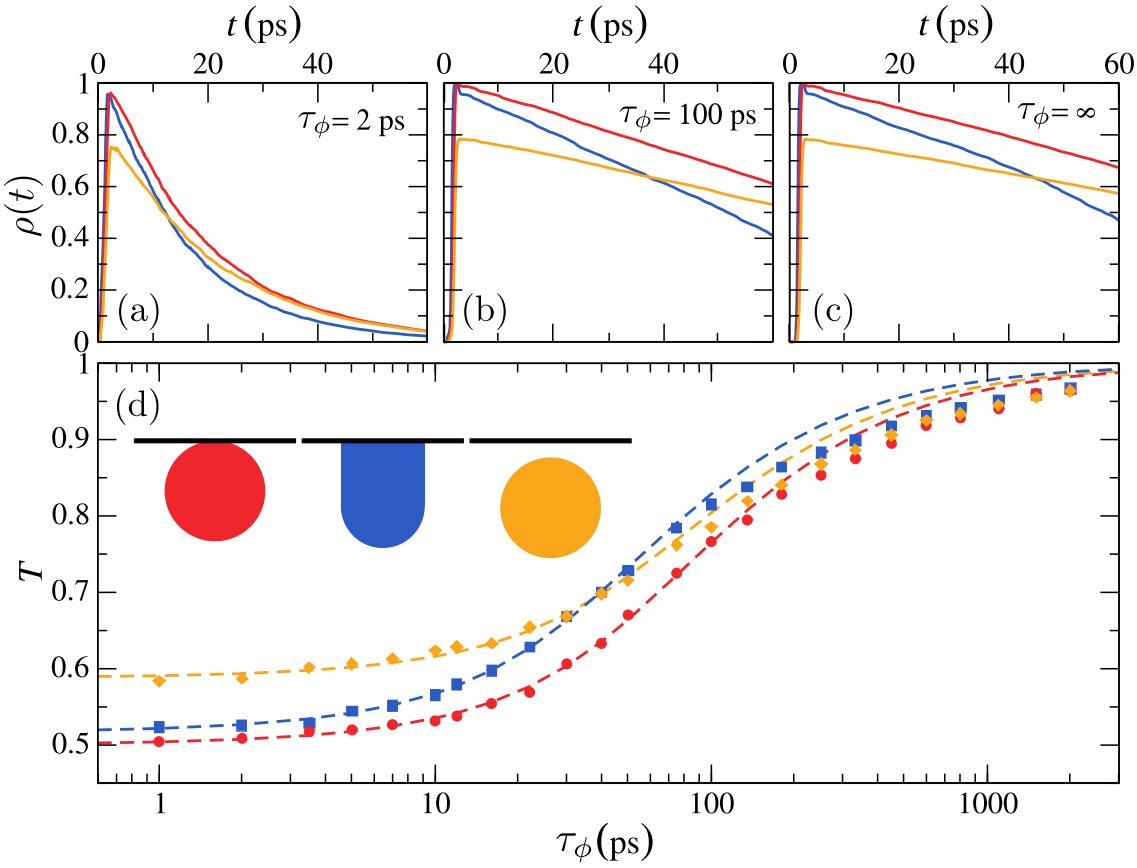

Figure 4.6: (a)–(c) show disorder-averaged results for the time-dependent probability density for finding the electron in the puddle using the numerical algorithm which includes dephasing. The calculation setup is the same as shown in Fig. 4.2. The horizontal extent of the puddle is fixed to 400 nm, but the puddle geometry is varied [different colors show results for different geometries as depicted in the inset of (d)]. The dephasing strength at each event is tuned such that ≈ 2.75 events are necessary to yield full coherence loss. The dephasing time τ_ϕ in the figure is the time constant for full dephasing. (d) shows the resulting transmissions extracted from the numerical calculations as a function of the dephasing time as symbols. The dashed lines show fits to the data in the short dephasing time limit using Eq. (4.7). Adapted from [22].

determines the strength of each dephasing event to $\frac{1}{2}$. According to Eq. (4.16), this implies that one needs on average $\pi/(\pi-2) \approx 2.75$ events to achieve full dephasing. In the numerical results shown in Fig. 4.6, we always state the dephasing time τ_ϕ, which is the time constant for the events τ_e divided by this factor.

Figure 4.6(a)–(c) show the time-dependent probability density in the puddle for such calculations which include dephasing for different choices of the dephasing time and for different puddle geometries (which are sketched in the inset). One clearly notices that dephasing speeds up the decay from the puddle. This is expected as it effectively opens up another exit channel (backscattering) for the electrons. It is also interesting to have a look at the dependence on the puddle geometry. We note that the geometries that are localized close to the edge, and which are depicted in blue and red, allow for a good coupling of the wave packet into the puddle [high maximal value of $\rho(t)$]. By the same token, this also comes with a faster decay of the density that couples into them. For the

puddle sketched in yellow on the other hand (also circular but further away from the edge), there is a large fraction ($\approx 20\%$) which bypasses the puddle ballistically. But, the density that couples into it decays relatively slowly, cf. Fig. 4.6(a)–(c). However, puddle dwell time and coupling to the puddle are not necessarily linked in this way as one can see by comparing the blue puddle (semi-stadion shaped) and the red (circular) puddle. The coupling to the edge of the blue puddle is similar to the coupling to the edge of the red one but the dwell time in the blue puddle is significantly shorter. This suggests that the influence of the puddle geometry and position is not universally described in terms of one parameter.

Looking at the total transmissions from this calculation setup, which are shown as symbols in Fig. 4.6(d), we find qualitatively very similar results as obtained from the model calculation in the previous section, cf. Fig. 4.4. In the limit of short dephasing times, the transmissions reported here can even be fitted using the formula that we found in the context of the model calculation assuming a linear decay, Eq. (4.7). These fits are shown as dashed lines in Fig. 4.6(d). To understand this good agreement obtained in the limit of short dephasing times, it is instructive to once again remind ourselves of the main difference between the presented numerical implementation of dephasing and the assumptions of the model calculation: the different strength of a single dephasing event. While the numerical data is calculated for a scenario in which one needs on average 2.75 events to bring about full phase loss, the model from Section 4.3.2 which is used for the fits assumes a scenario in which a single event is sufficient to lead to full dephasing. If we compare the two scenarios for the same choice of the dephasing time τ_ϕ, i. e., for the same product of event time constant and event strength, this means that we are effectively comparing the case of frequent but weak dephasing (numerical data: symbols) with the case of rare but strong dephasing (fits to the model: dashed lines).

With this in mind, the good agreement in the limit of strong dephasing ($\tau_\phi \ll 1$) is not surprising because with the average time for full coherence loss being short compared to the dynamics of the system, there should be no difference between “rare strong” or “frequent weak” dephasing. For long time intervals between the events, however, the two scenarios (frequent weak dephasing or rare strong dephasing) yield different results because the dephasing opens up a new decay channel for the system which in the case of frequent weak events can be at least partially opened already at an earlier time. This increases the backscattering due to dephasing in the frequent weak limit as can be nicely seen in Fig. 4.6(d), in which, the numerically calculated transmissions (frequent weak dephasing) for $\tau_\phi \gtrsim 100\,\mathrm{ps}$ are consistently below the dashed fit curves that use the model formula (rare strong dephasing). The influence of geometry on the puddle coupling and the dwell time in the puddle is also visible in the results for the transmission. The circular puddle that has a larger distance from the edge (yellow) shows a higher saturation value in the strong dephasing limit because of the lower coupling. At the same time, one finds that this plateau value persists up to higher dephasing times, a fact that reflects the longer dwell time in the puddle.

In conclusion, we find results that are quite consistent with the results of the previously presented model calculation, which we will subsequently discuss with respect to their applicability to experimental data.

4.5 Discussion of the results

It is now time to discuss the results obtained from our calculations for the average transmission of a single puddle on the edge of a 2d TI, cf. Figs. 4.4 and 4.6(d), and to relate them to experimental results on HgTe/CdTe samples. As already hinted to in Section 4.3.2, it is possible that they explain the temperature-independent backscattering which is ubiquitously observed in experiments. A prerequisite for that is that the actual dephasing time in the experiments is (at all accessible temperatures) below the extracted critical time below which the transmission is independent of the dephasing time. This time depends on the experimentally relevant puddle sizes (e. g., 10 ps for 500 nm sized puddles) and also on the puddle geometry and the coupling of the puddle to the edge as we saw in the previous sections. To see if our theory quantitatively agrees, one needs knowledge about the puddle sizes and the dephasing times in the experimental samples.

At the present day, it is still not easy to experimentally determine the size and distribution of charge puddles in typical samples. Yet, plausible estimates were obtained by scanning gate measurements, which hint to the existence of local scattering centers that can be tuned by an external gate potential [138]. The mean distance between such sites has been estimated to lie on the order of $1.5-2\,\mu$m. The size of them is difficult to estimate as the width of the potential induced by the scanning gate is already on the order of 500 nm. However, AFM measurements presented in the same publication, Ref. [138], reveal structures with a diameter of approximately $1\,\mu$m, which are attributed to stem from the substrate, i. e., they are believed to also be present in the quantum-well layer. It is thus not so easy to say something definite, however, it seems as if potential fluctuations on the order of $100\,\text{nm}-1\mu$m could be realistic.

The dephasing time is a bit easier to estimate as there are magnetoconductance measurements which probe weak (anti-)localization in samples of HgTe/CdTe quantum wells that are in principle sensitive to the phase coherence length l_ϕ and thereby also allow estimates of the phase coherence time. From such measurements, a phase coherence time of about 70 ps has been extracted from measurements on inverted quantum wells at a temperature of 0.2 K [176]. However, this number should also be taken with a grain of salt as comparable measurements at higher temperatures (≈ 1 K), at which a much shorter dephasing time is expected, yield a value for τ_ϕ which ranges from 3 ps [177] to 80 ps [178]. Also, it is not clear if the underlying fitting function that is used to extract the dephasing time from the measurements, the Hikami-Larkin-Nagaoka formula [132], is appropriate to describe weak antilocalization in these systems as it has been derived for the free electron gas. Extensions of this formula have been discussed [179, 180] but their validity is limited to a small range of Berry phases close to π and they cannot in general be used for a universal fit of the measurement data. Suppose that this dephasing time is realistic, one would be able to explain the experimentally observed temperature independence of the transmission only if the puddles occurring in the experimental samples are larger or deeper than the ones considered in the simulations of this chapter, i. e., larger than 500 nm or deeper than 40 meV. In our simulations, we are restricted to this depth as we are limited to the range of validity of the BHZ Hamiltonian. However, deeper puddles would lead to longer dwell times and this would lower the temperature below which a temperature-independent backscattering could be observed.

Another factor of uncertainty is the dependence of the dephasing time on the depth of the puddles. If the dephasing in the experimental samples is due to electron-electron interaction in the two-dimensional limit, which would be compatible with the experimentally observed temperature dependence in the magnetoconductance measurements $\tau_\phi \propto 1/T$ [176, 178], one would roughly expect the dephasing time to increase as

$$\tau_\phi = \frac{\hbar}{T}\frac{2\pi\hbar}{R_\square e^2}\Big/\ln\left(\frac{\pi\hbar}{e^2 R_\square}\right) \tag{4.19}$$

for decreasing sheet resistance $R_\square$ (i. e., increasing puddle depth) [181]. However, experimentally, one so far obtained controversial results on the dependence of the dephasing time on the electron density for HgTe/CdTe quantum-well samples, supporting [176] or contradicting [178] the theoretical predictions. It is therefore not so clear what to expect for the dependence of the dephasing time on the puddle depth.

Given these limitations, we suggest a control experiment in which a puddle is artificially created by means of an external gate, ideally in a sample which is free of puddles to start with. This could be achieved by starting with a very short edge section which is known to show the quantized conductance at low temperatures. The tuning of the external gate would then allow to steer the depth of the puddle by which one could probe the limit of small/shallow puddles for which a temperature dependence should be observable. Thereby one could also extract the dephasing time using our theory predictions and compare with the dephasing times that were extracted from magnetoconductance measurements.

Moreover, this would allow for the first time to check the validity of this mechanism as we now know in which range of parameters to look for effects. Even though it is understood that because of the mentioned loose ends, our theory may still be off by a factor of order 10, we think that our theory is quantitative enough not to deviate by many orders of magnitude. Depending on the experimental results, this may well be sufficient to make a definite statement on this mechanism. For example, suppose that one introduces a small and shallow $\approx 100\,\mathrm{nm}$ sized puddle (the depth of which should be tunable by an external gate) close to the edge of a quantum-well structure. If this extra puddle does not lead to any observable temperature dependence, we would consider this mechanism to be ruled out on experimental grounds. Equally, if the introduction of a large and deeper puddle does not lead to any extra backscattering, this would also imply that the mechanism discussed here is not the correct one (and it may hint to the fact that the studied edge states are not of topological origin as discussed in the introduction to this chapter). These estimates were impossible before as it remained highly unclear how large the puddle would have to be in order to certainly cause backscattering and for which range of puddle sizes one should definitively observe a temperature dependence. Given that this mechanism is one of the last not yet excluded explanations for backscattering of 2d-TI edge states, we consider this a very important step.

Chapter 5

Heterostructures of metals and 2d TIs: emergence of perfectly conducting channels

In this thesis, we have so far studied the transport properties at 2d-TI edges, where edge usually meant termination of the lattice, i. e., the boundary of the bulk material to vacuum. Due to the topological arguments discussed in Section 2.2.2, one expects similar results for edge states arising in heterostructures with other topologically trivial insulators. In this chapter, we will study the transport properties of heterostructures with metals, i. e., systems with extended states at the Fermi energy, which are therefore not classifiable using the scheme described in Section 2.2.3. A small preview of what to expect in such a structure has already been given in the study of charge puddles close to the edge in Chapters 3 and 4. Those charge puddles can in fact be interpreted as such a heterostructure of a system with extended states (the puddle) that is bordering a region of a bulk 2d TI. We saw that such heterostructures show the peculiar transport property of being perfectly transmitting as long as TR symmetry (and phase coherence) is not broken. So far, this could be explained in terms of the symmetry properties of the states in the leads that are connected to such a charge puddle. In this section, we will see that this perfect transmission can also be viewed as a property of the states in the puddle, and that it is induced by the bordering TI.

To study the effects arising in metal/TI heterostructures, we start off by considering a simplified model that is already capable of demonstrating the important emerging feature: the presence of a perfectly conducting channel (PCC). Such a channel is induced in the metallic region and is inherently protected by the same symmetry as the underlying TI. We show that this effect can also be seen in an even more simplified picture in which the presence of the TI is modeled by an effective boundary condition on the Hamiltonian for the metallic region. Another thing that we will learn from this treatment is that the natural boundary condition choice for a metal bordering a (strong) insulator—namely that the wave function should drop to zero at the boundary—needs to be revised when considering topologically non-trivial insulators. After this introduction to the expected phenomena, we study the presence of PCCs numerically using more realistic systems,

i. e., nanostructures made of HgTe/CdTe quantum wells and show how PCCs could be observed in experiments.

5.1 A model for 2d-TI/metal heterostructures

A minimal model that already shows the important physical effects that appear in 2d-TI/metal heterostructures is described in the following. Consider a wave-guide structure that is translationally invariant in the x-direction. In the y-direction, we assume a heterostructure composed of a finite strip of width L of a conducting material (a "metal"), i. e., a system with extended states, which is bordering vacuum on one side and a semi-infinite 2d-TI plane on the other side. A sketch of this geometry is shown in Fig. 5.1(b). We base our modeling of the subsystems (the metal and the 2d TI) on the BHZ Hamiltonian, Eq. (2.17). To simplify the problem, we first neglect the effective spin-orbit coupling in the quantum well, i. e., the parameter Δ, which couples the two spin blocks. Also, we neglect the parameter D, which is responsible for the electron-hole symmetry breaking in the Hamiltonian. In this way, the TI can simply be described by a 2×2-dimensional Hamiltonian for each spin block, which for the spin-up block is of the form,

$$H_{\mathrm{TI}}^{\uparrow} = \begin{pmatrix} M - B\mathbf{k}^2 & Ak_+ \\ Ak_- & -M + B\mathbf{k}^2 \end{pmatrix}, \tag{5.1}$$

with $k_\pm = k_x \pm ik_y$ and $\mathbf{k}^2 = k_x^2 + k_y^2$. From the discussion in Section 2.3.1, we know that this leads to a topologically non-trivial insulator for $B \cdot M > 0$. The "metal" is modeled by a Hamiltonian that is of the same form but does not feature a gap. To achieve this, we in addition set $A = M = 0$, leaving just a parabolically dispersing free electron-hole gas,

$$H_{\mathrm{met}} = \begin{pmatrix} -B\mathbf{k}^2 & 0 \\ 0 & B\mathbf{k}^2 \end{pmatrix}. \tag{5.2}$$

In general, the parameter B, which determines the curvature of the bands of the metal, may have a different value in the metal and in the TI region. To simplify the calculations, we choose it to be the same in this simple model study. The band structure of a metal ribbon defined by this Hamiltonian and confined by hard-wall boundary conditions, $\psi = \mathbf{0}$, at the two sides is shown in Fig. 5.1(a), displaying parabolical subbands. This figure also shows the band structure of one spin block (spin up) of a semi-infinite 2d TI defined by the Hamiltonian in Eq. (5.1) (with hard-wall boundary conditions on one side). As expected, there is a clear gap in the band structure with a single linearly dispersing chiral edge state (one spin block of the topologically non-trivial BHZ model behaves effectively like an integer quantum Hall system, in this case with Chern number $C_1 = 1$).

In the next step, the two systems are brought in contact. This is modeled by replacing the hard-wall boundary condition in between the two by boundary conditions which demand continuity of the wave function $\psi(y)$ and of the flux $v_y\psi(y)$ across the interface[1],

[1] v_y is the velocity operator in y-direction, i. e., $v_y = i\,[H, y]$. Note that in this and the following section,

i. e.,

$$\psi(L-\epsilon) = \psi(L+\epsilon), \tag{5.3}$$

$$\begin{pmatrix} 2iB\partial_y & 0 \\ 0 & -2iB\partial_y \end{pmatrix} \psi(L-\epsilon) = \begin{pmatrix} 2iB\partial_y & iA \\ -iA & -2iB\partial_y \end{pmatrix} \psi(L+\epsilon). \tag{5.4}$$

This way, we obtain the following secular equation:

$$\begin{aligned} &\frac{4B^2 f_p \left(\lambda_2 u_1 v_2 - \lambda_1 u_2 v_1\right)}{f_m \cosh(f_m L) \sinh(f_p L)} \\ &+ \frac{\left(4B^2 - A^2\right) \lambda_1 \lambda_2 \left(u_2 v_1 - u_1 v_2\right) - 2AB \left(\lambda_1 - \lambda_2\right) \left(u_1 u_2 - v_1 v_2\right)}{f_m f_p \cosh(f_m L) \cosh(f_p L)} \\ &= \frac{4B^2 f_p f_m \left(u_1 v_2 - u_2 v_1\right)}{\sinh(f_m L) \sinh(f_p L)} + \frac{4B^2 f_m \left(\lambda_2 u_2 v_1 - \lambda_1 u_1 v_2\right)}{\sinh(f_m L) \cosh(f_p L)}. \end{aligned} \tag{5.5}$$

Here,

$$f_p = \sqrt{k_x^2 + \frac{E}{B}}, \quad f_m = \sqrt{k_x^2 - \frac{E}{B}}, \tag{5.6}$$

and $u_{1/2}$, $v_{1/2}$ are the vector entries of the decaying free solutions $\xi_{1/2}(y)$ of the Hamiltonian in the TI region $H_{\mathrm{TI}}^{\uparrow}$,

$$H_{\mathrm{TI}}^{\uparrow} \xi_{1/2}(y) = E\, \xi_{1/2}(y), \tag{5.7}$$

with

$$\xi_{1/2}(y) = \begin{pmatrix} u_{1/2} \\ v_{1/2} \end{pmatrix} e^{\lambda_{1/2} y}, \tag{5.8}$$

$$u_{1/2} = -\frac{E + B\left(\lambda_{1/2}^2 - k_x^2\right) + M}{A\left(\lambda_{1/2}^2 - k_x \lambda_{1/2}\right)}, \tag{5.9}$$

$$v_{1/2} = \frac{1}{\lambda_{1/2}}. \tag{5.10}$$

The decay coefficients of the free solution in the TI region $\lambda_{1/2}$, which have a negative real part if the energy is in the gap, i. e., $|E| < |M|$, are given by

$$\lambda_{1,2} = -\sqrt{\frac{A^2 + 2B^2 k_x^2 - 2BM \mp \sqrt{A^4 + 4B^2 E^2 - 4A^2 BM}}{2B^2}}. \tag{5.11}$$

Equation (5.5) is solved numerically to yield the band structure of the combined system, which is shown in Fig. 5.1(b). It has a strong similarity with the obtained band structure of the metallic strip but it features an extra band, which is colored in blue to

which consider simple model systems, we make the choice of units such that $\hbar = 1$.

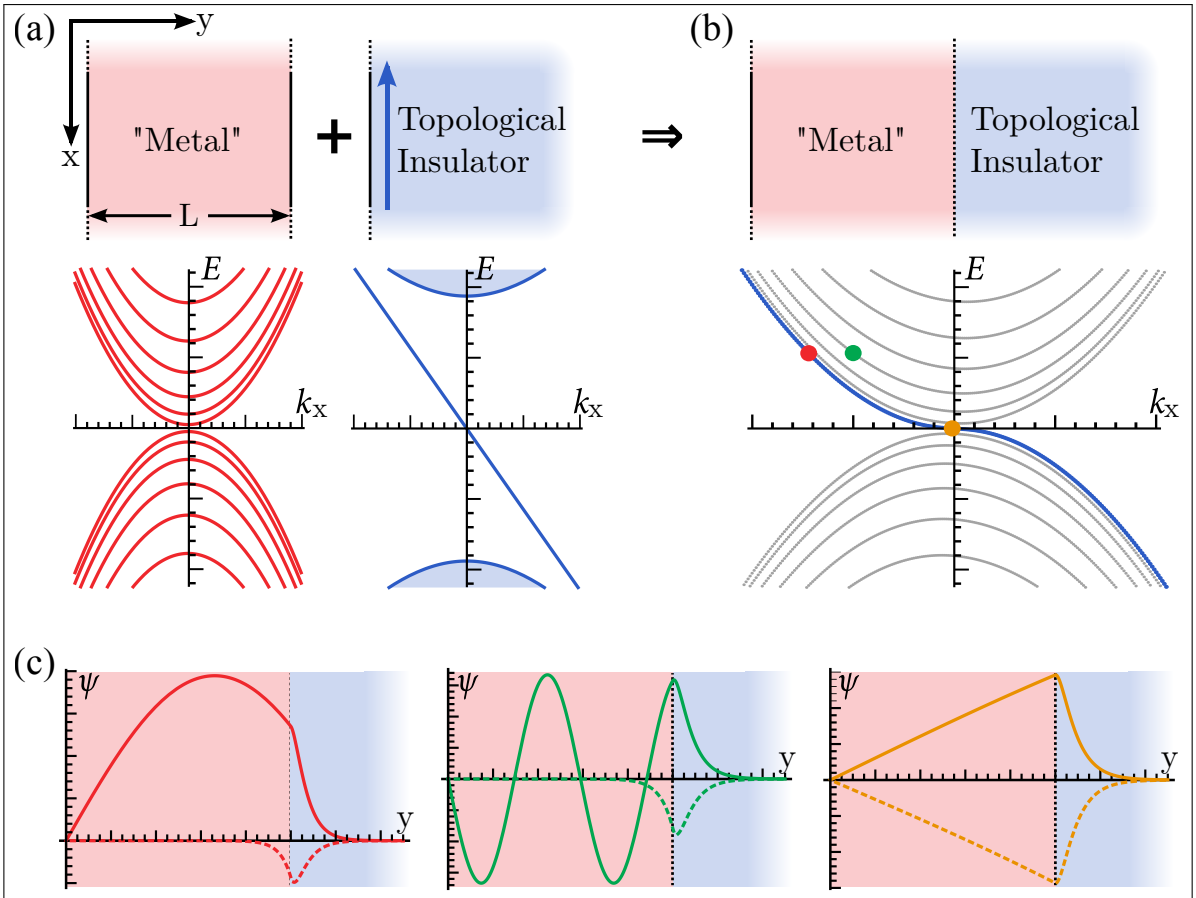

Figure 5.1: (a) shows the geometry and the band structure of the two separate systems which comprise the heterostructure: a "metallic" ribbon of width L and a semi-infinite 2d-TI plane. Only the band structure for one spin block is shown. (b) shows the geometry and the band structure of the heterostructure. The band marked in blue is the one spanning the energy window of electrons and holes which is induced due to the proximity of the 2d TI. (c) shows the transverse wave functions of selected states marked by colored dots in (c). Here, solid/dashed curves display the first/second component of the wave function. All wave functions are predominantly localized in the "metallic" region and only have exponentially decaying contributions in the TI. The parameters used in this plot are: $A = 5$, $B = -100$, $M = -0.05$, $L = 1000$. Adapted from [23].

make it more visible and to indicate that this is the band that stems from the topological edge state. The fact that the dispersion of this band is no longer linear but strongly curved already hints to band repulsion due to hybridization with the bands of the metal. Thus, it is likely that the character of the states belonging to this band also changed from being pure edge states (as in the 2d TI) to states that are hybridized with the metal and therefore have a larger probability density in the metallic bulk. Indeed, by closely studying the transverse eigenstates at different energies and momenta, one finds that *all* transverse eigenstates of the wave guide are predominantly located in the metallic ribbon and only have exponentially vanishing tails in the TI. This behavior is illustrated by a few characteristic snapshots of wave functions which are shown in Fig. 5.1(c). Seen from this perspective, the band which is colored in blue is no different from all the other bands. None of the bands show states that could be interpreted as "interface states" that live at the boundary between the TI and the metal or at the boundary of the metal to vacuum.

Thus, the proximity of the TI does not lead to an induced non-trivial topology as was reported in Ref. [182], where these relocated interface states were seen in heterostructures based on the Kane-Mele model. In this reference, however, only fully gapped systems were studied. Also, we do not observe any protection from hybridization for topological edge states as has been reported for a 2d quantum Hall insulator on top of a 3d metallic substrate [183]. However, in line with our results, a strong hybridization of the topological surface states has also been seen in metallic layers on top of 3d TIs [184].

At first sight, the above result of full hybridization of the former edge state with the bulk states seems somewhat disappointing as the states of the heterostructure look indistinguishable from the states in hybrid structures of metals with common insulators. There seems to be no obvious feature that is related to the non-trivial topology of the insulator. This view changes when considering the transport properties of the wave guide: At any fixed Fermi energy, there is an inherent imbalance of left- and right-moving modes (up- and down-moving modes in Fig. 5.1). This immediately implies that such a wave guide never shows full localization as at least the transport in one direction will have one mode which is perfectly transmitted. It features what is called a *perfectly conducting channel* (PCC).

So far, this argument only considered one single spin block. Due to TR symmetry there is of course always a second spin block for which the band structure looks exactly mirrored at the energy axis. Thus, the second spin block will also show an imbalance between left and right movers only that this will exactly cancel the imbalance of the first spin block. If looked at separately, it will exhibit a PCC propagating in the opposite direction. In total, however, there will be the same number of left- and right-moving modes. From this, one might suspect that any coupling of the two blocks (introduced by spin-orbit coupling) lifts the protection of these perfectly transmitting modes. Interestingly, it turns out that this is not the case as long as TR symmetry is still preserved. The reason for this is that the number of left- and right-moving modes will be equal but the number of modes moving in a single direction will be *odd*, from which one can quickly deduce that there must be a PCC [185, 186]: In the presence of TR symmetry, it can generally be shown that the scattering matrix S of a system can be written in a basis in which it is antisymmetric [186],

$$S^{\mathrm{T}} = -S. \tag{5.12}$$

As the reflection matrix r is contained as a subblock on the diagonal of S, this property also holds for r,

$$r^{\mathrm{T}} = -r. \tag{5.13}$$

The determinant of a matrix does not change under transposition, thus,

$$\begin{aligned} \det r &= \det r^{\mathrm{T}} = \det(-r) \\ &= (-1)^n \det r \\ &= -\det r \qquad \text{for } n \text{ odd.} \end{aligned} \tag{5.14}$$

Hence, an odd number of channels implies that r (and then also $r^\dagger r$) must at least have one eigenvalue which equals zero. The conservation of flux (the unitarity of the scattering matrix) enforces the following relation between the transmission and the reflection submatrices in a two-terminal device:

$$t^\dagger t = \mathbf{1} - r^\dagger r, \tag{5.15}$$

from which one sees that at least one eigenvalue of $t^\dagger t$ (one transmission coefficient) has to be equal to one. This shows that the existence of a PCC in each direction is ultimately protected by TR symmetry, the same symmetry that guarantees the edge states of the 2d TI. So in a sense, the wave guide does retain topological features. The one-dimensional edge state of the 2d TI relocates into the metal region, which induces one PCC in each direction. As all the modes in the wave guide are extended, the PCC—the superposition of modes that is perfectly transmitted—is also expected to be an extended, two-dimensional state that spans the whole metallic region. We believe that this behavior is rather general for interfaces between TIs and systems with extended states as long as the interface allows for sufficient hybridization. This might pave a way for inducing PCCs in systems which themselves do not have any inherent protection. These states inherit the protection of the underlying TI and are therefore expected to be very stable, e. g., under the influence of (non-magnetic) disorder.

5.2 An effective boundary condition for 2d-TI proximity

Before addressing the experimental realization and detection of these PCCs, we would like to dwell a bit more on the model in the previous section and derive a boundary condition that mimics the presence of the TI. This boundary condition will allow us to understand the mathematical reason for the emergence of PCCs and it even shows up ways how to create PCCs without TIs, just by implementing the discovered boundary condition. The idea behind the derivation of the boundary condition for the previously discussed model is simple: As is nicely illustrated in the wave functions depicted in Fig. 5.1(c), the TI only hosts exponentially decaying functions, the decay lengths of which are given by the decay coefficients λ, Eq. (5.11). In the limit where these lengths are small compared to the width of the metallic ribbon, it should be possible to replace the semi-infinite TI plane by an effective boundary condition without strongly modifying the spectrum or the wave functions.

In the following, we will explore this limit by making a particular choice of material parameters which achieves an infinitely fast decay of the wave functions in the TI and allows for the derivation of a boundary condition. As our model still involves quite a few parameters, this choice will not be unique meaning that also the resulting boundary condition will not be uniquely specified. However, we will see that it will be particularly simple and it will capture the most important feature, which is responsible for the emergence of the PCC.

The chosen limit in which the wave functions instantaneously decay when entering the TI is characterized by taking the band gap of the TI to infinity, $M \to -\infty$. As this

alone is not enough, we in addition rescale A in the following way, $A = X \cdot \sqrt{-M}$, where X is a constant parameter with units $\sqrt{\text{energy}} \cdot \text{length}$. In this joint limit of $M \to -\infty$ with $X = \frac{A}{\sqrt{-M}} = \text{const.}$, we find for the real parts of the decay coefficients $\lambda_{1/2}$,

$$\lim_{M\to-\infty} \operatorname{Re} \lambda_{1/2} = -\infty, \tag{5.16}$$

which implies that the wave functions in the heterostructure do not extend into the TI. In this limit, we can now derive the boundary condition, starting from the continuity of the wave function, Eq. (5.3),

$$\begin{pmatrix} \psi_1^{\mathrm{M}}(L) \\ \psi_2^{\mathrm{M}}(L) \end{pmatrix} = c_1 \begin{pmatrix} u_1 \\ v_1 \end{pmatrix} + c_2 \begin{pmatrix} u_2 \\ v_2 \end{pmatrix}, \tag{5.17}$$

where $\psi_{1/2}^{\mathrm{M}}$ are the components of the wave function in the metallic region, for which we aim to derive a proper boundary condition. c_1 and c_2 are so far unknown coefficients of the two free decaying solutions in the TI $\xi_{1/2}(y)$, cf. Eq. (5.8), which are to be matched at the interface. Taking the limit discussed above for the functions on the right-hand side, we run into the problem that

$$\lim_{M\to-\infty} \left|u_{1/2}\right| = \lim_{M\to-\infty} \left|v_{1/2}\right| = 0, \tag{5.18}$$

which enforces a corresponding rescaling of the coefficients $c_{1/2}$ to allow for a finite value of the metal wave function at the interface,

$$c'_{1/2} = \frac{c_{1/2}}{\sqrt{-M}}. \tag{5.19}$$

Thus,

$$\psi_1^{\mathrm{M}}(L) = c'_1\sqrt{-M}u_1 + c'_2\sqrt{-M}u_2, \tag{5.20}$$

$$\psi_2^{\mathrm{M}}(L) = c'_1\sqrt{-M}v_1 + c'_2\sqrt{-M}v_2. \tag{5.21}$$

Now the limiting process on the right-hand side yields finite coefficients, again keeping $X = \frac{A}{\sqrt{-M}} = \text{const.}$,

$$\lim_{M\to-\infty} u_1\sqrt{-M} = \frac{1}{2}\left(X + \sqrt{4B + X^2}\right), \tag{5.22}$$

$$\lim_{M\to-\infty} v_1\sqrt{-M} = -\frac{1}{2}\left(X + \sqrt{4B + X^2}\right), \tag{5.23}$$

$$\lim_{M\to-\infty} u_2\sqrt{-M} = \frac{1}{2}\left(X - \sqrt{4B + X^2}\right), \tag{5.24}$$

$$\lim_{M\to-\infty} v_2\sqrt{-M} = -\frac{1}{2}\left(X - \sqrt{4B + X^2}\right), \tag{5.25}$$

and additionally assuming that $B < 0$ and $X > 0$. Introducing the abbreviation

$$q_\pm(B, X) \coloneqq \frac{1}{2}\left(X \pm \sqrt{4B + X^2}\right), \tag{5.26}$$

Equations (5.20) and (5.21) yield

$$\psi_1^{\mathrm{M}}(L) = c_1' q_+(B, X) + c_2' q_-(B, X), \tag{5.27}$$
$$\psi_2^{\mathrm{M}}(L) = -c_1' q_+(B, X) - c_2' q_-(B, X), \tag{5.28}$$

from which we can directly read off the first boundary condition:

$$\psi_1^{\mathrm{M}}(L) = -\psi_2^{\mathrm{M}}(L). \tag{5.29}$$

This turns out to be independent of the choice of the parameters B and X. This will not be the case for the second boundary condition, which we obtain from the continuity of the flux across the interface. For this, we start from Eq. (5.4) and insert the free solutions for the TI Hamiltonian on the right-hand side,

$$\begin{aligned}(-i)\, v_y \begin{pmatrix} \psi_1^M(L) \\ \psi_2^M(L) \end{pmatrix} = c_1 2B\lambda_1 \begin{pmatrix} u_1 \\ -v_1 \end{pmatrix} + c_2 2B\lambda_2 \begin{pmatrix} u_2 \\ -v_2 \end{pmatrix} \\ + Ac_1 \begin{pmatrix} v_1 \\ -u_1 \end{pmatrix} + Ac_2 \begin{pmatrix} v_2 \\ -u_2 \end{pmatrix},\end{aligned} \tag{5.30}$$

and as above replace the constants c_1 and c_2 by rescaled versions according to Eq. (5.19). Subtracting the two rows of Eq. (5.30) yields

$$\begin{aligned}i\left(v_y\psi^M\right)_2(L) - i\left(v_y\psi^M\right)_1(L) = \quad & c_1'\left(2B\lambda_1 + A\right)(u_1 + v_1)\sqrt{-M} \\ & + c_2'\left(2B\lambda_2 + A\right)(u_2 + v_2)\sqrt{-M}.\end{aligned} \tag{5.31}$$

Before we now go through the limiting procedure on the right-hand side, we make an additional particular choice of parameters by setting $X = 2\sqrt{-B}$. This allows for a simpler result and we obtain

$$\lim_{M\to-\infty}\left(2B\lambda_1 + A\right)(u_1 + v_1)\sqrt{-M} = 4B\sqrt{-B}k_x, \tag{5.32}$$
$$\lim_{M\to-\infty}\left(2B\lambda_2 + A\right)(u_2 + v_2)\sqrt{-M} = 4B\sqrt{-B}k_x \tag{5.33}$$

for the limits of the coefficients on the right-hand side, always keeping $X = \frac{A}{\sqrt{-M}} = \text{const.} = 2\sqrt{-B}$. Put in Eq. (5.31), we obtain

$$i\left(v_y\psi^M\right)_2(L) - i\left(v_y\psi^M\right)_1(L) = 4Bk_x\left(c_1'\sqrt{-B} + c_2'\sqrt{-B}\right). \tag{5.34}$$

With the particular choice of X mentioned above, the functions $q_\pm(B, X)$, Eq. (5.26),

simplify to

$$q_{\pm}(B, X = 2\sqrt{-B}) = \sqrt{-B}. \tag{5.35}$$

In this way, from comparing Eqs. (5.27), (5.35), and (5.34), we deduce

$$i\left(v_y\psi^M\right)_2(L) - i\left(v_y\psi^M\right)_1(L) = 4Bk_x\psi_1^{\mathrm{M}}(L) \tag{5.36}$$

$$= 2Bk_x\left(\psi_1^{\mathrm{M}}(L) - \psi_2^{\mathrm{M}}(L)\right), \tag{5.37}$$

where we already made use of the first boundary condition, Eq. (5.29). In total, the two boundary conditions with which we can describe the TI in the discussed limit read as follows:

$$\psi_1(L) = -\psi_2(L), \tag{5.38}$$

$$i\left(v_y\psi\right)_1(L) - i\left(v_y\psi\right)_2(L) = 2Qk_x\left(\psi_1(L) - \psi_2(L)\right), \tag{5.39}$$

where the parameter B has been renamed to Q. The intention of this is to emphasize that this is a parameter of the boundary condition and to thereby distinguish it from the band curvature of the material, e. g., a metal, which is subjected to this boundary condition. This becomes necessary if one wants to go beyond the scenario shown in Fig. 5.1 in which the band curvature of the metal was chosen the same as the parameter B of the TI.

In the derivation, there is no restriction on the Hamiltonian on which this boundary condition could be applied. To compare the effect of the boundary condition with the above model in which we took the TI explicitly into account, we perform band-structure calculations, where a free electron-hole gas, using the same Hamiltonian as above, Eq. (5.2), is subjected to the boundary condition of Eqs. (5.38) and (5.39) on one side and to open boundary conditions on the other side of a ribbon with width L. The results of such calculations for different values of the parameter Q are shown in Fig. 5.2. If the value of the parameter Q is chosen the same as the band curvature of the electron-hole gas, Fig. 5.2(b), we obtain almost the same band structure as in Fig. 5.1(b). This could be already expected from the plots of the states in Fig. 5.1(c) from which we saw that the limit in which this boundary condition is applicable (a metallic ribbon that is wide compared to the penetration depth into the TI) is quite well satisfied for this choice of parameters. However, it was not clear from the start that the derived boundary condition yields so similar results for the considered system as the derivation made use of some non-unique limiting procedures. It seems that, at least in this case, it worked out reasonably well. A different choice of Q, Figs. 5.2(a) and (c), mainly influences the slope of the induced extra band. In the limit of $Q = 0$, a completely flat band is found.

As mentioned above, there is in principle no restriction on the Hamiltonian that is subjected to the boundary condition. For example, if the boundary condition is applied to a topologically non-trivial insulator, like the BHZ model with parameters in the topologically non-trivial regime that was used above, it turns out that one does not find any interface states at the boundary. This is also what one would expect in a real heterostructure of two topologically non-trivial insulators. In a way, this boundary

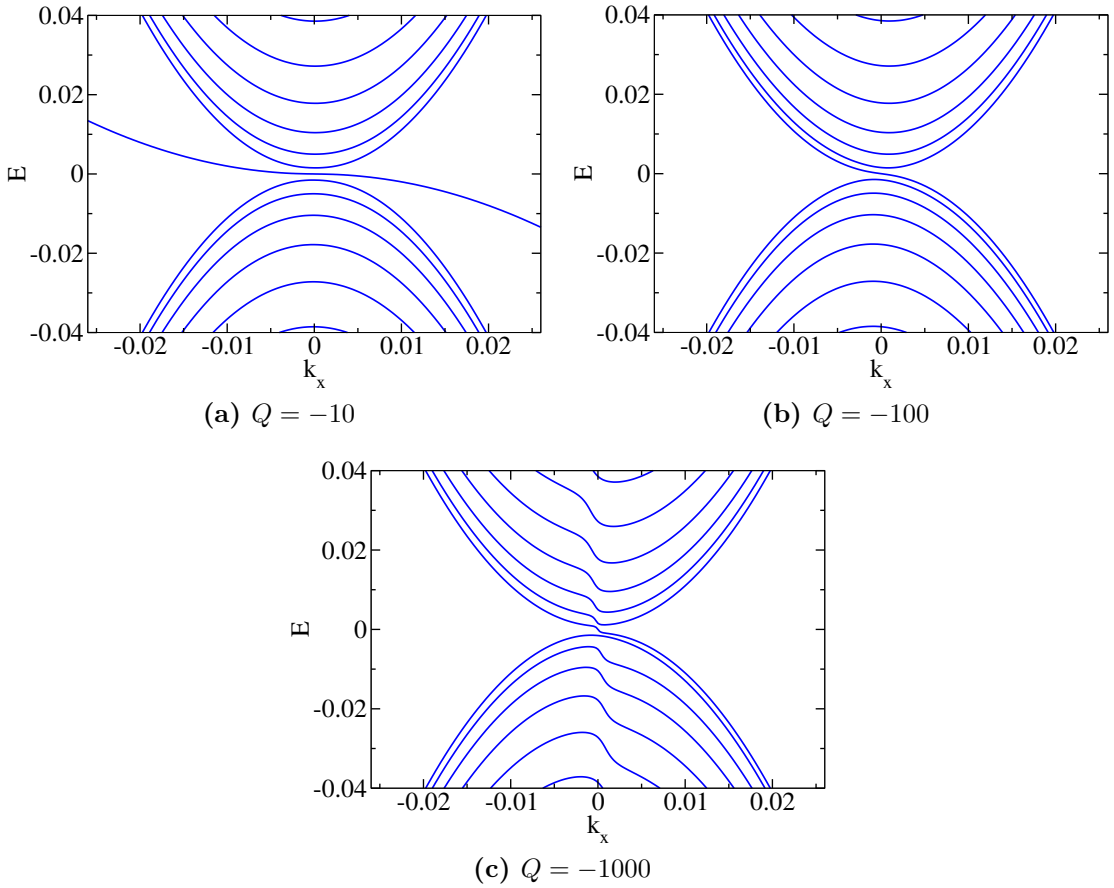

(a) $Q = -10$ **(b)** $Q = -100$

(c) $Q = -1000$

Figure 5.2: Band-structure plots using the set of boundary conditions, Eqs. (5.38) and (5.39), on one side of a metallic region (of width $L = 1000$) modeled by a free electron-hole gas Hamiltonian, Eq. (5.2) (using a band curvature of $B = -100$, as previously). The other side is subject to hard-wall boundary conditions. The three panels show different parameter choices for Q, which enters in the boundary condition. Adapted from [23].

condition seems to correctly describe the proximity to a non-trivial insulator also beyond metal-TI heterostructures.

In the derivation presented above, we made a special choice concerning the orientation of the heterostructure, namely we considered a boundary to a semi-infinite TI plane in the positive y-direction. Of course, one can redo the calculation for an arbitrary interface orientation. For the choice in which the TI plane extends to the negative y-direction, i. e., for a semi-infinite TI plane bordering the ribbon at $y = 0$, we obtain the following set of boundary conditions:

$$\psi_1(0) = \psi_2(0), \tag{5.40}$$

$$i\left(v_y\psi\right)_1(0) + i\left(v_y\psi\right)_2(0) = 2Qk_x\left(\psi_1(0) - \psi_2(0)\right), \tag{5.41}$$

which differs from the above boundary condition by an additional phase factor in front of one of the wave-function components. If this boundary condition is applied to a topologically trivial insulator, it leads to chiral states with an opposite chirality (for

the same spin block) compared to the previously shown boundary condition. This is expected as the propagating edge states of a TI with a fixed spin orientation should have different chiralities at opposite boundaries (as the two boundary orientations are related by a parity transformation which also flips the momentum, thus inverting the chirality of the edge states).

After having derived the boundary conditions, it is time to interpret them in order to shed a bit of light on why they give rise to this additional PCC. It turns out that this is mainly due to the second boundary condition, i. e., Eq. (5.39) or Eq. (5.41). Unlike the first boundary condition, which is of Dirichlet type, the second boundary condition is what is known as a *Robin boundary condition* [187], i. e., a boundary condition that is connecting the value of the wave function at the interface with its derivative. In addition, this mixing depends on the momentum in the wave-guide propagation direction. The combination of these two facts gives rise to an induced PCC as can be shown by considering a still simpler model system: a two-dimensional single-component free electron gas,

$$H_{\mathrm{2deg}} = B\left(k_x^2 + k_y^2\right). \tag{5.42}$$

If subjected to Dirichlet or Neumann boundary conditions on both sides of a wave guide of width L, i. e., $\psi(0) = \psi(L) = 0$ or $\partial_y\psi(0) = \partial_y\psi(L) = 0$, we obtain the well-known parabolic band structure that is shown in Fig. 5.3(a),

$$E^{\mathrm{NN/DD}} = B\left[k_x^2 + \left(\frac{n\pi}{L}\right)^2\right] \quad \text{for } n \in \{1, 2, \dots\}, \tag{5.43}$$

with the length of the interval being an integer multiple of half of the wavelength of the oscillating solution [see the illustrations above Fig. 5.3(a) for examples of wave functions]. Putting different kinds of boundary conditions on each of the two sides of the interval by requiring $\psi(0) = 0$ and $\partial_y\psi(L) = 0$, we find again a parabolic dispersion, where the wavelength in the transverse direction is quantized such that the interval is an odd multiple of a quarter of the wavelength of the oscillating solution,

$$E^{\mathrm{ND}} = B\left[k_x^2 + \left(\frac{(2n+1)\pi}{2L}\right)^2\right] \quad \text{for } n \in \{0, 1, \dots\}, \tag{5.44}$$

see Fig. 5.3(b). This different quantization condition is reflected in the different spacing of the parabolas.

It is becoming more interesting when choosing a wave guide which has a one-sided Dirichlet and a one-sided Robin boundary condition of the form

$$\partial_y\psi(L) = k_x Q\psi(L), \tag{5.45}$$

leading to the secular equation

$$\sqrt{\frac{E - Bk_x^2}{B}} = k_x Q \tan\left(\sqrt{\frac{E - Bk_x^2}{B}}L\right), \tag{5.46}$$

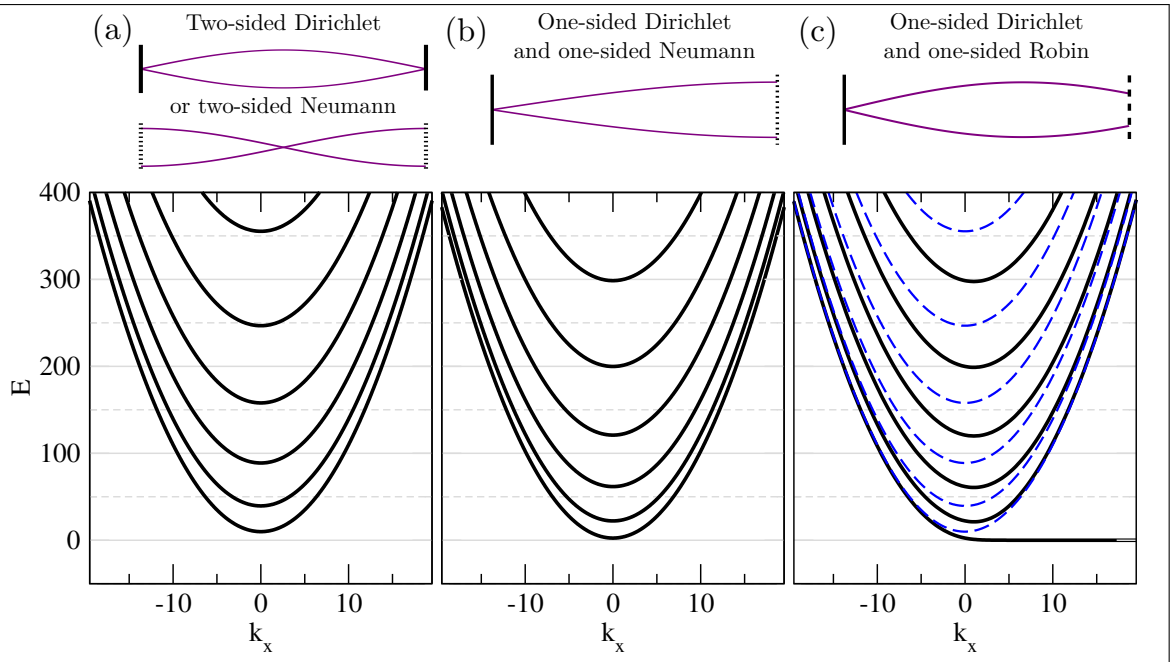

Figure 5.3: This plot shows band-structure calculations for a wave guide of a free electron gas, Eq. (5.42), with $B = 1$ confined to a unit interval in y-direction, $L = 1$, and free propagation in the x-direction. The three panels show the results for different boundary conditions at the edges of the interval. The band structure in (a) is obtained for Dirichlet or Neumann boundary conditions on both sides of the wave guide. The resulting wave functions are quantized such that the interval is divisible by integer multiples of half the wavelength as shown in the sketch above the figure. A mixed scenario with Dirichlet on one and Neumann on the other side results in the band structure shown in (b), where the quantization is such that the interval is an odd integer multiple of a quarter of the wavelength. (c) shows the behavior for a wave guide with one-sided Dirichlet and one-sided Robin boundary conditions, i. e., Eq. (5.45), with $Q = 1$. For $|k_x| \ll 1$, it resembles (b), while approaching the picture of (a) for $|k_x| \gg 1$ [the blue parabolas show the same data as (a) for comparison], differing only by an extra band at $E = 0$ for large k_x.

which can no longer be solved analytically. However, we show numerically obtained solutions in Fig. 5.3(c). Also, we have a good intuition for how the solutions should behave in certain limits. For $k_x = 0$, the Robin boundary condition reduces to a Neumann boundary condition, which is why the solution of the dispersion of Fig. 5.3(b) and Fig. 5.3(c) must agree close to $k_x = 0$, which is nicely seen in the figure. For $k_x \to \pm\infty$, the Robin boundary condition becomes similar to a Dirichlet boundary condition, which is why the spectrum agrees well with the superimposed dashed blue parabolas [which show the data from Fig. 5.3(a)] in this limit. However, there is one major difference: The Robin boundary condition allows for an additional solution in the limit $k_x \to \infty$ which is not compatible with neither Dirichlet nor Neumann boundary conditions. This solution is asymptotically given by

$$\psi^{\mathrm{R}}(y) = \sinh\left(k_x Q y\right), \tag{5.47}$$

which is plotted in Fig. 5.4(c). It can be shown to solve the free equation with energy

$$E^{\mathrm{R}} = B\left(1 - Q^2\right) k_x^2, \tag{5.48}$$

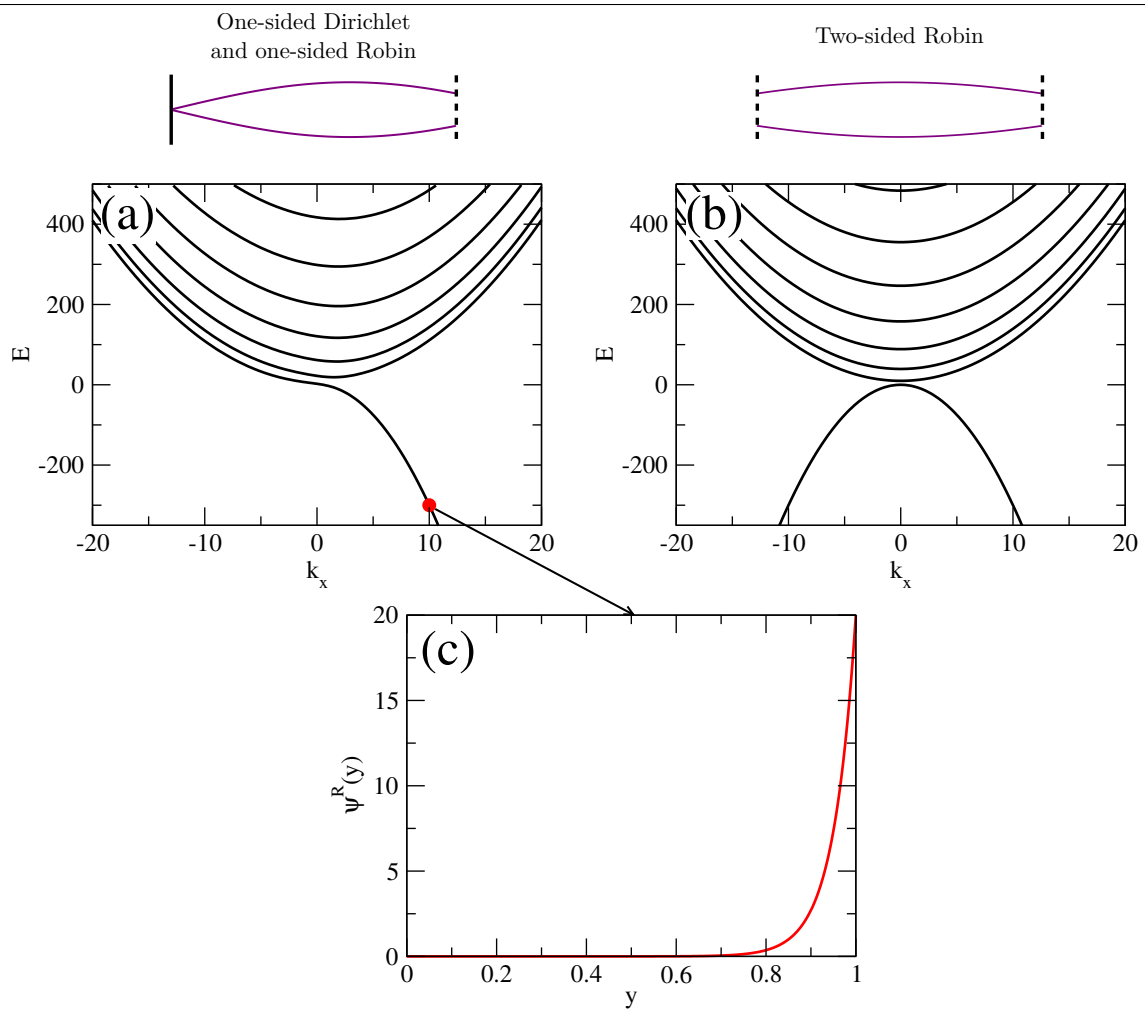

Figure 5.4: (a) like Fig. 5.3(c) shows the band structure of a unit interval with one-sided Dirichlet and one-sided Robin boundary condition with $B = 1$ but with a different choice of $Q = 2$, which makes the edge-state band tending to negative energies for large k_x. (c) shows a wave function of an eigenstate in this extra edge band, i. e., a plot of Eq. (5.47) using $k_x = 10$ and $Q = 2$. This solution asymptotically fulfills the Robin boundary condition at large k_x. (b) shows a band structure calculation for a unit interval with a two-sided Robin boundary condition as in Eq. (5.45) with $B = 1$ and $Q = 2$. The shown solutions are described by Eqs. (5.52) and (5.53).

and it immediately fulfills the Dirichlet boundary condition on the left side of the interval. The Robin boundary condition is fulfilled asymptotically because

$$\partial_y \psi^{\mathrm{R}}(L) - k_x Q \psi^{\mathrm{R}}(L) = k_x Q \cosh\left(k_x Q L\right) - k_x Q \sinh\left(k_x Q L\right) \tag{5.49}$$

$$= k_x Q \exp(-k_x Q L) \tag{5.50}$$

tends to zero for $k_x \to \infty$. In Fig. 5.3(c), we chose $B = Q = 1 \;\to\; E^{\mathrm{R}} = 0$, which is why we observe a completely flat band in the limit $k_x \to \infty$. This band smoothly connects to the other bands for $k_x \to -\infty$. By choosing $|Q| > 1$, we find a band that tends to negative infinite energies for $k_x \to \infty$ as illustrated in Fig. 5.4(a). This band behaves very similar to the extra band that was observed in the previous model calculation that involved a TI heterostructure [the band marked in blue in Fig. 5.1(b)]. In fact, this band leads to the existence of a PCC at every energy. Also, the fact that the wave function for this special mode that tends to negative energies is localized close to the boundary, cf. Fig. 5.4(c), makes sense: The bulk material is insulating in this energy region, similar to the situation in which we apply the TI boundary condition to a topologically trivial insulator in which we also obtain such a boundary mode in the bulk energy gap (not shown).

If one puts Robin boundary conditions as specified in Eq. (5.45) on both sides of the interval, one finds the following secular equation:

$$\left[E + B k_x^2 \left(Q^2 - 1\right)\right] \sin\left(\sqrt{\frac{E - B k_x^2}{B}} L\right) = 0, \tag{5.51}$$

which now trivially allows for analytical solutions,

$$E_n^{RR} = B\left[k_x^2 + \left(\frac{n\pi}{L}\right)^2\right] \quad \text{for } n \in \{1, 2, \dots\}, \tag{5.52}$$

$$E_0^{RR} = B\left(1 - Q^2\right) k_x^2. \tag{5.53}$$

The first set of bands, Eq. (5.52), turns out to be exactly identical to the dispersion found with both-sided Dirichlet or Neumann boundary conditions, Eq. (5.43). In addition, there is another band, Eq. (5.53), showing the dispersion which was asymptotically found for the edge band of the previous one-sided Robin problem. Here, this dispersion is an exact solution to the problem at all momenta and it yields a spectrum which is unbounded from below for $Q > 1$. A plot for such a spectrum in this parameter range is shown in Fig. 5.4(b). This spectrum does not feature a PCC as, at all energies, the number of conducting modes is the same in both directions. However, the band described by Eq. (5.53) gives rise to solutions,

$$\psi_0^{RR}(y) = \exp\left(k_x Q\, y\right), \tag{5.54}$$

which are strongly bound to the left edge for large negative and strongly bound to the right edge for large positive momenta. As the bulk material is insulating in this energy range, such a wave guide is similar to a Chern insulator: It features unidirectional edge

modes at each surface, which are protected from backscattering simply because of the absence of other modes to scatter into. Even though this is also interesting, it is of course different from the protection of the modes that are induced by the boundary conditions in Eqs. (5.38) and (5.39), which are protected by the odd mode number in each direction.

From a mathematical perspective, the appearance of an eigenvalue which tends to minus infinity for the Laplacian with a one-sided Robin boundary condition of the form

$$\partial_y \psi(L) = \alpha \psi(L) \tag{5.55}$$

for $\alpha \gg 1$ is well known [188]. It can, for example, be motivated by considering a Rayleigh-Ritz variational approach to the problem, i. e., by explicitly evaluating the energy of a test function $\psi(y)$,

$$\langle \psi | H \psi \rangle = \int_0^L dy\, \psi^*(y) \left(-\partial_y^2 \psi(y) \right) \tag{5.56}$$

$$= \int_0^L dy\ |\partial_y \psi(y)|^2 - \left[\psi^*(y) \partial_y \psi(y) \right]_0^L \tag{5.57}$$

$$= \int_0^L dy\ |\partial_y \psi(y)|^2 - \alpha\, |\psi(L)|^2 \,. \tag{5.58}$$

For two-sided Dirichlet or two-sided Neumann boundary conditions, the second term on the right-hand side, which is the surface term emerging from the integration by parts, vanishes and one is only left with the first term. This first term is obviously positive definite, which is why the spectrum of the Laplacian for such a choice of boundary conditions is strictly positive. With a Robin boundary condition given by Eq. (5.55), one additionally finds a surface term which always attains negative values for $\alpha > 0$. Thereby, for a test function that is sharply localized at the boundary, for example the exponentially localized test function

$$\psi(y) = \sqrt{2\alpha} \exp\left(\alpha \left(y - L \right) \right), \tag{5.59}$$

which satisfies the boundary condition at L and is normalized for $\alpha \gg 1$, we find for the energy expectation value

$$\langle \psi | H \psi \rangle = 2 \int_0^L dy\, \alpha^3 \exp\left(2\alpha \left(y - L \right) \right) - 2\alpha^2 \tag{5.60}$$

$$\approx 2 \int_{-\infty}^L dy\, \alpha^3 \exp\left(2\alpha \left(y - L \right) \right) - 2\alpha^2 = -\alpha^2, \tag{5.61}$$

proving that there must be at least one eigenvalue which tends to $-\infty$ for $\alpha \to \infty$.

Another aspect that might be worrying from a mathematical perspective is the Hermiticity of a Hamilton operator which is subjected to Robin boundary conditions. This is due to the fact that, as we saw above, Robin boundary conditions in general give rise to non-vanishing surface terms. For the Laplacian, which we studied above, this is not a problem. It can be shown to be Hermitian if defined on an interval with Robin

boundary conditions as the surface terms cancel when performing the integration by parts twice. However, when studying Hamilton operators with terms which are linear in the momentum, as the terms with coefficient A in the BHZ Hamiltonian, cf. Eq. (5.1), this cancellation may not be guaranteed. An example to illustrate this problem is provided by the momentum operator $p_y = -i\partial_y$ if it is defined on a function space for which one enforces a Robin boundary condition, Eq. (5.55), on one side of an interval and a Dirichlet boundary condition on the other side, $\psi(0) = 0$. In this case, it is easy to show that p_y is not Hermitian on this function space using an explicit test with two test functions $\phi(y)$ and $\psi(y)$,

$$\langle \phi | p_y \psi \rangle = \int_0^L dy\, \phi^*(y)\, (-i\partial_y)\, \psi(y) \tag{5.62}$$

$$= \int_0^L dy\, \left(-i\partial_y \phi(y)\right)^* \psi(y) - i\left[\phi^*(y)\psi(y)\right]_0^L \tag{5.63}$$

$$= \langle p_y \phi | \psi \rangle - i\phi^*(L)\psi(L), \tag{5.64}$$

which yields an extra term on the right-hand side that does not necessarily vanish. Of course, in this example, one faces the same problem when considering Neumann boundary conditions, $\partial_y \psi(L) = 0$. Even though the non-Hermiticity of the Hamiltonian does not necessarily imply a complex spectrum[2], it still greatly increase the complexity of the problem. Therefore, it is reassuring that one can show that the set of boundary conditions in Eqs. (5.38) and (5.39) guarantees Hermiticity of any quadratic Hamiltonian of the form

$$H = H_0 + H_1 k_y + H_2 k_y^2, \tag{5.65}$$

as long as H_i are Hermitian matrices that do not depend on k_y with H_1 and H_2 commuting with k_y. This is fulfilled for many model Hamiltonians among them the ones discussed in this chapter. As the proof of this result is a bit lengthy, we decided to defer it to Section 5.A.1 in the appendix to this chapter.

Before closing this section, we would like to emphasize that wave guides with a momentum-dependent Robin boundary condition as shown in Eq. (5.45) will generally feature PCCs. This means that if one is able to artificially implement this type of boundary condition, one can manufacture wave guides with PCCs without any need for a true TI. One might even think about an implementation in classical wave-transport setups like acoustic or optical systems. However, an actual implementation faces the problem that one needs to realize the dependence of the boundary condition on the longitudinal momentum, which, e. g., leads to the edge solution that tends to negative infinity for $k_x \to 0$. Of course, such a behavior can only be fulfilled in an effective description at low momenta and needs to turn over to a different behavior for large momenta in order to keep the spectrum bounded from below. This is clearly one of the main problems that one has to face: For large momenta the edge mode has to connect to another "band" of the wave guide, similar to the situation in a true TI. Otherwise,

[2] And there are even schemes how to define a meaningful quantum theory using non-Hermitian Hamilton operators [189].

the requirement that the band structure of the wave guide is periodic in the longitudinal momentum (with some periodicity given by the unit cell of the structure) together with the fact that the spectrum should be bounded from below will make the edge bands return to zero at large momenta and give rise to another transport channel that lifts the protection of the PCC. However, by using optical or acoustic metamaterials, such a connection to another band of the wave guide seems at least conceptually possible. Here, one should also emphasize that the dependence on the longitudinal momentum on the right-hand side of Eq. (5.45) is not required to be linear but could equally well be any other odd function of k_x.

5.3 Perfectly conducting channels in realistic HgTe/CdTe nanostructures

From the theoretical considerations of what to expect in metal/TI heterostructures, we now turn to the question whether the emerging PCCs can actually be observed in more realistic systems. For this, we present numerical calculations, which have been carried out by Viktor Krückl who also designed Figs. 5.5 and 5.6 as well as Figs. 5.8–5.11. As in Chapter 3, the transport calculations were done using the recursive Green's function framework by Michael Wimmer [100].

For a design of a realistic system, one faces the problem that one cannot assume a semi-infinite 2d-TI layer, which is why one has to change to a geometry which approximates this situation. This seems especially difficult in a two-lead device, which is why we propose a four-lead geometry, which is sketched in Fig. 5.5(a), and which makes it easier to address just one edge of the 2d TI. This decoupling of the two edges of the TI is necessary because the protection of the PCC is based on the *odd* number of scattering channels in the system (see Section 5.1). Such an odd number occurs for each edge of the TI, thus, any scattering matrix in which both edges of the TI are coupled is again even dimensional implying that it does not feature a protected PCC. However, as we will see below, a careful design of this four-lead geometry allows for a sufficient degree of decoupling in order to be able to observe the PCC.

As hinted to in the model study shown above, the important feature that is responsible for the appearance of an extended PCC in a metal/TI heterostructure is a sufficient hybridization of the 2d-TI edge state with the extended states of the adjacent material. In addition to this, there are no special requirements concerning the properties of the system with extended states. There is not even the need to build a true heterostructure made of different materials. Instead, to make the fabrication of the device as simple as possible, one could even build the whole structure from the same material (technically making it no longer a true heterostructure). With additional gates, one can locally tune the Fermi level of the material and thereby steer the presence or absence of extended states. The metal could then be mimicked by a region where the Fermi level is locally in the conduction (or valence) band. Results of band-structure calculations of such a ribbon in which the whole structure is made from a HgTe/CdTe quantum well with the upper part shifted in energy by means of a local gate are shown in Fig. 5.5(b). As in previous chapters, we use the BHZ Hamiltonian, Eq. (2.17), with material parameters

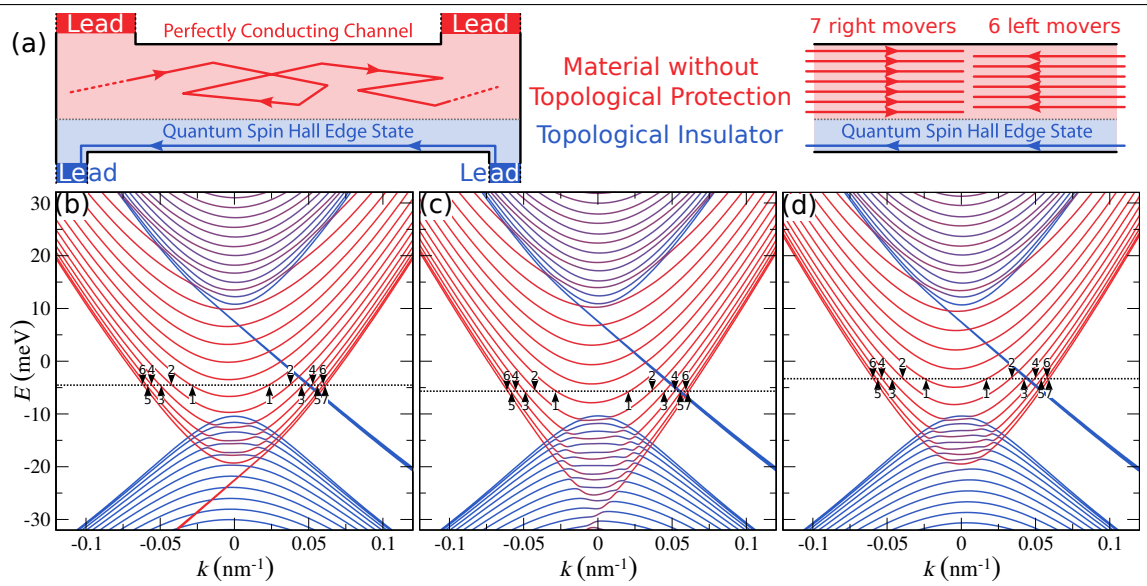

Figure 5.5: (a) shows a sketch of the proposed four-lead device geometry: An "H-bar" sample in which the upper region is metallic and the lower region is in a 2d-TI phase. (b) shows a band-structure plot of the central region of such an "H-bar", which is assumed to be fully made from HgTe/CdTe quantum-well material. The width of the metallic region was set to be $L = 350\,\mathrm{nm}$. The lower part is shifted in energy with respect to the upper part by an extra gate of $V_g = 30\,\mathrm{mV}$. In this way, a situation as sketched in the upper right emerges at some energies: The upper region has extended states while the lower region is in the 2d-TI limit. The color encodes the region in which the wave function of this state is located [red: in the upper (metallic) part, blue: in the lower (TI) part]. The dotted line indicates a Fermi energy at which one expects to observe a PCC, which can be immediately seen by counting the number of left- and right-moving states at this energy. To simplify this counting, small numbered arrows are added. (c) and (d) show the same plot for a system in which the mass of the upper part is modified, making it a semi metal, (c): $M = 0$, or making it a topologically trivial insulator, (d): $M = 10\,\mathrm{meV}$. Adapted from [23].

from Table 2.2. However, for this calculation, the spin-orbit coupling has been set to zero in order to allow an easy spin classification. Only the band structure of the spin-up block is plotted, which makes it directly comparable to the model calculation from Section 5.1, cf. Fig. 5.1(b). Being a band-structure calculation for a ribbon geometry [the central part of the structure shown in Fig. 5.5(a)], and no longer a calculation with a semi-infinite 2d-TI plane, we see states from both edges of the structure. For an easier interpretation, the states are color coded according to where most of their amplitude is situated: Red corresponds to the upper (metallic) part of the ribbon and blue corresponds to the lower part. In this way, we see that the upper edge state of the TI is fully hybridized with the bands of the "metallic" region (at least in the region of energies where extended states in the upper region exist, below this energy, we again see a single 2d-TI edge state as expected). In contrast to this, the blue band (the one from the lower TI region) disperses fully linearly in the whole gap and a closer look into its wave function (not shown) reveals that it is still a true one-dimensional edge state. The blue and the red states are decoupled from one another due to the insulating bulk of the lower 2d-TI region.

Counting the number of left- and right moving states at an energy where the upper

region is in the conduction band and the lower region is in the gap—as indicated by the numbered arrows—reveals indeed that there is one more right-propagating mode, thus a PCC, for this spin block. This PCC does not disappear if one changes the band ordering of the metallic region as can be seen in Figs. 5.5(b) and (c), in which the mass parameter of the metallic region is modified in a way to turn the metallic region into a gapless and a topologically trivial insulator respectively. The change in topology can be observed in the band structure by the absence of a surface state in the energy window in which the upper region is in the gap. But as one can confirm by counting the number of states, this topology change of the metallic part does not influence the presence of a PCC in the energy window in which the upper part is metallic. As discussed before, this is making us confident that this mechanism in principle allows to induce PCCs in all kinds of metallic systems irrespective of their topology (or to be precise of the topology of the corresponding insulator).

In terms of the experimental realization of such a heterostructure, this is fortunate as it is probably easier to pattern the system on the nanoscale and define the structure by additional gates instead of assembling a true heterostructure.

5.3.1 Detection by transport in the localized regime

The easiest way to observe a PCC in a transport experiment is to directly probe its persistent transport in the limit of strong disorder, i. e., its immunity to localization. As strong disorder is detrimental to the TI as also observed in the studies in Chapter 3, we propose to consider transport in a long sample where the localized regime is accessible already at smaller disorder strengths. For this reason, we propose a geometry that is shown in Fig. 5.6(a), i. e., a very elongated four-terminal structure. As discussed before, we assume it to be homogeneously made of HgTe/CdTe quantum-well material. The Fermi energy of the structure is assumed to be in the valence band of the material, $E_\mathrm{F} = -40\,\mathrm{meV}$, i. e., the ungated part is expected to be hole conducting. A stripe on the lower edge of the system is covered by a gate with which it may be tuned into the bulk gap, thus, converting it to a 2d TI. The whole system is assumed to be homogeneously disordered using on-site disorder at every grid point with an amplitude of $W = 30\,\mathrm{meV}$, a strength which—at the chosen discretization of the numerically used square grid of $a = 4\,\mathrm{nm}$—leads to localization when considering transport across the length of the device, $L_\mathrm{D} = 8\,\mu\mathrm{m}$. However, it is still too weak to destroy the TI (see Section 3.A.1 for a study of the influence of disorder at this lattice discretization). In the following calculations of the chapter, we are always using the full BHZ Hamiltonian including the coupling of the two spin blocks due to bulk inversion asymmetry, Eq. (2.22), with the strength Δ given by Table 2.2.

As long as there is no external gate voltage applied and the whole system is just one piece of hole-doped quantum well, the localization due to the disorder can be seen in a plot of the local density of states (LDOS) which is shown in Fig. 5.6(b). It was calculated with a small applied chemical-potential bias between the left and the right leads of the device. The LDOS decays rapidly over the length of the device (note the logarithmic scale of the color plot). This behavior changes if one tunes the gate such that the lower part of the system is in the TI regime as shown in Fig. 5.6(c). Now, the LDOS in the

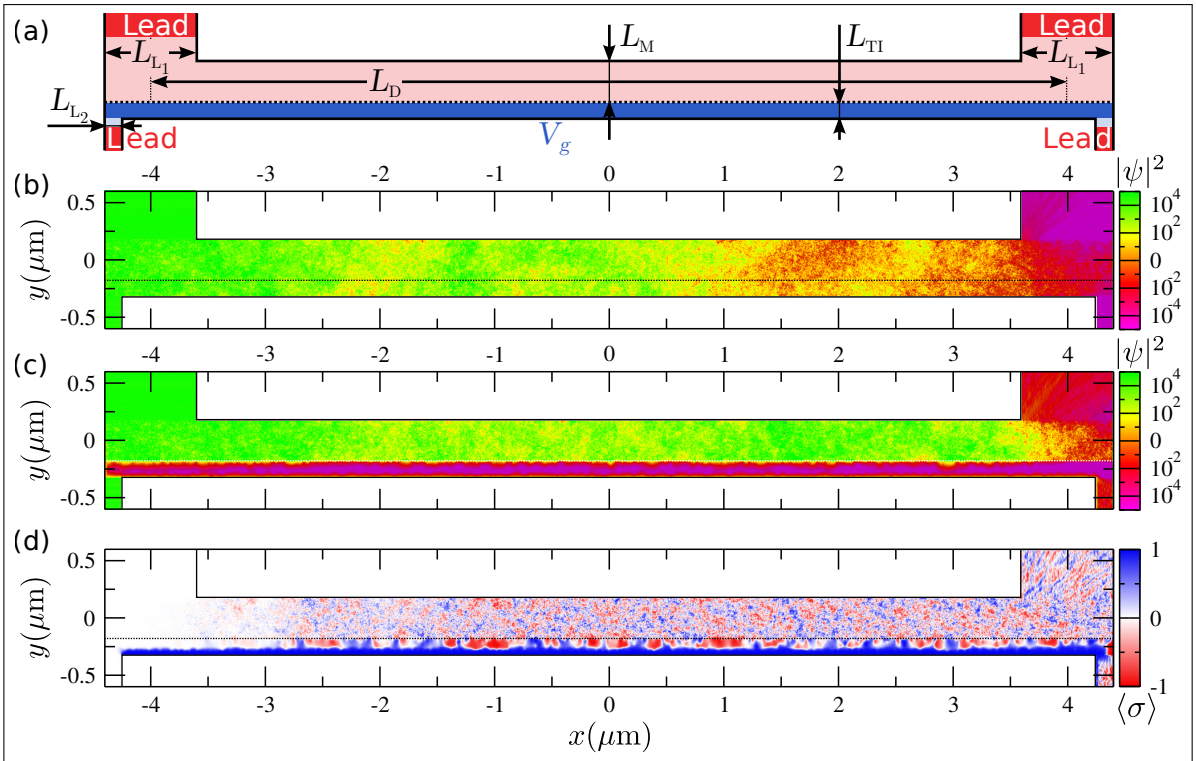

Figure 5.6: (a) shows a sketch of the geometry proposed to observe the induced PCC in a HgTe/CdTe quantum-well nanostructure by studying the regime of localized transport. We made the following choice of lengths for the geometry used in this section: $L_D = 8\,\mu$m, $L_M = 350\,$nm, $L_{TI} = 150\,$nm, $L_{L_1} = 800\,$nm, and $L_{L_2} = 150\,$nm. (b) shows a calculation of the LDOS when the gate voltage of the lower part is zero meaning that the Fermi energy of the whole system is homogeneously in the valence band, $E_F = -40\,$meV. The calculation is done for a single realization of on-site disorder with an amplitude of $W = 30\,$meV and a small voltage is applied between the left and the right leads. Spin-orbit coupling due to bulk inversion asymmetry, Eq. (2.22), was included using Δ from Table 2.2. (c) shows data from a calculation similar to (b) only with the lower part gated to $V_g = 40\,$mV turning it into a 2d TI, which immediately increases the extent of the states in the upper section due to the induced PCC. (d) shows a color plot of the spin density from the calculation shown in (c), in which it is visible that the PCC is not spin polarized while the lower 2d-TI edge channel shows a strong spin polarization. Adapted from [23].

upper part extends much further, a clear signature of the PCC that was induced due to the hybridization of the bulk states with the upper edge channel of the TI region. In addition, one notes that the lower part really became fully insulating except for the very thin edge channel at the lower boundary of the system, the expected signature of the 2d-TI regime.

A still clearer signature of the PCC can be observed in a calculation of the transport properties of such a structure. However, this requires some additional thought if one is really aiming at seeing a quantized single conductance quantum that survives the localization limit. The reason for this is that one has to make sure that the leads that one attaches couple well to the PCC in the central region. Because even though the transport in the channel is protected, perfect coupling to the channel is not per se guaranteed. Remember that the central argument for the protection of the PCC lies in the fact that, for each propagation direction, the system hosts an odd number of channels. However,

far away in the leads there will always be an even number of channels in each direction as they can usually safely be assumed to be spin-degenerate metallic contacts. So by zooming out on the system, at some stage, the scattering-matrix argument that we utilized should break down as we are then looking at a scattering matrix with an even number of channels all over and there would not be any kind of protection arising from that. Fortunately, this scenario can be circumvented by a smart design of the geometry, which ensures a certain degree of partitioning of the scattering matrix into subsystems which are almost decoupled and have an odd number of channels each.

The first thing that has to be taken into account is the lateral extent of the PCC. In the model study in Section 5.1, the PCC was always spanning the full metallic region, however, this model did not yet include any effects due to disorder. As we saw in Section 3.2, increasing disorder eventually causes a transition from a metal to a trivial Anderson insulator which leads to the well-known TI-insulator heterostructure with one-dimensional states at the boundary, cf. Fig. 3.5. Between these two limits, there is a smooth transition. In general, the lateral extent of the PCC will be given by the localization length in the metallic region, e. g., in the lowest panel of Fig. 3.5, the localization length in the material is already very small which is why the PCC only extends for a small distance into the disordered region (which at this disorder strength is no longer metallic). In the longitudinal direction, the PCC will always be extended, irrespective of the disorder strength. However, in order to allow for sufficient coupling to this channel by means of external leads, the localization length in the "metal" should be larger than the lateral extent of the structure in order for the PCC state to reach to the boundary at which the lead is attached. This explains why we propose a device with such a large aspect ratio: The localization length in the material should be larger than the width of the strip in order to allow a coupling to the leads but it should be smaller than the length of the strip in order to lead to localized transport for all channels but the PCC. This condition is fulfilled for our setup as one can see from the LDOS plots in Fig. 5.6: The disorder is weak enough in order to allow the PCC to span the whole device width without showing any noticeable decay.

The next important design consideration has to do with the fact that the leads always feature an even number of channels propagating in both directions as mentioned previously. In this way, at the interface to the lead, e. g., at the upper left (or equally at the upper right) corner, we find a situation that is sketched in Fig. 5.7(a), in which the channels in the lead and also the propagating modes in the different areas of the sample are shown as arrows. For simplicity, we only show the situation for one spin block, even though the argument will also extend to the case with spin-orbit coupling. The perspective that is taken in the illustration in Fig. 5.7 corresponds to what is known as an *open-mode approximation* [190], in which only the propagating modes in each section are taken into account for transport. Even though our full numerical calculation does not use this approximation, a discussion thereof is useful to qualitatively understand the behavior of the system. The shown number of propagating modes in the upper lead and in the channel section is much smaller than what we had in the numerical calculation but the shown parity of the number of modes is the same, i. e., whether the section features an even or an odd number of modes. At the interface to the lead, there will be a scattering matrix which links the amplitudes of the different incoming and outgoing channels. For

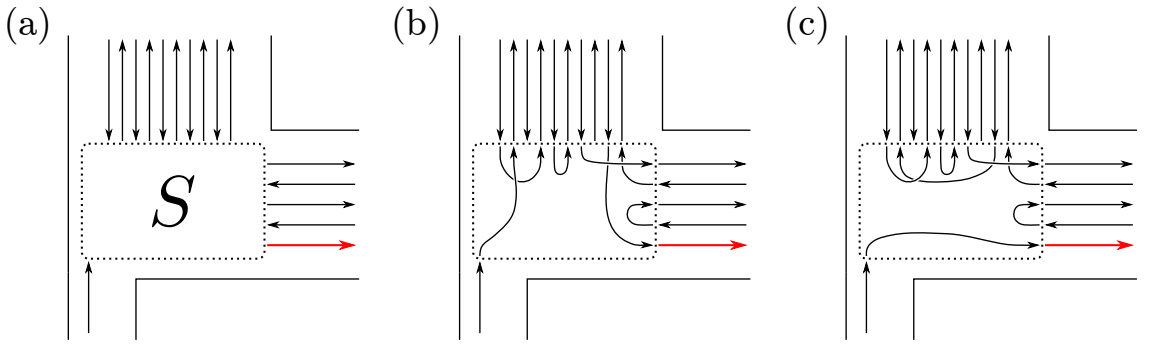

Figure 5.7: The sketches illustrate the possible coupling scenarios to the PCC. (a) shows an example of a situation at the left corner of the proposed device. The propagating modes of the leads and also of the right channel section are shown as arrows. For illustration purposes, only the modes of one spin block are shown and the number of modes in the channel and in the upper lead is chosen small, however, the parity of the number of modes (even number in the upper lead and odd number in the channel and in the lower lead) are shown correctly. In an open-mode approximation picture, those modes are linked by a scattering matrix S, which may lead to coupling scenarios as shown in (b) or (c). In (b), the PCC is fully coupled to the upper lead, while it is coupled to the lower lead in (c).

the very long channel lengths that we consider, all channels in the central part of the H-bar structure (the right section in Fig. 5.7) will localize except the PCC, which has been colored in red to distinguish it from the other channels. If the scattering matrix at the shown corner leads to a connection pattern as shown in Fig. 5.7(b), where the PCC fully couples into the upper lead, one expects full transmission from the upper lead to the right side of the structure. If on the other hand the connection is as shown in Fig. 5.7(c), the PCC does not couple to the upper lead and the transmission between the upper left lead and the right side of the structure should not show any sign of perfect transmission. In fact, if the other channels in the central section really localize, one would expect zero transmission from the upper left lead to the right side in this case. In principle, any intermediate coupling between those extreme scenarios could be present in practice. The key to enforce the scenario shown in Fig. 5.7(b) and to avoid the scenario from Fig. 5.7(c) is to make the upper lead very wide such that it features a large number of channels. Then, the PCC couples to one of the lead channels with a very high probability and the unwanted scenario from Fig. 5.7(c) becomes very unlikely as the section on the lower left always just contributes one channel and the chance of coupling the PCC to this very channel is small when the number of alternative couplings is large. As we can see from the illustration in Fig. 5.7(b), a perfect coupling of the PCC to the upper lead always comes with a perfect coupling of the upper lead to the 2d-TI edge channels of the lower left edge, which by its nature also is perfectly conducting. Thus, the upper lead will be simultaneously coupled perfectly to the lower and also to the right section of the system.

Now let us turn to the numerical results from the presented device, which are shown in Fig. 5.8. The displayed calculated transmissions were obtained by the recursive Green's function method. The first panel, Fig. 5.8(a), shows results for the transmission between the upper two terminals (in red) and between the lower two terminals (in blue) as a function of the applied gate voltage that steers the Fermi energy of the lower section of the structure, i. e., it is the handle that controls whether the lower section is a 2d TI or

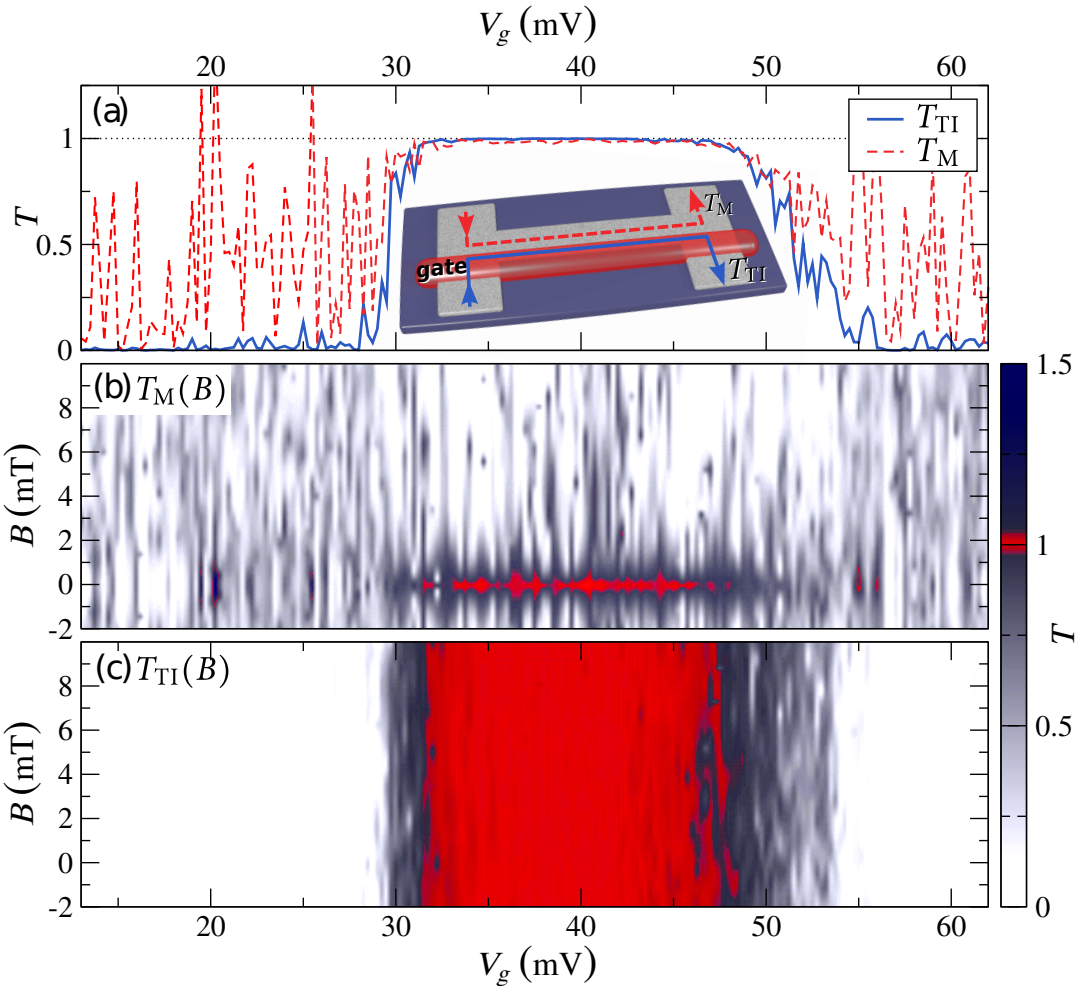

Figure 5.8: The figure shows the numerically calculated transmission through the setup sketched in Fig. 5.6(a). In (a), the calculated transmissions between the upper leads of the device T_{M} and between the lower leads of the device T_{TI} are shown as a function of the applied gate voltage. This gate voltage makes the lower part of the device a 2d TI in the voltage range of $30\,\mathrm{mV} < V_g < 50\,\mathrm{mV}$, where quantized conductance through both current paths is observed. The inset shows a sketch of the used geometry which illustrates the meanings of the calculated transmission coefficients. (b) and (c) also show the calculated transmissions T_{M} and T_{TI} in a color plot as an additional function of an applied perpendicular magnetic field B. All data in this figure was obtained on a single disorder realization with the amplitude $W = 30\,\mathrm{meV}$. Adapted from [23].

a gated semiconductor in the localized transport regime. As long as it is in the gated semiconductor regime ($V_g < 30\,\mathrm{mV}$ or $V_g > 50\,\mathrm{mV}$), we see clear signatures of localized transport with an average transmission below e^2/h and strong fluctuations because the figure is showing transport results of a single device (the data is not disorder averaged). The fact that the fluctuations in the blue curve are smaller than in the red curve even though the material is homogeneous for $V_g = 0\,\mathrm{mV}$ can be understood by the different widths of the upper and the lower leads, $L_{\mathrm{L}_1} = 800\,\mathrm{nm}$ and $L_{\mathrm{L}_2} = 150\,\mathrm{nm}$. As discussed before, the upper leads are chosen to be very wide in order to allow for a good coupling to the PCC while a good coupling to the edge channels on the lower edge can already be achieved with a small lead width. This explains the much smaller average transmission between the lower leads.

When the Fermi energy is tuned into the 2d-TI regime, the transmission T_{TI} between the lower leads shows a quantized plateau value of $1\,e^2/h$, which is the expected signature of the 2d-TI edge transport. However, in the same range of gate voltages, we also observe a plateau in the transmission T_{M} between the upper two leads that are not connected by 2d-TI material. This is the signature of the induced PCC. In this kind of experiment, the signature of the PCC looks very similar to the usual 2d-TI edge transport, however, the difference between the two can be probed in a magnetoconductance measurement: The color plots in Fig. 5.8(b) and Fig. 5.8(c) show again T_{M} and T_{TI}, this time as an additional function of an applied perpendicular magnetic field. As in Chapter 3, we only include orbital effects of the magnetic field, which is numerically implemented by multiplying a Peierls phase to the hopping matrix elements. Zeeman terms as in Eq. (2.24) are neglected because we know that their influence is small at the considered weak magnetic fields, cf. Section 3.A.2.

While the transport between the lower leads [Fig. 5.8(c)] that are linked by a long section of 1d topological edge channels is rather unaffected by the magnetic field as has also been demonstrated in Chapter 3, the quantized plateau for the transport between the two upper terminals [Fig. 5.8(b)] vanishes already for small magnetic fields. Similar to the transport in charge puddles discussed in Section 3.3, this has to do with the fact that the PCC is extended in nature which makes the TR-symmetry breaking in an external field much more effective. Already a field on the order of a single flux quantum piercing the size of the gated region, corresponding to $B \approx 2\,\mathrm{mT}$, is enough to fully eliminate the PCC. In this way, magnetoconductance measurements allow for an experimental distinction between transport in edge channels that are almost one dimensional and delocalized PCCs.

An additional important feature of the PCC that is noteworthy is the fact that it is totally spin mixed at realistic values of the spin-orbit parameter Δ, while the normal 2d-TI edge states remain almost fully spin polarized also up to higher values of spin-orbit coupling. This is illustrated in plots of the local spin density of states plotted in Fig. 5.6(d), which shows the very constant blue spin density at the lower edge and a strongly oscillating pattern in the upper region. It turns out that the net spin polarization is zero for the PCC.

5.3.2 Detection by transport in the diffusive regime

To reveal the special transport properties of the PCC in the previous setup, we studied a system in a parameter regime in which all other channels were localized. In practice, this is often not so easy to achieve and there are usually more channels contributing to transport, which, however, are not perfectly conducting but have a finite transmission amplitude. Thus, the total transmission between the upper leads T_{M} has contributions from many channels, $T_{\mathrm{M}} = \sum_n t_n$ with $0 < t_n < 1$, not just the PCC for which $t_{\mathrm{PCC}} = 1$.

Naively, one would expect that the presence or absence of a PCC in this scenario should be easy to detect as adding or removing it, e. g., by applying an additional magnetic field, should roughly change the total transmission by one. This however turns out not to be true. In fact, it can be rigorously shown that the expectation value and also the variance of the transmission of a diffusive wire with symplectic symmetry does not depend on the presence or absence of a PCC (i. e., on the fact that the channel number is even or odd) to lowest orders [191]. Also, a related study that deals with signatures of the PCC in shot noise—in a slightly different scenario of a true channel-number imbalance which corresponds to zero spin-orbit coupling in our case—shows that the PCC cannot be observed in the short-wire limit [192]. The underlying mathematical reason for this is that the transmission eigenvalue of the PCC, which is fixed at one, "repels" the other transmission eigenvalues as the distribution of the transmission eigenvalues in a diffusive system can be understood with an analogy to the one-dimensional Coulomb gas [193–195]. The repulsion of the eigenvalues in this analogy is due to the statistical repulsion obtained if one expresses the probability density of the scattering matrix ensemble in terms of the transmission eigenvalues. This extra repulsion due to the PCC pushes the other transmission eigenvalues to smaller values leaving the expectation value and also the second moment (which is relevant for the shot noise) unchanged.

This is of course somewhat discouraging but it turns out that our particular system allows for the detection of a PCC by means of a small trick. By adding a small tunnel barrier in the middle of the metallic region, as shown in the inset of Fig. 5.9, we can suppress all transmission eigenvalues but the PCC. This tunnel barrier is here implemented by an additional gate, which can be tuned independently, and the effect of it can be seen in Figure 5.9, which shows a calculation of the LDOS with a small bias between the left and the right leads, similar to the calculation shown in Fig. 5.6(b) for the case of the device that was proposed to probe the localized regime.

The effect of the tunnel barrier on the transmission eigenvalues of the transmission matrix between the upper two leads is shown in Fig. 5.10(a). Without the tunnel barrier and without an applied magnetic field, we observe a transmission-eigenvalue distribution which resembles the expected bimodal distribution that is ubiquitously found in two-terminal diffusive systems [193,196], and which is shown in the upper left. In this way, the PCC is masked by the contributions of other non-perfectly conducting channels. Raising the tunnel barrier to $V_t = 40\,\mathrm{mV}$ strongly suppresses these intermediate transmissions as also shown in Fig. 5.10(a). Now, it is only the PCC which contributes to transport. As hinted to in the previous section, the PCC can be destroyed by the application of an external perpendicular magnetic field. And indeed, the influence of such a field can be seen in the probability distribution for the transmission eigenvalues as shown in the figure

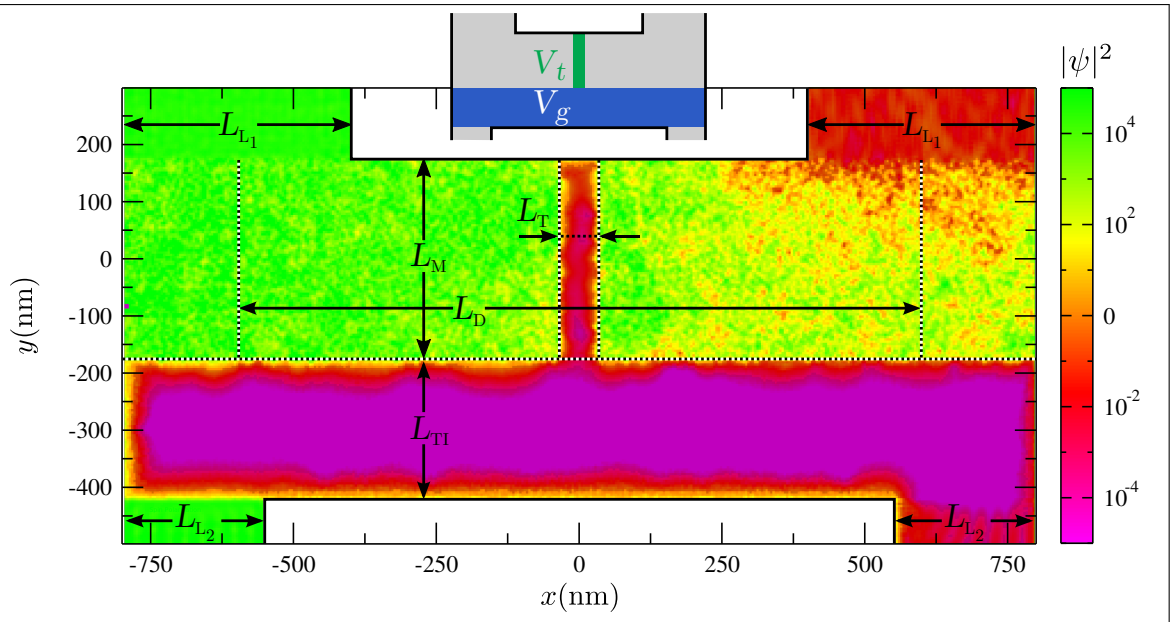

Figure 5.9: The small sketch above the figure illustrates the setup that is used to detect the PCC in the diffusive regime. In this setup, two gates are used: V_g for tuning the lower section into the TI regime and for inducing the PCC in the above metallic region and V_t for creating a tunnel barrier which decreases the transmission between the upper two leads and thereby allows for an observation of the PCC. The figure shows a color plot of the calculated LDOS with a small applied bias voltage between the left and the right leads. Here, both gates were set to $V_g = V_t = 40\,\mathrm{mV}$ to turn the gated regions into the 2d-TI regime, with the Fermi energy of the overall material being in the valence band at $E_F = -40\,\mathrm{meV}$. The data was obtained using a single disorder configuration with amplitude $W = 30\,\mathrm{meV}$. The geometry parameters that define the structure are chosen as $L_\mathrm{D} = 1.2\,\mu\mathrm{m}$, $L_\mathrm{M} = 350\,\mathrm{nm}$, $L_\mathrm{TI} = 250\,\mathrm{nm}$, $L_\mathrm{T} = 70\,\mathrm{nm}$, $L_{\mathrm{L}_1} = 400\,\mathrm{nm}$, and $L_{\mathrm{L}_2} = 250\,\mathrm{nm}$. Adapted from [23].

for the case that $B = 10\,\mathrm{mT}$ and $V_t = 40\,\mathrm{mV}$: The distribution is clearly broadened and no longer shows a distinct peak at $t = 1$.

The consequences of these transmission-eigenvalue distributions can also be observed in measurable quantities like the total transmission T_M and the shot noise, i. e., the zero-frequency current-current correlation. The total transmission between the upper left and upper right terminal T_M is displayed in Fig. 5.10(b) as a function of the applied voltage on the gate that steers the tunnel barrier. In the region where the tunnel barrier is active, i. e., if $30\,\mathrm{mV} < V_t < 60\,\mathrm{mV}$, the transmission drops to a value which is very close to the quantized value e^2/h for zero external magnetic field: a signature of the PCC. The fact that this feature disappears under the application of a magnetic field also hints to this being due to the PCC.

A still clearer signature is observed when using shot-noise measurements. In a two-terminal device, the low-temperature noise power is directly linked to the transmission coefficients between the two leads, $P \propto \sum_n t_n(1-t_n)$. In a multi-terminal device however, shot noise is in general not very easy to interpret. For a detailed discussion of this topic and a small overview on the phenomenon of shot noise, we refer to Section 5.A.2 of the appendix of this chapter. The main message from this discussion is that, with a well-chosen experimental setup, one can use shot-noise measurements to extract information on the higher moments of the transmission-eigenvalue distribution also in the multi-terminal

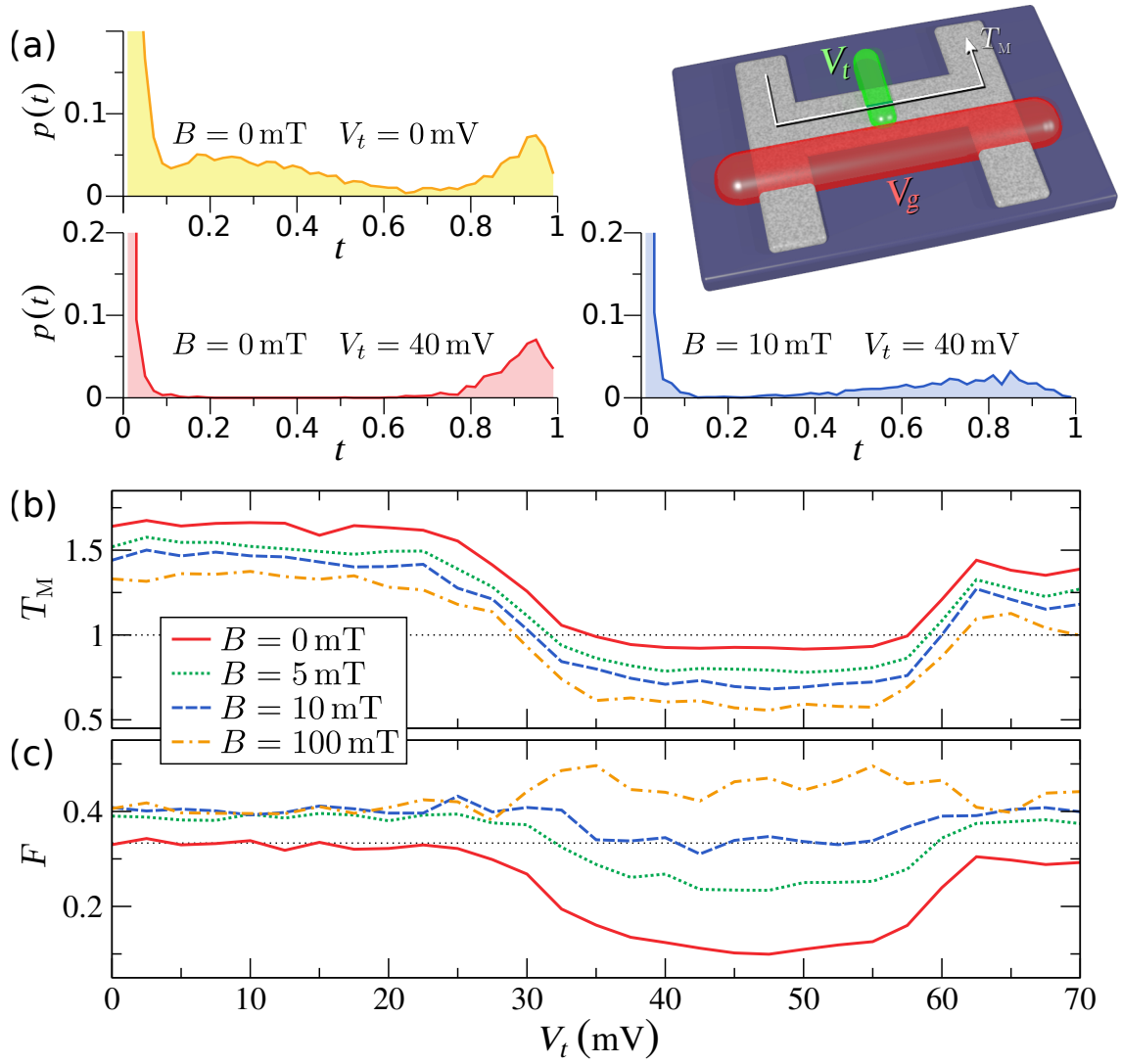

Figure 5.10: The setup shows transport results on the proposed transport setup for the detection of the induced PCC in the diffusive regime using the geometry that is shown in Fig. 5.9. The small sketch on the upper right illustrates the arrangement of gates and illustrates the calculated transmission between the upper two leads T_{M} on which the data in this figure is based. To obtain the results in this figure, we set $E_{\mathrm{F}} = -40\,\mathrm{meV}$ to make the bulk material metallic and choose $V_g = 40\,\mathrm{mV}$, which turns the red section in the sketch into a 2d TI. (a) shows histogram plots for the probability density of transmission eigenvalues for the transmission matrix between the upper two leads obtained from an ensemble of 1000 disorder configurations with a disorder strength of $W = 30\,\mathrm{meV}$ which is homogeneously applied throughout the whole sample. We see that we find an approximately bimodal shape for $B = 0\,\mathrm{mT}$ and $V_t = 0\,\mathrm{mV}$, or a distribution with a single PCC for $B = 0\,\mathrm{mT}$ and $V_t = 40\,\mathrm{mV}$. With an applied magnetic field, the PCC peak is washed out. (b) shows the transmission expectation values and (c) the Fano factor which one obtains from the transmission-eigenvalue distribution for the transport between the two upper leads as a function of the applied tunnel voltage for the same disorder ensemble at different values of the magnetic field. The dotted line in (b) denotes the expected value for the transmission from a single PCC, $T_{\mathrm{M}} = 1$. In (c), the dotted line indicates the expected value for the Fano factor for a diffusive two-terminal conductor, $F = \frac{1}{3}$. Adapted from [23].

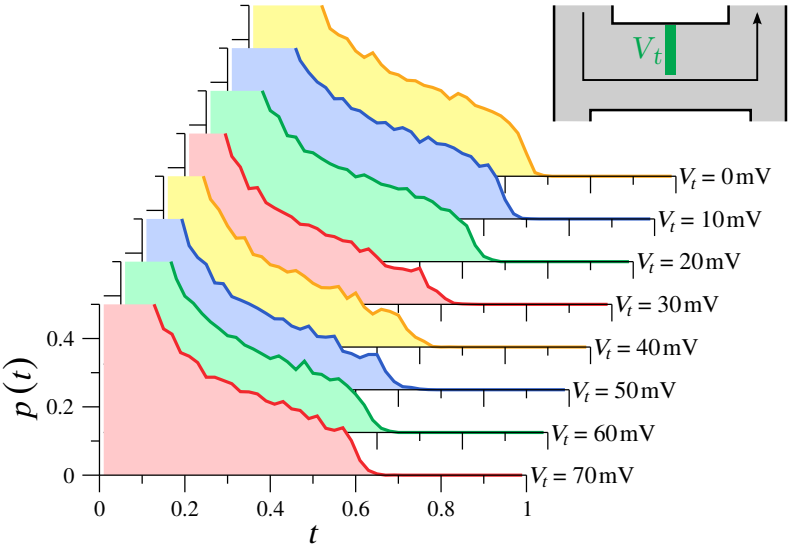

Figure 5.11: The figure shows plots of the eigenvalue distribution for the transmission matrix between the upper two leads of the structure shown in Fig. 5.6. For the calculations shown in this figure, the lower gate is not active, $V_g = 0\,\mathrm{mV}$, and the Fermi energy is chosen to be $E_\mathrm{F} = -40\,\mathrm{meV}$ making the gray area in the sketch metallic. Only the voltage of the tunnel-barrier gate V_t, which does not lead to the emergence of a full tunnel barrier in this setup, is varied. A disorder strength of $W = 30\,\mathrm{meV}$ is applied and 1000 disorder configurations were used to produce the histograms. The Fermi energy of the whole system is set to $E_\mathrm{F} = -40\,\mathrm{meV}$ making it hole conducting. Interestingly, the transmission-eigenvalue distribution in this case always displays a cutoff at around $t = 0.7$ above which the probability for finding an eigenvalue drops to zero. This feature is relatively independent of the strength of V_t. As we will discuss in Chapter 6 of this thesis, this is a rather general feature of many-lead devices.

case. In this way, one can experimentally access the so-called Fano factor,

$$F = \frac{\sum_n t_n(1-t_n)}{\sum_n t_n}, \tag{5.66}$$

which is the shot-noise power (in the specially chosen measurement setup, see Section 5.A.2) divided by the total transmission $T_\mathrm{M} = \sum_n t_n$. Calculation results of this quantity are shown in Fig. 5.10(c). In the case without a tunnel barrier, we find the universal Fano factor of $\frac{1}{3}$ (indicated as a dashed line), which is generally expected for two-terminal diffusive systems independently of the underlying symmetry class [197], i. e., independently of the presence or absence of a magnetic field. With an active tunnel barrier, all transmissions except the PCC are strongly suppressed, which is why the expectation value of the shot noise tends to zero without an applied magnetic field. The application of a magnetic field removes the protection of the PCC. This removes the suppression of the shot noise, which may even rise above $\frac{1}{3}$ due to the tunnel barrier (the expected limit for the value of the Fano factor for a weakly transmitting tunneling barrier is 1). In this way, the measurement of shot noise yields an especially well-suited means to probe the existence of a PCC in a diffusive system with a tunnel barrier.

Before concluding, we would like to show another interesting set of results that we obtained using the tunnel setup even though it is not directly related to transport in

TIs. For a calculation of the transmission-eigenvalue density for the transmission matrix between the upper two leads for the case in which the lower gate V_g is absent, $V_g = 0$, we find distributions which are shown in Fig. 5.11. Note that this gate configuration is different from the one that was used to obtain Fig. 5.10, in which the choice of $V_g = 40\,\mathrm{mV}$ led to an induced PCC in the upper section. Now, with $V_g = 0$, we are simply studying transport in a diffusive metallic system with no induced PCC. Fig. 5.11 shows histograms for different strengths of the tunnel gate V_t, which however does not lead to a formation of a full barrier in this case but instead only causes a reduction of the cross section of the transport channel. We see that this does not lead to a strong change of the distribution, which does not come as a very big surprise. What is however more interesting is the general shape of the distribution: It does not at all resemble the bimodal distribution that is commonly found in diffusive two-lead devices. Instead, it displays a clear cutoff at about $t = 0.7$ above which the probability density drops to zero. We found that this is indeed a direct consequence of the number of terminals of the diffusive device. For example, if one reduces the number of leads to only two, or equivalently if one combines the leads into "meta leads" and calculates the transmission eigenvalues of these combined transmission matrices, one recovers the bimodal distribution. In a detailed literature search, we found that while a similar change of the eigenvalue distribution function is known for multi-terminal quantum dots, we could not find studies that investigate the behavior of the distribution in multi-lead diffusive devices. This motivated us to investigate this interesting topic in more detail, the results of which will be presented in the next chapter of this thesis.

5.4 Discussion

In this chapter, we studied transport through metal/2d-TI heterostructures. We saw that we generally expect the edge states of the TI to hybridize with the metallic bulk states such that they lose their interface-state character. However, they lead to an odd channel number in the metallic part of the wave guide, which comes with the important consequence that an extended-state PCC is induced. This PCC is protected against backscattering as long as TR symmetry is preserved. However, as soon as there is some small amount of disorder, the PCC is in general not expected to be spin polarized.

Using model calculations, we found that the emergence of this PCC can be understood in terms of a set of effective boundary conditions, which can be more generally viewed as boundary conditions that mimic the boundary to a 2d TI. Thereby, they become an analogue of the commonly used hard-wall boundary conditions, which are typically used to describe the boundary to a trivial insulator. The emergence of a PCC through this set of boundary conditions could be traced back to the fact that one of the derived boundary conditions is of the Robin type, which, in addition, parametrically depends on the longitudinal momentum of the considered state in the wave guide. We realized that there is good mathematical reason for this and that this may be used to induce PCCs also in wave-guide structures without TIs if one can artificially realize this (or a similar) boundary condition. For example, one may try to realize such a boundary condition for electromagnetic waves by using photonic crystals.

In the second part of the chapter, we proposed experimental setups to demonstrate the induced PCCs in real devices. We saw that the PCC is particularly easy to observe in very long samples for which all other channels localize. However, the usage of an extra tunnel barrier also allows for a detection of the PCC in a shorter sample, in which there are in principle more modes that contribute to transport. Shot-noise measurements are particularly helpful in this scenario as they are expected to show a particularly strong signal, which complements the conductance signature. In agreement with the findings in Chapter 3, we saw that the PCC can be distinguished from the one-dimensional topological edge-state transport by means of an external magnetic field, which allows to selectively switch off the PCC already at small field strengths.

5.A Appendix

5.A.1 Test of Hermiticity for TI-proximity boundary conditions

We show that the boundary condition given by Eqs. (5.38) and (5.39) guarantees the Hermiticity of a general quadratic Hamiltonian,

$$H = H_0 + H_1 k_y + H_2 k_y^2, \tag{5.67}$$

where it is assumed that H_i are Hermitian matrices which do not depend on k_y and that H_1 and H_2 commute with k_y, thus, that they are independent of y. For this, we consider an interval for which we, for simplicity, assume Dirichlet boundary conditions, $\psi(0) = \mathbf{0}$, at one end and the TI-proximity boundary conditions, Eqs. (5.38) and (5.39), at the other end. We then find for the matrix element of two trial spinor wave functions $\phi(y)$ and $\psi(y)$

$$\langle \phi | H\psi \rangle = \int_0^L dy\, \phi^* H \psi \tag{5.68}$$

$$= \int_0^L dy\, \phi^* H_0 \psi + \int_0^L dy\, \phi^* H_1 \left(-i\partial_y\right) \psi + \int_0^L dy\, \phi^* H_2 \left(-\partial_y^2\right) \psi \tag{5.69}$$

$$= \int_0^L dy\, \left(H_0\phi\right)^* \psi + \int_0^L dy\, \left(-iH_1\partial_y\phi\right)^* \psi + \int_0^L dy\, \left(-H_2\partial_y^2\phi\right)^* \psi$$
$$- i\left[\phi^* H_1 \psi\right]_0^L - \left[\phi^* H_2 \partial_y \psi\right]_0^L + \left[\left(H_2 \partial_y \phi^*\right)\psi\right]_0^L \tag{5.70}$$

$$= \langle H\phi | \psi \rangle - i\phi^*(L) H_1 \psi(L) - \phi^*(L) H_2 \partial_y \psi(L) + \left(H_2 \partial_y \phi^*(L)\right) \psi(L), \tag{5.71}$$

where we did not explicitly write the wave-function argument in the intermediate steps to shorten the notation. To prove the Hermiticity of H, it remains to be shown that the three additional terms on the right-hand side vanish when we make use of the set of boundary conditions at L,

$$\psi_1(L) = -\psi_2(L), \tag{5.72}$$
$$i\left(v_y\psi\right)_1(L) - i\left(v_y\psi\right)_2(L) = 4Qk_x\psi_1(L), \tag{5.73}$$

which equivalently also hold for $\phi(y)$. For this, we explicitly evaluate the current operator v_y in this case,

$$v_y = i\left[H, y\right] = H_1 + 2H_2\left(-i\partial_y\right), \tag{5.74}$$

which we solve for $H_2\partial_y$ and insert this in Eq. (5.71), yielding

$$\langle \phi | H\psi \rangle = \langle H\phi | \psi \rangle - \frac{1}{2}\phi^*(L)\left[iv_y\psi(L)\right] + \frac{1}{2}\left[iv_y\phi(L)\right]^* \psi(L). \tag{5.75}$$

By writing out the scalar product explicitly in terms of components, we find

$$\begin{aligned}\langle\phi|H\psi\rangle &= \langle H\phi|\psi\rangle - \frac{1}{2}\phi_1^*(L)\left[iv_y\psi_1(L)\right] - \frac{1}{2}\phi_2^*(L)\left[iv_y\psi_2(L)\right] \\ &\quad + \frac{1}{2}\left[iv_y\phi_1(L)\right]^*\psi_1(L) + \frac{1}{2}\left[iv_y\phi_2(L)\right]^*\psi_2(L) \qquad (5.76)\\ &= \langle H\phi|\psi\rangle + \frac{1}{2}\phi_2^*(L)\left[iv_y\psi_1(L) - iv_y\psi_2(L)\right] \\ &\quad - \frac{1}{2}\left[iv_y\phi_1(L) - iv_y\phi_2(L)\right]^*\psi_2(L), \qquad (5.77)\end{aligned}$$

where we made use of the first boundary condition, Eq. (5.72), for ϕ and ψ. Using the second boundary condition, Eq. (5.73), we finally obtain

$$\begin{aligned}\langle\phi|H\psi\rangle &= \langle H\phi|\psi\rangle + 2Qk_x\phi_2^*(L)\psi_1(L) - 2Q^*k_x\phi_1^*\psi_2(L) \qquad (5.78)\\ &= \langle H\phi|\psi\rangle + 2\left(Q - Q^*\right)k_x\phi_2^*(L)\psi_1(L), \qquad (5.79)\end{aligned}$$

which implies that H is Hermitian as long as the parameter Q is chosen to be real. This line of argumentation can also be generalized to other boundary orientations, e. g., to the set of boundary conditions in Eqs. (5.40) and (5.41).

5.A.2 Shot noise in multi-terminal structures

The Landauer-Büttiker formalism [198,199] makes use of the fact that electronic transport (of effectively non-interacting carriers) in a mesoscopic conductor at low temperatures can be mapped to a wave-scattering problem [104, 105]. By solving this problem, one finds transmission and reflection probabilities of carriers and therefore obtains information about the experimentally expected mean currents. These currents will usually be subject to fluctuations, one of them being the so-called *Johnson-Nyquist noise* which arises from the thermal fluctuations in the reservoirs and is proportional to the sample temperature [200]. In addition, even at zero temperature, a mesoscopic conductor generally displays current fluctuations, which are known as *shot noise* or *partition noise*[3]. They reflect the fact that the current is, after all, carried by particles with a quantized charge, which are either fully reflected or fully transmitted, the probability of which is given by the coefficients mentioned above. This shot noise may well be the dominant source of noise at low temperatures and can nowadays be measured in experiments. As it carries information about the transmission and reflection properties of the current-carrying channels, it is a valuable tool to extract information about the transport properties of a mesoscopic conductor that go beyond the information that is contained in the average currents. This allows us to use it as a means to measure the existence of a perfectly conducting channel, as discussed in Section 5.3.2. For example, it is known that the current noise power, i. e., the mean-squared current fluctuations in a

[3]Ref. [201] provides a good review on this topic.

unit frequency interval,

$$S(f) = \frac{\langle \Delta I(f)^2 \rangle}{\Delta f}, \tag{5.80}$$

for a two-terminal device in the low-frequency and zero-temperature limit is given by [202, 203]

$$\lim_{f\to 0} S(f) = S = 2\frac{e^2}{h} \operatorname{Tr}\left(r^\dagger r t^\dagger t\right) e\,|V| \tag{5.81}$$

$$= 2\frac{e^3\,|V|}{h} \sum_n T_n\,(1 - T_n)\,, \tag{5.82}$$

where r and t are the reflection and transmission blocks of the scattering matrix and $|V|$ is the amplitude of the bias voltage. The sum in the second row runs over the eigenvalues of the transmission matrix $t^\dagger t$, which we named T_n. As we can see, a perfectly conducting channel $T_n = 1$ similar to a fully reflecting channel $T_n = 0$ does not contribute anything to the shot-noise signal. The shot noise provides access to the second moment of the transmission-eigenvalue distribution $p(T)$. As the shot noise is directly proportional to the bias voltage and therefore to the current, one often divides the noise by the current,

$$\frac{S}{\langle I \rangle} = 2e\frac{\sum_n T_n\,(1 - T_n)}{\sum_n T_n} = 2eF, \tag{5.83}$$

and defines the so-called *Fano factor* F, which is only depending on the transmission-eigenvalue distribution. This Fano factor can also be viewed as the factor by which the shot noise is decreased with respect to the *Poissonian value* (the value expected for a stream of uncorrelated particles) $S_\mathrm{P} = 2e\,\langle I \rangle$, which was already found in a classical work by Schottky [204].

In multi-terminal structures, however, the calculation of the zero-frequency shot-noise contribution is in general more complicated than in two-terminal devices. As detailed in Ref. [201, 202], the mean-squared current correlation of the current in lead α and the current in lead β,

$$S_{\alpha\beta}(f) = \frac{1}{2\Delta f}\,\langle \Delta I_\alpha(f)\Delta I_\beta(f') + \Delta I_\beta(f')\Delta I_\alpha(f)\rangle\,, \tag{5.84}$$

in the low-frequency and zero-temperature limit can be related to the scattering matrix in the following way:

$$\lim_{f\to 0} S_{\alpha\beta}(f) = \frac{e^2}{h} \sum_{\substack{\gamma,\delta \\ \gamma\neq\delta}} \int dE \operatorname{Tr}\left(s^\dagger_{\alpha\gamma} s_{\alpha\delta} s^\dagger_{\beta\delta} s_{\beta\gamma}\right) \{f_\gamma(E)\,(1 - f_\delta(E)) + f_\delta(E)\,(1 - f_\gamma(E))\}\,, \tag{5.85}$$

where $s_{\alpha\beta}$ is the subblock of the scattering matrix that connects lead β to lead α, and $f_\gamma(E)$ is the Fermi function of the electron distribution in lead γ, which is taken as a

step function at the corresponding electrochemical potential, $f_\gamma(E) = \theta\left(eV_\gamma - E\right)$, with V_γ being the voltage applied to lead γ.

The relation stated in Eq. (5.85) shows that the shot noise is given by a sum of products of scattering matrices and that it can in general not be reduced to a simple sum over transmission eigenvalues as in the two-terminal case, Eq. (5.82). In a way, the shot noise in these structures contains more information than the information that is contained in the first and second moment of the eigenvalue distribution, a fact that can be probed by exchange effects [205]. However, for the purpose of this thesis, this is an unnecessary complication as we would like to use shot noise to probe the first two moments of the transmission-eigenvalue distribution of the transmission matrix, also in a multi-terminal device. Luckily, this is possible by choosing a particular bias configuration. Suppose that we are interested in the eigenvalue distribution of the transmission matrix from lead 1 to lead 2, s_{21}, in a multi-lead setup. If we bias lead 1 with a positive voltage V and ground all the other leads, we find for the measurement of the autocorrelation of the current in lead 2 from Eq. (5.85):

$$\lim_{f\to 0} S_{22}(f) = S_{22} = 2\frac{e^3}{h} V \sum_{\gamma\neq 1} \mathrm{Tr}\left(s_{21}s_{21}^\dagger s_{2\gamma}s_{2\gamma}^\dagger\right) \tag{5.86}$$

$$= 2\frac{e^3}{h} V \,\mathrm{Tr}\left(s_{21}s_{21}^\dagger\left(\mathbf{1} - s_{21}s_{21}^\dagger\right)\right) \tag{5.87}$$

$$= 2\frac{e^3}{h} V \sum_{n=1}^{N} T_n\left(1 - T_n\right), \tag{5.88}$$

where T_n are the eigenvalues of $s_{21}^\dagger s_{21}$, the desired transmission matrix. This is the measurement scheme that is implied when we discuss shot noise in a multi-terminal setup in terms of this very simple dependence of S on the transmission-eigenvalue distribution.

As discussed above, the shot noise contains information about the correlation between particles and is therefore also a valuable tool to study interactions, which may even lead to noise levels above the Poissonian value. However, in this thesis we will neglect these and only study the non-interacting limit.

Chapter 6

Transmission-eigenvalue distribution of multi-terminal diffusive systems

6.1 Introduction

While investigating the transport signatures of a perfectly conducting channel in a metal-TI heterostructure, we came across probability distribution functions of transmission eigenvalues in many-lead diffusive devices. We were rather surprised to discover that not so much is known about these in the literature yet, which was the motivation for us to study these distribution functions in a bit more detail in this chapter. For a diffusive two-lead device, it is widely known that the probability for transmission eigenvalues t is given by an asymmetric "bimodal distribution" with only one parameter T, determining the average transmission per channel [193, 196, 206],

$$p(t) = \frac{T}{2}\frac{1}{t\sqrt{1-t}}, \tag{6.1}$$

as could be shown by solving the Dorokhov-Mello-Pereyra-Kumar (DMPK) equation [196, 207] for a strip geometry. However, it is less known what to expect in case of many-lead devices, and the distribution function that is found in these devices generally looks very different from this bimodal shape. As we already saw in Fig. 5.11, it generally exhibits a cutoff, meaning that there is a highest eigenvalue $t_{\max}$ above which the probability distribution is zero. We start off by studying this phenomenon by means of a scattering-matrix model in the open-mode approximation, which we will introduce in the following section. With the help of this model, we explain the origin of the cutoff and also derive analytical expressions for the transmission-eigenvalue distribution in a few limiting cases. Also, we discuss an interesting related observable, which measures how the eigenvectors and eigenvalues split in multi-lead devices in the low-transmission limit. Later in the chapter, we will compare the findings based on this model to full transport calculations on a disordered free-electron-gas structure.

We would like to emphasize that, even though we will be mainly targeting electronic transport, the derived results are in fact a lot more general as they only rely on wave

scattering in the diffusive regime. We will be only making use of the fact that two-lead subsystems of the full system have an eigenvalue distribution that is given by Eq. (6.1). This distribution, however, is generally obtained for wave transport in random media in the diffusive regime, thus our results, for example, also apply for classical (e. g., acoustic and optical) waves [208].

6.2 Model calculations for many-lead diffusive systems

6.2.1 Method

A relatively simple model that captures the effects in a multi-lead diffusive system, and which we will study in this section, is a "star-shaped" three-terminal device, which is shown in Fig. 6.1(a). We model it using the open-mode approximation in which we assume that the individual building blocks, i. e., the spoke segments of the star behave like diffusive two-terminal conductors, thus, their scattering matrices are well described by the transmission-eigenvalue distribution of Eq. (6.1). The eigenvectors corresponding to these transmission eigenvalues are assumed to be fully random, corresponding to the unitary symmetry class[1]. To construct such matrices, we make use of the polar decomposition of the scattering matrix [193, 207, 210],

$$S = \begin{pmatrix} U & 0 \\ 0 & V \end{pmatrix} \begin{pmatrix} -\sqrt{1-\mathcal{T}} & \sqrt{\mathcal{T}} \\ \sqrt{\mathcal{T}} & \sqrt{1-\mathcal{T}} \end{pmatrix} \begin{pmatrix} U' & 0 \\ 0 & V' \end{pmatrix}, \tag{6.2}$$

where U, V, U', and V' are unitary matrices and $\mathcal{T}$ is a diagonal matrix that contains the transmission eigenvalues of S. This decomposition is always possible for unitary matrices. For the special case of the spoke-scattering matrices, S_S, we assume U, V, U', and V' to be random matrices drawn from the circular unitary ensemble, which corresponds to the assumption of completely random eigenvectors. The eigenvalues of S_S, which enter the matrix $\mathcal{T}$, are taken to be drawn from the probability distribution for two-terminal diffusive systems, Eq. (6.1). This distribution has the peculiar property that it cannot be normalized on the interval $[0, 1]$ because of the non-integrable divergence at zero. Therefore, as is commonly done, we introduce a cutoff t_min at low transmissions such that the integral is normalized on the reduced interval,

$$\int_{t_\mathrm{min}}^{1} dt\, p(t) = \int_{t_\mathrm{min}}^{1} dt\, \frac{T}{2} \frac{1}{t\sqrt{1-t}} = 1 \tag{6.3}$$

$$\rightarrow\ t_\mathrm{min} = \left[\cosh\left(\frac{1}{T}\right)\right]^{-2}. \tag{6.4}$$

This cutoff depends on the choice of the parameter T of the distribution but it will be close to 0 for small T. From this one deduces that the parameter T is directly

[1] The eigenvalue distribution for a wire in the diffusive limit has been found to be independent of the symmetry class of the system [209], which is why we do not expect a strong change of our results when considering other symmetry classes.

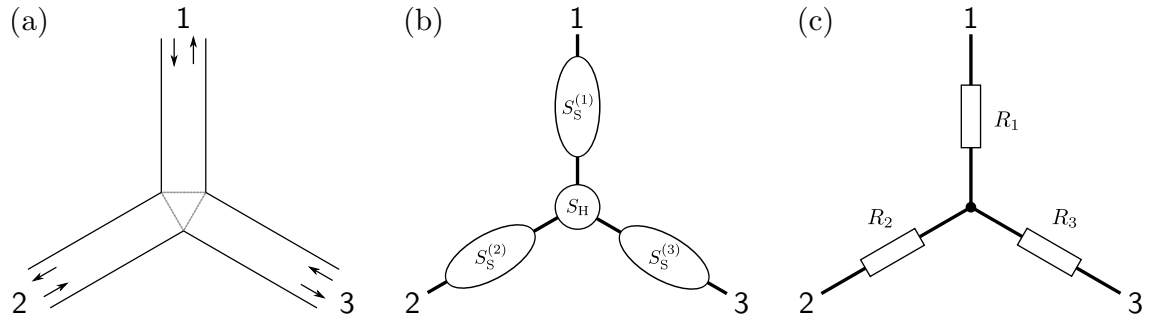

Figure 6.1: (a) shows a sketch of the device, which we want to model: a star-shaped junction of three long diffusive conductors. The joint in the middle is assumed to be small compared to the lengths of the spokes. (b) shows the implementation of this device in terms of scattering matrices, where $S_S^{(i)}$ are scattering matrices for the diffusive spoke sections and S_H is a matrix that models the central hub. (c) shows an equivalent circuit for our diffusive device. As diffusive conductors behave like ohmic resistors in terms of their transmission, the circuit can be used to work out the expectation value of the transmission for our device.

proportional to the transmission expectation value for small T as

$$\langle t \rangle = \int_{t_{\min}}^{1} dt\, t\, p(t) = \int_{t_{\min}}^{1} dt\, \frac{T}{2} \frac{1}{\sqrt{1-t}} \tag{6.5}$$

$$= T\sqrt{1-t_{\min}} \approx T \quad \text{for } t_{\min} \ll 1. \tag{6.6}$$

This limit of small transmission probability per channel combined with a large number of total channels is where the diffusive theory is expected to give a realistic description of the real-world situation. By tuning the parameter T in a range which does not leave this window of validity, we model star geometries with different total resistances but also asymmetric stars with spokes of different resistance, e. g., due to different lengths. The setup of scattering matrices used to represent such devices is schematically shown in Fig. 6.1(b).

The central hub of the star is modeled by a scattering matrix that links the scattering matrices of the spokes. We assume that this link does not cause any extra reflection on top of the built-in reflection of the spokes, which we believe is a realistic scenario if the extent of the hub is small compared to the length of the spokes. In this way, the whole system can be also understood in terms of the equivalent circuit shown in Fig. 6.1(c), in which three resistors are arranged in a star. We choose the following scattering matrix for the central hub, S_{H},

$$S_{\mathrm{H}} = \begin{pmatrix} r_{\mathrm{H},1} & t_{\mathrm{H},12} & t_{\mathrm{H},13} \\ t_{\mathrm{H},21} & r_{\mathrm{H},2} & t_{\mathrm{H},23} \\ t_{\mathrm{H},31} & t_{\mathrm{H},32} & r_{\mathrm{H},3} \end{pmatrix} = \begin{pmatrix} \mathbf{0} & \bar{\mathbf{1}} & \underline{\mathbf{1}} \\ \underline{\mathbf{1}} & \mathbf{0} & \bar{\mathbf{1}} \\ \bar{\mathbf{1}} & \underline{\mathbf{1}} & \mathbf{0} \end{pmatrix}, \tag{6.7}$$

where $\bar{\mathbf{1}} = \mathrm{diag}\,(1,0,1,\dots)$ and $\underline{\mathbf{1}} = \mathrm{diag}\,(0,1,0,\dots)$ are diagonal matrices with alternating ones and zeros, and $\mathbf{0}$ is a matrix that contains only zeros. The dimensionality of these matrices is given by the number of modes in the connected spoke, N, which

we assume to be the same for all spokes. This matrix fulfills the requirement of zero reflection. Also, with this choice, all spokes are linked such that the incoming flux from one lead is split equally between the other two spokes. Still, it might seem quite arbitrarily chosen in the way that certain modes are fully linked to certain terminals. However, we should keep in mind that it is coupled to spokes whose eigenmodes are random vectors. Therefore, we believe that the detailed mode structure of the central hub should not be too much of importance.

For later calculations, it is advantageous to group two of the spokes into one meta lead and to rewrite Eq. (6.7) to read

$$S_{\mathrm{H}} = \begin{pmatrix} r_{\mathrm{H}} & t'_{\mathrm{H}} \\ t_{\mathrm{H}} & r'_{\mathrm{H}} \end{pmatrix}, \tag{6.8}$$

with

$$r_{\mathrm{H}} = (\mathbf{0}), \tag{6.9}$$

$$t'_{\mathrm{H}} = \begin{pmatrix} \bar{\mathbf{1}} & \underline{\mathbf{1}} \end{pmatrix}, \tag{6.10}$$

$$t_{\mathrm{H}} = \begin{pmatrix} \underline{\mathbf{1}} \\ \bar{\mathbf{1}} \end{pmatrix}, \tag{6.11}$$

$$r'_{\mathrm{H}} = \begin{pmatrix} \mathbf{0} & \bar{\mathbf{1}} \\ \underline{\mathbf{1}} & \mathbf{0} \end{pmatrix}. \tag{6.12}$$

To calculate the total transmission through the structure and to study the individual transmission-matrix subblocks and their eigenvalues, we combine the scattering matrices using the general formula [211],

$$S_{I+II} = \begin{pmatrix} r_I + t'_I r_{II} \left(1/(\mathbf{1} - r'_I r_{II})\right) t_I & t'_I \left(1/(\mathbf{1} - r_{II} r'_I)\right) t'_{II} \\ t_{II} \left(1/(\mathbf{1} - r'_I r_{II})\right) t_I & r'_{II} + t_{II} r'_I \left(1/(\mathbf{1} - r_{II} r'_I)\right) t'_{II} \end{pmatrix}, \tag{6.13}$$

for the total scattering matrix of two scatterers (described by scattering matrices with block entries r_i, t_i, r'_i, and t'_i with $i \in \{I, II\}$ respectively) in series. We do this step by step, starting by connecting the scattering matrix of spoke 1, $S_{\mathrm{S}}^{(1)}$, to the central hub scattering matrix, S_{H}, for which we use the representation of Eq. (6.8), yielding

$$S_{(1)\&\mathrm{H}} = \begin{pmatrix} r_{(1)} & t'_{(1)} t'_{\mathrm{H}} \\ t_{\mathrm{H}} t_{(1)} & r'_{\mathrm{H}} + t_{\mathrm{H}} r'_{(1)} t'_{\mathrm{H}} \end{pmatrix}, \tag{6.14}$$

with $r_{(1)}$, $t_{(1)}$, $r'_{(1)}$, and $t'_{(1)}$ being the subblocks of $S_{\mathrm{S}}^{(1)}$. From this we obtain the total scattering matrix of the star structure by using Eq. (6.13) to combine $S_{(1)\&\mathrm{H}}$ with $S_{(2)\&(3)}$, a scattering matrix that is composed from the uncoupled subblocks of $S_{\mathrm{S}}^{(2)}$ and $S_{\mathrm{S}}^{(3)}$,

$$S_{(2)\&(3)} = \begin{pmatrix} r_{(2)} & \mathbf{0} & t'_{(2)} & \mathbf{0} \\ \mathbf{0} & r_{(3)} & \mathbf{0} & t'_{(3)} \\ t_{(2)} & \mathbf{0} & r'_{(2)} & \mathbf{0} \\ \mathbf{0} & t_{(3)} & \mathbf{0} & r'_{(3)} \end{pmatrix}. \tag{6.15}$$

The total result of this combination is given by

$$S_{\mathrm{tot}} = \begin{pmatrix} r_1 & t_{12} & t_{13} \\ t_{21} & r_2 & t_{23} \\ t_{31} & t_{32} & r_3 \end{pmatrix}, \tag{6.16}$$

where, e. g.,

$$r_1 = r_{(1)} + t'_{(1)} t'_{\mathrm{H}} \begin{pmatrix} r_{(2)} & 0 \\ 0 & r_{(3)} \end{pmatrix} \frac{1}{1 - \left(r'_{\mathrm{H}} + t_{\mathrm{H}} r'_{(1)} t'_{\mathrm{H}}\right) \begin{pmatrix} r_{(2)} & 0 \\ 0 & r_{(3)} \end{pmatrix}} t_{\mathrm{H}} t_{(1)}, \tag{6.17}$$

and

$$t_{21} = \begin{pmatrix} t_{(2)} & 0 \end{pmatrix} \frac{1}{1 - \left(r'_{\mathrm{H}} + t_{\mathrm{H}} r'_{(1)} t'_{\mathrm{H}}\right) \begin{pmatrix} r_{(2)} & 0 \\ 0 & r_{(3)} \end{pmatrix}} t_{\mathrm{H}} t_{(1)}, \tag{6.18}$$

$$t_{31} = \begin{pmatrix} 0 & t_{(3)} \end{pmatrix} \frac{1}{1 - \left(r'_{\mathrm{H}} + t_{\mathrm{H}} r'_{(1)} t'_{\mathrm{H}}\right) \begin{pmatrix} r_{(2)} & 0 \\ 0 & r_{(3)} \end{pmatrix}} t_{\mathrm{H}} t_{(1)}. \tag{6.19}$$

The other entries of S_{tot} can also be calculated from the above formula or can simply be recovered by symmetry arguments, e. g., r_2 can also be calculated from Eq. (6.17) by exchanging the components for spoke one and two, in combination with a flip of the primed and non-primed components for the two spokes, e. g., $r_{(1)} \to r'_{(2)}$, as well as an exchange of $\bar{\mathbf{1}} \leftrightarrow \underline{\mathbf{1}}$ in the involved hub matrices. However, the stated expressions will be enough for the discussion in this chapter.

6.2.2 Model results for a fully symmetric star

Using these formulas, we calculate the transmission between two spokes, i. e., Eq. (6.18), using randomly sampled diffusive scattering matrices. We start by considering the simplest case, in which we choose the transmission expectation values for all three spokes to take the same value, $T_{(1)} = T_{(2)} = T_{(3)} = T$. Probability distribution functions for the eigenvalues t of $t_{21}^{\dagger} t_{21}$ for different values of T are shown in Fig. 6.2(a) [see Fig. 6.2(c) for the legend]. Of course, an increase of the transmission T of the spokes leads to an increased probability for higher transmission eigenvalues. Thus, for better comparison, we renormalize the probability distributions by dividing by the expectation value of the transmission. These normalized distributions are shown in Fig. 6.2(c). In this way, we can nicely compare their shape and we find that we see a clear cutoff, which is slightly moving with a change of the spoke transmission and tends to disappear (to move toward 1) in the limit of very low transmission. However, the general shape of the probability distribution functions is very similar in a wide range of transmissions. This fact is also reflected by the shot-noise power that is expected for this transmission-eigenvalue distribution. Shot noise in a multi-terminal system is generally not so easy to interpret. Nonetheless, as detailed in Section 5.A.2, it can also be used as a tool to probe the second moment of

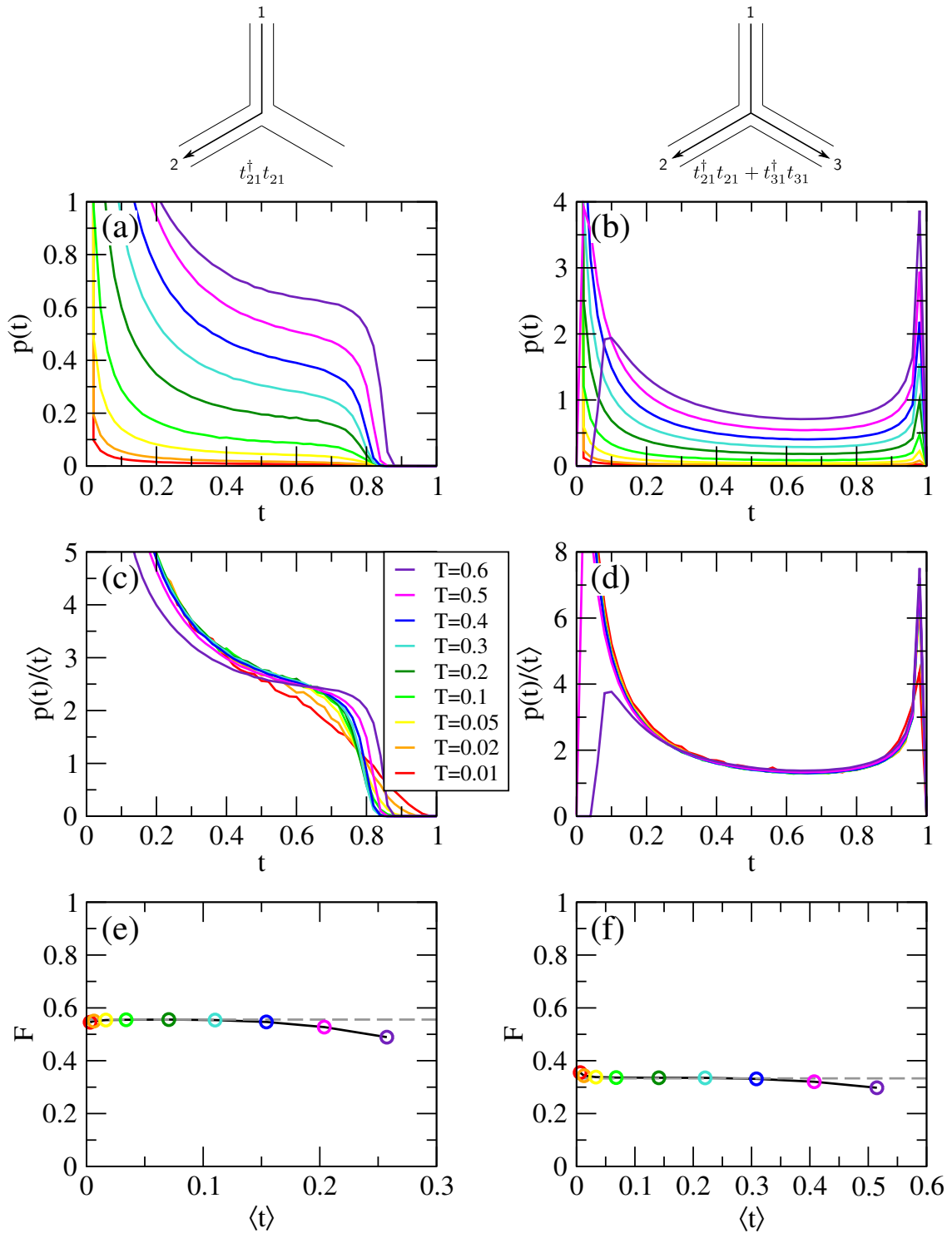

Figure 6.2: (a) and (b) show numerical results for the discussed scattering-matrix model for the transmission eigenvalues of a three-spoke star-shaped diffusive system, where (a) shows the eigenvalues of the transmission matrix between two leads $t_{21}^\dagger t_{21}$ and (b) shows the transmission eigenvalues for the transmission from one lead into a meta lead consisting of the two other leads $t_{21}^\dagger t_{21} + t_{31}^\dagger t_{31}$. (c) and (d) show the same data as (a) and (b) but renormalized by dividing by the expectation value of the transmission per channel. In this way, it is easier to compare the shape and one sees the prominent cutoff in the transmission between two terminals and the bimodal shape for the transmission into the meta lead. (e) and (f) show the calculated Fano factors for the respective scenarios. The gray dashed lines show the corresponding expected values, $F = \frac{5}{9}$ for the transmission between two terminals and $F = \frac{1}{3}$ for the diffusive bimodal distribution. The data was obtained from calculations with 300 channels per lead averaged over 20000 samples (50000 samples for $T < 0.1$).

the transmission-eigenvalue distribution if a proper measurement scheme is used. In particular, one can use this scheme to experimentally access the Fano factor,

$$F = \frac{\langle S \rangle}{2e \langle I \rangle} = \frac{\langle t(1-t) \rangle}{\langle t \rangle}, \tag{6.20}$$

which directly relates to the first and second moment of the transmission-eigenvalue distribution. We use our computed distribution functions in Fig. 6.2(a) to calculate the Fano factor according to Eq. (6.20), the result of which is shown in Fig. 6.2(e). It remains very constant with the change of the total transmission. The attained value of F agrees very well with the prediction for the shot noise in such star-shaped devices by Sukhorukov et al. [212, 213]. In this reference, shot noise in star-shaped multi-lead devices is treated very generally using a semiclassical Boltzmann-Langevin equation. It follows from this treatment that the Fano factor in such a device is given by

$$F = \frac{2}{3} \frac{T_2}{T_2 + T_3} \left(1 + \frac{2T_3}{T_1 + T_2 + T_3} \right), \tag{6.21}$$

which simplifies to $F = \frac{5}{9}$ for $T_1 = T_2 = T_3 = T$. This value for F is indicated by a dashed gray line in Fig. 6.2(e) and is very well reached in our data at least in the regime where the diffusive theory is expected to be applicable. For the larger transmissions per spoke ($T > 0.4$), we will see that we are already leaving this regime of validity.

It is instructive to also have a look at the transmission-eigenvalue distribution of the total transmission matrix that is found when we consider lead 2 and 3 as one "meta lead". This combination, which was previously introduced only as a trick to simplify the concatenation of scattering matrices, actually leads to very interesting results. Mathematically, this corresponds to studying the eigenvalues of the matrix that results from the sum of the two transmission matrices for the separate leads, $t_{21}^\dagger t_{21} + t_{31}^\dagger t_{31}$. The probability distribution of the eigenvalues of this matrix is shown in Fig. 6.2(b), again for different choices of T. If we, similar to before, plot a distribution that is renormalized by the total transmission, as shown in Fig. 6.2(d), we nicely see that almost all distributions trace out the same curve, which is exactly the discussed bimodal distribution function that is expected for a two-terminal diffusive device, Eq. (6.1). This is a very interesting feature that we already observed in Chapter 5: If one studies a diffusive multi-terminal device, then the transmission-eigenvalue distribution for the transmission between two leads generally displays a cutoff and looks not at all bimodal. But when combining the leads to meta leads such that there are only two (meta) leads in total, the transmission-eigenvalue distribution between this pair of leads seems to reproduce the known two-lead transmission-eigenvalue distribution. This agrees well with the finding of Nazarov [214], who finds the distribution for a diffusive two-lead device to be independent of the detailed shape of the conductor. As we can observe in the transmission-distribution functions in Fig. 6.2(d), for high transmissions ($T > 0.4$), the low-transmission cutoff $t_{\min}$ is already strongly visible in this bimodal distribution, so one should consider these to be already outside the regime of validity of the diffusive theory. The fact that one obtains a bimodal distribution is, of course, also reflected by an evaluation of the Fano factor from this distribution, cf. Eq. (6.20). The result of

this is shown in Fig. 6.2(f). We see that it agrees well with the expected value for a two-terminal diffusive wire, in which $F = \frac{1}{3}$ [197]. However, this fact should not be given too much experimental significance as it would probably be very difficult to measure the shot noise in such a meta lead.

6.2.3 Model results for an asymmetric star

One can learn more about the origin of the cutoff feature by turning to a device which is slightly more complicated, this being an asymmetric star, in which the transmission of one of the spokes differs from the transmission of the other two, $T_1 \neq T_2 = T_3$. Such a setup is sketched at the bottom of Fig. 6.3 for various choices of the asymmetry. We define such a geometry in terms of two parameters, one being the expected total transmission between spoke 1 and one of the other two spokes, $T^{2\leftarrow 1}$, which according to the equivalent circuit shown in Fig. 6.1(c) has the following relation with the transmission-expectation values of the spokes[2]:

$$T^{2\leftarrow 1} = \frac{1}{2}\frac{T_1\,(T_2+T_3)}{T_1+T_2+T_3}. \tag{6.22}$$

The other parameter, q, tunes the aspect ratio of the device between the two extreme cases that one of the two spokes is very short ($T_1 = 1$) and the other two are long, which corresponds to $q = 0$, and the scenario where one spoke is long and the other two are short ($T_2 = T_3 = 1$) corresponding to $q = 1$. The meaning of q is also illustrated in the lower panel of Fig. 6.3. We implement this parametrization in terms of $T^{2\leftarrow 1}$ and q by the following choice of T_1, T_2 and T_3:

$$T_1 = \frac{2T^{2\leftarrow 1}}{q}, \tag{6.23}$$

$$T_2 = T_3 = \frac{T^{2\leftarrow 1}}{1-q}. \tag{6.24}$$

From Eq. (6.21), one finds for the Fano factor for the shot-noise measurement in lead 2 in such a device:

$$F = \frac{1}{3}\,(1+q)\,, \tag{6.25}$$

thus, as seen in the symmetric device, it solely depends on the aspect ratio of the structure and is independent of the total transmission. Note that the completely symmetric aspect ratio that was discussed in the previous section corresponds to the choice $q = \frac{2}{3}$ (not $q = \frac{1}{2}$) in this parametrization. The case $q = \frac{1}{2}$ describes a geometry in which there is one shorter spoke and two longer spokes where the equivalent resistance of the two longer spokes in parallel equals the resistance of the shorter spoke.

In Fig. 6.3, we see results for calculations of an asymmetric star for which the total conductivity is roughly kept constant. This data is calculated using the spoke transmis-

[2]We approximate $\langle t\rangle \approx T$ in this section as we are limiting ourselves to low transmission expectation values, cf. Eq. (6.6).

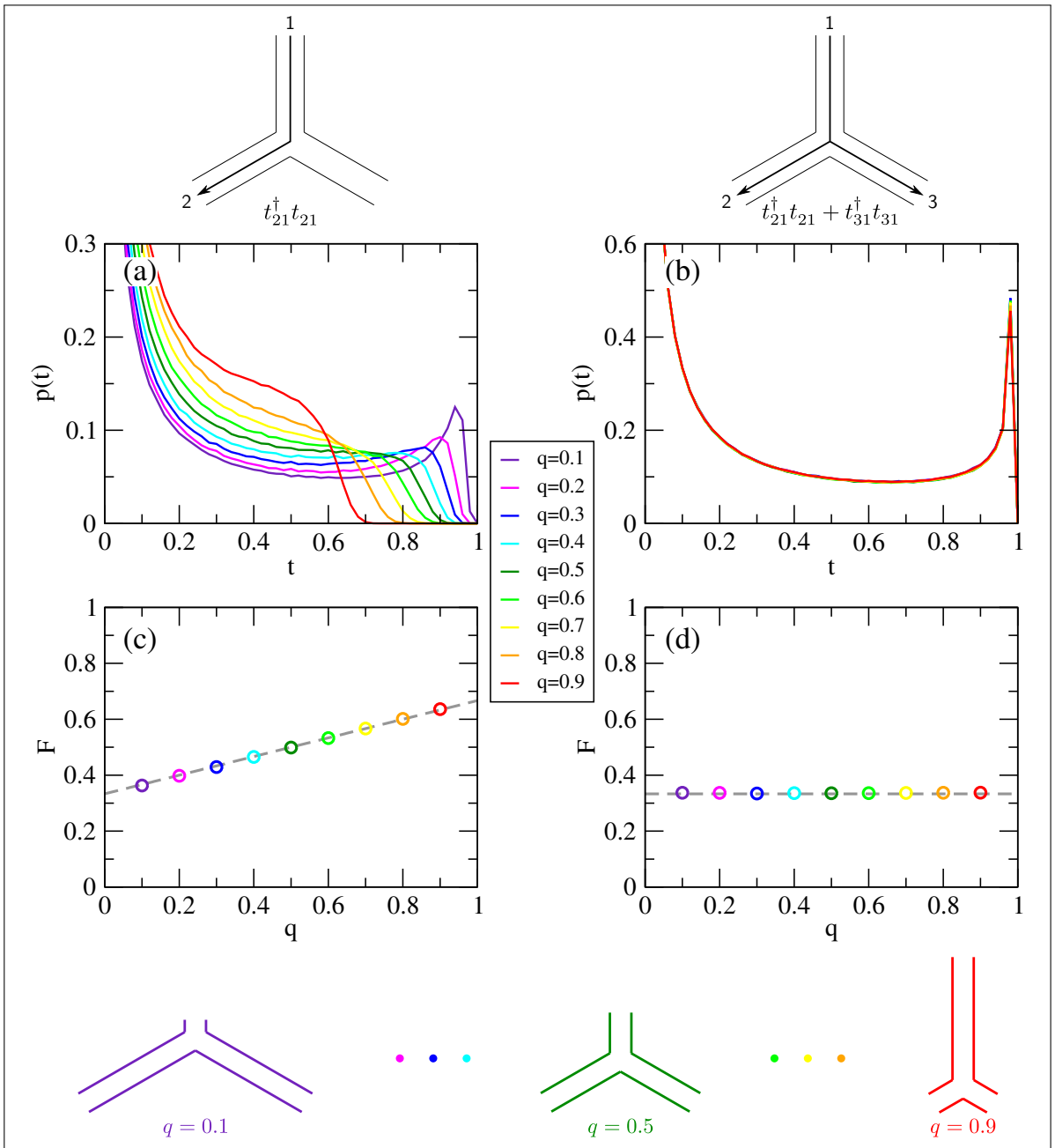

Figure 6.3: The first two panels of this figure show the probability density for the transmission eigenvalues (a) between spoke 1 and 2 (or equally between spoke 1 and 3) $t_{21}^\dagger t_{21}$, and (b) between spoke 1 and a meta lead consisting of the two other spokes $t_{21}^\dagger t_{21} + t_{31}^\dagger t_{31}$. The overall transmission of the structure is kept constant and the relative transmission of spoke 1 is varied compared to the two other spokes, cf. Eqs. (6.23) and (6.24), as well as the illustration at the bottom of the figure. (c) and (d) show the corresponding Fano factors which are calculated from the probability distributions in (a) and (b). In (c), the expectation from a Boltzmann-Langevin prediction, cf. Eq. (6.21), is plotted for comparison as a gray dashed line. The gray dashed line in (d) shows the expected value for a bimodal distribution, cf. Eq. (6.1). The data was obtained from calculations with 300 channels per lead averaged over 20000 samples.

sions from Eqs. (6.23) and (6.24) for a fixed value of $T^{2\leftarrow 1} = \frac{1}{30}$, which is in the regime in which we found good agreement with the Boltzmann-Langevin treatment in the above discussion of the fully symmetric star. It corresponds to the same total transmission as $T_1 = T_2 = T_3 = 0.1$ in the symmetric case. The asymmetry q, however, is varied between the two extreme cases $q = 0$ and $q = 1$. In Fig. 6.3(c), we see the results for the Fano factor calculated from the transmission distribution between lead 1 and lead 2, which is shown in Fig. 6.3(a). We note that the agreement with the expectation from Eq. (6.25), which is shown as a gray dashed line, is very good. With this in mind, it is interesting to look at the full distribution function shown in Fig. 6.3(a). Here, we see that with changing the aspect ratio of the star, there is a strong change in the distribution. In the limit $q \to 1$, there is a pronounced cutoff, which increases with decreasing q and disappears in the limit $q \to 0$. Before we discuss this and aim at explaining this, we would like to draw the attention to Figs. 6.3(b) and (d). In these panels, similar to the results for the symmetric star, we also plot the probability distribution and the Fano factor that result from the study of the transmission from lead 1 to the meta lead that consists of the two other leads. Here, we once again find a behavior which is in perfect agreement with a bimodal distribution, Eq. (6.1), completely independently of the value of q. From a mathematical perspective, this means that the sum of the two matrices $t_{21}^\dagger t_{21} + t_{31}^\dagger t_{31}$ shows a spectrum which follows the bimodal distribution for any q while the separate matrices $t_{21}^\dagger t_{21}$ (or equivalently $t_{31}^\dagger t_{31}$) show a spectrum which depends on the aspect ratio of the structure. While this spectrum of the separate matrices resembles the bimodal shape for small q, it attains a more and more pronounced cutoff in the limit $q \to 1$.

This can be understood a bit better when considering the problem in the $q \to 1$ limit, in which the structure consists of a long channel that is split into two leads, i. e., the spoke-scattering matrices of the spokes 2 and 3 do not give rise to reflection, corresponding to $r_{(2)} = r_{(3)} = r'_{(2)} = r'_{(3)} = \mathbf{0}$. Then the expression for the transmission matrix from Eq. (6.18) simplifies to

$$\lim_{q\to 1} t_{21}^\dagger t_{21} = t_{(1)}^\dagger \underline{\mathbf{1}} t_{(1)}. \tag{6.26}$$

Here, $t_{(1)}$, cf. Eq. (6.2), is a matrix with random eigenvectors and a known distribution of random eigenvalues [the bimodal distribution, Eq. (6.1)], and $\underline{\mathbf{1}}$ can be understood as a projector that selects a subset of rows from $t_{(1)}$. Eigenvalue distributions of such submatrices have been studied before in the context of quantum dots with many leads [215, 216], where—similar to our case—the transmission matrix into one of the leads is given by a projection of a full transmission matrix. Different from our scenario, however, the eigenvalue distribution of the projected matrix in these studies was given by the symmetric bimodal distribution for quantum cavities (the distribution for a two-lead quantum dot). It was also observed that a quantum dot with multiple leads displays a cutoff in the eigenvalue spectrum, very similar to the one observed by us.

Very recently, Goetschy et al. [217] solved the problem of determining the eigenvalue distribution of a filtered random matrix in the form of Eq. (6.26), i. e., $\tilde{A} = PA$, in a more general form using free probability theory [218], which is a suitable method to obtain the probability distribution of eigenvalues in the limit of infinite matrix dimensionality,

$N \to \infty$. This solution can be employed for any eigenvalue distribution $p_{A^\dagger A}(t)$ of the matrix $A^\dagger A$ that is being filtered and it is given in the form of the following implicit system of equations:

$$g_{A^\dagger A}\left(\frac{z g_{\tilde{A}^\dagger \tilde{A}}(z)}{Q(z)}\right) = Q(z), \tag{6.27}$$

with the auxiliary function $Q(z)$ being defined as

$$Q(z) = g_{\tilde{A}^\dagger \tilde{A}}(z) + \frac{m-1}{z}. \tag{6.28}$$

The system of equations relates the *resolvent* $g_{A^\dagger A}(z)$ of the probability distribution of the unfiltered matrix,

$$g_{A^\dagger A}(z) = \int_{-\infty}^{\infty} dt \frac{p_{A^\dagger A}(t)}{z-t}, \tag{6.29}$$

to the resolvent of the filtered matrix $g_{\tilde{A}^\dagger \tilde{A}}(z)$, from which one can infer the probability density of the eigenvalues of $\tilde{A}^\dagger \tilde{A}$ using

$$p_{\tilde{A}^\dagger \tilde{A}}(t) = -\frac{1}{\pi} \lim_{\eta \to 0^+} \operatorname{Im} g_{\tilde{A}^\dagger \tilde{A}}(t + i\eta). \tag{6.30}$$

The parameter m in Eq. (6.28) represents the fraction of the number of channels that are retained by the projection. Thus, this can be employed for our problem by setting $A = t_{(1)}$ and $\tilde{A} = \underline{\mathbf{1}} t_{(1)}$, which implies $m = \frac{1}{2}$. We can calculate the resolvent for the unfiltered matrix A by evaluating Eq. (6.29) using the bimodal distribution, Eq. (6.1), yielding

$$g_{A^\dagger A}(z) = \frac{1}{z} - \frac{T}{z\sqrt{1-z}} \operatorname{artanh}\left(\frac{\tanh\left(\frac{1}{T}\right)}{\sqrt{1-z}}\right). \tag{6.31}$$

Using this one can now numerically search for a solution of Eqs. (6.27) and (6.28), and use it in Eq. (6.30) to extract the resulting probability distribution of the filtered matrix. This was already done in Ref. [217] for the case of the diffusive bimodal distribution, and we also show results for such a numerical search in Fig. 6.4 for various choices of the parameter T of the distribution, which controls the expectation value of the transmission, cf. Eq. (6.6).

However, for small T, the system of equations, Eqs. (6.27) and (6.28), also allows for an analytical solution (see Section 6.A.1 for a derivation),

$$p_{\tilde{A}^\dagger \tilde{A}}(t) = \begin{cases} \frac{T}{2} \frac{1}{t\sqrt{1-\frac{t}{m}}} + \mathcal{O}(T^2) & m\left[\cosh\left(\frac{1}{T}\right)\right]^{-2} \leq t \leq m \\ 0 + \mathcal{O}(T^2) & \text{else,} \end{cases} \tag{6.32}$$

which was not noticed in Ref. [217], and which will become important when we try to understand the behavior of the asymmetric star in other limits of the asymmetry

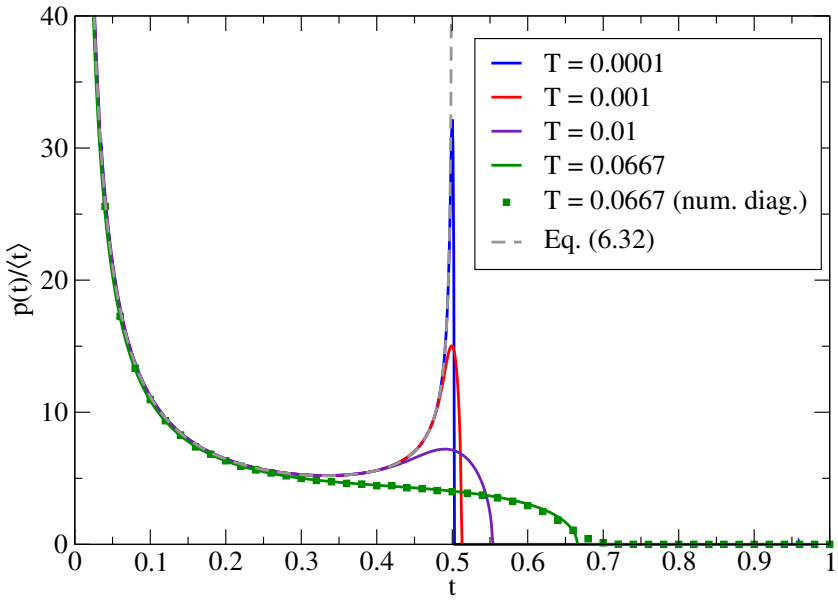

Figure 6.4: The plot shows the numerical solution of Eqs. (6.27) and (6.28) for different values of the transmission T (full lines). For low transmissions, the distribution converges toward the analytical solution from Eq. (6.32) (gray dashed line). For $T = 0.0667$, the square symbols show results obtained from a numerical diagonalization of filtered matrices (with dimension $N = 300$) with random eigenvectors and bimodal eigenvalues. This matrix-diagonalization result corresponds to the calculation for $q = 0$ in the open-mode scattering-matrix approach for the asymmetric star shown above. The shown data from the diagonalization is an average over 20000 realizations.

parameter q. This limiting solution has the form of a rescaled bimodal distribution with a sharp cutoff at $t = m$. It is also shown as a gray dashed line in Fig. 6.4 and we see that it indeed matches the numerical solutions in the limit $T \to 0$. However, we also note that the total transmission for which we find good agreement with this rescaled bimodal distribution has to be very low. For larger values of T, the solution differs from the asymptotic form by the absence of the second peak close to the cutoff and by a significant shift of the cutoff to higher transmissions. The numerical solution for $T = \frac{2}{30}$ for example, which is the proper transmission for $q = 1$ in the above treatment of the asymmetric star, is still comparatively far from this limiting behavior. However, it already shows a pronounced cutoff. The free probability theory can also be compared to a numerical diagonalization of the projected matrix, thus, to a calculation similar to the one that yielded the data in Fig. 6.3. The result of this is shown for $T = \frac{2}{30}$ as square symbols. As one can see, the agreement to the "analytical" result is already quite good showing that free probability theory, which is valid in the limit of infinite matrix dimension, also applies well in the case of a moderate number of channels as studied in the numerical calculation ($N = 300$). Small deviations appear only close to the cutoff, which is less pronounced in the calculations with finite matrices.

The limiting distribution, which shows the second peak close to the cutoff, is probably difficult to observe in practice as it requires a very low average transmission per channel, $T \lesssim 0.001$, in combination with a very large number of channels such that the total transmission is well above one conductance quantum such that the system is in the

applicable range of the diffusive regime. However, it is conceptually insightful as it has a quite intuitive interpretation, which we will discuss in the next section and which will be a source of inspiration for explaining the behavior in other limits.

Before doing so, we stop for a short summary of the main results of this section. We saw that the cutoff that is seen in the transmission-eigenvalue probability density of the asymmetric star is particularly prominent in the $q = 1$ limit, in which there is one long spoke which is connected to two short leads. In this limit, the eigenvalue distribution can be formally viewed as stemming from a matrix with a bimodal eigenvalue distribution from which some columns have been projected out. The emergence of such a cutoff due to projection was already observed in other studies, e. g., it is not expected to be particular to the diffusive bimodal distribution but it could also be found for chaotic cavities with many leads. In the $q = 0$ limit, on the other hand, we find that the cutoff tends to disappear and we seem to recover the original bimodal distribution, something that is so far just an observation. We will be able to explain this in the next section. For intermediate values of q, we observe a continuous transition between the two limiting cases, which also makes the appearance of the cutoff in the fully symmetric star plausible. However, as we will also see in the next section, this cutoff for the fully symmetric star is expected to disappear in the $T \to 0$ and $N \to \infty$ limit.

6.2.4 Analytical treatment in the low-transmission limit

In this section, we want to rederive the probability distribution that one expects in the $q = 1$ limit at very low transmissions, Eq. (6.32), using a partly heuristic argument. As we will see, this argument will also transfer to the $q = 0$ case and will even allow us to make a good guess for the fully symmetric star. To be able to make this argument, however, we will start out by some general remarks, which we expect to hold for all values of the parameter q.

As we saw in the discussion above, the matrix of the total transmission to the combined meta lead $t_{21}^\dagger t_{21} + t_{31}^\dagger t_{31}$ always shows a bimodal distribution for all transmissions. For the special case of $q = 1$, this can even be formally shown as in this limit

$$\lim_{q\to 1}\left(t_{21}^\dagger t_{21} + t_{31}^\dagger t_{31}\right) = t_{(1)}^\dagger \left(\underline{\mathbf{1}} + \bar{\mathbf{1}}\right) t_{(1)} = t_{(1)}^\dagger t_{(1)} = U'^\dagger \mathcal{T} U', \tag{6.33}$$

as can be seen from Eqs. (6.18) and (6.19). Here, $\mathcal{T}$ is a diagonal matrix with bimodally distributed eigenvalues and U' is a random unitary matrix, cf. Eq. (6.2). Because of the special shape of the bimodal distribution, in the limit of very low transmission, almost all eigenvalues of this matrix are very close to zero but there is still a relatively large probability to find eigenvalues close to one. Such "open channels" are known to carry most of the current in the diffusive regime [206, 219].

Knowing that the matrices $t_{21}^\dagger t_{21}$ and $t_{31}^\dagger t_{31}$, for which we observe the cutoff, sum up to yield a matrix with the bimodal distribution, we can make use of this fact to learn something about their eigenvalues from a mathematical perspective. We will restrict this attempt to the limit in which the transmission is so low that one can assume that $t_{21}^\dagger t_{21} + t_{31}^\dagger t_{31}$ only has one non-zero eigenvalue. In this limit, we will be using the following inequality which is one of the few known inequalities that relate the eigenvalues of a sum

of Hermitian matrices to the eigenvalues of the summand matrices [220]:

Theorem 6.1 (**Dual Lidskii inequality**)**.** Given two n-dimensional Hermitian matrices A and B with the sequences of eigenvalues $\lambda_1(A) \geq \cdots \geq \lambda_n(A)$ and $\lambda_1(B) \geq \cdots \geq \lambda_n(B)$, respectively. Let $\lambda_1(A+B) \geq \cdots \geq \lambda_n(A+B)$ be the eigenvalue sequence of the sum of the two matrices. Then,

$$\begin{aligned}\lambda_{i_1}(A+B) + \cdots + \lambda_{i_k}(A+B) \geq \lambda_{i_1}(A) + \cdots + \lambda_{i_k}(A) \\ + \lambda_{n-k+1}(B) + \cdots + \lambda_n(B),\end{aligned} \tag{6.34}$$

for every set of integers $1 \leq i_1 < \cdots < i_k \leq n$.

By choosing $i_j = j+1$ for $j = 1, \ldots, n-1$, we find

$$\begin{aligned}\lambda_2(A+B) + \cdots + \lambda_n(A+B) \geq \lambda_2(A) + \cdots + \lambda_n(A) \\ + \lambda_2(B) + \cdots + \lambda_n(B),\end{aligned} \tag{6.35}$$

which implies that $\lambda_i(A) = \lambda_i(B) = 0$ for all $i \geq 2$ if $\lambda_i(A+B) = 0$ for all $i \geq 2$. So, in the limit that $t_{21}^\dagger t_{21} + t_{31}^\dagger t_{31}$ only has one non-zero eigenvalue, the matrices $t_{21}^\dagger t_{21}$ and $t_{31}^\dagger t_{31}$ will also just have one non-zero eigenvalue each. As the traces of the matrices are additive, those eigenvalues will be simply related by

$$\lambda_1(t_{21}^\dagger t_{21} + t_{31}^\dagger t_{31}) = \lambda_1(t_{21}^\dagger t_{21}) + \lambda_1(t_{31}^\dagger t_{31}), \tag{6.36}$$

which in turn implies that the three matrices also share the same eigenvector(s). So suppose that v is the eigenvector of $t_{21}^\dagger t_{21} + t_{31}^\dagger t_{31}$ that corresponds to the largest eigenvalue, which from a physical point of view means that it is the superposition of incoming modes that leads to a transmission of $\lambda_1(t_{21}^\dagger t_{21} + t_{31}^\dagger t_{31})$ from the incoming lead to the meta lead consisting of the two outgoing leads. Then the same superposition of incoming modes will lead to a transmission $\lambda_1(t_{21}^\dagger t_{21})$ to lead 2 and $\lambda_1(t_{31}^\dagger t_{31})$ to lead 3 respectively. Another interesting physical interpretation of the fact that the eigenvalues of the three matrices are the same is found when calculating the superposition of outgoing modes that one will observe at the leads 2 and 3 when choosing the incoming modes according to v. This vector of outgoing modes can be directly obtained from v by the application of t_{tot}, the transmission matrix into the meta lead,

$$t_{\mathrm{tot}} v = \begin{pmatrix} t_{21} v \\ t_{31} v \end{pmatrix}. \tag{6.37}$$

This vector is $2N$-dimensional (because of $2N$ outgoing modes) and we see that the squared modulus of the first N components of this vector,

$$v^\dagger t_{21}^\dagger t_{21} v = \lambda_1(t_{21}^\dagger t_{21}), \tag{6.38}$$

equals the eigenvalue of the transmission matrix into this lead. So, in the low-transmission limit, one can gain information about how the vector $t_{\mathrm{tot}} v$, which carries the transmission

into the meta lead, is distributed across lead 2 and lead 3 by comparing the eigenvalue of the full matrix, $\lambda_1(t_{21}^\dagger t_{21} + t_{31}^\dagger t_{31})$, with the eigenvalues of the transmission matrices into the leads, e. g., $\lambda_1(t_{21}^\dagger t_{21})$.

These relations hold for a single realization of random matrices, but what do they imply for the relation between the probability distributions $p_{t_{21}^\dagger t_{21}}(t)$ and $p_{t_{21}^\dagger t_{21}+t_{31}^\dagger t_{31}}(t)$? To quantify this, we introduce a function $w(r,t)$ that describes the probability for an eigenvalue t of the full matrix $t_{21}^\dagger t_{21} + t_{31}^\dagger t_{31}$ to split into the two eigenvalues rt and $(1-r)\,t$ of the two summand matrices. Because of the symmetric choice of our junction, we know that $w(r,t) = w(1-r,t)$. Given this function, we have the following relation between the probability densities $p_{t_{21}^\dagger t_{21}+t_{31}^\dagger t_{31}}(t)$ and $p_{t_{21}^\dagger t_{21}}(t)$:

$$p_{t_{21}^\dagger t_{21}}(t) = \int_0^1 dt' \int_0^1 dr\, w(r,t')\, p_{t_{21}^\dagger t_{21}+t_{31}^\dagger t_{31}}(t')\, \delta\left(rt' - t\right) \tag{6.39}$$

in the limit where Eq. (6.36) holds. According to the above discussion, the function $w(r,t)$ also carries information about how the vector $t_{\mathrm{tot}}v$ is distributed across the two outgoing leads. It can generally be calculated as

$$w(r,t) = \left\langle \delta\left(r - \frac{v^\dagger t_{21}^\dagger t_{21} v}{v^\dagger \left(t_{21}^\dagger t_{21} + t_{31}^\dagger t_{31}\right) v} \right) \right\rangle, \tag{6.40}$$

where v is the eigenvector corresponding to the eigenvalue t and the brackets indicate the average over the random-matrix ensemble. Note that this definition quantifies the amount of the outcoming flux into sublead 2 for an incoming superposition of modes that matches the eigenvector v to the eigenvalue t of the matrix $t_{21}^\dagger t_{21} + t_{31}^\dagger t_{31}$. Therefore, we will in the following call $w(r,t)$ *eigenvector-splitting distribution*. As we discussed above, in the low-transmission limit, this function can also be viewed as an eigenvalue-splitting distribution into the subleads as we found that the matrices $t_{21}^\dagger t_{21}$ and $t_{21}^\dagger t_{21} + t_{31}^\dagger t_{31}$ share the same eigenvector v in this limit. Away from the low-transmission limit, this will no longer be the case, and the function $w(r,t)$ as defined in Eq. (6.40) does not necessarily describe the splitting of eigenvalues. This is understandable as the relation between the eigenvalues of the summand matrices and those of the total sum matrix is usually not just given by a pairwise sum. Instead the relation may be much more involved, as partly expressed by the Dual Lidskii inequality stated above. The function $w(r,t)$ as we define it still has physical meaning even when going away from the low-transmission limit as it describes the transmission pattern of the eigenvectors of the transmission matrix into the meta lead. This pattern is a well-defined quantity, which is at least in principle also experimentally accessible, and we will consider it in our later numerical studies.

We would like to add that even if the relation in Eq. (6.40) can formally only be derived for the case of only one non-zero eigenvalue, we also expect it to be valid for our case when the system is in the "dilute limit" where the number of non-zero eigenvalues is larger than one but the total dimension of the scattering matrix is very large such that the density of non-zero eigenvalues is almost zero. In this way, the relation becomes useful in the true diffusive limit, where $N \cdot \langle t \rangle > 1$, i. e., there is more than one open channel, but in which at the same time the density of non-zero eigenvalues is very low

because $\langle t \rangle \ll 1$.

In the $q = 1$ limit, we can derive an analytical expression for $w(r,t)$ as we know that all the eigenvectors of $t_{21}^\dagger t_{21} + t_{31}^\dagger t_{31}$ are just columns of a random circular unitary matrix $U'^\dagger$ in this limit, cf. Eq. (6.33). This also applies to the vector v, i. e., $U'v = e^{i\phi}v$. The function $w(r,t)$ is then simply given by

$$w(r,t) = \left\langle \delta\left(r - \sum_{i=1}^{N} V_{1,2i}^\dagger V_{2i,1}\right)\right\rangle, \tag{6.41}$$

in the derivation of which we made use of Eqs. (6.2), (6.18), and (6.19). Thus, in this case, the function $w(r,t)$ is related to the average sum of the squared absolute values of half the components of a single column vector of a CUE matrix. Also, we note that $w(r,t)$ does not depend on the eigenvalue t in this case. Even though the components of a column of a CUE matrix are not fully independent because of the normalization constraint, for $N \gg 1$, we may well treat them as independent in this context. The following expectation values for moments of the entries of a circular unitary matrix V_{ij} of dimension $2N \times 2N$ are known [221]:

$$\left\langle |V_{ij}|^2 \right\rangle = \frac{1}{2N}, \tag{6.42}$$

$$\left\langle |V_{ij}|^4 \right\rangle = \frac{1}{N(2N+1)}, \tag{6.43}$$

from which one deduces $\mathrm{Var}\left(|V_{ij}|^2\right) \approx \frac{1}{(2N)^2}$. From that, due to the central limit theorem, for large N, it follows that

$$w(r,t) = \frac{N}{\sqrt{\pi}} \exp\left(-N^2\left(r - \frac{1}{2}\right)^2\right) \tag{6.44}$$

$$\to \lim_{N\to\infty} w(r,t) = \delta\left(r - \frac{1}{2}\right), \tag{6.45}$$

which shows that for $q = 1$, at low transmissions and in the limit of large N, the eigenvectors and also the eigenvalues always split completely equally between the two leads. This may not be too surprising as we already knew from the above analysis that the eigenvectors of $t_{21}^\dagger t_{21} + t_{31}^\dagger t_{31}$ in this limit are random vectors [cf. Eq. (6.33)] for which such a behavior would be expected. However, it is interesting when considering that this eigenvector splitting also holds for the eigenvectors of the "open channels", i. e., the channels that carry a transmission close to one into the meta lead made out of lead 2 and 3. Because of the equal splitting, even these vectors will only lead to a transmission of 0.5 into, for example, sublead 2. This intuitively explains the origin of the hard cutoff of the eigenvalues of $t_{21}^\dagger t_{21}$ at 0.5 in this limit.

However, this result for $w(r,t)$ does not only give an explanation for the cutoff: By inserting this expression for $w(r,t)$ from Eq. (6.45) in Eq. (6.39) and performing the integral, we recover the full expression for the probability density of the transmission eigenvalues in the low-transmission limit, Eq. (6.32), i. e., a rescaled bimodal distribution. Thus, we were able to derive Eq. (6.32) from a study of the eigenvector-splitting distri-

bution $w(r,t)$ in the case of $q=1$. Of course, it would be nice to also obtain results for other values of q. Here, the application of free probability theory in the same spirit as in the $q=1$ limit turns out to be difficult as the formulas become much more involved. However, a heuristic derivation that employs the function $w(r,t)$ is still possible as we will see. Though our line of reasoning will be a bit different than before.

Remember that in the $q=1$ case, we could argue directly how $w(r,t)$ should behave in the low-transmission limit, and then used Eq. (6.39) together with the fact that the probability distribution of the total matrix, $t_{21}^\dagger t_{21} + t_{31}^\dagger t_{31}$, is bimodal to rederive Eq. (6.32). Now we would like to partly invert the argument. We start by recognizing that, in the low-transmission limit, there should be a well-defined function $w(r,t)$ that is directly related to the eigenvalue distribution via Eq. (6.39) and therefore governs all the observables for all values of q. As we already know something about the expected observables in this limit, e. g., the transmission and the Fano factor, cf. Eq. (6.25), we may hope to use this information to learn about the form of $w(r,t)$ and, thus, about the full probability distribution. For example, it can be easily shown that a symmetric choice of $w(r,t) = w(1-r,t)$ that is inserted in Eq. (6.39) leads to

$$\langle t \rangle_{t_{21}^\dagger t_{21}} = \frac{1}{2} \langle t \rangle_{t_{21}^\dagger t_{21} + t_{31}^\dagger t_{31}}, \tag{6.46}$$

as can already be expected from symmetry. A second important observable, the Fano factor, can also be calculated for a general $w(r,t)$. From inserting the bimodal distribution in Eq. (6.39) and from using the definition of the Fano factor, Eq. (6.20), we find

$$F = \frac{\langle t(1-t) \rangle_{t_{21}^\dagger t_{21}}}{\langle t \rangle_{t_{21}^\dagger t_{21}}} \tag{6.47}$$

$$= \int_0^1 dt' \int_0^1 dr\, w(r,t') \frac{1}{2t'\sqrt{1-t'}} \left[t'(1-t') + 2r(1-r)t'^2 \right] \tag{6.48}$$

$$= \int_0^1 dt' \int_0^1 dr\, w(r,t') \frac{r(1-r)t'}{\sqrt{1-t'}} + \frac{1}{3}, \tag{6.49}$$

which yields $F = \frac{2}{3}$ when inserting Eq. (6.45), as expected. In the $q=0$ limit, however, we know that the Fano factor should yield $F = \frac{1}{3}$. As the factor that multiplies $w(r,t')$ in Eq. (6.49) is greater or equal to zero, there is only one possible choice for $w(r,t')$ which can satisfy this, namely,

$$w(r,t') = w(r) = \delta(r) + \delta(r-1). \tag{6.50}$$

In this way, we are in the lucky situation of being able to infer the probability of the splitting of the eigenvalues (and eigenvectors) across the two leads, $w(r,t)$, in the limit of low transmission by only using the knowledge of the value of the Fano factor in this limit, Eq. (6.21). Note that we, as in the $q=1$ limit, find the function $w(r,t)$ to be independent of the eigenvalue t. However, the obtained behavior of the eigenvectors in this limit is completely the opposite compared to the case of $q=1$. Now all eigenmodes of the transmission matrix into the meta lead either fully transmit to one of the leads of the

star, or fully to the other, but never into both. Knowing the probability of an eigenvalue split, we can go one step further and insert this function into Eq. (6.39) to obtain the full probability density of eigenvalues for $q = 0$ in the limit of low transmission,

$$p_{t_{21}^\dagger t_{21}}(t) = \begin{cases} \frac{T}{4}\frac{1}{t\sqrt{1-t}} + \frac{1}{2}\delta(t) & \left[\cosh\left(\frac{1}{T}\right)\right]^{-2} \leq t \leq 1 \\ 0 & \text{else.} \end{cases} \tag{6.51}$$

This probability distribution turns out to be once again the bimodal distribution, this time unshifted. In the interpretation of the numerical results shown in Fig. 6.3, we already speculated that this might be the correct limiting distribution for $q = 0$. Now, we are able to prove it, at least in the low-transmission limit.

It is of course tempting to also make a statement for the low-transmission limit at intermediate values of q. Here, the mere knowledge of the value of the Fano factor is not enough to infer $w(r, t)$. However, knowing that the distribution changes from a delta distribution around $r = \frac{1}{2}$ to delta distributions at $r = 0$ and $r = 1$ with changing values of q, an educated guess for an intermediate distribution would be a completely flat box distribution for all t,

$$w(r, t) = 1. \tag{6.52}$$

It turns out that this distribution yields $F = \frac{5}{9}$, which is the value that we already obtained in the fully symmetric star (corresponding to $q = \frac{2}{3}$). The probability distribution for the eigenvalues that is obtained from this choice of $w(r, t)$ is

$$p_{t_{21}^\dagger t_{21}}(t) = \begin{cases} \frac{T}{2}\left[\frac{\sqrt{1-t}}{t} + \operatorname{artanh}\left(\sqrt{1-t}\right)\right] & \left[\cosh\left(\frac{1}{T}\right)\right]^{-2} \leq t \leq 1 \\ \frac{1}{4}\left(2 + T\sinh\left(\frac{2}{T}\right)\right) & 0 \leq t \leq \left[\cosh\left(\frac{1}{T}\right)\right]^{-2}. \end{cases} \tag{6.53}$$

It seems reasonable to assume that this probability distribution is the expected $N \to \infty$, $T \to 0$ limit for the fully symmetric star, and we will check whether we can back this hypothesis by numerical calculations. Before doing this, we wrap up the findings from the study of the "splitting" of the eigenvectors at low transmissions by visualizing the results in Fig. 6.5. It shows the derived or hypothesized functions for $w(r, t)$ and $p(t)$ for the discussed cases of the extremely asymmetric or the fully symmetric star. In addition, it also shows the expected Fano factor and sketches of the corresponding geometries in the three discussed limiting cases. For the eigenvalue distribution functions, we already saw in the numerical calculations above that the limiting distributions for $p(T)$ for $q = 0$ and $q = 1$ are indeed given by bimodal distributions. For the case $q = \frac{2}{3}$, the fully symmetric star, our numerical observation only showed that the cutoff seemed to disappear in the zero-transmission limit, which would be consistent with the derived analytical result. However, a more thorough numerical check for the validity of the derived expression will be given in the next section.

It is also interesting to discuss the obtained expressions for the eigenvector splitting $w(r, t)$. Notice that we found or assumed $w(r, t) = w(r)$, i. e., independence of t, in the discussed limits. As we saw above, the function $w(r)$ contains information about the eigenvalue and eigenvector splitting in the low-transmission limit. This eigenvector

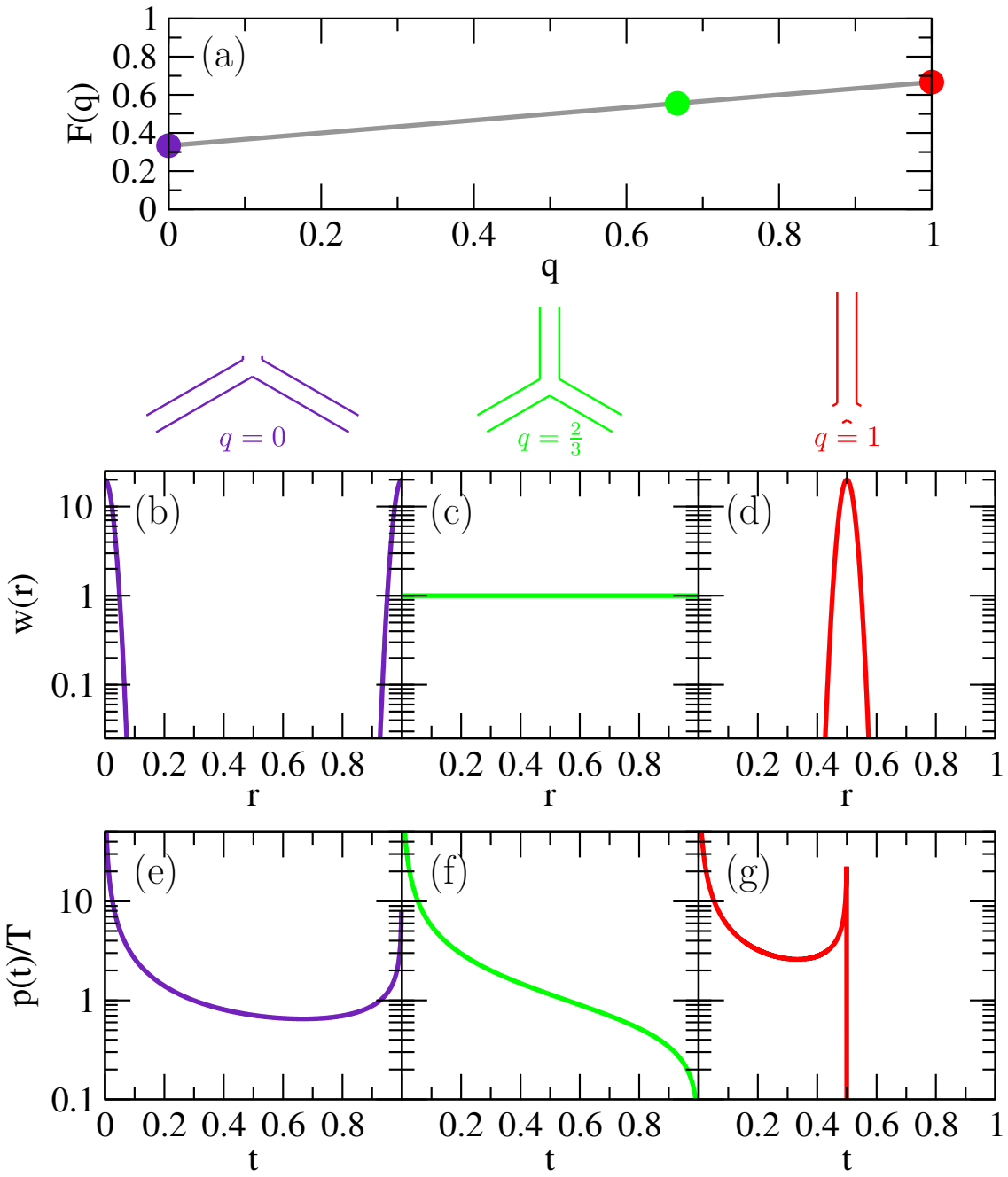

Figure 6.5: The figure shows the analytically derived results for the eigenvector splitting (b)–(d) and the probabitility distributions (e)–(g) in the three discussed limiting cases of the asymmetric star ($q = 0$, $q = \frac{2}{3}$, $q = 1$). The geometries that correspond to these limits are sketched above the panels. The functions plotted in (e)–(g) each correspond to the first rows of Eqs. (6.51), (6.53), and (6.32). Hence, it is assumed that T is so small that the behavior of the distribution close to $t = 0$, i. e., the second rows in the respective equations can be neglected. (a) shows the Fano factor as a function of the asymmetry q, cf. Eq. (6.21), which was used in the derivation of the analytical results.

splitting (even away from the $T \to 0$ limit) may be directly probed experimentally. For this, one would have to control the input channels of one of the spokes, e. g., of spoke 1 of the diffusive device, in such a way that one can fully couple to one of the "open channels" of the device. Such an open channel gives rise to a high transmission into the meta lead consisting of lead 2 and 3. The function $w(r)$ now tells us the likelihood that one would observe an output that is evenly spread across the two subleads [which will always be observed for $w(r)$ as in Fig. 6.5(d)], or whether the output will be either in one or the other sublead [as would be the result for $w(r)$ as in Fig. 6.5(b)]. Even though it is so far difficult to control the coupling to specific channels, it is not impossible as has been demonstrated by a recent experiment using acoustic waves. In this experiment, one achieved the coupling to such an open mode and could thereby observe almost perfect transmission through a diffusively scattering medium [222]. With a similar technique, also direct measurements of $w(r)$ seem to be in experimental reach.

We would like to add that the analytical calculations shown in this section can even be generalized to star-shaped diffusive structures with more than 3 leads. In this limit, one can also obtain generalized analytical expressions in the limiting cases of extreme asymmetry. This is shown in Section 6.4.

6.2.5 Numerical verification of the analytical results

We already saw in the numerical calculations above that the limiting distributions for $p(t)$ for $q = 0$ and $q = 1$ are indeed given by bimodal distributions, which agrees well with the analytical results derived in the last section, i. e., with Eqs. (6.32) and (6.51). In the case of the completely symmetric star, however, the agreement with the analytical result in the $T \to 0$, $N \to \infty$ limit, and thus to the distribution in Eq. (6.53), which is shown in Fig. 6.5(f), was not so clearly observed. For example, most of the calculations for the symmetric star in Fig. 6.2(c) showed a clear cutoff, which is not predicted by the analytical result. However, we at least observed a tendency for this cutoff to disappear at small transmissions. One reason for this poor agreement may be that one has to study really small transmissions to reach the low-transmission limit in which the analytical results are derived. This would at least be compatible with the result from the discussion of Fig. 6.4, where we studied a comparison of the analytical results with numerical calculations in the $q = 1$ limit. However, as the analytical result in the $q = \frac{2}{3}$ case is based on an "educated guess" of the splitting distribution of the eigenvalues $w(r)$, unlike in the case of $q = 1$ or $q = 0$ in which a more serious derivation was possible, we think that a more thorough numerical check is adequate for this symmetric scenario. Therefore, we consider not only the $T \to 0$ but in particular also the $N \to \infty$ limit (the number of channels was kept constant in Fig. 6.2).

For this, we again performed numerical calculations using the scattering-matrix model and extracted the transmission-eigenvalue distribution function $p_{t_{21}^\dagger t_{21}}(t)$ and the function $w(r)$. The eigenvector splitting $w(r)$ is extracted from the eigenvectors of the transmission matrix into the meta lead, as prescribed by Eq. (6.40), i. e., we numerically search for eigenvectors v of $t_{21}^\dagger t_{21} + t_{31}^\dagger t_{31}$ with eigenvalues t and then make histograms of $v^\dagger t_{21}^\dagger t_{21} v/t$. We find that the results for $w(r)$ do not seem to depend on the size of the eigenvalue t, which is why we present averaged results for $w(r)$ over the obtained eigenvalues. This in

good agreement with the analytical derivation in which we assumed that $w(r,t) = w(r)$.

The numerical results of these calculations are shown in Fig. 6.6. As we are now considering much larger matrices and need to take many averages to find sufficient convergence in the limit of low transmissions, we no longer calculated all transmission eigenvalues of the scattering matrix. Instead, we used an iterative diagonalization method which only computes the few largest eigenvalues and the corresponding eigenvectors and used them to extract $p(t)$ and $w(r)$. In this way, one can understand the fact that the obtained probability distributions in Fig. 6.6(b) display a cutoff at small t, which is prominently seen for the eigenvalue distributions for $T = 0.1$ (shown in red). This is simply an artifact of the calculation because we are only looking at the probabilities of the topmost eigenvalues. For our comparison, we found this to be of minor importance as we are mainly interested in the behavior of the distribution of the eigenvalues close to 1, where we previously observed the strongest deviation from the analytical result. This part of the distribution is obtained correctly.

At first sight, Fig. 6.6 may seem confusing as it shows many curves for various choices of N and T. We start by discussing Fig. 6.6(a), i. e., the numerically obtained results for the eigenvector-splitting distribution $w(r)$. Here, we expect a completely flat distribution in the $N \to \infty$, $T \to 0$ limit, which is shown in the plot as a gray dashed line. To judge whether this is compatible with our numerical calculations, it is helpful to first focus on results with a fixed choice of T and varying N. In the plot, such data correspond to curves with the same color but with differing line shapes. Here, we generally find that an increase of N for fixed T leads to a narrower distribution of $w(r)$. This may first seem to contradict our expectation that we obtain a completely flat distribution for $N \to \infty$, and indeed, for fixed T we do not find convergence toward the dashed gray curve. However, we see that curves with fixed T and varying N cross at fixed values of r, which seem to be independent of N. These crossing points have been marked by colored arrows. They suggest that the limiting distributions in the $N \to \infty$ limit for fixed T will also cross these points. This implies that the distributions at fixed T do not become "infinitely-narrow" in the $N \to \infty$ limit. Instead, they will have a non-zero amplitude for all values between the crossing points and it seems likely to us that the limiting distributions for fixed T are box distributions between the marked crossings. Note that the black lines in the figure (the results for $T = 0.001$) also show another crossing at intermediate values of r. However, between these crossing points the scaling with increasing N is exactly opposite such that this observation is also compatible with a limiting box distribution between the two crossings that are marked by arrows in the $N \to \infty$ limit. With this knowledge, the behavior for $T \to 0$ can be inferred from the fact that the crossing points tend to move outward with decreasing T, which convinces us that the limiting distribution in the combined $N \to \infty$, $T \to 0$ limit is indeed given by $w(r) = 1$, at least if the limit is taken in such a way that the system can still be considered to be in the diffusive regime, i. e., $N \cdot T = \text{const.} \gtrsim 1$.

In Fig. 6.6(b), which shows the plot of the transmission-eigenvalue probability distributions in the window close to $t = 1$ for the same choices of N and T, the convergence to the analytical result (shown again as a gray dashed line) is more difficult to observe. Here, we are facing the problem that the statistical convergence is not as good as in Fig. 6.6(a), which is predominantly visible for calculations at low values of T. In Fig. 6.6(a), we

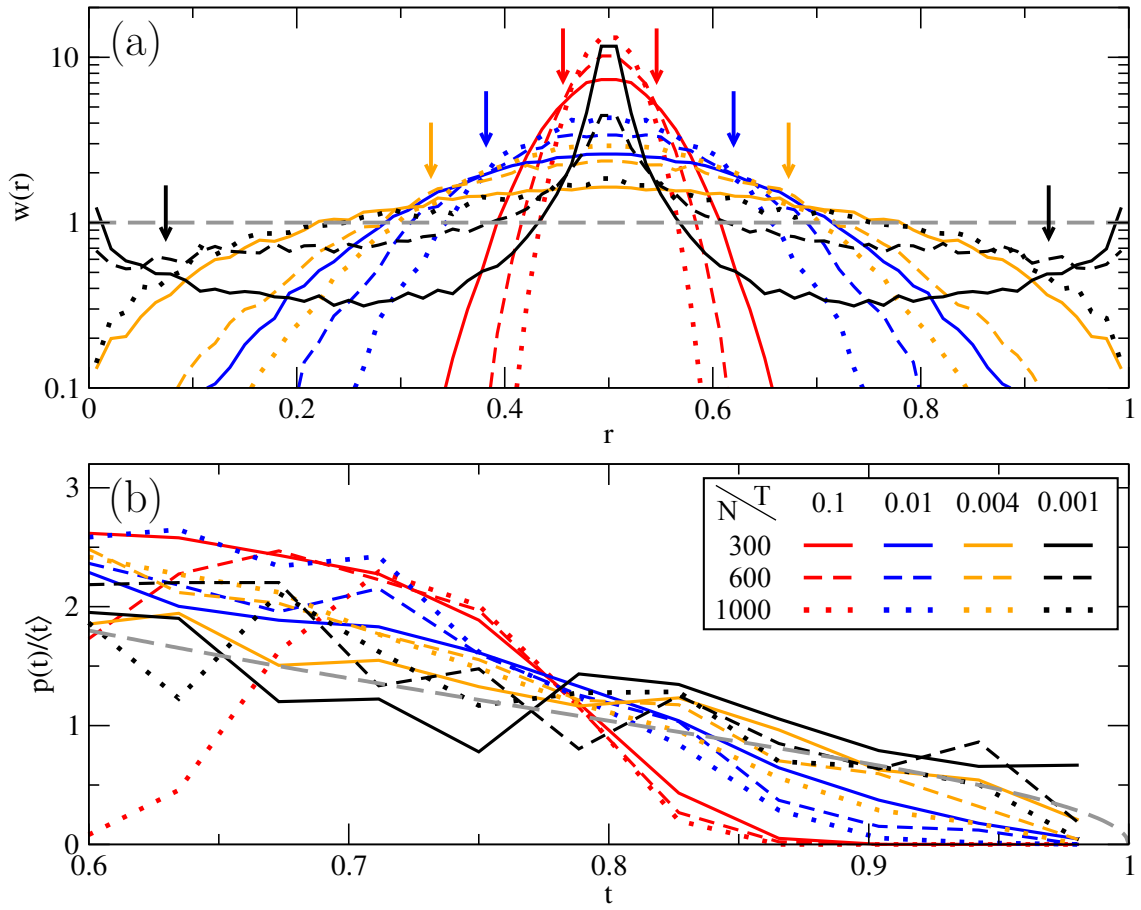

Figure 6.6: The figure shows numerical results obtained using the scattering-matrix model based on the open-mode approximation in a fully symmetric star geometry. In contrast to the data presented in Fig. 6.2, we now explore smaller total transmissions T and also consider a varying number of channels N. (a) shows the numerically obtained eigenvector-splitting distribution $w(r)$ and the analytical expectation in the $N \to \infty$, $T \to 0$ limit, which is shown as a gray dashed line. The results for fixed T and varying N cross at points which are marked by colored arrows. (b) shows the obtained probability distributions of transmission eigenvalues. Here, we also plot the analytical expectation, Eq. (6.53), as a gray dashed line. The shown data for $T \geq 0.01$ is obtained from 5000 configurations. For smaller transmissions, more configurations were used (12000 for $T = 0.004$ and 25000 for $T = 0.001$).

had the advantage that the numerically obtained distributions of $w(r)$ were not seen to depend on the value of the eigenvalue, which is why we presented averaged results over the 10 largest eigenvalues which improved the statistical convergence. For the transmission-eigenvalue distribution such an averaging is not possible and we denote that, especially for $T = 0.001$, more averages would be required. Still, a tendency of convergence toward the gray dashed line can be seen even though it is not so easy to extrapolate to the combined $N \to \infty$, $T \to 0$ limit.

The numerical results presented in Fig. 6.6 are not a thorough proof but we take them as a strong indication that Eqs. (6.52) and (6.53) are the correct limiting distributions for $w(r)$ and $p(t)$ in the true diffusive limit. However, we also note that our numerical calculations presented in Figs. 6.2 and 6.3 are still far away from this limit. In the symmetric-star scenario that we investigated above, we saw that this in particular also holds for the eigenvector splitting $w(r)$. It is therefore interesting to study the numerically obtained behavior for $w(r)$ in other limits. Therefore, using the method we sketched above, we extracted $w(r)$ from the scattering-matrix calculations of the asymmetric star that we discussed in Section 6.2.3 and for which the corresponding plots for $p(t)$ are shown in Fig. 6.3(a). The extracted results are shown in Fig. 6.7. We find a slightly surprising result: a splitting that looks very much like a Gaussian distribution with a maximum of the amplitude at 0.5, thus a distribution which always favors the completely equal splitting of the eigenvectors. This should be compared to the analytical expectations in the low-transmission limit, which are sketched in Figs. 6.5(b)–(d). For $q \to 1$, the distribution roughly matches our expectation in the low-transmission limit, where we expect a sharp peak at equal distribution. However, for $q \to 0$, the low-transmission limit prediction is to find a distribution that shows two sharp peaks around $r = 0$ and $r = 1$, very different from what we observe in Fig. 6.7. Here, we should remind ourselves that the numerical calculations do not yet reach this very-low-transmission limit for which $w(r)$ also describes the splitting of the eigenvalues. Instead, it is likely that the numerical calculations are done in a regime where the eigenvectors of $t_{21}^\dagger t_{21}$ and $t_{21}^\dagger t_{21} + t_{31}^\dagger t_{31}$ do not yet agree. For example, in the limit of high transmissions, we would expect the eigenvectors of the two matrices to be completely independent, and therefore we would expect the eigenvector splitting of the full transmission matrix that is described by $w(r)$ to converge to that of completely random eigenvectors, where one expects a Gaussian distribution, cf. Eq. (6.44). What we observe is something between these two limiting cases: a distribution that is roughly Gaussian and which broadens for smaller values of q. The main message from this is that one needs to study systems at very low average transmission if one wants to see the eigenvector correlations $w(r)$ that we derived in Section 6.A.1 in experiments.

6.3 Numerical study of a diffusive three-spoke star

So far, we exclusively studied diffusive transport using the open-mode approximation introduced in Section 6.2.1. In this section, we want to compare the results obtained using this approximation to full wave-transport calculations to see whether this can be considered a good description for the diffusive transport in a star-shaped structure. The

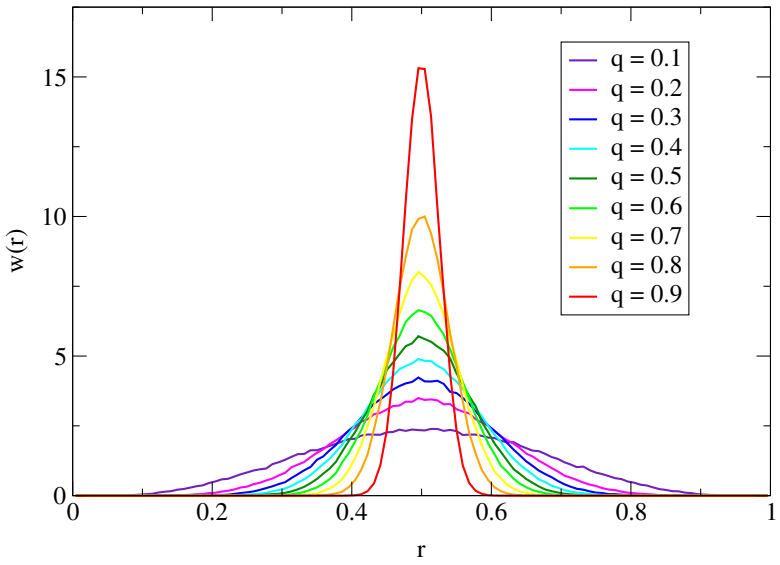

Figure 6.7: The figure shows the numerically extracted eigenvector-splitting distributions for an asymmetric star (the asymmetry being controlled by q) using the random scattering-matrix calculations in the open-mode approximation. This is the same set of calculations that was used to extract the probability densities for the transmission eigenvectors which are shown in Fig. 6.3.

numerical results that we present in this section were computed by Viktor Krückl using the transport framework by Michael Wimmer [100]. As a simple model for transport in the diffusive regime, a quadratic Hamiltonian,

$$H = -\partial_x^2 - \partial_y^2 + V(\mathbf{x}), \tag{6.54}$$

was used. It was discretized with a lattice constant $a = 1$, and on-site disorder from the interval $V_{\text{dis}} \in [-W, W]$ was added to tune the system into the diffusive regime. The considered geometry is star-shaped, very similar to the sketch in Fig. 6.1(a), with a transverse extent of the leads of ≈ 750 lattice sites and a length-to-width ratio of the spokes of ≈ 7. At the chosen Fermi energy of $E_{\text{F}} = 1$, this gives rise to 252 transverse modes per spoke. In Fig. 6.8, we see numerical results for different choices of the disorder strength in a fully symmetric star. They are presented in a similar fashion as the model results from the open-mode approximation shown in Fig. 6.2. In general, the obtained normalized transmission-eigenvalue probability distributions that are shown in Fig. 6.8(a) and the Fano factors, Fig. 6.8(c), agree well with their counterparts of the open-mode scattering-matrix calculation, Figs. 6.2(c) and (e). The agreement is particularly good for $0.2 \leq W \leq 0.3$, where the obtained distributions are very similar to the calculations for $0.1 \leq T \leq 0.4$ in Fig. 6.2(c). For this choice of the disorder strength, we also see that the obtained probability distribution for the eigenvalues of the transmission into the meta lead, Fig. 6.8(b), matches the bimodal distribution, Eq. (6.1), which is shown as a gray dashed line. For smaller disorder, $W = 0.1$, the agreement with the open-mode approximation is still good, e. g., when comparing to the calculation with $T = 0.6$ in Fig. 6.2(c), however, at these disorder strengths the system cannot be considered to be in the diffusive regime as can be seen from the obtained value of the Fano factor, which

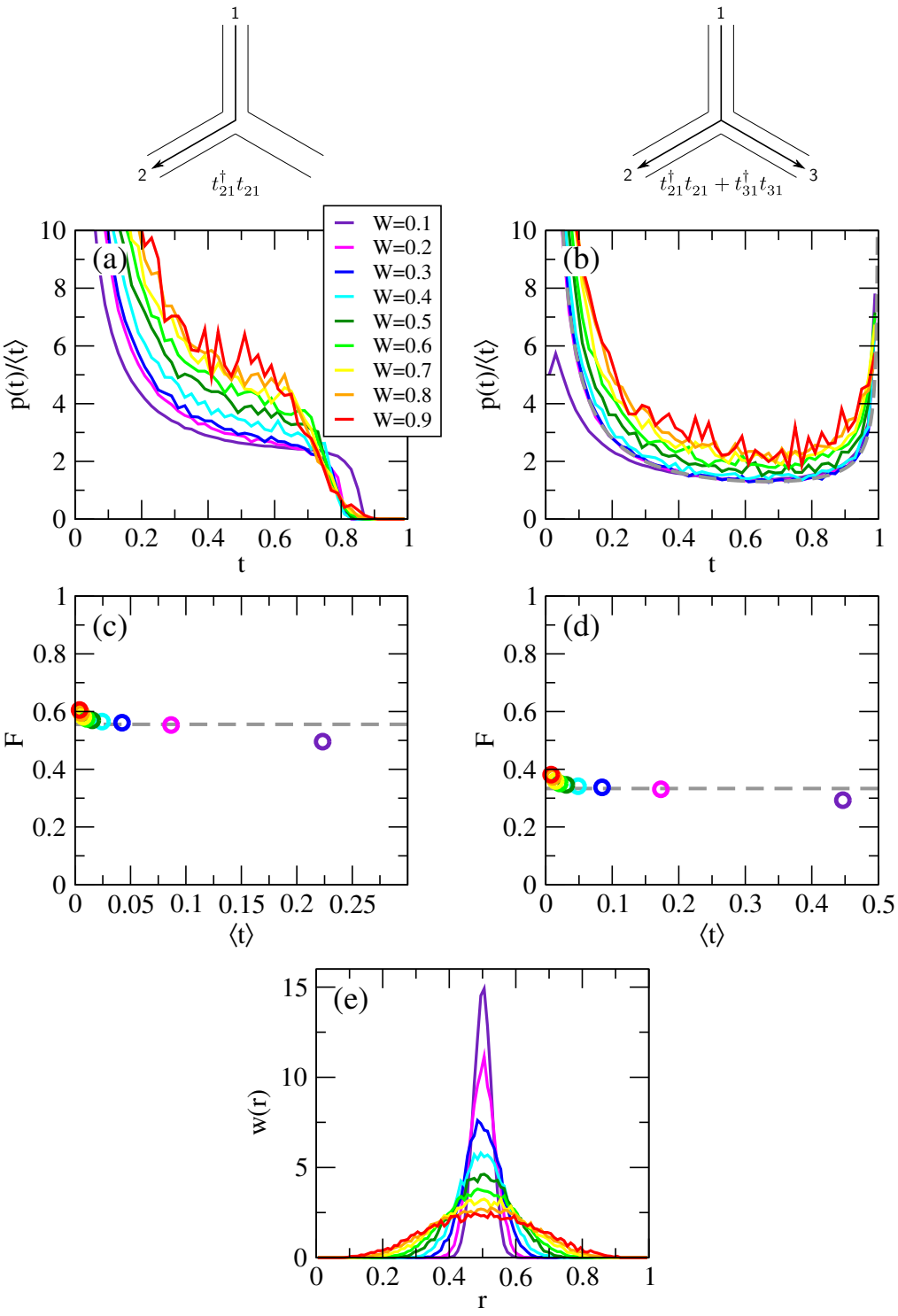

Figure 6.8: Transport results for a diffusive fully symmetric star, which were obtained using the recursive Green's function method to study transport in a system with a quadratic Hamiltonian with on-site disorder, cf. Eq. (6.54). The different colors denote different disorder strengths W. (a) and (b) show the obtained probability densities of the transmission eigenvalues of the transmission matrix between spokes 1 and 2, $t_{21}^\dagger t_{21}$, and of the transmission matrix into the meta lead consisting of spokes 2 and 3, $t_{21}^\dagger t_{21} + t_{31}^\dagger t_{31}$. The distributions are normalized by the average transmission per channel, the gray dashed line shows the bimodal distribution that is expected in the two-terminal case. (c) and (d) show the Fano factors that are obtained from the probability distributions in (a) and (b) as a function of the transmission per channel. The gray dashed line shows the expectation from Boltzmann-Langevin theory, $F = \frac{5}{9}$ and $F = \frac{1}{3}$. (e) shows the numerically calculated eigenvector-splitting distribution. The shown results are disorder averages over 1000 disorder configurations.

is well below the expected value of $F = \frac{5}{9}$ in this case. For very strong disorder, we see that there is a tendency that the agreement between the model and the numerical transport calculations becomes worse, which is particularly noticeable in the probability distribution of the transmission eigenvalues into the meta lead, Fig. 6.8(b), where we start to see stronger deviations from the bimodal distribution. Also, the value of the Fano factor starts to increase and to depart from the expectation in the diffusive limit when going to very low transmissions. This is perfectly understandable as the system starts to enter the localized regime, in which the transmission-eigenvalue distribution function is known to deviate from the bimodal shape, Eq. (6.1), even in the two-terminal case. Instead, in the limit of a very strongly localized system, one expects to see a phenomenon known as "crystallization of the eigenvalues", i. e., one expects an eigenvalue probability distribution function which is only finite in the vicinity of certain transmissions that are regularly spaced on a logarithmically scaled axis (similar to particles in a 1d crystal)[3]. The highest of these transmissions dominates the transport properties of the system and this eigenvalue exponentially decreases upon an increase of the length of the system, thus leading to the expected localization phenomenon. Such a distribution also gives rise to a Fano factor of 1 as expected for a system with a very low transmission probability, which explains the increase of the Fano factor at very low transmissions in Fig. 6.8(c). While the full wave-transport calculations are able to capture this change of the distribution in the strongly localized regime, this is not possible for the open-mode scattering-matrix model, in which we from the start assumed that the spoke-scattering matrices always have a transmission-eigenvalue distribution which is given by Eq. (6.1). This also explains why, in the model, we do not observe the increase of the Fano factor for very low transmissions in Fig. 6.2(e). As we are mainly interested in the behavior in the diffusive regime, this does not bother us very much. We want to emphasize that this does not imply that it is impossible to study diffusive systems at low average transmission per channel $\langle t \rangle$, which is anyway the limit in which we found interesting analytical results. However, to study such systems, one has to make sure that the number of channels N is large enough, $N \cdot \langle t \rangle \gg 1$, so that the system does not localize. In the full wave-transport calculations, it is computationally very costly to consider systems with a much larger number of transverse channels than what was used in the presented results ($N = 252$). However, as we saw from the scattering-matrix model, one would require $\langle t \rangle < 0.001$, i. e., $N \gg 1000$ to enter the limit in which we could derive the analytical results. Knowing that the transport calculations scale unfavorably with respect to the number of transverse channels ($\propto N^3$), we realize that it is currently practically impossible to see these analytical results explicitly in a full wave-transport calculation. Still, from the fact that the full wave-transport calculation agrees well with the scattering-matrix model in the range where the transport is diffusive, we are confident to assume that they also agree for lower average transmissions if one studied more transverse channels. In experiments, it may actually be possible to realize systems with a very high number of transverse channels and a very low average transmission, such that they can still be considered to be in the diffusive regime where our analytical results apply.

In line with this argument, the numerical results for the eigenvector splitting in the

[3] as discussed in Refs. [223, 224]. For a plot of such a distribution, see for example Ref. [225].

wave-transport calculation, Fig. 6.8(e), are consistent with the results of the scattering-matrix model, cf. results for $N = 300$ in Fig. 6.6(a), in the range where the system is still diffusive but they also do not show the completely flat distribution, Eq. (6.52), which is expected at very low transmission.

We also analyzed asymmetric star structures using full wave-transport calculations, the result of which is shown in Fig. 6.9. This was implemented by explicitly changing the geometric length of the spokes in the scattering geometry, e. g., building a structure with one short and two long spokes. To compare with the model calculations in Fig. 6.3, this was done in such a way that the transmission expectation value between two spokes stays roughly constant (it varies from $\langle t \rangle = 0.018$ to $\langle t \rangle = 0.010$ over the full range of asymmetries). In principle, one should be able to derive the asymmetry q from the geometry using Eqs. (6.23) and (6.24), in which one should insert the transmissions of all the spokes, which scale reciprocally with their lengths. However, in practice, this turns out to be not so easy as the numerical calculation unavoidably also has a hub region of non-zero extent which also contributes a finite resistance and complicates the analysis. We therefore took a more pragmatic approach to estimate q: We determined the Fano factor from the calculated transmission-eigenvalue distribution between two spokes, Fig. 6.9(b), and used the relation Eq. (6.25) to obtain a rough estimate for q, which we used to label the curves in Fig. 6.9. In the calculation, we set the disorder strength to $W = 0.75$, which in hindsight turned out to be maybe a bit too strong as we see that the eigenvalue distribution function for the transmission matrix into the meta lead in Fig. 6.9(b) already significantly deviates from the bimodal distribution, which is shown as a gray dashed line. Thus, the system is already slightly starting to localize, which is also signaled by the slightly increased Fano factor for the transmission into the meta lead, which is shown in the inset of Fig. 6.9(b). Still, we find that the agreement of the transmission-eigenvalue distributions in Fig. 6.9(a) with the model results for the asymmetric star, Fig. 6.3(a), is very good.

Qualitatively, a good agreement is also found for the comparison of the eigenvector-splitting distributions in Fig. 6.9(c) with the model results shown in Fig. 6.7. However, in detail the agreement between the two is not perfect which may be due to the fact that the system in the wave-transport calculations already shows signs of localization. Also, we should take into account that the number of channels in the two setups is not exactly the same and we saw in Fig. 6.6(a) that a change of N does influence the detailed shape of $w(r)$.

In summary of this section, we established that the results of the full wave-transport calculations are in good agreement with the scattering-matrix model based on the open-mode approximation, at least if the wave transport is safely in the diffusive regime, i. e., $\langle t \rangle \ll 1 \ll N \cdot \langle t \rangle$. At the very low average transmissions which are necessary to find good agreement with the derived analytical results, the number of transverse channels that is required to keep the system in the diffusive regime is too large to be numerically feasible for the full wave-transport calculations, which is why those results could not be explicitly verified. However, as the agreement in the diffusive regime is good, we have no reason to assume that this should no longer be the case for lower average transmissions. We are therefore confident that the obtained results in the open-mode approximation do apply to wave transport in realistic systems.

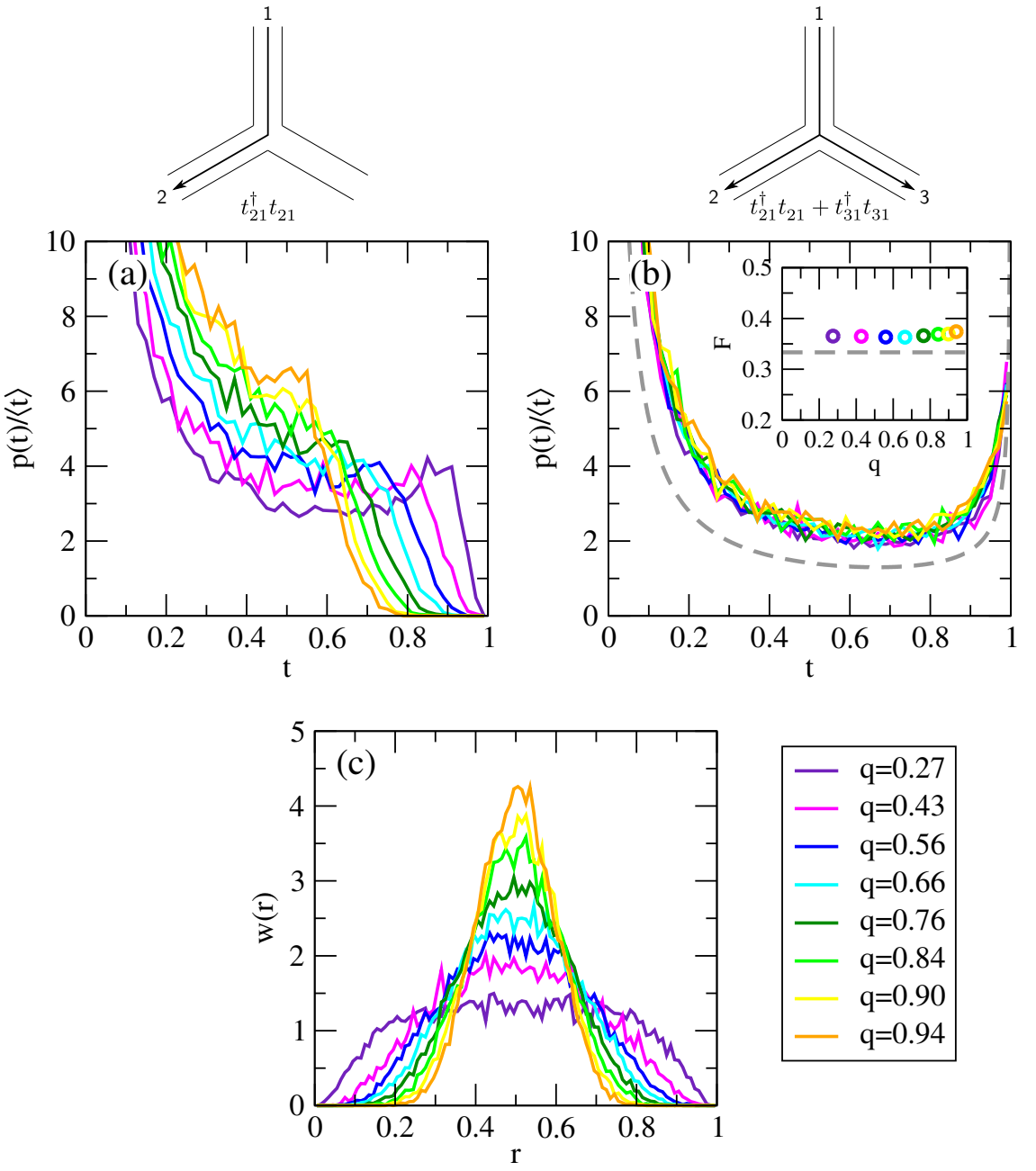

Figure 6.9: The figure shows results from the full-wave transport calculations for an asymmetric star geometry, using the Hamiltonian of Eq. (6.54) and including on-site disorder with an amplitude of $W = 0.75$. The calculations, which are performed for different star geometries, are labeled by the asymmetry parameter q. This parameter was calculated from Eq. (6.25) using the obtained Fano factor for the transmission between two leads. (a) shows the probability distribution for the eigenvalues of the matrix $t_{21}^\dagger t_{21}$, which describes the transmission between two leads. This data is normalized by the transmission expectation value $\langle t \rangle$. (b) shows the same quantity for the matrix $t_{21}^\dagger t_{21} + t_{31}^\dagger t_{31}$, which describes the transmission into the meta lead consisting of leads 2 and 3. The inset of (b) shows the obtained Fano factor from the distributions in (b) in comparison to the expectation for a diffusive two-lead device which is shown as a gray dashed line. (c) shows the extracted eigenvector-splitting distribution, which was computed as an average of the splittings from the largest 10 eigenvectors of the matrix $t_{21}^\dagger t_{21} + t_{31}^\dagger t_{31}$. The shown results are disorder averages over 1000 disorder configurations.

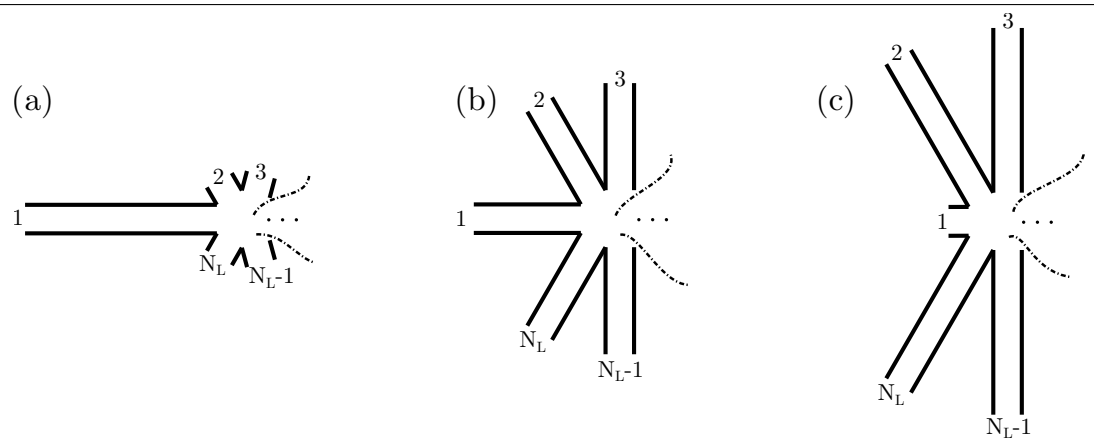

Figure 6.10: This figure shows the geometries of the N_L-spoke generalizations of the three discussed cases in Section 6.2.4, which are sketched in Fig. 6.5. (a) shows the analogue of the $q = 1$ case with one very long spoke and $N_\mathrm{L} - 1$ short spokes. (b) shows the analogue of $q = \frac{2}{3}$ with N_L spokes of equal length. (c) shows the analogue of $q = 0$ with one short and $N_\mathrm{L} - 1$ long spokes.

6.4 Generalization to star geometries with N_L spokes

The analytical results that we derived in the low-transmission limit of the asymmetric diffusive star geometry with 3 spokes can be generalized to star geometries with N_L spokes. Here, one would again consider three different cases, which are sketched in Fig. 6.10. The limit in which one spoke is very long and all the others are short, cf. Fig. 6.10(a), can again be mapped to a random matrix projection as discussed in Section 6.2.3. Then the result for the probability distribution for the transmissions from the lead attached to spoke 1 to any other lead is immediately given by Eq. (6.32) when choosing $m = \frac{1}{N_\mathrm{L}-1}$, thus

$$p(t) = \begin{cases} \frac{T}{2} \frac{1}{t\sqrt{1-(N_\mathrm{L}-1)t}} & \frac{1}{(N_L-1)\left[\cosh\left(\frac{1}{T}\right)\right]^2} \leq t \leq \frac{1}{N_\mathrm{L}-1} \\ 0 & \text{else.} \end{cases} \tag{6.55}$$

It can equally be derived using Eq. (6.39) when choosing the following eigenvector splitting:

$$w(r,t) = w(r) = \delta\left(r - \frac{1}{N_\mathrm{L}-1}\right), \tag{6.56}$$

which also matches the expectations from the knowledge that the eigenvectors are columns of random matrices from the circular unitary ensemble in this limit. Moreover, the value of the Fano factor, which can be calculated from the probability distribution in Eq. (6.55), yields

$$F = 1 - \frac{2}{3\,(N_\mathrm{L}-1)}, \tag{6.57}$$

which matches the expectation from Boltzmann-Langevin theory [213]. From this theory, it can be easily shown that a star with N_L leads should give rise to a Fano factor of

$$F = \frac{(N_\mathrm{L}-1)\,\alpha_2}{(1-\alpha_1)}\left(1-\frac{2}{3}\,(\alpha_1+\alpha_2)\right), \tag{6.58}$$

with $\alpha_i = \frac{T_i}{\sum_n T_n}$ being the transmission of the i-th spoke divided by the sum of all spoke transmissions. Here, we implicitly assumed that the Fano factor is extracted from a noise measurement in lead 2 (S_{22}) and an applied bias in lead 1, see also Section 5.A.2. It therefore probes the second moment of the probability distribution for the eigenvalues $p_{t_{21}^\dagger t_{21}}(t)$. For the simple case of three leads, it simplifies to Eq. (6.21). For the splitting scenario in an N_L-spoke star that we just discussed, cf. Fig. 6.10(a), one obtains Eq. (6.57) from Eq. (6.58) by setting $\alpha_1 = 0$ (spoke 1 has a high resistance) and $\alpha_2 = \frac{1}{N_\mathrm{L}-1}$ (all other spokes are equally perfectly conducting). Thus, all the results can be consistently generalized to this limit.

If spoke 1 is very short and all other spokes are long, cf. Fig. 6.10(c), we can use a similar line of reasoning as outlined in Section 6.2.4 and argue that only the following eigenvector splitting

$$w(r,t) = w(r) = \frac{2\,(N_\mathrm{L}-2)}{N_\mathrm{L}-1}\delta\,(r) + \frac{2}{N_\mathrm{L}-1}\delta\,(r-1) \tag{6.59}$$

gives the correct transmission $\langle t\rangle = \frac{T}{N_\mathrm{L}-1}$ and the expected Fano factor of $F = \frac{1}{3}$ (as can be obtained from Eq. (6.58) by replacing $\alpha_1 = 1-\epsilon$, $\alpha_2 = \frac{\epsilon}{N_\mathrm{L}-1}$ and letting $\epsilon \to 0$). Therefore this eigenvector splitting should be considered as the generalization of Eq. (6.50) for a star with N_L leads. The corresponding probability distribution for the eigenvalues is found to be

$$p_{t_{21}^\dagger t_{21}}(t) = \begin{cases} \frac{T}{2(N_\mathrm{L}-1)}\frac{1}{t\sqrt{1-t}} + \frac{N_\mathrm{L}-2}{N_\mathrm{L}-1}\delta(t) & \left[\cosh\left(\frac{1}{T}\right)\right]^{-2} \leq t \leq 1 \\ 0 & \text{else.} \end{cases} \tag{6.60}$$

This is again nothing but a rescaled bimodal distribution, meaning that the generalizations to the case with many spokes are so far very straightforward and the results are very much expected.

It becomes more interesting when generalizing to the fully symmetric star with N_L spokes that is sketched in Fig. 6.10(b). Here, we previously made use of an educated guess for the splitting of the eigenvectors (namely that they should equally distribute between the two outgoing spokes, yielding $w(r) = 1$), which allowed us to derive an analytical expression for the full eigenvalue distribution that yielded the correct Fano factor and which we could later show to be in good agreement with our numerical calculations in the low-transmission limit. Here, we will attempt a similar approach in the limit of a star with N_L leads. Yet, we will limit ourselves to a check of the Fano factor and will not do full scattering-matrix calculations, which would quickly become intractable in the case of many spokes.

Our educated guess for $w(r)$ will be a generalization of the "equal distribution" of

the eigenvectors among the outgoing leads. We realize that, for two leads, we recover $w_{N_\mathrm{L}=3}(r) = 1$ from the following expression:

$$w_{N_\mathrm{L}=3}(r) = \int_0^1 dq_1\, \delta(r + q_1 - 1) = 1. \tag{6.61}$$

This is intuitive when we interpret this as the mathematical formulation of the fact that the original eigenvalue may split into any portion r that exits through spoke 2 and any other portion q_1 that exits through spoke 3. The only limitation that restricts this splitting is the fact that the portions should add up to 1, which is ensured by the delta function. From this point of view, there is a natural generalization to Eq. (6.61) for the case of more than $N_L = 3$ spokes,

$$w_{N_\mathrm{L}}(r) \propto \int\!\cdots\!\int_0^1 dq_1 \cdots dq_{N_\mathrm{L}-2}\, \delta\left(r - 1 + \sum_{n=1}^{N_\mathrm{L}-2} q_n\right) =: s_{N_\mathrm{L}}(r), \tag{6.62}$$

where we only write proportional as the expression obtained from the integral on the right-hand side, which we name $s_{N_\mathrm{L}}(r)$, is not properly normalized for a general N_L. To find a normalized expression for $w_{N_\mathrm{L}}(r)$, we analytically evaluate $s_{N_\mathrm{L}}(r)$. This can for example been done by induction, i. e., one can easily show that

$$s_{N_\mathrm{L}=3}(r) = 1, \tag{6.63}$$

$$\frac{\partial}{\partial r} s_{N_\mathrm{L}+1}(r) = -s_{N_\mathrm{L}}(r), \tag{6.64}$$

$$s_{N_\mathrm{L}+1}(0) = \int_0^1 dr\, s_{N_\mathrm{L}}(r), \tag{6.65}$$

which one can solve to find

$$s_{N_\mathrm{L}}(r) = \frac{1}{(N_\mathrm{L}-3)!}\,(1-r)^{N_\mathrm{L}-3}. \tag{6.66}$$

Normalizing this on the interval $[0, 1]$, we can find the corresponding expression for the eigenvector-splitting distribution,

$$w_{N_\mathrm{L}}(r) = (N_\mathrm{L}-2)\,(1-r)^{N_\mathrm{L}-3}. \tag{6.67}$$

Thus, the splitting of the eigenvectors tends to a more and more peaked function around $r = 0$ when increasing the number of spokes in the star. This behavior is also illustrated in Fig. 6.11(a). By using this function in Eq. (6.39), one can find the properly generalized eigenvalue probability distribution of a fully symmetric star with N_L spokes in the low-transmission limit,

$$p_{t_{21}^\dagger t_{21}}(t) = \begin{cases} \frac{T}{2}\frac{\sqrt{\pi}\Gamma(N_\mathrm{L}-1)}{\Gamma\left(N_\mathrm{L}-\frac{3}{2}\right)}\,(1-t)^{N_\mathrm{L}-\frac{5}{2}} & \\ \quad \times {}_2F_1\left(\frac{1}{2}, N_\mathrm{L}-1; N_\mathrm{L}-\frac{3}{2}; 1-t\right) & \left[\cosh\left(\frac{1}{T}\right)\right]^{-2} \le t \le 1 \\ Q_{N_\mathrm{L}}(t) & 0 \le t \le \left[\cosh\left(\frac{1}{T}\right)\right]^{-2}, \end{cases} \tag{6.68}$$

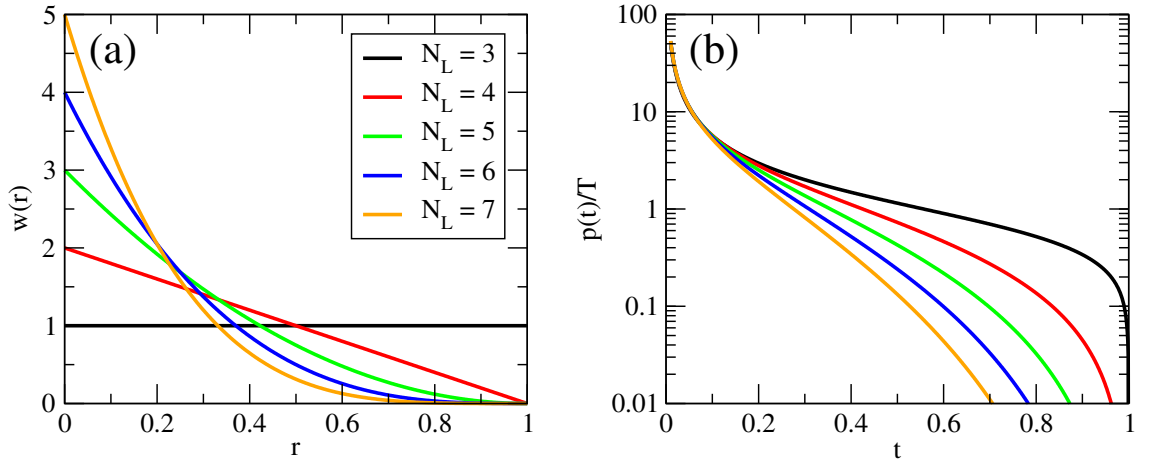

Figure 6.11: This figure shows plots of the analytical results for the low-transmission limit of the diffusive fully symmetric star with N_L spokes, cf. Fig. 6.10(b). (a) shows the splitting of the eigenvectors as given by Eq. (6.67) for a few selected values of N_L. (b) shows the corresponding results for the probability distribution of transmission eigenvalues between any two spokes, Eq. (6.68).

where $\Gamma(a)$ denotes the Gamma function and ${}_2F_1\,(a,b;c;d)$ the hypergeometric function (as defined in §15.1.1 in [150]). Here, $Q_{N_\mathrm{L}}(t)$, i. e., the distribution for very small values of t can be found to be a polynomial of degree $N_\mathrm{L}-3$, which is difficult to write down in a closed form explicitly. However, it is not of much importance for our discussion as we are focusing on the low-transmission limit in which $\left[\cosh\left(\frac{1}{T}\right)\right]^{-2}$ is very close to 0 for all practical purposes such that the detailed behavior around $t=0$ can usually be neglected. The expression in Eq. (6.68) can be shown to simplify to Eq. (6.53) for $N_\mathrm{L}=3$. Also, it yields the correct expectation value for the transmission $\langle t\rangle = \frac{T}{N_\mathrm{L}-1}$ and the Fano factor,

$$F = 1 - \frac{4}{3N_\mathrm{L}}, \tag{6.69}$$

which is the same result as the one that one obtains from Eq. (6.58) when inserting the corresponding values for the relative transmissions, $\alpha_1 = \alpha_2 = \frac{1}{N_\mathrm{L}}$. This is making us confident that this expression is the correct eigenvalue distribution in the low-transmission limit of a diffusive N_L-spoke star structure. In Fig. 6.11(b), we plot this distribution for a few selected values of N_L, which shows that the qualitative behavior of the distributions is similar to the $N_\mathrm{L}=3$ case. They are in principle not showing a hard cutoff close to $t=1$, however, for large N_L, their decay away from the peak at $t=0$ becomes very fast. Therefore, for large N_L, they almost look as if they are only non-zero in a finite region around $t=0$.

In summary, in this section we derived or motivated eigenvalue distribution functions in the low-transmission limit of a diffusive star geometry with N_L spokes. We obtained analytical expressions in a few limiting cases, from which one can in principle calculate all moments of the distribution. In this way, one can go beyond shot noise and also study higher current correlations, which we however did not do in this work as these quantities are experimentally very difficult to access. In addition, we also derived expressions for the eigenvector-splitting distributions $w(r)$ in the discussed limits, which—given sufficient

control of the incoming channels—are also measurable quantities that may be interesting for future experiments.

6.5 Discussion of the results

In this chapter, we studied transmission-eigenvalue distributions in diffusive multi-terminal devices. We focused on star-shaped systems and mainly discussed the special case of three terminals. For this, we analyzed a scattering-matrix model based on the open-mode approximation, which we later verified using full wave-transport calculations. By choosing different asymmetries, we could see that the cutoff of the transmission-eigenvalue distribution, which we ubiquitously observe in such a multi-terminal device, can be explained in terms of a random matrix projection when considering a system in an extremely asymmetric star configuration (one spoke long and two very short). When moving away from this configuration, the cutoff persists at first but disappears in the opposite limit (one spoke short and two very long). As we later showed with an analytical analysis of the model, in the limit of many modes and small transmission probability per mode (the true diffusive limit), a distribution without any cutoff at high transmission eigenvalues is already expected in a fully symmetric configuration. In practice, however, the range of applicability of the low-transmission approximation is restricted to very low transmissions and it may be difficult to observe it experimentally. Conceptually, a study of this low-transmission regime is still insightful as it allows for analytical solutions in all important limiting cases of asymmetry and those solutions can even be generalized to stars with an arbitrary number of spokes as we showed in Section 6.4. Such analytical solutions allow for the evaluation of arbitrary moments of the transmission-eigenvalue distribution and therefore also provide access to higher current correlations which go beyond shot noise.

Throughout our investigations, we noticed that if one combines some of the leads into one meta lead in such a way that the total number of (meta) leads is only two, the transmission-eigenvalue distribution between the two meta leads always shows the well-known bimodal distribution. Characteristic for this bimodal shape is the existence of "open channels", thus a high probability for eigenvalues close to perfect transmission. Therefore, a multi-lead star device in which the flux is incoming at one spoke also features such channels that lead to high transmission into the meta lead that consists of all other spokes of the star but those are usually distributed among the subleads of the meta lead. Hence, one does not see perfect transmission when only studying transport to one such sublead. This motivated us to propose the investigation of a new observable that we called eigenvector-splitting distribution. It quantifies how the outgoing flux that results from an incoming flux that corresponds to an eigenvector of the "total transmission matrix" (from one spoke into the meta lead) is distributed among the subleads of the meta lead. We saw that this quantity, which is experimentally accessible given a good control of the incoming channels, is directly related to the splitting of transmission eigenvalues among the meta leads in the low-transmission limit. In this limit, we could make use of this property to derive analytical expressions for the eigenvector-splitting for the symmetric and the fully asymmetric limits, which also generalize to stars with more

spokes. Away from the low-transmission limit, however, we numerically observe that the eigenvector splitting tends to become less sensitive to the geometry and it approaches a Gaussian distribution with increasing disorder, in good agreement with the expectation for uncorrelated random eigenvectors. Thus, an experimental detection of the eigenvector splitting is most interesting in the regime of low transmission.

6.A Appendix

6.A.1 Perturbative solution of Eqs. (6.27) and (6.28)

To solve Eqs. (6.27) and (6.28) to lowest order in T, it is crucial to recognize that in the limit $T \to 0$, Eq. (6.31) can be simplified,

$$g_{A^\dagger A}(z) = \frac{1}{z} - \frac{T}{z\sqrt{1-z}} \operatorname{arcoth}\left(\sqrt{1-z}\right), \tag{6.70}$$

as $\lim_{T\to 0}\left(\tanh\left(\frac{1}{T}\right)\right) = 1$. Inserting this expression in Eqs. (6.27) and (6.28) leads to the following implicit equation for $g_{\tilde{A}^\dagger \tilde{A}}(z)$:

$$1 - T\frac{\operatorname{arcoth}\left[\sqrt{1-\frac{g_{\tilde{A}^\dagger\tilde{A}}(z)z^2}{m-1+g_{\tilde{A}^\dagger\tilde{A}}(z)z}}\right]}{\sqrt{1-\frac{g_{\tilde{A}^\dagger\tilde{A}}(z)z^2}{m-1+g_{\tilde{A}^\dagger\tilde{A}}(z)z}}} = g_{\tilde{A}^\dagger\tilde{A}}(z)z. \tag{6.71}$$

To zeroth order in T,

$$g_{\tilde{A}^\dagger\tilde{A}}(z) = \frac{1}{z} + \mathcal{O}(T) \tag{6.72}$$

is obviously a solution to this equation. Inserting Eq. (6.72) in (6.71), we find to linear order in T,

$$g_{\tilde{A}^\dagger\tilde{A}}(z) = \frac{1}{z} - T\frac{\operatorname{arcoth}\left(\sqrt{1-\frac{z}{m}}\right)}{z\sqrt{1-\frac{z}{m}}} + \mathcal{O}(T^2), \tag{6.73}$$

which using Eq. (6.30) can be shown to yield the probability distribution of eigenvalues that is given in Eq. (6.32).

Chapter 7
Conclusion and Outlook

In this thesis, we discussed various aspects of transport in 2d TIs. Now, we will summarize the main findings and try to interrelate them. In addition, we will show up interesting questions for future research projects, which would provide a valuable extension to our work.

In Chapter 3, we studied transport at the edges of a 2d TI under the influence of a perpendicular magnetic field. We found that—even though the external field breaks TR symmetry and may therefore induce backscattering—such a field does not lead to backscattering as long as the transport is to a good approximation one dimensional. We find that this is often the case, even when considerable bulk disorder is present—at least if the disorder strength is still well below the critical disorder strength that leads to a phase transition of the bulk material to a topologically trivial Anderson insulator. Our finding of robustness against external fields agrees well with measurements on some short 2d-TI samples [115], however, in long samples, one observes considerably increased backscattering when applying a magnetic field [17, 114]. We saw that this could be explained by the presence of small metallic regions close to the edges of the sample, so-called charge puddles. In our calculations, these metallic puddles lead to a cusp-like magnetoconductance signature, which is in good qualitative agreement with the measurements on long samples. This finding suggested the following interpretation of the experimental data: Short samples do not show a strong dependence on the magnetic field because they are almost free of puddles, while long samples unavoidably contain puddles and therefore show the characteristic dependence of the resistance on the magnetic field. This interpretation would be in line with the hypothesis that the puddles are also responsible for the backscattering at zero field: Edge-state transport with no backscattering has so far only been observed in short samples, which could be due to the fact that those can be produced without puddles. Long samples always show a higher resistance, which grows linearly with the length of the edge.

It is precisely this zero-field backscattering which we tried to understand in Chapter 4, where we studied how dephasing due to inelastic processes affects the edge transport. We noticed that, also for this model, puddles play a dominant role as they provide the spin mixing which is a necessary ingredient for backscattering. We were particularly interested in the question whether there is a parameter regime in which one could understand

the experimentally observed temperature independence of the backscattering at zero field. In the end, we found that there is indeed such a regime, however, it comes with a strong restriction on the type of puddles that is allowed to be present close to the sample edge. Namely, all the puddles should be large and deep such that the dwell time of charge carriers in the puddles is much longer than the dephasing time due to the inelastic process even at the lowest experimentally observable temperatures. For the puddle depth that we studied with the BHZ model, this meant that they should at least be larger than 500 nm in diameter. Then, all the puddles give rise to a constant backscattering probability, which only depends on the coupling of the puddle to the edge and is independent of the dephasing time (thus independent of the temperature).

An obvious question that comes to mind is whether this regime of puddles with very long dwell times, which give rise to a temperature-independent backscattering, would still be able to explain the magnetoconductance results that we discussed in Chapter 3. At first sight, it seems that this is not the case because if the puddles already give rise to random backscattering of all the electrons that enter the puddle, one might think that an additional magnetic field should not lead to any extra backscattering. Hence, it would be difficult to explain the observed magnetic-field dependence of the transmission. For the average transmission of a single large puddle on the edge, this is certainly true. Here, we expect that "enough magnetic field" (more than a few flux quanta) and strong dephasing yield the same limiting transmission. However, if we are thinking about a series of puddles, it is not so clear whether the two limits necessarily agree. Here, it comes into play that a "strong enough" magnetic field induces the CUE scattering regime discussed in Chapter 3, which is characterized by a broad transmission distribution for a single puddle. A series of such puddles leads to a much lower transmission than a series of puddles which all scatter with a fixed transmission (something that would be expected for backscattering due to dephasing) as we discussed on the example of scatterers with an average transmission of 50 % in Section 3.4.1. Of course, it is not so clear whether an applied magnetic field of the strength used in the experiments (a few flux quanta) can really dominate the strong dephasing and is able to induce the broad transmission distribution. Therefore, an important extension to the work presented in this thesis would be to study transport through large puddles under the combined effect of dephasing and magnetic field. This is numerically challenging as one would probably have to study a series of puddles to see the effects due to the broad transmission distribution. Here, we would also like to emphasize that an experiment with artificial puddles could be used to verify or rule out one or both of the mechanisms proposed in Chapters 3 and 4. This would, in our opinion, be very helpful for the progress of the field. In this way, one would get a better idea of whether the non-interacting description used in this thesis is really a good model of the current experimental situation.

In Chapter 5, we took it for granted that the BHZ model is a good description of HgTe/CdTe quantum wells and studied some of the implications of the model. In particular, we considered heterostructures of 2d TIs described by the BHZ Hamiltonian with systems that have extended states. We found that one can in general expect the emergence of a perfectly conducting channel in such a heterostructure and we even showed how one could understand this effect in terms of an effective boundary condition. This boundary condition seems to correctly encode the "topology" of the boundary to a TI

and therefore can be considered an extension to the commonly used hard-wall boundary condition that is often used to model the proximity to a trivial insulator. Of course, the boundary condition can only be used in a wave-guide geometry and loses its meaning when considering a finite system as it depends on the momentum in transport direction, which is assumed to be a good quantum number. Still, it is conceptually interesting and it shows how one could induce PCCs in wave guides by emulating this boundary condition, even without the need for TIs. As an extension to this, one might try to consider boundaries with three-dimensional TIs by deriving a corresponding boundary condition for a boundary to a 3d-TI half-space. In such a structure which is infinite in two dimensions, one does not expect a "perfectly conducting channel" as there is no notion of a fixed transport direction in which one would have well-defined transverse modes. In this way, transport in this heterostructure would be very similar to transport on surfaces of 3d TIs for which one also does not expect to find a quantized value of the conductance. Still, a proper boundary condition should guarantee the existence of an extended state at every energy if it is applied to a system with trivial topology.

In the second part of Chapter 5, we discussed ways to detect PCCs in actual nanodevices made from HgTe/CdTe quantum wells. We showed that, assuming that the BHZ model is a good description of the experimental situation, such a detection should be possible by either using devices in which all other channels are localized or by introducing an additional tunnel barrier. Another possibility, which we did not discuss in this work, would be to build metallic ring devices in which the core of the ring is made of a 2d-TI material. By applying an external magnetic field, one can study Aharonov-Bohm interferences in which the PCC should show a particularly strong signature as it is not reflected while traveling around the ring and therefore may traverse the ring many times. However, in the design, one should make sure that the inner area is large such that one only needs to apply weak fields to observe the periodic interference pattern. The ring section, on the other hand, should be thin such that the applied flux through the metallic region is still well below one flux quantum such that the field does not destroy the PCC. Preliminary results with this setup show promising results, which might lead to an alternative detection scheme of induced PCCs in such devices.

Inspired by the calculation of the transmission-eigenvalue distributions, which were used in Chapter 5 to extract a signature of the PCC in the diffusive regime, we decided to devise a more general study of diffusive transport in many-terminal devices in Chapter 6. This allowed us to explain the emergence of the most prominent feature in these distributions—a cutoff in the transmission eigenvalue spectrum—by a comparison to random matrix projections. Also, we were able to motivate and numerically check analytical expressions for the transmission-eigenvalue distributions for some limiting geometries of star-shaped diffusive devices with many leads in the true diffusive limit ($N \to \infty$, $\langle t \rangle \to 0$, $N \cdot \langle t \rangle \gg 1$). In addition, we proposed an interesting observable: the eigenvector splitting. It may be used to quantify to which degree the "open channels" into the meta leads (combination of a number of leads such that the system effectively reduces to two terminals) distribute among the true leads of the system. One obvious extension to the work in this chapter would be to attempt a more in-depth study of the employed scattering-matrix model, which we saw to be in very good agreement with numerical results in the diffusive regime. Here, it would be very interesting to work out next-order corrections to the analytical

solutions in the large N limit using other random matrix theory methods. Alternatively, one might try to obtain analytical results for a star geometry of intermediate aspect ratio using such "general purpose" methods because we saw that free probability theory, which is simple and powerful in the $q = 1$ limit, becomes very difficult to use in other limits. Also, one might think about considering other geometries. We think that the results of this chapter are conceptually interesting as they generally apply to diffusive wave-transport problems for which we think that there is still a lot to be understood in structures with many terminals.

Coming back to transport in 2d TIs, we summarize the work of this thesis by stating that there are still many open questions when it comes to quantitative explanations for the observed behavior of actual implementations of 2d-TI nanostructures. A better understanding of these puzzling observations is necessary for estimating whether—or under which circumstances—the topological peculiarities of TIs can be used for the exciting new applications that are envisioned. In this thesis, we worked into that direction by trying to understand the current experimental findings in terms of models based on the non-interacting BHZ Hamiltonian. We succeeded in proposing possible explanations for several observations. These proposed mechanisms now need to face a thorough experimental test. However, we expect this only to be the beginning of further intense research activities because the field of TIs is still rapidly and heavily developing and is constantly getting input of surprising and difficult to explain experimental results [19, 110, 153, 154]. For example, the importance of interactions (which we did not include in this thesis) on transport in 2d-TI nanostructures needs to be clarified in the future. By close collaborations between experimental and theoretical approaches, a more reliable framework for 2d-TI nanostructures can be established that might pave the road toward exciting novel devices with unprecedented properties.

Bibliography

[1] Bernevig B.A., Hughes T.L., and Zhang S.C., *Quantum spin Hall effect and topological phase transition in HgTe quantum wells*, Science **314**, 1757 (2006).

[2] Kane C.L. and Mele E.J., *Z_2 Topological Order and the Quantum Spin Hall Effect*, Phys. Rev. Lett. **95**, 146802 (2005).

[3] Landau L.D., *On the Theory of Phase Transitions*, Zh. Eks. Teor. Fiz. **7**, 19 (1937).

[4] Kitaev A., *Periodic table for topological insulators and superconductors*, AIP Conf. Proc. **1134**, 22 (2003).

[5] Schnyder A.P., Ryu S., Furusaki A., and Ludwig A.W.W., *Classification of topological insulators and superconductors in three spatial dimensions*, Phys. Rev. B **78**, 195125 (2008).

[6] Halperin B.I., *Quantized Hall conductance, current-carrying edge states, and the existence of extended states in a two-dimensional disordered potential*, Phys. Rev. B **25**, 2185 (1982).

[7] Qi X.L. and Zhang S.C., *Topological insulators and superconductors*, Rev. Mod. Phys. **83**, 1057 (2011).

[8] Kitaev A.Y., *Unpaired Majorana fermions in quantum wires*, Physics-Uspekhi **44**, 131 (2001).

[9] Nayak C., Simon S.H., Stern A., Freedman M., and Das Sarma S., *Non-Abelian anyons and topological quantum computation*, Rev. Mod. Phys. **80**, 1083 (2008).

[10] Fu L., Kane C.L., and Mele E.J., *Topological Insulators in Three Dimensions*, Phys. Rev. Lett. **98**, 106803 (2007).

[11] Nielsen H.B. and Ninomiya M., *A no-go theorem for regularizing chiral fermions*, Phys. Lett. B **105**, 219 (1981).

[12] Hasan M.Z. and Moore J.E., *Three-Dimensional Topological Insulators*, Annu. Rev. Condens. Matter Phys. **2**, 55 (2011).

[13] Žutić I., Fabian J., and Das Sarma S., *Spintronics: Fundamentals and applications*, Rev. Mod. Phys. **76**, 323 (2004).

[14] Alicea J., *New directions in the pursuit of Majorana fermions in solid state systems*, Reports Prog. Phys. **75**, 076501 (2012).

[15] Beenakker C.W.J., *Search for Majorana Fermions in Superconductors*, Annu. Rev. Condens. Matter Phys. **4**, 113 (2013).

[16] Fu L. and Kane C.L., *Superconducting Proximity Effect and Majorana Fermions at the Surface of a Topological Insulator*, Phys. Rev. Lett. **100**, 096407 (2008).

[17] König M., Wiedmann S., Brüne C., Roth A., Buhmann H., Molenkamp L.W., Qi X.L., and Zhang S.C., *Quantum Spin Hall Insulator State in HgTe Quantum Wells*, Science **318**, 766 (2007).

[18] Kane C.L. and Mele E.J., *Quantum Spin Hall Effect in Graphene*, Phys. Rev. Lett. **95**, 226801 (2005).

[19] Du L., Knez I., Sullivan G., and Du R.R., *Robust Helical Edge Transport in Gated InAs/GaSb Bilayers*, Phys. Rev. Lett. **114**, 096802 (2015).

[20] Liu C., Hughes T.L., Qi X.L., Wang K., and Zhang S.C., *Quantum Spin Hall Effect in Inverted Type-II Semiconductors*, Phys. Rev. Lett. **100**, 236601 (2008).

[21] Essert S. and Richter K., *Magnetotransport in disordered two-dimensional topological insulators: signatures of charge puddles*, 2D Mater. **2**, 024005 (2015).

[22] Essert S., Krueckl V., and Richter K., *Two-dimensional topological insulator edge state backscattering by dephasing*, Phys. Rev. B **92**, 205306 (2015).

[23] Essert S., Krueckl V., and Richter K., *Using topological insulator proximity to generate perfectly conducting channels in materials without topological protection*, New J. Phys. **16**, 113058 (2014).

[24] Dirac P.A.M., *Quantised Singularities in the Electromagnetic Field*, Proc. R. Soc. Lond. A **133**, 60 (1931).

[25] Nash C., *Topology and physics—a historical essay*, in I.M. James, ed., *History of Topology*, 359–415, Elsevier–North Holland, Amsterdam (1999).

[26] Niu Q., Thouless D.J., and Wu Y.S., *Quantized Hall conductance as a topological invariant.*, Phys. Rev. B **31**, 3372 (1985).

[27] Thouless D.J., Kohmoto M., Nightingale M.P., and Den Nijs M., *Quantized Hall Conductance in a Two-Dimensional Periodic Potential*, Phys. Rev. Lett. **49**, 405 (1982).

[28] Hosur P. and Qi X., *Recent developments in transport phenomena in Weyl semimetals*, C. R. Phys. **14**, 857 (2013).

[29] Turner A.M. and Vishwanath A., *Beyond Band Insulators: Topology of Semimetals and Interacting Phases*, arXiv Prepr. 1301.0330 (2013).

[30] Young S.M., Zaheer S., Teo J.C.Y., Kane C.L., Mele E.J., and Rappe A.M., *Dirac Semimetal in Three Dimensions*, Phys. Rev. Lett. **108**, 140405 (2012).

[31] Fulga I.C., van Heck B., Edge J.M., and Akhmerov A.R., *Statistical topological insulators*, Phys. Rev. B **89**, 155424 (2014).

[32] Zhang L., Ren J., Wang J.S., and Li B., *Topological magnon insulator in insulating ferromagnet*, Phys. Rev. B **87**, 144101 (2013).

[33] Süsstrunk R. and Huber S.D., *Observation of phononic helical edge states in a mechanical topological insulator*, Science **349**, 47 (2015).

[34] Yang Z., Gao F., Shi X., Lin X., Gao Z., Chong Y., and Zhang B., *Topological Acoustics*, Phys. Rev. Lett. **114**, 114301 (2015).

[35] Goldman N., Satija I., Nikolic P., Bermudez A., Martin-Delgado M.A., Lewenstein M., and Spielman I.B., *Realistic Time-Reversal Invariant Topological Insulators with Neutral Atoms*, Phys. Rev. Lett. **105**, 255302 (2010).

[36] Goldman N., Dalibard J., Dauphin A., Gerbier F., Lewenstein M., Zoller P., and Spielman I.B., *Direct imaging of topological edge states in cold-atom systems.*, Proc. Natl. Acad. Sci. U. S. A. **110**, 6736 (2013).

[37] Kraus Y.E., Lahini Y., Ringel Z., Verbin M., and Zilberberg O., *Topological States and Adiabatic Pumping in Quasicrystals*, Phys. Rev. Lett. **109**, 106402 (2012).

[38] Lindner N.H., Refael G., and Galitski V., *Floquet topological insulator in semiconductor quantum wells*, Nat. Phys. **7**, 490 (2011).

[39] Rechtsman M.C., Zeuner J.M., Plotnik Y., Lumer Y., Podolsky D., Dreisow F., Nolte S., Segev M., and Szameit A., *Photonic Floquet topological insulators.*, Nature **496**, 196 (2013).

[40] Bernevig B.A. and Hughes T.L., *Topological Insulators and Topological Superconductors*, Princeton University Press, Princeton and Oxford (2013).

[41] Franz M. and Molenkamp L., eds., *Topological Insulators*, vol. 6 of *Contemporary Concepts of Condensed Matter Science*, Elsevier (2013).

[42] Ortmann F., Roche S., and Valenzuela S.O., eds., *Topological Insulators*, Wiley-VCH, Weinheim (2015).

[43] Avron J.E., Seiler R., and Simon B., *Homotopy and Quantisation in Condensed Matter Physics*, Phys. Rev. Lett. **51**, 51 (1983).

[44] Berry M.V., *Quantal phase factors accompanying adiabatic changes*, Proc. R. Soc. Lond. A **392**, 45 (1984).

[45] Kohmoto M., *Topological invariant and the quantization of the Hall conductance*, Ann. Phys. (N. Y.) **160**, 343 (1985).

[46] Hatsugai Y., *Chern Number and Edge States in the Integer Quantum Hall Effect*, Phys. Rev. Lett. **71**, 3697 (1993).

[47] Mong R.S.K. and Shivamoggi V., *Edge states and the bulk-boundary correspondence in Dirac Hamiltonians*, Phys. Rev. B **83**, 125109 (2011).

[48] Shtrikman S. and Thomas H., *Remarks on Linear Magneto-Resistance and Magneto-Heat-Conductivity*, Solid State Commun. **3**, 147 (1965).

[49] Chang C.Z. et al., *Experimental Observation of the Quantum Anomalous Hall Effect in a Magnetic Topological Insulator*, Science **340**, 167 (2013).

[50] Haldane F.D.M., *Model for a Quantum Hall Effect without Landau Levels: Condensed-Matter Realization of the"Parity Anomaly"*, Phys. Rev. Lett. **61**, 2015 (1988).

[51] Fu L. and Kane C.L., *Time reversal polarization and a Z_2 adiabatic spin pump*, Phys. Rev. B **74**, 195312 (2006).

[52] Altland A. and Zirnbauer M.R., *Novel Symmetry Classes in Mesoscopic Normal-Superconducting Hybrid Structures*, Phys. Rev. B **55**, 1142 (1997).

[53] Cartan É., *Sur une classe remarquable d'espaces de Riemann. I*, Bull. la Soc. Math. Fr. **54**, 214 (1926).

[54] Cartan É., *Sur une classe remarquable d'espaces de Riemann. II*, Bull. la Soc. Math. Fr. **55**, 114 (1927).

[55] Chiu C.K., Yao H., and Ryu S., *Classification of topological insulators and superconductors in the presence of reflection symmetry*, Phys. Rev. B **88**, 075142 (2013).

[56] Morimoto T. and Furusaki A., *Topological classification with additional symmetries from Clifford algebras*, Phys. Rev. B **88**, 125129 (2013).

[57] Fu L., *Topological Crystalline Insulators*, Phys. Rev. Lett. **106**, 106802 (2011).

[58] Chiu C.K., Teo J.C.Y., Schnyder A.P., and Ryu S., *Classification of topological quantum matter with symmetries*, arXiv Prepr. 1505.03535 (2015).

[59] Wigner E., *Über die Operation der Zeitumkehr in der Quantenmechanik*, Gött. Nach. Mathem. Phys. Klasse **1932**, 546 (1932).

[60] Mong R.S.K., Bardarson J.H., and Moore J.E., *Quantum Transport and Two-Parameter Scaling at the Surface of a Weak Topological Insulator*, Phys. Rev. Lett. **108**, 076804 (2012).

[61] Pauly C. et al., *Subnanometre-wide electron channels protected by topology*, Nat. Phys. **11**, 338 (2015).

[62] Yoshimura Y., Matsumoto A., Takane Y., and Imura K.I., *Perfectly conducting channel on the dark surface of weak topological insulators*, Phys. Rev. B **88**, 045408 (2013).

[63] Essin A.M. and Moore J.E., *Topological insulators beyond the Brillouin zone via Chern parity*, Phys. Rev. B **76**, 165307 (2007).

[64] Fukui T. and Hatsugai Y., *Quantum Spin Hall Effect in Three Dimensional Materials: Lattice Computation of Z_2 Topological Invariants and Its Application to Bi and Sb*, J. Phys. Soc. Japan **76**, 053702 (2007).

[65] Fulga I.C., Hassler F., and Akhmerov A.R., *Scattering theory of topological insulators and superconductors*, Phys. Rev. B **85**, 165409 (2012).

[66] Prodan E., *Robustness of the spin-Chern number*, Phys. Rev. B **80**, 125327 (2009).

[67] Mehta M.L., *Random Matrices*, vol. 142 of *Pure and Applied Mathematics*, Elsevier Academic Press (2004).

[68] Fu L. and Kane C.L., *Topological insulators with inversion symmetry*, Phys. Rev. B **76**, 045302 (2007).

[69] Soluyanov A.A. and Vanderbilt D., *Computing topological invariants without inversion symmetry*, Phys. Rev. B **83**, 235401 (2011).

[70] Gmitra M., Konschuh S., Ertler C., Ambrosch-Draxl C., and Fabian J., *Band-structure topologies of graphene: Spin-orbit coupling effects from first principles*, Phys. Rev. B **80**, 235431 (2009).

[71] Qi X.L., Wu Y.S., and Zhang S.C., *Topological quantization of the spin Hall effect in two-dimensional paramagnetic semiconductors*, Phys. Rev. B **74**, 085308 (2006).

[72] Winkler R., *Spin-Orbit Coupling Effects in Two-Dimensional Electron and Hole Systems*, vol. 191 of *Springer Tracts in Modern Physics*, Springer, Berlin, Heidelberg (2003).

[73] Chang Y.C., Schulman J.N., Bastard G., Guldner Y., and Voos M., *Effects of quasi-interface states in HgTe-CdTe superlattices*, Phys. Rev. B **31**, 2557 (1985).

[74] Pankratov O.A., *Electronic properties of band-inverted heterojunctions: supersymmetry in narrow-gap semiconductors*, Semicond. Sci. Technol. **5**, S204 (1990).

[75] Volkov B.A. and Pankratov O.A., *Two-dimensional massless electrons in an inverted contact*, JETP Lett. **42**, 178 (1985).

[76] Dai X., Hughes T.L., Qi X.L., Fang Z., and Zhang S.C., *Helical edge and surface states in HgTe quantum wells and bulk insulators*, Phys. Rev. B **77**, 125319 (2008).

[77] Bouvier C., Meunier T., Kramer R., Lévy L.P., Baudry X., and Ballet P., *Strained HgTe: a textbook 3D topological insulator*, arXiv Prepr. 1112.2092 (2011).

[78] Brüne C. et al., *Quantum Hall Effect from the Topological Surface States of Strained Bulk HgTe*, Phys. Rev. Lett. **106**, 126803 (2011).

[79] Crauste O., Ohtsubo Y., Ballet P., Delplace P., Carpentier D., Bouvier C., Meunier T., Taleb-Ibrahimi A., and Lévy L.P., *Topological surface states of strained Mercury-Telluride probed by ARPES*, arXiv Prepr. 1307.2008 (2013).

[80] Guldner Y., Rigaux C., Mycielski A., and Couder Y., *Magnetooptical Investigation of $Hg_{1-x}Cd_xTe$ Mixed Crystals II. Semiconducting Configuration and Semimetal → Semiconductor Transition*, Phys. Status Solidi B **82**, 149 (1977).

[81] Krueckl V., *Wave packets in mesoscopic systems: From time-dependent dynamics to transport phenomena in graphene and topological insulators*, PhD thesis, Universität Regensburg (2012).

[82] Rothe D.G., Reinthaler R.W., Liu C.X., Molenkamp L.W., Zhang S.C., and Hankiewicz E.M., *Fingerprint of different spin-orbit terms for spin transport in HgTe quantum wells*, New J. Phys. **12**, 065012 (2010).

[83] Budich J.C. and Trauzettel B., *Local topological phase transitions in periodic condensed matter systems*, Eur. Phys. J. B **85**, 94 (2012).

[84] König M., Buhmann H., Molenkamp L.W., Hughes T., Liu C.X., Qi X.L., and Zhang S.C., *The Quantum Spin Hall Effect: Theory and Experiment*, J. Phys. Soc. Japan **77**, 031007 (2008).

[85] Krueckl V. and Richter K., *Switching Spin and Charge between Edge States in Topological Insulator Constrictions*, Phys. Rev. Lett. **107**, 086803 (2011).

[86] Zhou B., Lu H.Z., Chu R.L., Shen S.Q., and Niu Q., *Finite Size Effects on Helical Edge States in a Quantum Spin-Hall System*, Phys. Rev. Lett. **101**, 246807 (2008).

[87] Kainaris N., Gornyi I.V., Carr S.T., and Mirlin A.D., *Conductivity of a generic helical liquid*, Phys. Rev. B **90**, 075118 (2014).

[88] Schmidt T.L., Rachel S., von Oppen F., and Glazman L.I., *Inelastic Electron Backscattering in a Generic Helical Edge Channel*, Phys. Rev. Lett. **108**, 156402 (2012).

[89] Klipstein P.C., *Structure of the quantum spin Hall states in HgTe/CdTe and InAs/GaSb/AlSb quantum wells*, Phys. Rev. B **91**, 035310 (2015).

[90] Medhi A. and Shenoy V.B., *Continuum theory of edge states of topological insulators: variational principle and boundary conditions.*, J. Phys. Condens. Matter **24**, 355001 (2012).

[91] Tkachov G. and Hankiewicz E.M., *Spin-helical transport in normal and superconducting topological insulators*, Phys. Status Solidi B **250**, 215 (2013).

[92] Jiang Y. and Hu L., *Kinetic magnetoelectric effect in a two-dimensional semiconductor strip due to boundary-confinement-induced spin-orbit coupling*, Phys. Rev. B **74**, 075302 (2006).

[93] Xing Y., Sun Q.f., Tang L., and Hu J., *Accumulation of opposite spins on the transverse edges of a two-dimensional electron gas in a longitudinal electric field*, Phys. Rev. B **74**, 155313 (2006).

[94] Knez I., Du R.R., and Sullivan G., *Evidence for Helical Edge Modes in Inverted InAs/GaSb Quantum Wells*, Phys. Rev. Lett. **107**, 136603 (2011).

[95] Mueller S., Pal A.N., Karalic M., Tschirky T., Charpentier C., Wegscheider W., Ensslin K., and Ihn T., *Non-local transport via edge-states in InAs/GaSb coupled quantum wells*, Phys. Rev. B **92**, 081303(R) (2015).

[96] Qu F. et al., *Electric and Magnetic Tuning Between the Trivial and Topological Phases in InAs/GaSb Double Quantum Wells*, Phys. Rev. Lett. **115**, 036803 (2015).

[97] Lee P.A. and Fisher D.S., *Anderson Localization in Two Dimensions*, Phys. Rev. Lett. **47**, 882 (1981).

[98] MacKinnon A., *The Calculation of Transport Properties and Density of States of Disordered Solids*, Z. Phys. B **59**, 385 (1985).

[99] Thouless D.J. and Kirkpatrick S., *Conductivity of the disordered linear chain*, J. Phys. C **14**, 235 (1981).

[100] Wimmer M. and Richter K., *Optimal block-tridiagonalization of matrices for coherent charge transport*, J. Comp. Phys. **228**, 8548 (2009).

[101] Tal-Ezer H. and Kosloff R., *An accurate and efficient scheme for propagating the time dependent Schrödinger equation*, J. Chem. Phys. **81**, 3967 (1984).

[102] Kramer T., Kreisbeck C., and Krueckl V., *Wave packet approach to transport in mesoscopic systems*, Phys. Scr. **82**, 038101 (2010).

[103] Wimmer M., *Quantum transport in nano-structures: From computational concepts to spintronics in graphene and magnetic tunnel junctions*, PhD thesis, Universität Regensburg (2008).

[104] Datta S., *Electronic Transport in Mesoscopic Systems*, Cambridge University Press, Cambridge (2002).

[105] Di Ventra M., *Electrical Transport in Nanoscale Systems*, Cambridge University Press, Cambridge (2008).

[106] Brüne C., Roth A., Buhmann H., Hankiewicz E.M., Molenkamp L.W., Maciejko J., Qi X.L., and Zhang S.C., *Spin polarization of the quantum spin Hall edge states*, Nat. Phys. **8**, 485 (2012).

[107] Ezawa M., Tanaka Y., and Nagaosa N., *Topological Phase Transition without Gap Closing.*, Sci. Rep. **3**, 2790 (2013).

[108] Scharf B., Matos-Abiague A., and Fabian J., *Magnetic properties of HgTe quantum wells*, Phys. Rev. B **86**, 075418 (2012).

[109] Scharf B., Matos-Abiague A., Žutić I., and Fabian J., *Probing topological transitions in HgTe/CdTe quantum wells by magneto-optical measurements*, Phys. Rev. B **91**, 235433 (2015).

[110] Ma E.Y. et al., *Unexpected edge conduction in mercury telluride quantum wells under broken time-reversal symmetry*, Nat. Commun. **6**, 7252 (2015).

[111] Anderson P.W., *Absence of Diffusion in Certain Random Lattices*, Phys. Rev. **109**, 1492 (1958).

[112] Mott N.F. and Twose W.D., *The theory of impurity conduction*, Adv. Phys. **10**, 107 (1961).

[113] Gusev G.M., Kvon Z.D., Shegai O.A., Mikhailov N.N., and Dvoretsky S.A., *Aharonov Bohm effect in 2D topological insulator*, Solid State Comm. **205**, 4 (2014).

[114] Gusev G.M., Olshanetsky E.B., Kvon Z.D., Mikhailov N.N., and Dvoretsky S.A., *Linear magnetoresistance in HgTe quantum wells*, Phys. Rev. B **87**, 081311 (2013).

[115] Buhmann H., Private Communication (2013).

[116] Knez I., Rettner C.T., Yang S.H., Parkin S.S.P., Du L., Du R.R., and Sullivan G., *Observation of Edge Transport in the Disordered Regime of Topologically Insulating InAs/GaSb Quantum Wells*, Phys. Rev. Lett. **112**, 026602 (2014).

[117] Chen J.C., Wang J., and Sun Q.F., *Effect of magnetic field on electron transport in HgTe/CdTe quantum wells: Numerical analysis*, Phys. Rev. B **85**, 125401 (2012).

[118] Delplace P., Li J., and Büttiker M., *Magnetic-Field-Induced Localization in 2D Topological Insulators*, Phys. Rev. Lett. **109**, 246803 (2012).

[119] Maciejko J., Qi X.L., and Zhang S.C., *Magnetoconductance of the quantum spin Hall state*, Phys. Rev. B **82**, 155310 (2010).

[120] Pikulin D.I., Hyart T., Mi S., Tworzydło J., Wimmer M., and Beenakker C.W.J., *Disorder and magnetic-field-induced breakdown of helical edge conduction in an inverted electron-hole bilayer*, Phys. Rev. B **89**, 161403 (2014).

[121] Luttinger J.M., *The Effect of a Magnetic Field on Electrons in a Periodic Potential*, Phys. Rev. **84**, 814 (1951).

[122] Prodan E., *Three-dimensional phase diagram of disordered HgTe/CdTe quantum spin-Hall wells*, Phys. Rev. B. **83**, 195119 (2011).

[123] Li J., Chu R.L., Jain J., and Shen S.Q., *Topological Anderson Insulator*, Phys. Rev. Lett. **102**, 136806 (2009).

[124] Evers F. and Mirlin A.D., *Anderson transitions*, Rev. Mod. Phys. **80**, 1355 (2008).

[125] Huckestein B., *Scaling theory of the integer quantum Hall effect*, Rev. Mod. Phys. **67**, 357 (1995).

[126] Kramer B., Ohtsuki T., and Kettemann S., *Random network models and quantum phase transitions in two dimensions*, Phys. Rep. **417**, 211 (2005).

[127] Gilbert M.J., Bernevig B.A., and Hughes T.L., *Signature of phase transitions in the disordered quantum spin Hall state from the entanglement spectrum*, Phys. Rev. B **86**, 041401(R) (2012).

[128] Obuse H., Furusaki A., Ryu S., and Mudry C., *Two-dimensional spin-filtered chiral network model for the $\mathbb{Z}_2$ quantum spin-Hall effect*, Phys. Rev. B **76**, 075301 (2007).

[129] Onoda M., Avishai Y., and Nagaosa N., *Localization in a Quantum Spin Hall System*, Phys. Rev. Lett. **98**, 076802 (2007).

[130] Yamakage A., Nomura K., Imura K.I., and Kuramoto Y., *Disorder-Induced Multiple Transition involving $\mathbb{Z}_2$ Topological Insulator*, J. Phys. Soc. Japan **80**, 053703 (2011).

[131] Ando T., *Numerical study of symmetry effects on localization in two dimensions*, Phys. Rev. B **40**, 5325 (1989).

[132] Hikami S., Larkin A.I., and Nagaoka Y., *Spin-Orbit Interaction and Magnetoresistance in the Two Dimensional Random System*, Prog. Theor. Phys. **63**, 707 (1980).

[133] Abrahams E., ed., *50 Years of Anderson Localization*, World Scientific Publishing, Singapore (2010).

[134] Obuse H., Furusaki A., Ryu S., and Mudry C., *Boundary criticality at the Anderson transition between a metal and a quantum spin Hall insulator in two dimensions*, Phys. Rev. B **78**, 115301 (2008).

[135] Ryu S., Mudry C., Obuse H., and Furusaki A., *The $\mathbb{Z}_2$ network model for the quantum spin Hall effect: two-dimensional Dirac fermions, topological quantum numbers, and corner multifractality*, New J. Phys. **12**, 065005 (2009).

[136] Nowack K.C. et al., *Imaging currents in HgTe quantum wells in the quantum spin Hall regime.*, Nat. Mater. **12**, 787 (2013).

[137] Schubert G., Fehske H., Fritz L., and Vojta M., *Fate of topological-insulator surface states under strong disorder*, Phys. Rev. B **85**, 201105(R) (2012).

[138] König M. et al., *Spatially Resolved Study of Backscattering in the Quantum Spin Hall State*, Phys. Rev. X **3**, 021003 (2013).

[139] Grabecki G. et al., *Nonlocal resistance and its fluctuations in microstructures of band-inverted HgTe/(Hg,Cd)Te quantum wells*, Phys. Rev. B **88**, 165309 (2013).

[140] Roth A., Brüne C., Buhmann H., Molenkamp L.W., Maciejko J., Qi X.L., and Zhang S.C., *Nonlocal Transport in the Quantum Spin Hall State*, Science **325**, 294 (2009).

[141] Väyrynen J.I., Goldstein M., Gefen Y., and Glazman L.I., *Resistance of helical edges formed in a semiconductor heterostructure*, Phys. Rev. B **90**, 115309 (2014).

[142] Väyrynen J.I., Goldstein M., and Glazman L.I., *Helical Edge Resistance Introduced by Charge Puddles*, Phys. Rev. Lett. **110**, 216402 (2013).

[143] Baranger H.U. and Mello P.A., *Mesoscopic Transport through Chaotic Cavities: A Random S-Matrix Theory Approach*, Phys. Rev. Lett. **73**, 142 (1994).

[144] Jalabert R.A., Pichard J.L., and Beenakker C.W.J., *Universal Quantum Signatures of Chaos in Ballistic Transport*, Europhys. Lett. **27**, 255 (1994).

[145] Anderson P.W., Thouless D.J., Abrahams E., and Fisher D.S., *New method for a scaling theory of localization*, Phys. Rev. B **22**, 3519 (1980).

[146] Abrahams E., Anderson P.W., Licciardello D.C., and Ramakrishnan T.V., *Scaling Theory of Localization: Absence of Quantum Diffusion in Two Dimensions*, Phys. Rev. Lett. **42**, 673 (1979).

[147] Lee P.A. and Ramakrishnan T.V., *Disordered electronic systems*, Rev. Mod. Phys. **57**, 287 (1985).

[148] Sheng P., *Introduction to Wave Scattering, Localization and Mesoscopic Phenomena*, Springer, Berlin Heidelberg (2006).

[149] Girschik A., Libisch F., and Rotter S., *Topological insulator in the presence of spatially correlated disorder*, Phys. Rev. B **88**, 014201 (2013).

[150] *NIST Digital Library of Mathematical Functions*, http://dlmf.nist.gov/, Release 1.0.10 of 2015-08-07, online companion to [226].

[151] Spanton E.M., Nowack K.C., Du L., Sullivan G., Du R.R., and Moler K.A., *Images of Edge Current in InAs/GaSb Quantum Wells*, Phys. Rev. Lett. **113**, 026804 (2014).

[152] Gusev G.M., Kvon Z.D., Olshanetsky E.B., Levin A.D., Krupko Y., Portal J.C., Mikhailov N.N., and Dvoretsky S.A., *Temperature dependence of the resistance of a two-dimensional topological insulator in a HgTe quantum well*, Phys. Rev. B **89**, 125305 (2014).

[153] Nichele F. et al., *Edge Transport in the Trivial Phase of InAs/GaSb*, arXiv Prepr. 1511.01728 (2015).

[154] Olshanetsky E.B., Kvon Z.D., Gusev G.M., Levin A.D., Raichev O.E., Mikhailov N.N., and Dvoretsky S.A., *Persistence of a Two-Dimensional Topological Insulator State in Wide HgTe Quantum Wells*, Phys. Rev. Lett. **114**, 126802 (2015).

[155] Cheianov V. and Glazman L.I., *Mesoscopic Fluctuations of Conductance of a Helical Edge Contaminated by Magnetic Impurities*, Phys. Rev. Lett. **110**, 206803 (2013).

[156] Maciejko J., Liu C., Oreg Y., Qi X.L., Wu C., and Zhang S.C., *Kondo Effect in the Helical Edge Liquid of the Quantum Spin Hall State*, Phys. Rev. Lett. **102**, 256803 (2009).

[157] Tanaka Y., Furusaki A., and Matveev K.A., *Conductance of a Helical Edge Liquid Coupled to a Magnetic Impurity*, Phys. Rev. Lett. **106**, 236402 (2011).

[158] Lunde A.M. and Platero G., *Hyperfine interactions in two-dimensional HgTe topological insulators*, Phys. Rev. B **88**, 115411 (2013).

[159] Budich J.C., Dolcini F., Recher P., and Trauzettel B., *Phonon-Induced Backscattering in Helical Edge States*, Phys. Rev. Lett. **108**, 086602 (2012).

[160] Crépin F., Budich J.C., Dolcini F., Recher P., and Trauzettel B., *Renormalization group approach for the scattering off a single Rashba impurity in a helical liquid*, Phys. Rev. B **86**, 121106(R) (2012).

[161] Geissler F., Crépin F., and Trauzettel B., *Random Rashba spin-orbit coupling at the quantum spin Hall edge*, Phys. Rev. B **89**, 235136 (2014).

[162] Lezmy N., Oreg Y., and Berkooz M., *Single and multiparticle scattering in helical liquid with an impurity*, Phys. Rev. B **85**, 235304 (2012).

[163] Ström A., Johannesson H., and Japaridze G.I., *Edge Dynamics in a Quantum Spin Hall State: Effects from Rashba Spin-Orbit Interaction*, Phys. Rev. Lett. **104**, 256804 (2010).

[164] Wu C., Bernevig B.A., and Zhang S.C., *Helical Liquid and the Edge of Quantum Spin Hall Systems*, Phys. Rev. Lett. **96**, 106401 (2006).

[165] Xu C. and Moore J.E., *Stability of the quantum spin Hall effect: Effects of interactions, disorder, and $\mathbb{Z}_2$ topology*, Phys. Rev. B **73**, 045322 (2006).

[166] Pikulin D.I. and Hyart T., *Interplay of Exciton Condensation and the Quantum Spin Hall Effect in InAs/GaSb Bilayers*, Phys. Rev. Lett. **112**, 176403 (2014).

[167] Jiang H., Cheng S., Sun Q.F., and Xie X., *Topological Insulator: A New Quantized Spin Hall Resistance Robust to Dephasing*, Phys. Rev. Lett. **103**, 036803 (2009).

[168] Schlosshauer M., *Decoherence, the measurement problem, and interpretations of quantum mechanics*, Rev. Mod. Phys. **76**, 1267 (2004).

[169] Zurek W.H., *Decoherence, einselection, and the quantum origins of the classical*, Rev. Mod. Phys. **75**, 715 (2003).

[170] Zurek W.H., *Pointer basis of quantum apparatus: Into what mixture does the wave packet collapse?*, Phys. Rev. D **24**, 1516 (1981).

[171] Dittes F.M., Harney H.L., and Müller A., *Nonexponential decay of a stochastic one-channel system*, Phys. Rev. A **45**, 701 (1992).

[172] Zozoulenko I.V. and Blomquist T., *Time-resolved dynamics of electron wave packets in chaotic and regular quantum billiards with leads*, Phys. Rev. B **67**, 085320 (2003).

[173] Paz J.P. and Zurek W.H., *Quantum Limit of Decoherence: Environment Induced Superselection of Energy Eigenstates*, Phys. Rev. Lett. **82**, 5181 (1999).

[174] Zurek W.H., *Environment-induced superselection rules*, Phys. Rev. D **26**, 1862 (1982).

[175] Unruh W.G. and Zurek W.H., *Reduction of a Wave Packet in Quantum Brownian-Motion*, Phys. Rev. D **40**, 1071 (1989).

[176] Kozlov D.A., Kvon Z.D., Mikhailov N.N., and Dvoretsky S.A., *Weak Localization of Dirac Fermions in HgTe Quantum Wells*, JETP Lett. **96**, 730 (2013).

[177] Olshanetsky E.B., Kvon Z.D., Gusev G.M., Mikhailov N.N., Dvoretsky S.A., and Portal J.C., *Weak Antilocalization in HgTe Quantum Wells near a Topological Transition*, JETP Lett. **91**, 347 (2010).

[178] Minkov G.M., Germanenko A.V., Rut O.E., Sherstobitov A.A., Dvoretski S.A., and Mikhailov N.N., *Weak antilocalization in HgTe quantum wells with inverted energy spectra*, Phys. Rev. B **85**, 235312 (2012).

[179] Mühlbauer M., Budewitz A., Büttner B., Tkachov G., Hankiewicz E.M., Brüne C., Buhmann H., and Molenkamp L.W., *One-Dimensional Weak Antilocalization Due to the Berry Phase in HgTe Wires*, Phys. Rev. Lett. **112**, 146803 (2014).

[180] Tkachov G. and Hankiewicz E.M., *Weak antilocalization in HgTe quantum wells and topological surface states: Massive versus massless Dirac fermions*, Phys. Rev. B **84**, 035444 (2011).

[181] Aleiner I.L., Altshuler B.L., and Gershenson M.E., *Interaction effects and phase relaxation in disordered systems*, Waves Random Media **9**, 201 (1999).

[182] Li X.G., Zhang G.F., Wu G.F., Chen H., Culcer D., and Zhang Z.Y., *Proximity effects in topological insulator heterostructures*, Chinese Phys. B **22**, 097306 (2013).

[183] Yang B.J., Bahramy M.S., and Nagaosa N., *Topological protection of bound states against the hybridization*, Nat. Commun. **4**, 1524 (2013).

[184] Wang X., Bian G., Miller T., and Chiang T.C., *Topological quantum well resonances in metal overlayers*, Phys. Rev. B **87**, 235113 (2013).

[185] Ando T. and Suzuura H., *Presence of Perfectly Conducting Channel in Metallic Carbon Nanotubes*, J. Phys. Soc. Japan **71**, 2753 (2002).

[186] Bardarson J.H., *A proof of the Kramers degeneracy of transmission eigenvalues from antisymmetry of the scattering matrix*, J. Phys. A Math. Theor. **41**, 405203 (2008).

[187] Gustafson K. and Abe T., *The third boundary condition—Was it Robin's?*, Math. Intell. **20**, 63 (1998).

[188] Levitin M. and Parnovski L., *On the principal eigenvalue of a Robin problem with a large parameter*, Math. Nachr. **281**, 272 (2008).

[189] Bender C.M., *Making sense of non-Hermitian Hamiltonians*, Reports Prog. Phys. **70**, 947 (2007).

[190] Wu H. and Sprung D.W.L., *Validity of the Transfer-Matrix Method for a Two-Dimensional Electron Waveguide*, Appl. Phys. A **58**, 581 (1994).

[191] Sakai H. and Takane Y., *Random-matrix theory of electron transport in disordered wires with symplectic symmetry*, J. Phys. Soc. Japan **75**, 054711 (2006).

[192] Takane Y., *Nonuniversal Shot Noise in Disordered Quantum Wires with Channel-Number Imbalance*, J. Phys. Soc. Japan **79**, 104706 (2010).

[193] Beenakker C.W.J., *Random-matrix theory of quantum transport*, Rev. Mod. Phys. **69**, 731 (1997).

[194] Dyson F.J., *Statistical Theory of the Energy Levels of Complex Systems. II*, J. Math. Phys. **3**, 157 (1962).

[195] Wigner E.P., *Statistical Properties of Real Symmetric Matrices with Many Dimensions*, in C.E. Porter, ed., *Stat. Theor. Spectra Fluctuations*, Academic Press, New York (1965).

[196] Dorokhov O.N., *Transmission coefficient and the localization length of an electron in N bound disordered chains*, JETP Lett. **36**, 318 (1982).

[197] Beenakker C.W.J. and Büttiker M., *Suppression of shot noise in metallic diffusive conductors*, Phys. Rev. B **46**, 1889 (1992).

[198] Büttiker M., *Symmetry of electrical conduction*, IBM J. Res. Dev. **32**, 317 (1988).

[199] Landauer R., *Spatial Variation of Currents and Fields Due to Localized Scatterers in Metallic Conduction*, IBM J. Res. Dev. **1**, 223 (1957).

[200] Nyquist H., *Thermal Agitation of Electric Charge in Conductors*, Phys. Rev. **32**, 110 (1928).

[201] Blanter Y.M. and Büttiker M., *Shot noise in mesoscopic conductors*, Phys. Rep. **336**, 1 (2000).

[202] Büttiker M., *Scattering Theory of Thermal and Excess Noise in Open Conductors*, Phys. Rev. Lett. **65**, 2901 (1990).

[203] Lesovik G.B., *Excess quantum noise in 2D ballistic point contacts*, JETP Lett. **49**, 513 (1989).

[204] Schottky W., *Über spontane Stromschwankungen in verschiedenen Elektrizitätsleitern*, Ann. Phys. **362**, 541 (1918).

[205] Blanter Y.M. and Büttiker M., *Shot-noise current-current correlations in multiterminal diffusive conductors*, Phys. Rev. B **56**, 2127 (1997).

[206] Dorokhov O.N., *On the coexistence of localized and extended electronic states in the metallic phase*, Solid State Commun. **51**, 381 (1984).

[207] Mello P.A., Pereyra P., and Kumar N., *Macroscopic Approach to Multichannel Disordered Conductors*, Ann. Phys. (N. Y.) **181**, 290 (1988).

[208] van Rossum M.C.W. and Nieuwenhuizen T.M., *Multiple scattering of classical waves: microscopy, mesoscopy, and diffusion*, Rev. Mod. Phys. **71**, 313 (1998).

[209] Mello P.A. and Pichard J.L., *Maximum-entropy approaches to quantum electronic transport*, Phys. Rev. B **40**, 5276 (1989).

[210] Martin T. and Landauer R., *Wave-packet approach to noise in multichannel mesoscopic systems*, Phys. Rev. B **45**, 1742 (1992).

[211] Mello P.A. and Kumar N., *Quantum Transport in Mesoscopic Systems: Complexity and Statistical Fluctuations*, Oxford University Press, New York (2004).

[212] Sukhorukov E.V. and Loss D., *Universality of Shot Noise in Multiterminal Diffusive Conductors*, Phys. Rev. Lett. **80**, 4959 (1998).

[213] Sukhorukov E.V. and Loss D., *Noise in multiterminal diffusive conductors: Universality, nonlocality, and exchange effects*, Phys. Rev. B **59**, 13054 (1999).

[214] Nazarov Y.V., *Limits of Universality in Disordered Conductors*, Phys. Rev. Lett. **73**, 134 (1994).

[215] Forrester P.J., *Quantum conductance problems and the Jacobi ensemble*, J. Phys. A Math. Gen. **39**, 6861 (2006).

[216] Simon S.H. and Moustakas A.L., *Crossover from Conserving to Lossy Transport in Circular Random-Matrix Ensembles*, Phys. Rev. Lett. **96**, 136805 (2006).

[217] Goetschy A. and Stone A.D., *Filtering Random Matrices: The Effect of Incomplete Channel Control in Multiple Scattering*, Phys. Rev. Lett. **111**, 063901 (2013).

[218] Speicher R., *Free Probability Theory and Random Matrices*, in A. Vershik, ed., *Asymptotic Combinatorics with Application to Mathematical Physics*, 53–73, Springer-Verlag, Berlin Heidelberg (2003).

[219] Imry Y., *Active Transmission Channels and Universal Conductance Fluctuations*, Europhys. Lett. **1**, 249 (1986).

[220] Tao T., *Topics in random matrix theory*, vol. 132 of *Graduate Studies in Mathematics*, American Mathematical Society, Providence (2012), pdf draft available here: https://terrytao.files.wordpress.com/2011/08/matrix-book.pdf.

[221] Hiai F. and Petz D., *The Semicircle Law, Free Random Variables and Entropy*, vol. 77 of *Mathematical Surveys and Monographs*, American Mathematical Society (2000).

[222] Gérardin B., Laurent J., Derode A., Prada C., and Aubry A., *Full Transmission and Reflection of Waves Propagating through a Maze of Disorder*, Phys. Rev. Lett. **113**, 173901 (2014).

[223] Pichard J.L., Zanon N., Imry Y., and Stone A.D., *Theory of random multiplicative transfer matrices and its implications for quantum transport*, J. Phys. France **51**, 587 (1990).

[224] Stone A.D., Mello P.A., Muttalib K.A., and Pichard J.L., *Random Matrix Theory and Maximum Entropy Models for Disordered Conductors*, in B.L. Altshuler, P.A. Lee, and R.A. Webb, eds., *Mesoscopic Phenomena in Solids*, 369, Elsevier–North Holland, Amsterdam (1991).

[225] Frahm K., *Equivalence of the Fokker-Planck Approach and the Nonlinear σ Model for Disordered Wires in the Unitary Symmetry Class*, Phys. Rev. Lett. **74**, 4706 (1995).

[226] Olver F.W.J., Lozier D.W., Boisvert R.F., and Clark C.W., eds., *NIST Handbook of Mathematical Functions*, Cambridge University Press, New York, NY (2010), print companion to [150].

List of Publications

- Essert, S., Richter K., *Magnetotransport in disordered two-dimensional topological insulators: signatures of charge puddles*, 2D Mater. **2**, 024005 (2015). [Chapter 3]
- Essert, S., Krueckl V., Richter K., *Two-dimensional topological insulator edge state backscattering by dephasing*, Phys. Rev. B **92**, 205306 (2015). [Chapter 4]
- Essert, S., Krueckl V., Richter K., *Using topological insulator proximity to generate perfectly conducting channels in materials without topological protection*, New J. Phys. **16**, 113058 (2014). [Chapter 5]

Acknowledgments

Now, after the completion of this work, I would like to express my sincere gratitude to the many people that, in one way or another, supported me over the years.

First, I would like to thank Klaus Richter for giving me the opportunity to work in his group, the very pleasant working atmosphere of which is to a good part induced by his calm and thoughtful leadership. Without knowing me much, he immediately had faith in me and constantly supported me throughout.

Next, I am deeply indebted to Viktor Krückl with whom I had a very fruitful scientific collaboration. I always drew a lot of pleasure from our team work and it led, amongst other things, to many of the results shown in this thesis.

Special thanks also go to İnanç Adagideli, Cosimo Gorini, and Michael Wimmer. When I will be leaving academic research, it will be our hours-long discussions that I will miss, and which I will always remember as "the beautiful side of science as it should be".

Moreover, I would like to thank the members of our weekly topical group meeting for their inspiring ideas: Jan Bundesmann, Cosimo Gorini, Lisa Heße, Raphael Kozlovsky, Viktor Krückl, Ming-Hao Liu, Dmitry Ryndyk, Andrea Spichtinger, Matthias Stosiek, and Fedor Tkatschenko.

I am also grateful to Petra Högl, Raphael Kozlovsky, Viktor Krückl, and Andrea Spichtinger for patient and thorough proofreading of parts of this thesis and I thank my fellow system administrators Tobias Frank and Josef Michl for sparing me from much of the work in the last months.

In addition, I would like to thank my office mates Thomas Engl and Andrea Spichtinger as well as all other members of the chair for making my life at the university the very enjoyable experience that it was.

I acknowledge funding from the DFG within FOR 1483 and SPP 1666 as well as from the Elite Network of Bavaria within the graduate school "Topological Insulators".

Finally, I am deeply thankful to Beate who was not only a constant source of personal support but who also proofread the whole thesis and provided many good suggestions.